Magnetic anisotropies and exchange bias in ultrathin cobalt layers for the tunnel anisotropic magnetoresistance

Filippo Jacopo Ferraro

UNIVERSITÉ GRENOBLE ALPES

THÈSE

Pour obtenir le grade de

DOCTEUR DE L'UNIVERSITÉ GRENOBLE ALPES

Spécialité : **Physique/Nanophysique**

Arrêté ministériel : 7 août 2006

Présentée par

Filippo Jacopo FERRARO

Thèse dirigée par **Alain MARTY**
co-encadrée par **Laurent Ranno** et **Anne BERNAND-MANTEL**

préparée au sein de **l'Institut Néel**
dans **l'École Doctorale de Physique de Grenoble**

Magnetic Anisotropies and Exchange Bias in Ultrathin Cobalt Layers for the Tunnel Anisotropic MagnetoResistance

Thèse soutenue publiquement le **14 décembre 2015**,
devant le jury composé de :

Mme. Véronique PIERRON-BOHNES
Directrice de Recherche CNRS Strasbourg, Rapporteur
M. Marc RESPAUD
Prof. INSA Toulouse LPCNO, Rapporteur
M. Frédéric OTT
Ingénieur-chercheur CEA, Membre
M. Mairbek CHSHIEV
Prof. UJF (ou UGA) Spintec, Président du jury
M. Alain MARTY
Chercheur HDR CEA, Directeur de thèse
Mme. Anne BERNAND-MANTEL
Chargée de Recherche CNRS, Co-encadrant de thèse

A nonna Dina e nonna Cecilia

Declaration

I hereby declare that except where specific reference is made to the work of others, the contents of this dissertation are original and have not been submitted in whole or in part for consideration for any other degree or qualification in this, or any other university. This dissertation is my own work and contains nothing which is the outcome of work done in collaboration with others, except as specified in the text and Acknowledgments.

Filippo Jacopo FERRARO
March 2016

Acknowledgements

First I would like to acknowledge Véronique Pierron-Bohnes and Marc Respaud, who have kindly accepted to evaluate this thesis work and secondly Frédéric Ott and Mairbek Chshiev, who have accepted to be members of the jury. I also acknowledge the financial support of the French National Research Agency (ANR), which allowed me to pursue this Ph.D. research.

My gratitude goes to Laurent Ranno and Anne Bernand-Mantel for their help and guidance over the past three years, without them and all the constructive discussions none of this would have been possible. I am very grateful to Alain Marty, my Ph.D. thesis director, for the advices and the support provided, thanks which extend to the whole INAC/NM group. I would also like to thank Dominique Givord for all the insight and encouragement to carry on my research. A special mention goes to Nora Dempsey, who "adopted" me in her group and was a constant friend over these years.

I am also very grateful to all the collaborators and staff of the Institut Néel. A thanks to all the Nanofab group and to Philippe David, Eric Mossang and Didier Dufeu for their precious help. My gratitude goes to all the people of the lab and towards the group of "colleagues" or should I say friends, that I had the opportunity to meet during this experience: Heidi, Nilay, Ozan, Damien, Dmitry, Geta, André, Anja, Yannick, Thibaut, Gildas, Doan, Marine and many many others, my great thanks.

A special thanks to my friends Zini, Panz and Giulio, *the Wolfpack*, for everything they represent and have meant during these years. I have also an obligation towards another group of people, we are far away but you always managed to make me feel home, it is an honor to be your friend and the president of the association, thanks *i Ratti*.

Finally, I want to thank my Dad, my Mum and my sister Ludovica for all their support. You are the best family I could have asked for.

Grazie a tutti.

Table of contents

List of figures

List of tables

Introduction

In a series of lectures called "The Character of Physical Law" [50] delivered in 1964 at Cornell University, the physicist Richard Phillips Feynman said:

> *"There was a time when the newspapers said that only twelve men understood the theory of relativity. I do not believe there ever was such a time. [...] On the other hand, I think I can safely say that nobody understands quantum mechanics." [R.P. Feynman, 1964] [50].*

If it rightful to say that we do not understand how the quantum description of nature gives rise to the reality we perceive and even if it seems to be the most implausible theory ever formulated, it is unavoidably true that countless observation made it necessary. Quantum mechanics very accurately describe the physics of very small objects and it is often the only tool to reveal the physical law playing at the nanoscale ($1 - 100 \cdot 10^{-9}$m) and, if we go further, the behavior of the subatomic particles that make up all forms of matter.

Spintronics is a relatively new science, closely related to the quantum mechanical nature of electrons and one of the attractive frontiers in condensed matter and solid state physics due to its potential application in nanoscale devices [47]. The basic concept of spintronics is the manipulation of spin currents, the charge and the spin of the electrons are simultaneously considered and exploited. In spintronics the information is carried by the spin, whereas in classic microelectronics only the charge is considered. Adding the spin degree of freedom offers the opportunity for a new generation of devices which combine standard microelectronics with spin-dependent effects that arise from the interaction with the magnetic properties of the material [232]. In conventional microelectronics the charges are manipulated with an electric field and the spins are ignored. The spin was considered in magnetic recording, although solely through its macroscopic manifestation: the magnetization of a ferromagnet [46].

The second half of the 20th century can be considered the microelectronics era. During that period the world went through a revolution based on the digital logic of electrons [178]. From the earliest transistor to the powerful microprocessor in today's computers, most electronic devices have employed circuits that express data as binary flow of electric

charges. These data are called bits, made of ones and zeros, represented by the presence or absence of electric charges. The technology which emerged from this simple logic has created a multi-trillion dollar industry. The growth of microelectronics and the technological progress are summarized by the popular Moore's Law [134], which theorize the doubling of chip performance (speed and density) every 18 months. Yet even Moore's law will run out of momentum as the size of individual bits approaches the dimension of atoms [178]. To surpass Moore and to enhance the multi-functionality of devices researchers want to exploit the spin property of the electron. The spins can point either 'up' (↑) or 'down' (↓), hence they are naturally coded in binary logic and moreover spins can be easily manipulated with an external magnetic field. For these reasons, in parallel to the conventional semiconductor development, a series of diversified technology started to be investigated in order to improve and enrich electronic devices with new functionalities. This approach is know as "More than Moore" and it is inserted in the International Technology Roadmap for Semiconductors [8, 70].

Historically the influence of the spins on the mobility of the electrons in ferromagnetic metals was first observed in 1856 by Thomson who discovered the MagnetoResistance (MR) of Fe and Ni [213]. The MR relationship with the electron spin was suggested 80 years later, by Mott [137, 138]. This discovery, as often happen in spintronics (and physics in general), was overlooked for many years. The pure microelectronic picture started to change drastically in 1988, when Baibich (Albert Fert's group) [11] and Binash (Peter Grünberg's group) [19] independently reported the discovery of the Giant Magneto Resistance (GMR) in magnetic multilayers. The GMR was the first step on the road of the utilization of the spin degree of freedom in magnetic nanostructures and triggered the development of an active field of research which we now call spintronics [47]. From that milestone, research and technology developments in the field of spintronics have grown tremendously and already have had a major impact on the data storage industry. In relation with data storage, in 2005 Scientific American published an article called "Kryder's law" [223] where they claim: *"The doubling of processor speed every 18 months is a snail's pace compared with rising hard-disk capacity"*. This is true if we consider the amazing evolution of Hard Disk Drives over the last 60 years. The transformation is incredible, we passed from the first commercialized hard disk by IBM in 1956, which could store 3.75 MB and was the size of a wardrobe, to today where the amount of information that can be stored in a square-inch reached 1.5 TB. Using data storage densities as reference that means passing from 2000 bits to 1.5 terabyte per squared inch, which represents a 6-billion-fold increase. This technological revolution was made possible by the constant improvement and advancement of experimental techniques. In order to show the GMR effect the layer thicknesses must be in the nm range (inferior

to the spin diffusion length of the electrons). This was not possible until the development of techniques like the Molecular Beam Epitaxy (MBE), which allowed the fabrication of multilayers composed by very thin individual layers.

The spintronics research field is mostly technologically driven, the time between a scientific discovery and its technological application is vastly reduced nowadays and the economical impact of each discovery cannot be underestimated. Nevertheless, it would be a fallacy to consider the eventual applications more important than the fundamental insight provided by spintronics research. The spin is a purely quantum-mechanical entity and its interaction with the electron charge or the atomic environment provides a unique opportunity to understand the quantum nature of matter and solid state physics. Because electronic, crystalline and magnetic properties are crucial in spintronics, solid states physics and material science research were particularly boosted during this evolution [231].

The current efforts in designing spintronics devices involve two different approaches. The first is perfecting the existing technology by either developing new materials or making improvements (variations) in the existing devices which would allow further scalability. The second effort, which is more radical, focuses on finding novel ways of both generation and utilization of spin-polarized currents. The second way requires to change the way we normally look at things, like the discovery of GMR changed the way we look at microelectronics. Many effects that were unimaginable are now being observed and could lay the foundation for new spintronics discoveries that promise to have even bigger impact on future technologies. We can choose some examples between the most promising effects of today's spintronics:

- The spin transfer torque (STT) [193, 201] and the current induced magnetization reversal [67, 81, 114]. In spin transfer experiments, one manipulates the magnetic moment of a ferromagnetic body without applying any magnetic field but only by transfer of spin angular momentum from a spin-polarized current. The magnetization switching by spin transfer will be applied to the writing process of the next generation of STT-MRAM.

- The electric field (E-field) control of magnetization [17, 36, 181]. An E-field can help to locally reduce the anisotropy in a short time period to help the magnetization reversal. Moreover an E-field can control the DW velocity, providing a first step towards electrical control of domain wall devices, like racetrack memories [161]. This opens up possibilities of real-time control of DW motion at extremely low power cost.

- The antiferromagnetic spintronics(an emerging field). In spintronics, antiferromagnetic (AFM) materials, lacking magnetization and spin polarization, are almost completely neglected. One exception is the passive use of AFM to pin the magnetization of a

ferromagnet (FM), also known as the exchange bias (EB) [125, 153]. Due to the nature of AFM materials (complex magnetic structure, essential role of exchange interactions, absence of macroscopic magnetization) and due to the lack of response to an external magnetic field, studying these materials is rather challenging [192]. Nevertheless, even without macroscopic magnetization, antiferromagnets are affected by spin-polarized currents. Thus one can think of a new device where the rotation of the moment in a magnetic element (FM or AFM), taking into account the Spin-Orbit Coupling (SOC) could affect the Density of States (DOS), this will result in a change of the tunnel resistance across a barrier. This resistance change can be the signal exploited in a new class of magnetic tunnel junction (MTJ) devices with just one magnetic electrode. This effect is called Tunnel Anisotropic Magneto Resistance (TAMR). One of the most challenging scenarios foresees the replacement of ferromagnetic electrodes with antiferromagnetic ones. The rigidity to external magnetic fields and the absence of stray fields make AFMs particularly favorable materials for ultrafast and ultrahigh-density spintronics [191]. A first antiferromagnetic spin valve like based on the TAMR has recently been demonstrated by the group of Jungwirth [116, 159].

Spintronics is a fast paced world where exciting phenomena, often unimaginable just a few years ago, are now being actively investigated. A world where effects neglected for years are suddenly rediscovered (or reimagined) and whose properties could result decisive in new, more appropriate, context. It is essential to point out that these effects are usually not new, no new physic was invented, no new materials were discovered, these effects were always there, we were just not looking or we did not observe with the right prospective.

Within that spirit, the focus of the research in this dissertation is to deepen the understanding on nanomagnetism and spintronics phenomena occurring at the nanoscale, when one dimension is pushed to the lowest limit. We investigated the interplay of magnetic properties and interfacial effect in asymmetric structure, more specifically Pt/Co/AlOx trilayers where the ultrathin Co is interfaced with Pt (a heavy metal) on one side and with AlOx (a light metal oxide) on the other. These asymmetric structures, with just one magnetic electrode, are the key ingredient and starting point to the micro and nanofabrication of TAMR devices. To build a working perpendicular TAMR device requires both, good understanding of the magnetic anisotropies origin and a good mastering of the thin film growth and characterization techniques to obtain suitable electric and magnetic properties. Hence, within the described spirit, this thesis will address several aspects of Pt/Co/AlOx system and the associated fundamental physics properties. Particular attention will be dedicated to the perpendicular magnetic anisotropy (PMA) [64] and to the exchange bias effect [125] which both appear in this system. These effects are far from being completely understood and some open questions

still remain unanswered. One of the peculiarities of this work is the tentative to probe and observe these effects near their physical limit (i.e. reducing layer thickness for the EB) or in particular geometry (i.e. with the possibility to tailor the properties in a continuous way for PMA). This manuscript is organized as follows:

Chapter 1: provides some fundamental notions needed to follow the arguments discussed in this thesis. The chapter is divided in two small sections. The first will be dedicated to general magnetism concepts, the second part will be committed to the understanding of the crucial discoveries that lead the spintronics field. The idea for this chapter is to uniform the concepts and to provide a general background for the readers.

Chapter 2: will describe the main experimental techniques utilized to grow, design/pattern and characterize the samples measured during this thesis. The theoretical principles and the details/limitations of each experimental technique will be provided. Particular interest will be dedicated to describe the wedged deposition geometry used in this thesis.

Chapter 3: is committed to the study of the anisotropies in ultrathin Cobalt layer, with particular attention on Pt/Co/MOx systems (M=Al or Co). The perpendicular magnetic anisotropy in these two systems will be studied as a function of the wedge geometry with varying temperature. The role of the antiferromagnetic CoO and the effect of the annealing temperature on the PMA will be investigated and discussed.

Chapter 4: will focus on exchange bias in ultrathin Co/CoO bilayer. In the beginning we will provide a description of the fundamental aspect and of the diverse models proposed to explain the EB phenomenon. Afterward we will focus on exchange bias measurements in the sub-nanometer regime, which is the ultimate frontier for planar devices. The idea is to use our system to shed new light on the fundamental aspects of this effect and discuss its existence in limit conditions.

Chapter 5: is dedicated to the investigation of the Tunnel Anisotropic Magneto Resistance. We first present the state of the art on TAMR research with particular attention to metallic system. We will then describe the experimental devices geometry, the encountered challenges and their solutions. Afterwards we will proceed to analyze and discuss the TAMR measurements comparing our work on Pt/Co/AlOx with similar ones. To conclude with the perspective and ideas for future studies.

Finally in the **General Conclusions** a summary of the most relevant results and some perspective on the analyzed system and phenomena concludes the manuscript.

Chapter 1

Notions of Magnetism and Spintronics

1.1 Magnetism

1.1.1 Magnetic order

The beginning of modern magnetism dates back to 1922, when Stern and Gerlach experimentally found that the electron is defined not only by its charge e but also by two possible magnetic states. The discovery was done by firing a beam of silver atoms across an applied magnetic field, the atoms where deflected by the gradient field and split into two distinct populations [59]. With this brilliant experiment the two scientists proved the space quantization of the magnetic moments [51]. Three years later, in 1925, a theoretical explanation was found by Uhlenbeck and Goudsmit. They postulated that the electron possesses an intrinsic angular momentum, named spin [217], with two possible states, 'spin up' ($\uparrow$) and 'spin down' ($\downarrow$). This angular momentum gives rise to a magnetic moment m_s in the electron when interacting with a magnetic field. We can define the spin of an electron as:

$$m_s = \pm \mu_B z \tag{1.1}$$

With z being the moment axis and μ_B being the Bohr magneton [104]. μ_B is a physical constant and the natural unit for expressing the magnetic moment of an electron. μ_B can originates from either the orbital or the spin angular momentum and is defined as:

$$\mu_B = \frac{e\hbar}{2m_e} \tag{1.2}$$

The sum of the spins of the electrons in an atom gives the total spin magnetic moment$S$. Its value depends on the number of energy shells and sub-shells which are filled according to Hund's rule and Pauli's exclusion principle. Filled sub-shells do not contribute to magnetism, having all the magnetic moments compensated; only partially filled sub-shells contribute to magnetism. On a macroscopic scale, the coupling between magnetic moments determines the type of magnetic order present in the considered material. The coupling energy is defined as:

$$E_{ij} = -J_{ij}\vec{m}_i.\vec{m}_j \tag{1.3}$$

With J_{ij} the coupling constant and i and j the indices of first neighbours spins. Depending on J_{ij} we can obtain different spin configurations:

- If $J_{ij} > 0$, the magnetic moments align in the same direction and the material is defined as ferromagnetic (FM) (see figure 1.1a).
- If $J_{ij} < 0$, the spins align in opposite directions. If the net moment is equal to zero, the material is named antiferromagnetic (AFM) (see figure 1.1b), otherwise, in case of unbalance, it is named ferrimagnetic (see figure 1.1c).
- The coupling energy is an ordering energy, when thermal energy overpasses it, the magnetic order is lost and the material becomes paramagnetic (see figure 1.1d).

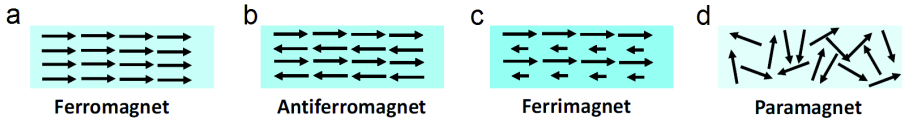

Fig. 1.1 Schematic of the spin configurations for paramagnetic, ferromagnetic, antiferromagnetic and ferrimagnetic materials.

The temperature at which a FM material passes to its paramagnetic state is named Curie temperature (T_C); for the AFM case, it is named Néel temperature (T_N) [155]. Examples of strongly FM materials are iron (Fe), cobalt (Co) and nickel (Ni). Ferromagnetism may also be found in alloys, like CoFe or NiFe. Antiferromagnetic materials can be single elements like manganese (Mn) or chromium (Cr), oxides (NiO, FeO, CoO, MnO) or alloys (IrMn, PtMn, FeMn, CrMn).

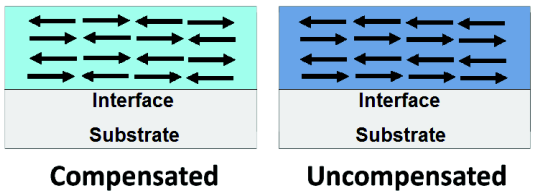

Fig. 1.2 Schematics spin configurations for a compensated or uncompensated antiferromagnetic material.

In the case of AFM materials, the spin configuration necessary to have a zero net magnetic moment may assume different forms. At the interface, the AFM can be modeled as compensated or as uncompensated, see figure 1.2. In the first case each atomic plane presents spins with opposite directions, giving a net moment equal to zero. For the uncompensated configuration, each plane has a net moment with alternating spin directions. During this thesis we will mostly deal with ferromagnetic Co and its oxide CoO, which is a natural antiferromagnet. For completeness, in the next subsection we will briefly describe their characteristics.

Cobalt: a ferromagnetic material

Cobalt is the principal ferromagnetic materials used in this thesis. Co is ferromagnetic at room temperature and has a rather large Curie temperature (T_C) of 1115°C [28]. Co magnetic moment is equal to $1.6-1.7$ Bohr magnetons per atom [139]. Metallic cobalt has two crystallographic structures: hcp and fcc. At room temperature and without any annealing the usual structure is hcp. A transition between hcp and fcc structures ideally occurs at 450°C, but in practice, the energy difference is so small that random inter-growth between the two structure is common [99]. We will never measure (or grow) samples at temperatures higher than room temperature, therefore we will consider only hcp structure. Different values for the spontaneous magnetization are reported in literature, for bulk Co, the value of $1.44 \cdot 10^6$ A/m at 300K is the most reported and commonly accepted [109, 140, 188]. The bulk Co magnetization increases with decreasing temperature, the increase for pure bulk Co is only $\sim$1% between 300K and 5K. This low increase is due to the large T_C of Cobalt, which allows the material magnetization to be stable for large temperature ranges.

This picture can change in thin film, where T_C is reduced due to the lower Co thickness [183], this can create a larger variation for the magnetization (compared to bulk Co), when the system is cooled down from room temperature to cryogenic temperature. To understand its impact on our system, we performed VSM-SQUID measurements on Pt/Co/AlOx multilayer at different temperatures, the curves show that for relatively thick Co layers ($0.5-2$ nm) there

is no large change in the measured magnetization value between 300K and 5K. Moreover, in our experimental work on thin layers the uncertainty on the extracted values, such as the anisotropy field (see chapter 3), or the exchange bias energy (see chapter 4) normally comes from the deposited layer thickness and not from the magnetization value. Therefore, even if the work that will be carried out during this thesis will be mostly performed on thin Co layers, the choice will be to assume that the Co magnetization does not vary with temperature.

Cobalt is a weakly reducing metal that is protected from oxidation by a passivating oxide film. In relatively thick Co film ($t_{Co} > 5$nm), 2.5 nm of CoO are formed at the surface in contact with the atmosphere [195]. CoO is a natural antiferromagnet, the Co/CoO bilayer system is the one in which the Exchange Bias phenomenon was discovered by Meiklejohn and Bean in 1956 [125].

Cobalt Oxide: an antiferromagnet

CoO (Cobalt monoxide) is an antiferromagnet with a bulk Néel temperature (T_N) of 294K [79, 215], which is usually reduced in thin film [72, 75, 131]. CoO has a cfc rock-salt structure (NaCl-like) where Co^{2+} and O^{2-} planes alternate along the (111) direction in an hexagonal mesh (see figure 1.3). The antiferromagnetic transition is associated to a cubic-to-monoclinic crystallographic distortion. In CoO AFM structure, Co forms ferromagnetic planes antiferromagnetically coupled along the (111) direction. Due to the spin-orbit coupling interaction, the orbital moment and the spin tend to be oriented nearly along the FM plane axis with a collinear spin structure.

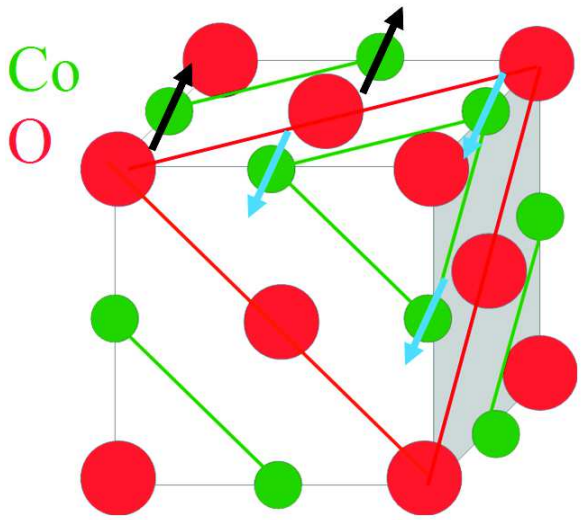

Fig. 1.3 CoO typical pseudo face-centered cubic structure.

It is generally accepted that the CoO magnetic moments are all oriented in the monoclinic plane, pointing closely in the cubic (001) axis [97]. In Figure 1.3 the moments are oriented along the (117) direction [75], which is a trade-off between the magnetic dipole forces and the crystal anisotropy which tend to order the moments within the (111) plane and parallel to (001) respectively. The magnetic moment per atom is evaluated around 3.98 μB, revealing a large orbital contribution. The strong interaction between spin and orbital magnetic moment through the spin-orbit coupling is at the origin of the large CoO magnetic anisotropy energy [97, 184]. CoO has a magnetocrystalline anisotropic of $K_{V,CoO} = 28MJ/m^3$, which was calculated from ab-initio in 1957 by Kanamori [79].

1.1.2 Magnetic energies

We will now briefly review the energy governing the magnetic behavior of a ferromagnetic layer, in which (for simplicity) only a single magnetic domain is present. The equilibrium status will be determined by a trade-off between four competing energies [168]. The total energy will be given by:

$$E_{TOT} = E_{ex} + E_{dip} + E_{anis} + E_{Zeeman} \tag{1.4}$$

The energies are the exchange energy, the dipolar energy (shape anisotropy), the magnetocrystalline anisotropy energy, and the Zeeman energy respectively. We can describe them as follows:

- Exchange energy: it is the main energy and is related to a short range coupling, which involves wavefunction overlap. Coulomb repulsion is a main ingredient of this magnetic coupling. For a FM material, the coupling is positive and tends to align all the spins along the same direction (for the various possible coupling constant see equation 1.3).

- Dipolar energy: describes the influence on each spin of the magnetic field generated by all the other spins in the material. It is a long range interaction. This coupling energy decreases as the cube of the distance and depends on the magnetization of the material. Although the dipolar energy is small when compared to the exchange coupling at atomic distance, it becomes dominant at long distance. E_{dip} tends to create a demagnetization field antiparallel to the direction of the magnetization. This field tends to demagnetise the sample and reduces the energy originating from the presence of poles in the FM materials. The magnetic field creastes flux lines outside the material.

It is called the stray field or the dipolar field. Exchange energy and dipolar energy play two opposite roles. The resulting magnetic configuration is a compromise between both energies.

- Magnetocrystalline anisotropy energy: it is an energy which depends on the crystallographic directions of the material and acts individually on each spin. The symmetry of the crystal of the FM (or AFM) material tends to align the moments along one axis, defined as the easy axis. For a uniaxial anisotropy, the magneto-crystalline energy can be written as: $E_{anis} = -K_{anis} V \cos^2 \theta$, where K_{anis} is the anisotropy constant of the material, V the volume and θ the angle between the magnetization and the easy axis. Positive K_{anis} corresponds to an easy axis, negative K_{anis} corresponds to a hard axis (and easy plane).

- Zeeman energy: it is the energy which tends to align the spins along the direction of the applied magnetic field H_a. The Zeeman energy can be defined as: $E_{zeeman} = -V \mu_0 M_S H_a$, with M_S the saturation magnetization of the material, H_a the applied field and V the magnetic volume.

1.1.3 Stoner-Wohlfarth model

In 1948 Edmund Clifton Stoner and Erich Peter Wohlfarth developed and published the Stoner-Wohlfarth model [203]. The model describes the response of randomly oriented magnets (a FM material) under an applied field. The authors of this model considered the case of an ellipsoidal-shaped FM material [211]. One of the hypothesis of the model consists in assuming a uniform magnetized ferromagnet. The system must also be small enough to be modeled as a macrospin, for a sketch of the ellipsoidal system see figure 1.4a. Under an applied magnetic field H_a, the magnetization reverses coherently in the field plane. The energy of the system will be:

$$E = K_{anis} V \sin^2(\theta) - \mu_0 M_S V H_a \cos(\phi - \theta) \tag{1.5}$$

where ϕ is the angle between the field and the easy axis and θ the angle between the magnetization and the easy axis. K_{anis} is the magnetic anisotropy, V is the volume of the magnet, M_S is the saturation magnetization, and μ_0 is the vacuum permeability. The first term is the magnetic anisotropy and the second the energy of coupling with the applied field (Zeeman). When the field is along the easy axis, the system presents two equilibrium states at $\theta = 0°$and $\theta = 180°$separated by an energy barrier equal to:

$$\Delta E_{\pm} = K_{anis} V \left(1 \pm \frac{\mu_0 M_S H}{2K_{anis}}\right)^2 \tag{1.6}$$

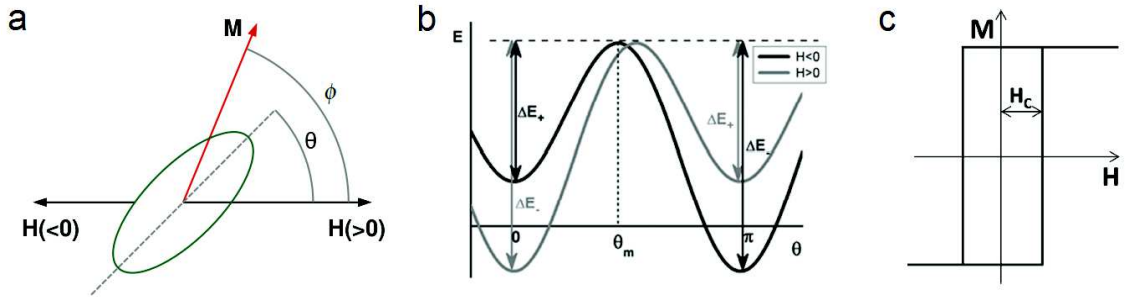

Fig. 1.4 a. Ellipsoid used in the Stoner-Wohlfarth model. The dashed line is the easy axis of the particle. b Two equilibrium states of the Stoner-Wohlfarth model for $\theta = 0$ and $\theta = \pi$. c. A typical hysteresis loop (adapted from [203]).

For a large enough H the barrier is overpassed and the magnetization is reversed, switching from one equilibrium state to the other. The field at which the switching takes place is called the coercive field and it is calculated to be :

$$H_C = \frac{2K_{anis}}{\mu_0 M_S} \tag{1.7}$$

When a field larger than H_C is applied back and forth along the axis, a full M(H) loop is performed. The magnetization curve as a function of the applied field takes the name of hysteresis loop, shown in figure 1.4c. If the field is applied with an angle ϕ with respect to the easy axis of magnetization, the field necessary to reverse the magnetization is reduced; the minimum field occurs for $\phi = 45°$. $H_c(\phi)$ describes the Stoner-Wolhfarth astroid.

1.2 Spintronics

Spintronics is the field of electronics which exploits the electron spin and it has developed as one of the major area of condensed physics. Spintronics has both great fundamental interest and high potential for applications in Information Technologies and Telecommunications. The discoveries that lead to spintronics and on which the spintronics field has its foundation will be now briefly discussed.

1.2.1 Anisotropic Magneto Resistance

The first step towards the spintronics world was the discovery of Magneto Resistance. Magneto Resistance (MR) defines the property of a conducting material to change the value of its electrical resistance under an applied external magnetic field. The effect was first discovered by William Thomson (better known as Lord Kelvin) in 1851 on Iron and Nickel [213]. Thomson noticed how the resistance of the material changed according to the direction of the applied magnetic field with respect to the flowing current. The resistivity decreased if they were perpendicular ($\rho \perp$) and increased if they were parallel ($\rho //$) to each other. The difference $\Delta\rho = \rho \perp -\rho //$ is called Anisotropic Magneto Resistance (AMR). The effect is in the order of few percents (0.1-1%).

The effect arises from the scattering of conduction electrons on magnetic moments. It requires some spin-orbit interaction and it depends on the material. The general effect is a deformation of the electron cloud which changes slightly as the direction of the magnetization rotates, consequently there is a change in the numbers of scattering events in the flowing electron current. The effect of the magnetization rotation is to change the scattering cross section with the current density J flowing into the medium. Even if the AMR never exceeds few percents [123], this change was large enough for technological application in hard disk read heads (field sensing). The two major advantages of AMR devices with respect to magneto-inductive coils was the possibility of downscaling and the ability to work in the static conditions. For these reasons AMR sensors soon replaced the classical magneto-inductive coils in hard-drive read heads. AMR read heads were first commercialized in the early 1990s by IBM, with the IBM 9345 HDD.

1.2.2 Giant Magneto Resistance

The second huge step towards current technology was the discovery of Giant Magneto Resistance (GMR) in 1988. Baibich et al. (Albert Fert's group) [11] and Binash et al. (Peter Grünberg's group) [19] reported independently a large magneto resistance in magnetic multilayers, one order of magnitude larger than AMR. The first GMR measurements are shown in figure 1.5.

The main applications of GMR are in magnetic field sensors, read head for hard disk drives, biosensors, microelectromechanical systems (MEMS) and magnetoresistive random-access memory (MRAM) to mention some. The GMR discovery changed the world of magnetic recording, as a recognition Fert and Grünberg were awarded the Nobel Prize in Physics in 2007.

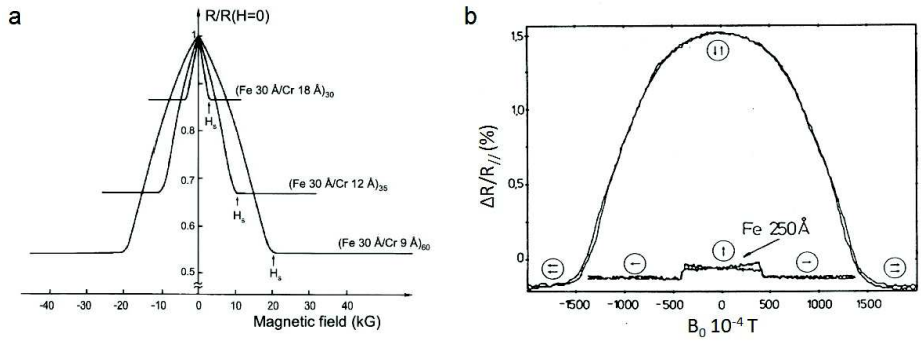

Fig. 1.5 GMR measurement as first reported by a. Fert's [11] and b. Grünberg's [19] groups. When the magnetic field is increased, the resistance decreases until the magnetizations of the Fe layers are parallel to the applied field.

GMR is based on a multilayer system in which the simplest stack is composed of two ferromagnetic (FM) layers separated by a nanometer-thin non-magnetic (NM) metal. The NM spacer thickness controls the FM layers coupling which configuration can be made parallel or antiparallel at zero applied field. The coupling between thin layers of magnetic materials separated by a non-magnetic spacer material was found to oscillate between parallel and antiparallel configuration as a function of the distance between the layers. This ferromagnetic/antiferromagnetic oscillation is predicted by the RKKY theory [27, 174]. The thickness of the NM spacer must be carefully controlled in the sub-nm range, this was only possible with the invention of new deposition techniques like the Molecular Beam Epitaxy. A sketch of the system can be seen in figure 1.6.

The spin-flip scattering is less likely to happen than spin-preserving scattering, therefore this phenomenon can be modeled with a two spin current model [48], one with spin 'up' ($\uparrow$) and one with spin 'down' ($\downarrow$). The coupling between both currents is really small, therefore almost no interaction occurs between them. It is also important to notice that the spin is conserved after a scattering event, which makes spin-flip events less frequent. Moreover, if the NM layer thickness is smaller than the electron mean free path its resistance can be neglected [48].

If we now consider the band structure of a 3d FM metals (i.e. Fe, Co, Ni) we notice that the density of states at the Fermi level is different for spin $\uparrow$ and spin $\downarrow$ populations. In the current perpendicular to plane (CPP) configuration, applying an electric field to the material will cause the conduction electrons to cross the GMR stack (see figure 1.6). The larger is the density of state at the Fermi level, the larger are the number of diffusion events. Consequently the majority-spin electrons will scatter less than the minority ones [48]. This picture holds if the spin diffusion length is larger than the NM layer thickness (t_{NM}).

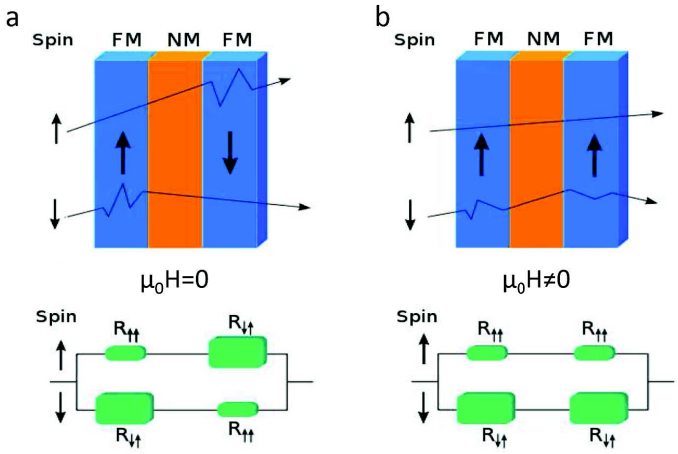

Fig. 1.6 Schematic representation of two fluids model electron transport in a FM/NM/FM stack and equivalent resistor networks in the a. anti-parallel and b. parallel configuration.

Taking into account the trilayer structure of Binash's paper [19]. At zero applied field the two FM layers are antiferromagnetically coupled (see figure 1.6a). When the current is sent through the trilayer, the spin-up electrons of the current will have a weak scattering with the first FM layer and a strong one with the second one; the opposite will occur for the spin-up populations. When a large magnetic field is applied (see figure 1.6b), both FM layers are aligned along the direction of the applied field. In this case, one of the two spin current population is weakly scattered and the other one highly scattered. This can be modeled with an equivalent resistor scheme (in green in figure 1.6). In the two cases the equivalent resistances are:

$$R_{\mu_0 H=0} = \frac{R+r}{2} \qquad and: \qquad R_{\mu_0 H\neq 0} = \frac{2rR}{r+R} \tag{1.8}$$

With R for strong scattering and r for weak scattering. The larger the resistance difference, the larger the GMR which is defined as the relative difference of these two resistances:

$$GMR = \frac{R_{\mu_0 H=0} - R_{\mu_0 H\neq 0}}{R_{\mu_0 H\neq 0}} = \frac{(R-r)^2}{4rR} \tag{1.9}$$

GMR does not depend on the direction of the current but on the relative orientation of the magnetization of the two F layers (in contrast with AMR). Nonetheless, the magnetic fields required to align the magnetizations of the different FM layers is rather large making

it difficult to implement this effect onto magnetic recording devices. To overcome this limitation the spin valve structure was proposed by Dieny et al in 1991 [42].

1.2.3 Spin Valve structure

In a spin valve structure the relative orientation of the magnetization of two FM layers is still field dependent, although the saturation field required to align them parallel (or anti-parallel) is considerably reduced thanks to the exchange bias coupling, which allows to pin one electrode, the second one being essentially free to rotate. The spin valve structure will consist of a stack with a pinned electrode (an AFM/FM bilayer), a non-magnetic metal and a free electrode made of a soft ferromagnet [42]. This is sketched in figure 1.7 a. The NM layer magnetically decouples the two FM layers and maximizes the transmission of polarized electrons [41].

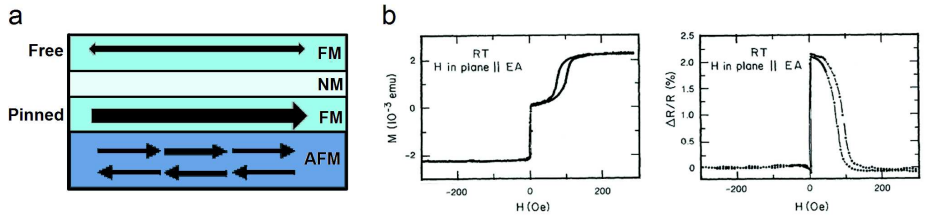

Fig. 1.7 a. Schematic view of the layers composition in a spin valve structure. b. Magnetization curve and relative change in the resistance (adapted from [209])

The uncoupled NiFe layer, indicated with (free) in figure 1.7, being a soft ferromagnet, reverses at very low applied fields. On the other hand, the interface coupling at the AFM-FM interface creates a unidirectional anisotropy in the bilayer (pinned) that stabilizes the magnetization along the easy axis direction. This results in a shift of the hysteresis loop of the bilayer as shown in figure 1.7b. The different switching fields of the two FM layers are due to the presence of exchange bias coupling. The fundamental improvement introduced by the spin valve structure is the possibility to observe the resistance switch at very low fields (compared to the high fields required in a RKKY-coupled GMR multilayers). In Dieny's paper [41, 42], the spin valve structure presented a magneto resistance of maximum 5% at room temperature (RT). Further improvements of the spin valve stack allowed to reach 24% GMR at RT [45]. Its main technological application, still present in nowadays devices, is in MR read heads for hard disk drives and in mobile phone as compass.

1.2.4 Tunnel Magneto Resistance

Tunnel Magneto Resistance was first observed in 1975 by Jullière [78]. Jullière reported a 14% effect on a Fe/Ge/Co trilayer junction at 4.2K. TMR is based on a stack similar to the one used in GMR devices. CPP-TMR takes places between two ferromagnetic layers separated by a thin insulator, which acts as a tunnel barrier. If the insulating layer is sufficiently thin, the electron can quantum-mechanically tunnel through it. The probability of tunneling depends on the density of states (DOS) at the Fermi level (E_F) and on the avalaibility of unoccupied states where electrons can jump, see figure 1.8.

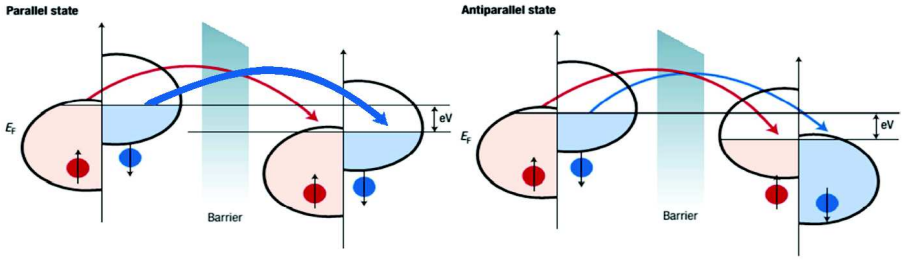

Fig. 1.8 Schematic representation of the spin tunneling through an insulating layer (adapted from [34]).

Similarly to what has been done for the GMR, we can consider two spin currents (↑ and ↓) which are independent from each other and the electron spin is conserved in the tunneling process.

$$TMR = \frac{R_{antiparallel} - R_{parallel}}{R_{parallel}} = \frac{2P_1P_2}{1 - P_1P_2} \tag{1.10}$$

where P_i is the polarization of the electrode i, defined as the normalized difference of density of states D_i for the two spin states up and down, expressed by:

$$P_i = \frac{D_i^{\uparrow} - D_i^{\downarrow}}{D_i^{\uparrow} + D_i^{\downarrow}} \tag{1.11}$$

In 1995, Moodera et al. [133] and Miyazaki et al. [130] reported the possibility of having a significant TMR at room temperature, renewing the interest for applications. An example of TMR is shown in figure 1.9.

The first results on a CoFe/AlOx/Co junction showed a TMR of 24% at 4.2K and of 12% at room temperature. After these early works a huge development on TMR devices has been made and in particular with a thin crystalline MgO insulating barrier which shows TMR up

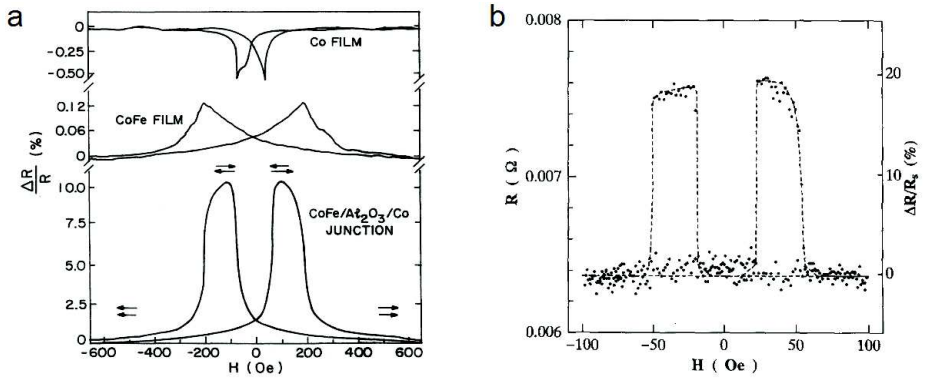

Fig. 1.9 TMR measurement of CoFe/AlOx/Co junction at room temperature, as reported by a. Moodera et al. [133] and b. Miyazaki et al. [130].

to 200% at RT [156, 162, 238]. This large ratio is due to an additional spin filtering effect which originates from the crystalline MgO. The electron are filtered based on the symmetry of their wave function which is based on the symmetry of the Bloch states at the Fermi energy. As results the TMR stack behaves as if its electrodes are fully spin-polarized [30, 119]. This effect does not occur in amorphous barrier (such as AlOx). Many parameters play a role in the quality of these magnetic tunnel junction (MTJs), like the quality of the interfaces, the crystallographic growth, quantity of defects and spin polarization. In nowadays technology the TMR devices have replaced GMR due to the higher performance than can be achieved at RT. Optimized TMR devices based on CoFeB/MgO/CoFeB pseudo spin valve reached the record value of 604% at 300K [73] while in GMR the maximum ratio does not exceed 40%. TMR devices are exploited in magnetic sensors since 2000 and in HDD read heads since 2005.

Chapter 2

Materials and Methods

In this chapter we will describe the deposition methods, the micro and nanofabrication techniques and the characterization performed during this thesis. The relevant aspect of each machine will be discussed, with particular attention to the aspect directly related to this work.

We are interested in multilayer structures composed of *(heavy metal) / (ferromagnetic metal) / (light metal oxide)* trilayers and in particular Pt/Co/MO_x system. This system has attracted more and more interest in the past few years. Ultrathin Co layer $(0.4 - 1)$ nm thick, is used as a model system to study surface perpendicular magnetic anisotropies (PMA) [32, 112], current induced magnetization reversal [67, 114] and electric field control of magnetization [17, 36, 181].

In these structures the Co is interfaced with Pt (a heavy metal) on one side and with a light metal oxide such as Al on the other. This introduces a source of asymmetry and could enhance original effect of the magnetic properties and is particularly interesting for recent study on Dzyaloshinskii-Moriya Interaction (DMI) [14], Rashba splitting [128] and Spin Hall contribution [105]. See figure 2.2 for the typical sample structure.

Other studies [57, 109, 198] rely on periodic multilayer stack (n-repetition for each stack) and need the assumption of identity of the layers and interfaces. The assumption is based on the idea that each unit of the stack behaves as the others. To obtain the properties of a single unit is then sufficient to divide the measured properties by the number of repetitions. During this work we decided to investigate the properties of a single Pt/Co/MO_x multilayer, where MO_x = Al_2O_x or CoO. The advantage is that there is no need to assume the identity of interfaces and individual layers. On the other hand, if the measured signal depends on the total magnetic volume of the sample (i.e. in VSM-SQUID measurements, see 2.3.3) it will be intrinsically smaller compared to former studies. An uncertainty based on the signal to noise ratio (S/N) must be taken into consideration whatever the study.

2.1 Deposition Methods

In this section the different deposition techniques utilized during this thesis will be discussed. Different techniques where used for different aims:

- Multi Cathodic Magnetron Sputtering was used to deposit the magnetic multilayer stack.
- Atomic Layer Deposition (ALD) was used to deposit a thick AlOx insulating layer which was necessary for the electrical insulation of the tunnel barrier.
- Electron Beam Physical Vapor Deposition (EBPVD) was used to deposit the top electrode.

The RF magnetron sputtering technique will be discussed in details, with particular attention to the characteristics of the wedge geometry. ALD and EBE are less important for the aim of this thesis because of the non-magnetic nature of the deposition, and the deposited layers are not the active ones. Therefore we will just briefly describe them.

2.1.1 Magnetron Sputtering

Multi cathodic Magnetron Sputtering is a deposition technique widely used in research and industry for the preparation of thin films. This technique is particularly interesting for magnetic thin film deposition because of the advantages over other existing technique such as Molecular Beam Epitaxy (MBE) or Chemical Vapor Deposition (CVD). The principal advantages are:

- High vacuum (UV) and ultra high vacuum (UHV) base background.
- High deposition rate (usually in the range of Å/sec).
- Deposition of all type of materials (metals, (oxide) dielectric, alloys, ...).
- Good thickness homogeneity over large substrate (up to meter long windows).
- Good control of layer thicknesses (down to few tenth of nm).
- Good adherence of the deposited layers (sputtered particles have large energies).

The technique consists in depositing atoms mechanically sputtered by a ion plasma from a target. The target is bombarded by accelerated ions, the extracted material is deposited on the substrate as shown in figure 2.1a. The sputtering chamber is kept under vacuum (around $5 \cdot 10^{-7}$ mbar). An inert gas, usually Argon, is introduced in the chamber. Argon is a common choice for sputtering since it is chemically inert, non toxic, easily ionized and has a high sputter yield (ionized particles over sputtered atoms) for most metals. Argon is also quite cheap respect to other noble gases as Krypton and Xenon. The required pressure to ignite the plasma is 10^{-3} mbar. The Argon plasma is obtained by electrical discharge. A negative voltage is applied between the target (cathode) and the surrounding shield maintained at zero potential. The electrical discharge will ionize the argon atoms by collisions with the electrons. The positive ionized Argon atoms are attracted by the target, they will extract the desired atoms when colliding with it. The extracted atoms will deposit on the substrate. Since the sputtered atoms have large energies (around 5 to 20 eV [107, 204] depending on the target material), the deposited layer interfaces are likely to be mixed (at least on one atomic plane). The energies are usually 50 to 100 times larger than the one generated from thermal evaporation sources, which are in the order of 0.1 to 10eV [80]. These large energies are the reason for the greater adherence of sputter-deposited layers compared to thermally evaporated films.

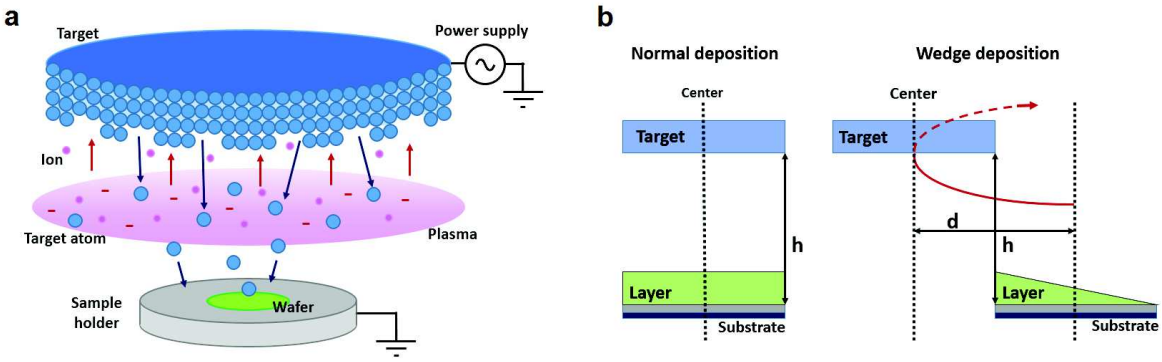

Fig. 2.1 a. Schematic representation of a RF Magnetron Sputtering system, b. Normal and Wedge deposition geometries. In the wedge deposition the target is rotated away with respect to the substrate, this is done in order to create a misalignment and the wedged deposition.

The film growth is influenced by several factor such as:

- Surface energy and chemical nature of the deposited materials
- Preferential crystallography orientation of the substrate.
- Substrate temperature, for this thesis all samples were deposited at Room Temperature.

- Background pressure, higher pressure leads to more pollution, large quantity of water and higher oxygen concentration in the film [105, 200].
- Deposition rate (may differentiate between crystalline, polycrystalline or amorphous material growth, similarly to what can be done by controlling the temperature).

An optimal control of these parameters leads to higher reproducibility and better quality of the deposited layers. The power supply can be designed to be either DC (for metallic deposition) or to apply a radio frequency (RF) polarization on the target (for dielectrics and oxides deposition, metals are also possible). The RF polarization reduces the positive charges accumulation, eliminating the problem of low deposition rate and plasma ignition.

This is not the only method for oxide deposition. There are other ways to deposit oxides from a metallic target. For example the method chosen for this thesis is to deposit a metallic layer and proceed, after the deposition, to oxidize it with an oxygen plasma. A technique first introduced by Moodera [133]. It is possible to tune the time and the power of the oxygen plasma in order to achieve the desired properties.

In our Alliance Concept (based in Annecy, France) DP850 multi-cathode sputtering system it is possible to prepare layers presenting a thickness gradient. This was done by misaligning the target and the substrate holder, as shown in figure 2.1 b. and by tuning the misaligning angle and the distance between the substrate and the target. The usual choice for the angle was 8 degree, while the distance h was tuned between 100 and 60 mm. By tuning the distance it was possible to obtain different thickness gradients. This particular deposition geometry will now be described.

Details about the wedge geometry

In the deposited Pt/Co/AlOx system, the top Al metal is deposited with a thickness gradient (wedge) and post-oxidized in an oxygen plasma for 50 sec. The Al is a good capping layer choice because it will protect the underneath Co layer from natural oxidation [53], allowing the sample properties to be stable in time. Furthermore, the Co/Al interface, when the Al is perfectly oxidized, will contribute to the perpendicular magnetic anisotropy, this particular feature will be discussed in chapter 3.

The idea of using a wedge deposition was developed at Spintec (CEA - Grenoble) by Monso et al. [132], they showed that controlling the oxidation in the nanometer regime was possible and that leads to large out of plane anisotropy. We will now list some of the advantages of the wedge deposition technique:

- With one deposition it is possible to obtain a gradient of magnetic properties controlled by the Al thickness and the oxygen plasma.

- The Pt/Co bottom interface is in common, the top magnetic/oxide interface changes gradually.
- Possibility to control the oxidation and the thicknesses of the oxide and different layers in the sub nanometer range.
- The oxygen plasma forms an oxide layer that caps the stack and preserves the magnetic properties.

The wedge technique has an interest in situation where controling the thickness is quite demanding. With a wedge deposition it is relatively easy to obtain the desired thickness at least in a small zone on the sample. The wedged sample, usually 8 to 10 cm long, can be cut in smaller pieces (to fit in the various measurement instruments). Another advantage of the wedge technique lies in the fact that the deposition conditions of these samples will be exactly the same, making the comparison of the properties and statistical analysis of the different cut samples more accurate.

In our study, we decided to overoxidize such structures (creating a CoO layer underneath the Al), to precisely analyze both the Co and the CoO layer and their interplay (a sketch of the wedge can be seen in figure 2.2).

As briefly explained in chapter 1.1.1, CoO is an antiferromagnet with a bulk Néel temperature (T_N) of 294K. By cooling down the system it would be possible that the CoO starts to behave as a antiferromagnet. Having such AFM layer could bring new source of asymmetries and change the magnetic properties. The sample can be ideally divided in five zones along the wedge direction, indicated in figure 2.2:

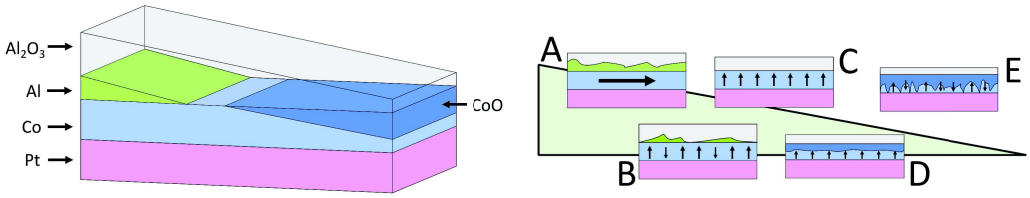

Fig. 2.2 Sketch of the multilayer structure and change in the oxidation level along the wedge direction

A. Underoxidized zone, the top magnetic interface is Co/Al. The magnetization lies In Plane (IP)

B. The oxidation starts to reach the Co layer, the first Co-O bonds are created preferentially through grain boundaries. The sample is not fully magnetized in one direction.

C. Optimal oxidation, the Al is totally oxidized and Co-O bonds are formed. The Co/AlOx interface contributes to the perpendicular magnetic anisotropy (PMA). The sample is fully Out-Of-Plane (OOP).

D. Co starts to oxidize and a CoO layer begins to form. Magnetization is still OOP (helped by the reduction of the Co thickness). CoO plays a role when the sample is cooled down below the CoO Néel temperature (T_N).

E. Sample is over-oxidized and non-magnetic at room temperature (RT).

These multilayer structures will be the core ingredient for these thesis studies. Unpatterned multilayer will be used to investigate surface anisotropies (chapter 3) and exchange bias in the subnanometer range (chapter 4). They will be also used as the active magnetic layer for Tunnel Anisotropic MagnetoResistance (TAMR) devices and magnetic tunnel junctions (MTJ) 5.

2.1.2 Atomic Layer Deposition (ALD)

ALD is a thin film deposition technique used to deposit insulating layers. The thin film is growth on a substrate by exposing its surface to alternate gaseous species (referred as precursors). The precursors are never present simultaneously in the reactor, but they are inserted as a series of non overlapping pulses. The film growth is controlled by the number of cycles performed.

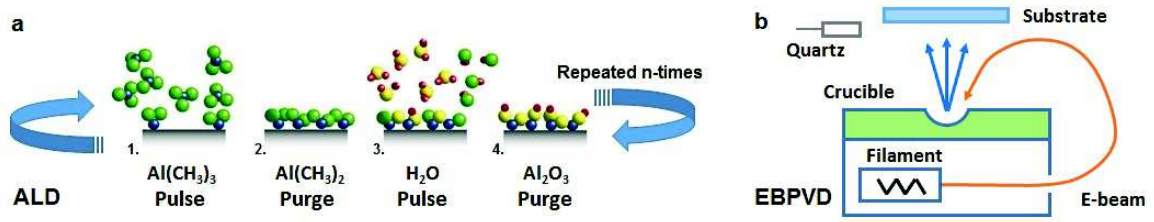

Fig. 2.3 a. A schematic of the Atomic Layer Deposition (ALD) process for Alumina. b. Principal components of a Electron Beam Physical Vapor Deposition (EBPVD) system.

The concept of the ALD process was first proposed by Prof. V.B. Aleskovskii in his Ph.D. thesis published in 1952 [3]. In 1974 Dr. Suntola patented the application as "Atomic Layer Epitaxy" in Finland [206]. ALD was one of the techniques used to deposit the insulating layer of the TAMR devices. To clarify, we define the insulating layer as the one dedicated to electrically insulate the bottom and top electrode of the Magnetic Tunnel Junction (MTJ) 1.2.4. We used Alumina (AlOx) as material for the insulating layer. In the ALD deposition

technique (for alumina): 1 cycle corresponds roughly to a deposited thickness of 0.1 nm. The number of cycles was varied from 200 to 300, so the resulting electrically insulating layer was 20 to 30 nm thick. The electrode insulation was verified with electrical measurement, the breakdown tension for the layer was found to be larger than 20V. This large voltage assures a complete insulation at the junction's operative tension, which rarely exceed 1V.

A typical example of the cycle for Alumina deposition is shown in fig 2.3 a. The cycled deposition is the following:

1. The precursor (in green) is added to the reaction chamber with a controlled pulse of 0.015 s.
2. After the precursor has been adsorbed on the surface (chosen time was 5 s), any gas excess is removed from the reaction chamber using a vacuum pump (purge).
3. Water gas (yellow) is added and reacts with the precursor, with a controlled pulse of 0.015 s, to create the desired layer on the surface.
4. After 5 seconds the water is then purged from the reaction chamber.

The process is repeated n-times, until the desired thickness is achieved. To control the quality of the deposition it is possible to tune the chamber temperature, the length of the pulse and the waiting (purge) time between two pulses. To achieve perfect AlOx layers, with very good electrical properties, it is necessary to use long adsorption time (30 sec) and higher deposition temperature (250°C). In this thesis work we deposited relatively thick Alumina layer and to achieve perfect dielectrical properties of the insulating layer was not necessary. The bottleneck was the exposure of the S1818 resist (used in the photo-lithography) to high temperature for long time. Annealing at 250°C could change the wedge magnetic properties, causing intermixing at the interfaces of the sample and oxygen absorption in the stack. Furthermore at that temperature the S1818 resist is likely to burn, denying the possibility of a lift-off (see section 2.2.1).

A good trade-off between Alumina electrical insulating properties and time/resist lift-off optimization was found setting the chamber temperature to 100 °C and using purge time of 5sec. In this condition the time to complete a cycle was found to be around 10 sec, therefore a 200 cycles deposition took roughly 35 minutes, conditions which allow to perform the necessary lift-off without problem even after the AlOx deposition.

2.1.3 Electron Beam Physical Vapor Deposition (EBPVD)

EBPVD was used to deposit the top conductive electrode. In EBPVD deposition technique the metallic target is bombarded with an electron beam. The beam is generated by thermionic

emission from a hot filament in a vacuum chamber. The electron beam causes the atoms on the target to evaporate. The atoms then reach the substrate where they condense creating the desired deposited layer. The deposition rate is controlled by a quartz oscillator. A shutter is used to start and stop the deposition on the substrate and to control the thickness. A schematic view for a EBPVD system is shown in figure 2.3 b.

The typical top electrode choice was a 15 nm thick wetting layer of Ti, followed by 100 nm of Au. The typical deposition rates are in the order of 0.1-0.2 nm per second and the minimum vacuum to start the deposition was 10^{-5} mbar. The Ti layer is mandatory, because when placed in contact with the bottom AlOx it partly oxidizes. By doing so the adhesion between the Ti and AlOx is granted. The deposition of 15nm allows the top Ti (the one far from the AlOx) to return to its metallic state. The metallic Ti will bond with the Au granting the necessary adhesion with the top Au layer. The EBPVD technique allows low energy power for the deposited atoms. The lower adhesion compared to sputtering techniques create the conditions for an easy lift-off, even for deposited thicknesses larger than 100 nm. A 100 nm layer thickness was the minimum amount of Au metal necessary to perform the micro-bonding on the top without destroying the underlaying insulating layer.

2.2 Photolithography

Photolithography or UV lithography, is a process used in micro and nanofabrication to pattern thin film on a substrate. It is commonly used to define the geometry of a device at the nanometer level and it uses light to transfer a geometric pattern from a photomask to a light-sensitive chemical (photoresist) on the substrate. It allows to either engrave the exposed pattern (etching) or the deposition of a new material (lift-off) into the desired area.

We will now describe the procedure to apply the photoresist and open the device geometry onto the sample. If not specified otherwise we will utilized a standard Shipley S1818 photoresist. The procedure is sketched in figure 2.4:

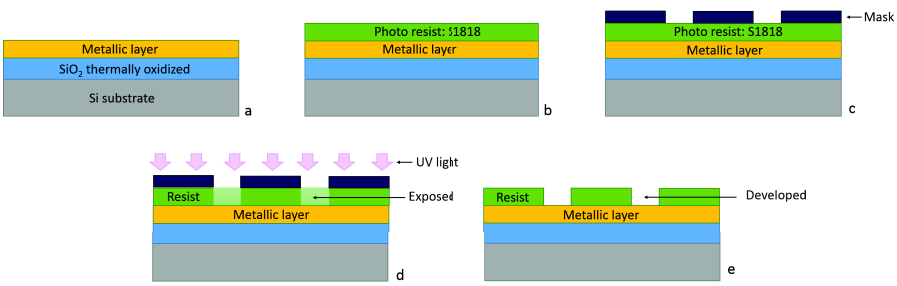

Fig. 2.4 Schematic of the steps necessary to open the mask geometry onto the sample.

a. Initial situation: the sample is ready to have a new geometry open upon it.

b. Spin coating and pre-anneal: the sample is covered with the photoresist by spin coating. The liquid S1818 solution is spread onto the wafer, and the wafer is spun rapidly to produce a uniformly-thick layer. Spin-coating the S1818 at 4000rpm gives a thickness of $\sim$1.8μm. After the spin coating the resist is annealed for 1 min at 115°C (prebaking). The thermal annealing is performed in order to drive off excess photoresist solvent.

c. Geometry alignment: the mask is placed in contact with the sample and (if necessary) an alignment to previous patterns is performed.

d. Exposure: the photoresist is exposed to a pattern of intense light. The exposure to light causes a chemical change that allows some of the photoresist to be removed by a chemical solution, called "developer".

e. Final situation: after being placed into the developer, the geometry is open on the sample. Positive photoresist, the most common type and the choice for this thesis, becomes soluble in the developer when exposed (negative photoresist, unexposed regions are soluble in the developer).

Two main procedures to define the device geometry have been used, the lift-off and the etching technique, see figure 2.5.

2.2.1 Lift-Off and Etching

The **lift-off** process is a method to create structures (patterning) on the sample surface using a sacrificial material (the photoresist). It is an additive technique (opposed to subtracting technique like etching). The scale of the structures can vary from the nanoscale up to the centimeter scale or further, but are typically of micrometric dimensions. Target material, usually a thin metal layer, is deposited on the whole surface of the wafer. This layer covers the remaining resist as well as the parts of the wafer that were previously exposed (figure 2.4 d). After the deposition the sacrificial material is washed out (usually in acetone for S1818) together with the target material covering it. At the end only the material that was in direct contact with the underlying layer remains, see lift-off technique in figure 2.5.

The advantage of lift-off is associated to its versatility, furthermore it is a fast technique that does not require special equipment and is usually used in the micro and nanofabrication of simple devices at the research-shell level (rarely in industrial application). This is due to

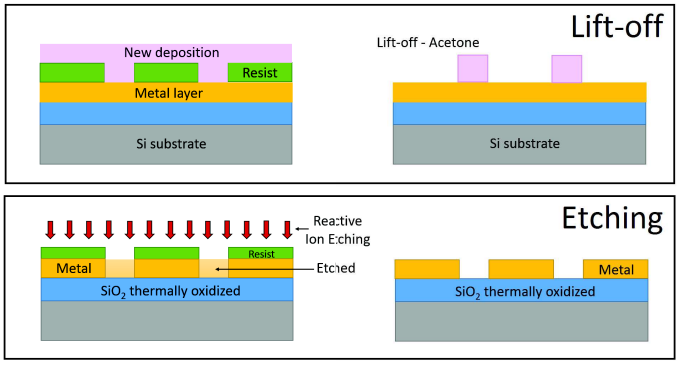

Fig. 2.5 Schematic of the lift-off and etching techniques.

the fact that there are several disadvantages which do not cause problem in research but are unacceptable for industrial applications, such as:

- Retention: unwanted parts of the metal layer will remain on the wafer. This can be the cause of the disruption of the active part of the device, in our case the tunnel junction, which will not be defined.

- Ears: When the metal is deposited, if it covers the sidewalls of the resist, "ears" can be formed. These are made of the metal along the sidewall which will be standing upwards from the surface. This can cause shortcutting of the electrodes or unwanted connection.

- Redeposition: during the liftoff process it is possible that particles of metal or flakes will become reattached to the surface, at a random location. It is very difficult to remove these particles after the wafer has dried. Again this can cause damage or create unwanted connection on the device.

The **etching** method is conceptually opposite to the lift-off technique. Etching is a subtracting technique and consists in removing part of the layers from the surface with some means (chemical or physical). We will describe the ion etching technique which was used for this thesis. For the etch step, part of the wafer is protected with a mask of material which resists to the etching. For this thesis, the masking material is a photoresist which has been patterned using photolithography, see etching technique in figure 2.5. Other situations require a more durable mask, such as silicon nitride.

The ion etching (or ion milling) consists in bombarding the wafer with energetic ions which knock atoms out of the substrate by transferring momentum. Because the etching is performed by ions, which approach the wafer approximately from one direction, this process is highly anisotropic. On the other hand, it tends to display poor selectivity. Ion etching

is often performed into a chamber with a mass spectrometry that can detect which layer is being etched giving information on the etching process. Ion etching is a cleaner technique which requires some more complex equipment to be performed (compared to lift-off) and a higher understanding of the process.

Both technique have been used for this thesis accordingly to the situation. More details on the sample geometry will be given in section 5.2.1 where we will describe the microfabrication of the devices used for this thesis.

2.3 Film Characterization

In the following section the principal characterization techniques used to analyze and study the samples will be discussed. The idea is to give to the reader a fast review on the theoretical principles and details about the main characterization techniques utilized for this thesis.

2.3.1 Transport Measurements

Transport Magneto-Electrical measurements were carried out in a pumped Helium cooled cryostat. The cryostat is equipped with a super-conductive coil, which can reach a maximum magnetic field of $\pm$5T. The temperature can be varied between 2K and 300K. The sample can be placed parallel or perpendicular with respect to the magnetic field, the orientation must be chosen before the measurement. The cryostat is directly cooled with liquid He, a sketch of the set-up can be seen in figure 2.6 a.

The principal components of the system are:

- A pre-pumped external shield (vacuum space), which is the major thermal insulation mechanism.
- A superconductive coil, which can reach a maximum field of $\pm$5T; the current to field ratio is $\sim$10A/T.
- Three He-level sensors, which control and regulate the cryostat automatic He refill.
- The internal vacuum space, which isolates the external He bath from the sample holder. This space is always pumped with a diffusion pump.
- The temperature control system, which is composed by a capillary impedance and a heating system. By pumping on the sample space (He pump), cold He gas flows through an impedance from the liquid He tank. A heating block then adjusts the

gas temperature to the temperature set-point and makes it possible to regulate the temperature between 2K and 300K.

- The sample holder, which contains the sample and the electrical wires for the contact and the sample temperature sensors.

The evaporated He gas is recycled and is directly sent back to the liquefactor of the Néel Institute.

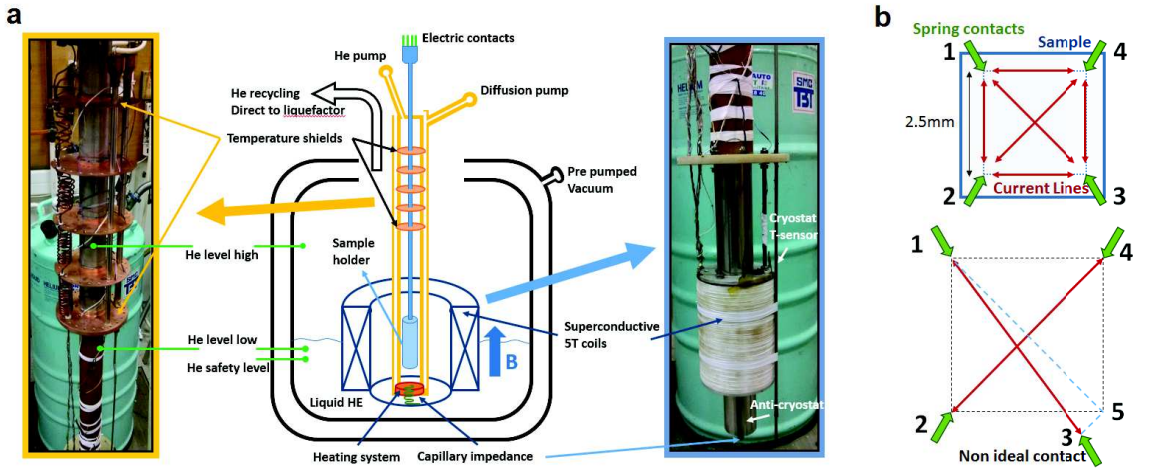

Fig. 2.6 a. Schematic view of the He pumped cryostat system and associated pictures, b. Sketch of the Hall cross spring contacts

Principles

MagnetoResistance (MR) and Anomalous Hall effect (AHE) measurements were performed on patterned and unpatterned samples. The calculation method for unpatterned sample will now be discussed. The contacts geometry sketch can be seen in figure 2.6 b. The contacts are in a squared geometry and named counter clockwise. The contacts are taken with 4 spring-loaded probes. The Van der Pauw method [221] allows to measure the resistivity and the Hall coefficient of a sample of arbitrary shape. In order to apply this method some conditions must be respected:

- The sample is approximately two-dimensional (i.e. much thinner than wide).
- The contacts are small and placed at the sample perimeter.
- The surface of the sample must be simply connex (no holes).
- The resistivity is isotropic.

Our measurement setup almost falls into this scenario, the spring contacts are not exactly on the perimeter, although it is possible to utilize a geometrical correction to obtain the real value for R_S. Anisotropic MR makes also that the resistivity is not exactly isotropic The measurements methods is the following: a I_{13} current is applied and the V_{24} tension is measured. The same kind of measurement is repeated for every pair of contacts, in the end a total of four measurements will be performed along the direction 1-3, 2-4, 1-2 and 2-3. Is it possible to define: $R_{12,34} = \frac{V_{34}}{I_{12}}$. To minimize measurement errors (i.e. voltage offsets and thermal effect) we can invert the current and then measure $R_{21,43}$. By doing so we can obtain:

$$R_{vertical} = \frac{R_{12,34} + R_{21,43}}{2} \qquad and: \qquad R_{horizontal} = \frac{R_{23,41} + R_{32,14}}{2} \tag{2.1}$$

The Van der Pauw formula can now be written as:

$$e^{-\pi R_{vertical}/R_S} + e^{-\pi R_{horizontal}/R_S} = 1 \tag{2.2}$$

The formula is implicit, we need to find the best R_S value. $R_S = \rho/t$ is the sheet resistance and is expressed in (Ω or Ω/square). In the particular case in which $R_{vertical} = R_{horizontal} = R$ we can explicitate the sheet resistance R_S:

$$R_S = \frac{\pi R}{\ln 2} \tag{2.3}$$

Otherwise, in normal cases, R_S is given by the solution of equation 2.2. MagnetoResistance (MR) measurements are performed if the voltage is measured parallel to the current, instead if the measured voltage is perpendicular to the current we measure a Hall effect (HE). In transport measurement, it is impossible to place the two contacts (for measuring MR) exactly parallel to the current direction. Similarly, for measuring HE, it is impossible to place them exactly perpendicular. Even in patterned samples, the MR and HE signal are always a little mixed, therefore they need to be separated from each other. The situation is similar to the one shown in figure 2.6 b. where a non ideal geometry is considered. The contacts 3 is in a non-ideal position. We can theoretically write:

$$V_{31}(+H) = V_{35}(+H) + V_{51}(+H) = V_{MR}(+H) + V_{Hall}(+H) \tag{2.4}$$

and by inverting the field:

$$V_{31}(-H) = V_{35}(-H) + V_{51}(-H) = V_{MR}(-H) + V_{Hall}(-H) \tag{2.5}$$

Because MR is an even function and HE is an odd function of the applied field H:

$$V_{MR} = V_{MR}(+H) = V_{MR}(-H)\text{even} \tag{2.6}$$

$$V_{Hall} = V_{Hall}(+H) = -V_{Hall}(-H)\text{odd} \tag{2.7}$$

In our measurement setup system the applied magnetic field will not be invert. To separate the two signals the Van der Pauw formulation is used. Similarly to what has been done before (see 2.1), we can define:

$$R_{\diagdown} = \frac{R_{13,24} + R_{31,42}}{2} \qquad \textit{and}: \qquad R_{\diagup} = \frac{R_{24,13} + R_{42,31}}{2} \tag{2.8}$$

By substituting and deriving, eventually the formulas for MR and HE signal are found as:

$$V_{Hall} = \frac{V_{\diagdown} - V_{\diagup}}{2} \tag{2.9}$$

$$V_{MR} = \frac{V_{\diagdown} + V_{\diagup}}{2} \tag{2.10}$$

Where V_{Hall} depends only to the odd Hall signal and V_{MR} depends on the even Magneto Resistance signal, eliminating the problem of geometry and of a misalignment of the contacts.

Details about our system: Anomalous Hall Effect

This section will be dedicated to explain the Anomalous Hall Effect (AHE) and how we can combine it with the Van der Pauw formulation to exploit it in our cryostat system. Transport measurements are sensitive to the perpendicular component of the magnetization.

The measured signal will have a certain Hall amplitude which depends on the magnetization and on the Hall coefficient. The Hall coefficient is directly related to the environment in which the magnetic layer is placed. For example this technique is very sensitive when the magnetic layer (Co) is placed into contact with a metal (i.e. on our case Pt). On the

other hand if the same Co magnetic layer is sandwiched between two oxides we would have almost zero Hall signal. The thickness of the buffer and capping layer (in our case Ta and Al respectively) also plays a crucial role. The thicker the layer the lower the Hall effect, because part of the current will now flow in these layers and not in the magnetic one.

Our experimental design and the thicknesses of our magnetic stack are well optimized for this kind of measurement. Adapting the sketch of figure 2.6 b, in the perfect geometry case the current is injected along the in-plane x-direction and the Hall voltage is measured along the in-plane y-direction. The Hall resistivity (R_H) would be the sum of two contributions:

$$R_H = BR_0 + M_z R_E \tag{2.11}$$

where B is the magnetic induction, M_z the magnetization normal to the layer and R_0 is the ordinary Hall coefficient related to the Lorentz force and R_E is the extraordinary Hall coefficient due to the spin-orbit coupling. This coefficient in magnetic material is usually much larger than the normal one ($R_E \gg R_0$).

If the magnetic field is applied along the easy axis (H perpendicular to M) the Hall resistance will vary rapidly until the magnetization is saturated and then linearly with field (extraordinary contribution). This extraordinary contribution can be expressed as a function of the longitudinal resistivity:

$$R_E = a\rho_{xx} + b\rho_{xx}^2 \tag{2.12}$$

where a and b are the skew scattering and side jump coefficients. A recent review by Nagaosa et al. [141] gives an exhaustive description of the AHE, such description is behind the objective of this thesis and therefore will only briefly resumed here.

Briefly resuming, the two mechanisms have their origin in the spin-orbit interaction. The classical asymmetric scattering [196], gives a linear variation with longitudinal resistivity, basically one channel is favored with respect to the other (see picture 2.7a). The other effect is called side-jump [15] and is a non-classical mechanism based on the later displacement for spin-up and spin-down (see figure 2.7b).

In material with high polarization, the current will be spin polarized, therefore there will be more electron flowing in one perpendicular direction respects to the other. This will result in an added term to the Lorentz force charge separation which can be detected by voltage measurements. The schematic view of the measurement can be seen in figure 2.8 a. for a

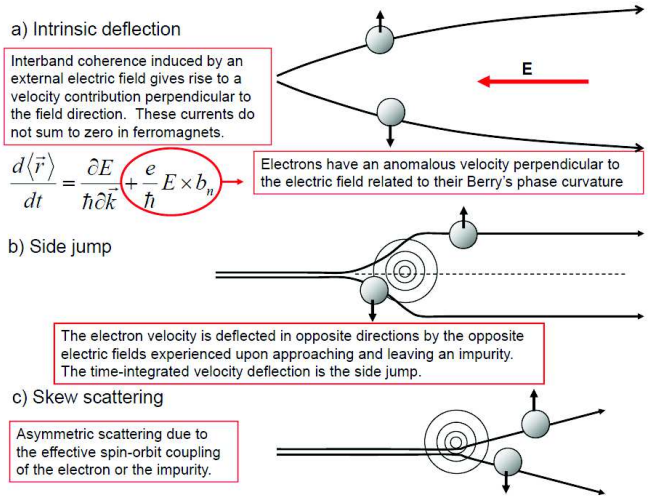

Fig. 2.7 a. Standard Hall effect mechanism. b. Side-jump mechanism and . c. Skew scattering mechanism contributions to the anomalous Hall effect (figure from [141]).

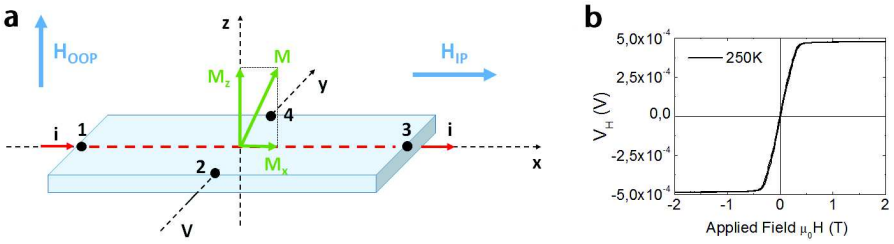

Fig. 2.8 a. Schematic view of the AHE measurement system and b. typical loop recorded along the hard axis OOP direction for IP magnetized sample.

sample with IP magnetization (M along the x-axis) and the field applied along the hard axis (H_{OOP}) the typical obtained loop will be similar to figure 2.8 b.

AHE measurements are sensitive to any deviation from the perfect orthogonality of the contacts disposition. If the contacts are not perfectly positioned (figure 2.6 b.) the Hall voltage will contain a contribution from the longitudinal resistivity ρ_{xx}. For a sample with IP magnetization the total signal will be the sum of those two. That is where the Van der Pauw formulation (eq: 2.2) comes into play to separate the AMR and the Hall effect signal from each other.

An example of the data processing can be seen in figure 2.9. On the right the two unprocessed measured signal $V_{\diagdown}$ and $V_{\diagup}$ are shown. Then the data are processed and the MR and HE signal are extracted.

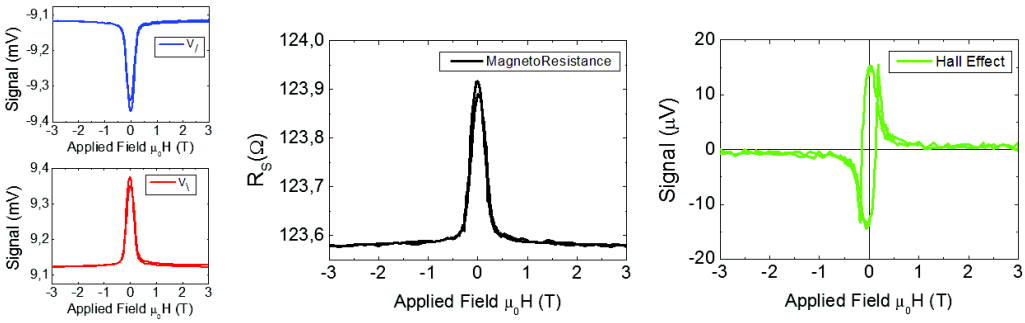

Fig. 2.9 Example of data processed with the Van der Pauw formulation, for sample S4 - Ta/Pt/Co/AlOx measured at 200K.

2.3.2 X-Ray Reflectivity

X-Ray Reflectivity (XRR) is a non-destructive and fast technique with Angstroem resolution. It probes a large surface area and is still relevant for layers of just some atomic layers [117]. XRR is based on monitoring the reflected intensity of a X-Ray beam at grazing incident angle. XRR is employed to characterize surfaces, thin films and multilayers deposited on flat substrates. From this technique it is possible to obtain information such as film thickness, electron density and roughness of single layers and multilayers [55].

In the XRR technique the scattered intensities are measured as a function of the scattering angle. A monochromatic X-Ray beam of wavelength λ irradiates the sample at a grazing angle θ, the reflected intensity is recorded by a detector at an angle 2θ (see fig: 2.10 a. for the typical experimental setup).

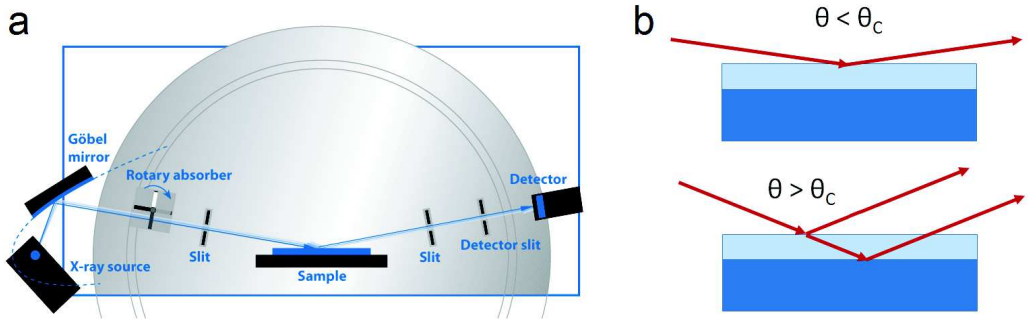

Fig. 2.10 a. Schematic representation of Bruker's XRR experimental setup (adapted from [25]), b. Two experimental configurations, above and belove the critical angle θ_c

If the interface is not perfectly sharp and smooth then the reflected intensity will deviate from the one predicted by Fresnel's law of reflectivity. For multilayers, different electron densities in the distinct layers correspond to different refractive indexes. Below a critical

angle (θ_c) total reflection occurs (see fig: 2.10 b for the two configurations above and below the critical angle). The density of the materials is determined by this critical angle [83].

Above θ_c X-rays are refracted and reflected and can interfere constructively giving rise to peaks and Kiessig oscillations, called Kiessig fringes [84]. The fringe amplitude depends on the surface and interface roughness. The periodicity of the fringes is characteristic of the film thickness of the analyzed sample (see fig: 2.11 a).

Principles

The refractive index for a homogeneous medium can be written as:

$$n - 1 = \delta + i\beta \tag{2.13}$$

where δ and β represent the dispersion and the absorption, respectively. In the X-ray range of energy δ and $\beta \ll 1$ then $n \simeq 1$. For frequencies $\upsilon \gg \upsilon_0$ (υ_0 = resonance frequency) δ can be expressed by the following equations:

$$\delta = \frac{e^2 n_e}{2\varepsilon_0 m(2\pi c)^2}\lambda^2 = \frac{r_0\lambda^2}{2\pi} \times n_e \tag{2.14}$$

where r_0 is the Bohr atomic radius and n_e is the electron density. For a more precise expression of δ, we can express $n_e = Z \cdot n_{atom}$. Z is the atomic number of electron per atom. For a more precise expression of δ, Z is usually replaced with a complex form factor: $f = f_0 + f' + if'' = Z + f' + if''$. f stands for $\delta + i\beta$ therefore, the terms f' and f" are the real and imaginary anomalous dispersion factors. They describe the X-Ray absorption edge. It follows that:

$$\delta = \frac{r_0\lambda^2}{2\pi} \times (Z + f') \times n_{atom} \tag{2.15}$$

$$\beta = \frac{r_0\lambda^2}{2\pi} \times f'' \times n_{atom} \tag{2.16}$$

At the interface air/sample the direction of the refracted beam can be obtained from Snell-Descartes's law. For a qualitative discussion we can consider an absorption free film ($\beta = 0$). Below a certain critical incident angle, known as θ_c, total reflection occurs. Therefore is possible to write:

$$1-\delta=\cos\theta_c\approx 1-\frac{\theta_c^2}{2}\longrightarrow\theta_c=\sqrt{2\delta} \tag{2.17}$$

The atomic concentration is given by: $n_{atom}=\frac{N_A}{A}\times\rho$, where N_A is Avogadro's number and A the atomic weight. The critical angle is a function of the density and composition of the layer. Therefore, from θ_c it is possible to determine the density of the analyzed material ρ. Substituting in the formula:

$$\theta_c=\sqrt[2]{2\delta}=\sqrt{\frac{r_o\lambda^2}{\pi}}\sqrt{N_A}\sqrt{\frac{Z+f'}{A}}\sqrt{\rho} \tag{2.18}$$

For incident angles $\theta > \theta_c$ the X-rays penetrate inside the film and are refracted (and reflected), for a schematic view see fig 2.10 b. The reflectivity and the transmittivity at each interface are described by Fresnel equations derived from Snell's law. The critical angle for a layer is a function of its electron density. If one is known, the other can be determined. For example, for a given composition, as the density of the film increases the critical angle θ_c often increases.

The interference fringes are angle dependent, the contribution of different reflected beams decay as $\approx 1/\theta^4$. If we consider a multilayer as comparable to N-layers sitting on top of an infinitely thick substrate, the m-th interface fringe maximum will be located at:

$$\Delta=m\lambda\approx 2d\sqrt{\theta_m^2-2\delta} \tag{2.19}$$

Considering d the film thickness, θ_m is expressed by:

$$\theta_m^2\approx m^2\frac{\lambda^2}{4d^2}+2\delta=m^2\frac{\lambda^2}{4d^2}+\theta_c^2 \tag{2.20}$$

If $\theta_m \gg \theta_c$ it is possible to employ equation 2.20 to determine the thickness d:

$$d=\frac{\lambda}{2\left[\sqrt{\theta_{m+1}^2-\theta_c^2}-\sqrt{\theta_m^2-\theta_c^2}\right]}\approx\frac{\lambda}{2(\theta_{m+1}-\theta_m)} \tag{2.21}$$

The distance between the fringes is inversely proportional to the thickness of the layer, because of this, thicker films need better resolution (like a monochromator) and thinner films

need more intensity. The thickness is often determined with a precision better than 1Å.The reflected intensity of a stratified medium can be analyzed with a recursive algorithm based on the recursive method developed by Parrat [163].

The last important quantity that can be determined via XRR measurement is the roughness. The roughness determines how quickly the reflected signal decays because it causes X-rays to be scattered rather than reflected. The roughness of the substrate and of each layer can be determined by measuring the diffusive scattering. Névot and Croce developed a formalism to calculate the roughness assuming non-homogeneous thickness [146]. They assumed a quadratic mean distribution for the roughness: $\sigma = \sqrt{< z^2 >}$ where z is the thickness mean value and σ the standard deviation. Typical roughness values for sputtered multilayers are in the order of one-tenth of the considered layer thickness.

Details about our system

The XRR experiments were performed at the Néel Institute with a Bruker D8 Discover diffractometer, using Cu K-alpha radiation. The focused beam on the sample is 50μm large in the incidence plane. The data were collected using a scintillation detector with incident angles up to a maximum of 16deg, the increment between two consecutive measurements was 0.02deg and the acquisition time was 10sec/step. The fitting model to reproduce experimental scans with theoretical curves has been done using the Genetic algorithm of Brucker LEPTOS [218], which is based on the recursion formula 2.21 first announced by Parrat [163].

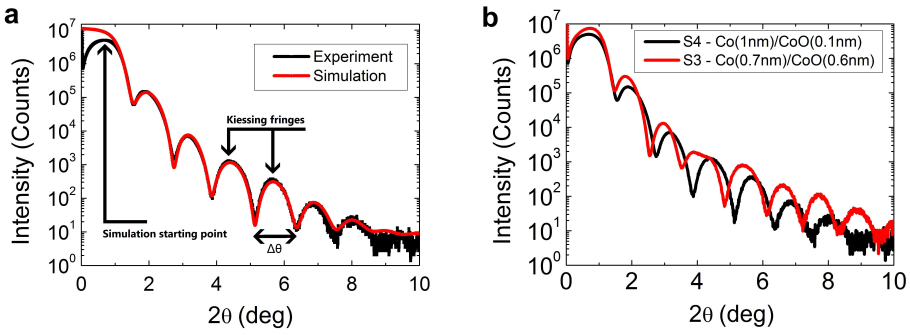

Fig. 2.11 a. Kiessig fringes and periodicity λ of a typical XRR measurement, b. Comparison of two different samples. Different wedge positions (S4=4cm and S3=3cm) lead to different XRR experimental curves, reflecting the change of Co oxidation and AlOx and CoO thicknesses.

Multilayer samples were cut and analyzed along the wedge direction. The distance between each measurements is 1cm. A theoretical fit was performed for each sample. As shown in fig: 2.11 b. the differences between two adjacent fits are consistent. It was possible to fit all the samples with good accuracy. The number of oscillations goes up to 10deg,

indicating a good quality (low roughness) for the deposited layer. The results of the XRR fit were crosschecked with VSM-SQUID magnetization measurements (see 2.3.3). An example of XRR fit for the Aluminum wedge can be seen in figure 2.11a.

For these studies on wedge deposited samples, a total of eight samples were cut out of the initial sample which was 8 cm long (the maximum size allowed in our sputtering chamber). The two samples at the edge (s8 and s1) are not included in this report due to inhomogeneity in layer thicknesses deposited at the very edge of the sample holder. We took care to position the wedged samples perpendicularly oriented with respect to the X-ray beam in order to reduce the possibility to obtain averaged thickness values due to the wedge gradient.

The standard procedure followed to obtain a XRR fit will now be described. At first there is need to choose a suitable XRR model stack for the sample from which the simulation will start to converge. The model sample is built following the material deposition order. Due to the large numbers of parameters in the model there is need to choose which parameters will be free to iterate and which will be fixed. The initial choice will be to let the thicknesses and the roughness free to iterate keeping the density fixed.

Then there is need to define on which part of the experimental spectrum the fit will be performed. We chose the first peaks to start the fit convergence (i.e. the fit will be performed only on the first three Kiessing fringes). Once a good convergence is obtained on these peaks, we extended the length on which the fit is performed including more fringes, in the end we will include the whole XRR experimental spectrum. Once a good convergence is obtained, the densities are unlocked and left free to iterate (taking care that they do not surpass their physical upper value) to obtain the best fit.

From the results we will see that the bottom Ta/Pt layers are in common and unchanged along the wedge. The bottom magnetic interface Pt/Co is constant along the wedge. The evolution occurs at the top interface, which controls the multilayer properties. Once the top metallic Al becomes thin enough the oxidation reaches the Co and a CoO layer starts to form.

2.3.3 VSM-SQUID measurement

A Superconducting Quantum Interference Device (SQUID) was used to perform magnetization measurements. The SQUID sensor is part of a Magnetic Property Measurement System (MPMS) a commercial system developed by Quantum Design. With this instrument it was possible to perform extremely sensitive magnetic measurements. The system is designed to optimize speed and sensitivity. Specifically, the sample is vibrated at a known frequency and phase-sensitive detection is employed for rapid data collection by the superconducting coil sensor, therefore the name Vibrating Sample Magnetometer (VSM-SQUID) [122].

Principles

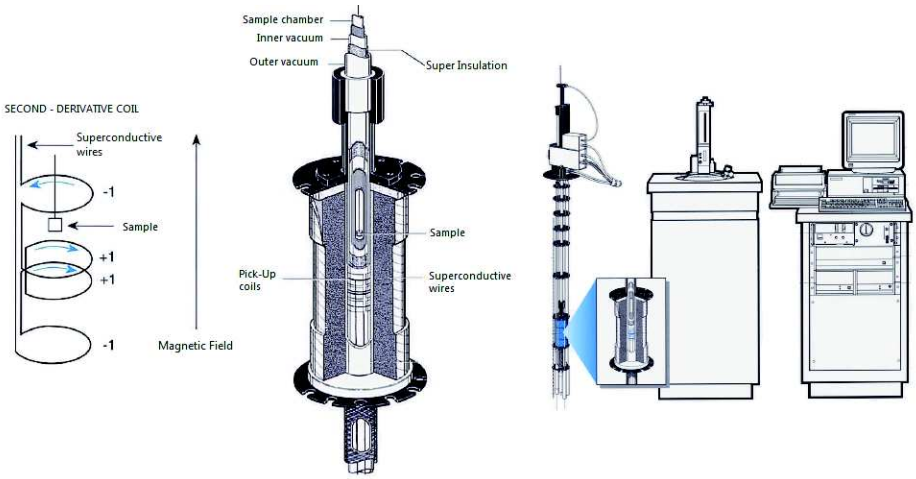

Fig. 2.12 MPMS: system schematic (adapted from [165]).

The MPMS VSM-SQUID utilizes a superconducting magnet (a solenoid of superconducting wire) to subject samples to magnetic fields up to 7 T, with a field homogeneity of 0.01% over 4 cm. The remanence of the coil is less than 1mT. The SQUID and coil must both be cooled with liquid helium. Liquid helium is also used to cool the sample chamber, providing temperature control of samples from 400 K down to 1.8 K, the minimum temperature ramp is 0.01 K/min, the maximum is 30 K/min and the stability is in the order of the mK. It is possible to mount the sample in two different configurations with respect to the magnetic field: In-Plane (IP) and Out-Of-Plane (OOP). Is it therefore possible to perform measurement in-plane and out-of-plane with respect to the substrate plane.

The main elements of the magnetometer are:

1. A superconductive magnet to generate large field.
2. A superconductive detection coil (inductively coupled to the sample).
3. A SQUID connected by superconductive wires to the detection coils.
4. A superconductive magnetic shield to insulate the chamber from external magnetic field.

The SQUID doesn't measure directly the magnetic field from the sample. Instead, the sample moves through a system of superconductive detection coils which record the magnetic flux variations. A schematic of the MPMS system can be seen in figure 2.12 [122].

Assuming the sample dimensions are much smaller than the dimensions of the detection coils, the current in the detection coils is a function of the sample position. The SQUID VSM measurement technique vibrates at frequency ω, the sample is positioned at the very center of the detection coils. The signal peaks as a function of sample z-position. This generates a SQUID signal, V, as a function of time, t:

$$V(t) = AB^2 sin^2(\omega\, t) \tag{2.22}$$

For small vibration amplitudes $V(z) = Az^2$, and $z(t) = Bsin(\omega t)$. A is the scaling factor related to the magnetic moment of the sample and B is the amplitude of the oscillations. Since $sin^2(\omega t) = \frac{1}{2} - \frac{1}{2}\, cos(2\omega t)$ (by identity) to isolate and quantify the signal occurring at frequency 2ω, a lock-in amplifier is used. The obtained signal should depends exclusively on the sample magnetic properties. This is achieved by sampling the measured signal with a phase-corrected reference signal (2ω) and by extracting the DC component of the result. The DC component is proportional to the 2ω component of the measured signal.

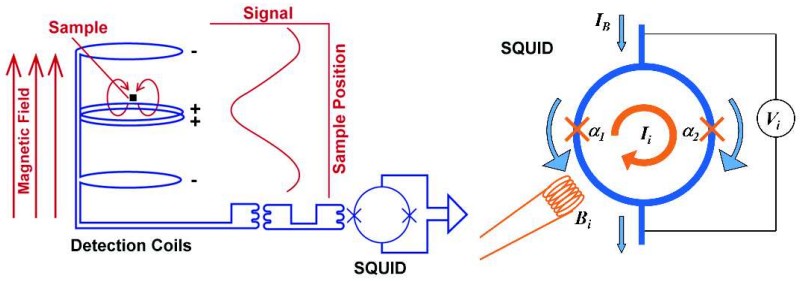

Fig. 2.13 VSM-SQUID: system details (adapted from [165]).

As the sample moves through the coils, the magnetic moment of the sample induces an electric current in the detection coils. The detection and the SQUID coil are in a closed superconducting loop, therefore any change of magnetic flux in the detection coils produces a change in the persistent current in the detection circuit. This change is proportional to the change in magnetic flux. Since the SQUID is a highly linear current-to-voltage converter, the variations in the current in the detection coils produce a corresponding variation in the SQUID output voltage which is proportional to the magnetic moment of the sample. See figure 2.13. The measurements of the voltage variations provide a measurement of the sample's magnetic moment. To obtain correct values the SQUID must be calibrated using a piece of material with a well known volume and magnetic susceptibility, for example a YIG magnetic sphere with a known mass.

Details about our system

In this section some general results will be presented. The idea is to evidence the advantages and the limitation of this technique. The minimum noise registered with this machine is around $5 \cdot 10^{-12} Am^2$. For this test Quantum Design utilized an optimized 0.05mg YIG sphere. On the other hand, in our measurement the magnetic volume is just a tiny fraction of the total. Our typical multilayer structure is deposited on top of a silicon wafer. The magnetic signal captured by the VSM-SQUID will be mostly associated to the diamagnetic response of the Si. Therefore the centering of the sample will be done at high field on the Si diamagnetic signal. The measurement noise is related to the shape of the sample, the flat square shape is not optimal for this kind of flux measurement. The usual measurement noise was in the order of $10^{-10} Am^2$ as shown in figure 2.14, where few magnetic hysteresis loops are plotted. The signal to noise ratio was sufficiently large for most measurements.

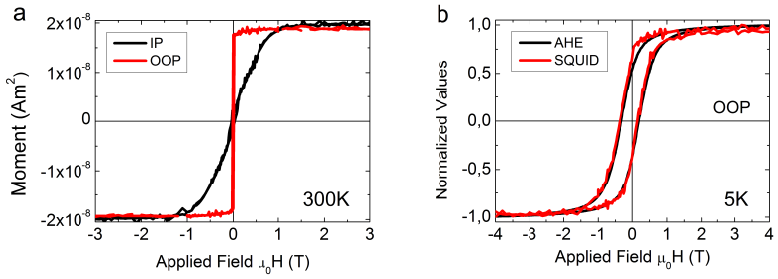

Fig. 2.14 a. Example of IP and OOP magnetization loops on the same sample and b. comparison between AHE and VSM-SQUID loop on the same sample.

In figure 2.14a, it is shown sample *S3* of the Al wedge and the measured magnetic moment for both IP and OOP cases. M_s value is related to the active magnetic volume of the sample. From this value we can calculate the thickness of the magnetic Co layer. If we assume that the magnetization of the Co layer is the one of bulk cobalt:$M_{Co} = 1.4 \cdot 10^6 Am^2$ and knowing the surface area, $A_{Co} = 2.93 \cdot 10^{-5} m^2$ of the measured sample we can calculate:

$$M_s = M_{Co} \cdot Vol = M_{Co} \cdot A_{Co} \cdot t_{Co} \quad then: \quad t_{Co} = \frac{M_s}{M_{Co} \cdot A_{Co}} = 0.678\ [nm] \tag{2.23}$$

Which is in good agreement with the thickness measured with the XRR, equal to 0.65nm. Finally, in figure 2.14b, two different magnetic measurements are compared. AHE (see chapter 2.3.1) and VSM-SQUID hysteresis loops both recorded at 5K and after a +5T field cool procedure. The agreement between the AHE and VSM-SQUID measurements is particularly good. The small change may be due to the fact that the two techniques do not measure exactly the same area.

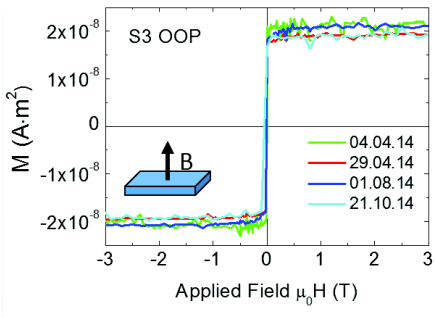

Fig. 2.15 Different VSM-SQUID measurements on sample *S3*, the date of each measurement is reported.

In figure 2.15 we show the reliability of our VSM-SQUID system. The sample was mounted on a different sample holder (a plastic straw) for each measurement (performed over a six months period). The sample holder does not influence the measured magnetic moment and furthermore there is no time evolution for m_S value during the measured period. The Al capping layer is thick enough to protect the underneath Co. The discrepancies on the measurements of m_S are estimated to be around $\pm 2 \cdot 10^{-9} A \cdot m^2$. To conclude the MPMS VSM-SQUID is a powerful tool to study and characterize the magnetic response of multilayers. The results obtained with this technique are comparable and can be crosschecked with other magnetic measurements.

2.3.4 Magneto-Optic Kerr Effect

The Magneto-Optic Kerr Effect (MOKE) was discovered by John Kerr in 1877. He observed that the light polarization would rotate after being reflected by a magnetized surface. Moreover, he discovered that the rotation was proportional to the magnetization.

Principles

There are three possible MOKE configurations, see fig: 2.16.

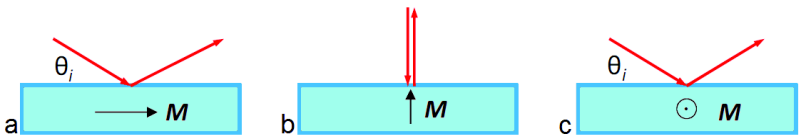

Fig. 2.16 Schematic representation of a. longitudinal, b. polar and c. transversal MOKE configuration.

- Longitudinal Kerr effect: used for samples with an IP magnetization, parallel to the light plane of incidence. Linearly polarized light, with E parallel or perpendicular to the plane of incidence, hit the surface with a certain angle θ_i. The reflected light is elliptically polarized, the change in polarization is proportional to the sample magnetization.

- Polar Kerr effect: used for samples with OOP magnetization. Linearly polarized light hits the sample with normal incidence. Reflected light has an angular polarization rotation proportional to the magnetization.

- Transversal Kerr effect: used for samples with an IP magnetization perpendicular to the light plane of incidence. Light arrives with an angle θ_i, the magnetization is measured by the variations of reflectivity r.

Details about the Kerr system

During this thesis, polar MOKE measurements were performed with a Light Emitting Diode (LED) microscope system. The instrumentation, was developed at the Institut Néel - CNRS by Lukas Flajsman under the supervision of Laurent Ranno and Pierre Molho. The main elements of the MOKE microscope are:

1. Hamamatsu acquisition camera (resolution 1920 x 1440 pixels)

2. High power LED light source (blue, red and green)

3. Light polarizer and analyzer (see fig: 2.17 a)

4. Soft iron "KUBE" electromagnet, formed by 8 different coils (x,y,z field, fig: 2.17b).

5. Controlled micromotor, possible to arbitrary move the sample holder in x,y,z via a LabView interface.

The motor controlled system allows an automatic 2D scan of a certain area (maximum area = 5 x 3 cm^2) with tunable step (minimum step = 1μm). The automatic micro-controlled motor allows different features. The principals are the possibility to calculate the surface area of a given sample and to automatically scan a sample, recording a Kerr loop in each point.

In this way it was possible to scan and characterize various multilayer samples. The maximum field which is possible to apply is 100mT. Within this limit it is possible to create arbitrary field in any θ and ϕ direction (see fig: 2.18 a). The B_Z field component has a very good homogeneity in a 5mm area around the center of the coils (see figure 2.18 b).

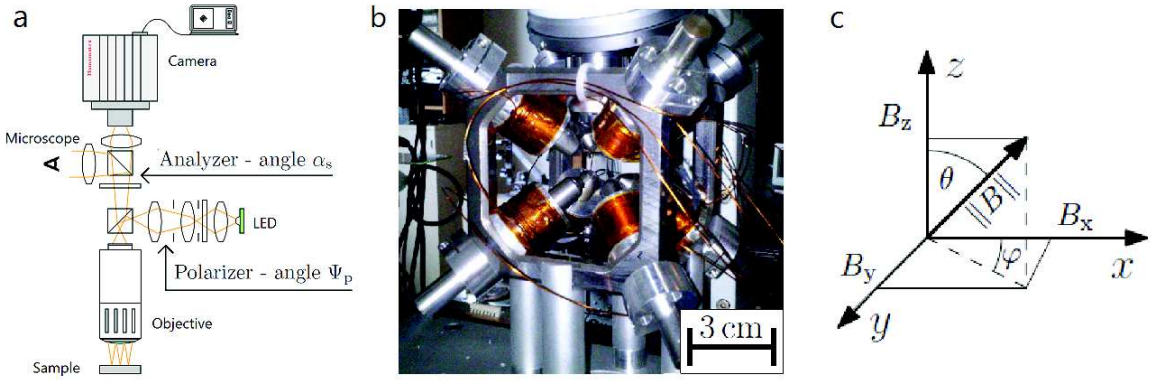

Fig. 2.17 a. MOKE schematic description, b. picture of the MOKE soft iron "KUBE", c. description of arbitrary field in θ and ϕ.

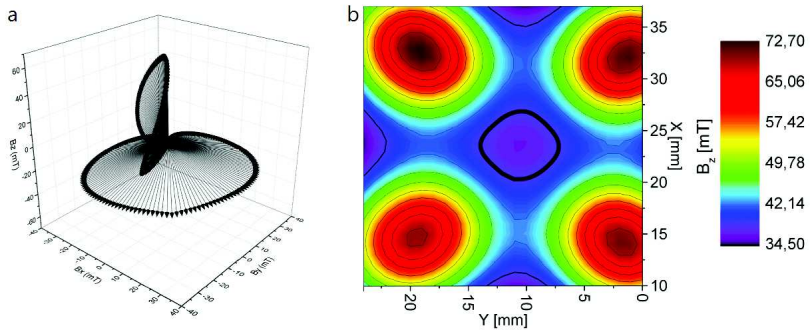

Fig. 2.18 a. Example of arbitrary fields selection in the MOKE system, b. z-component of the field and (x,y)-plane homogeneity.

To conclude the MOKE system is optimized for OOP magnetization measurement. Due to the high motor precision and thanks to the possibility to program the MOKE system to automatically scan a sample and to record a large amount of data in a simple way, it was possible to perform very precise studies along the full wedge length. The obtained results were fitted with a semiautomatic MATLAB program in order to understand and characterize the change of magnetic properties along the wedge.

Chapter 3

Ultrathin Cobalt films: Perpendicular anisotropy

3.1 Introduction and Motivation

Materials with perpendicular magnetic anisotropy (PMA) are now being widely employed in magnetic recording because they allow more storage density with respect to traditional longitudinal recording. One of the main challenges in designing magnetic information storage media is to retain the magnetization of the medium despite thermal fluctuations caused by the superparamagnetic limit. To retain the information the following expression must hold:

$$K_u \cdot V > 40 - 60 k_B \cdot T \tag{3.1}$$

where K_u is the material anisotropy, V is the magnetic volume, k_B is the Boltzmann constant and T the temperature. The factor 40 to 60 depends on the required retention time. If the thermal energy ($k_B \cdot T$) is too large it is possible to reverse the magnetization in a bit, losing the data stored in that region [229]. Thus, there is a minimum volume for a magnetic region at a given temperature and anisotropy, below that threshold (if the bit get any smaller) it is likely to be spontaneously remagnetized by local thermal fluctuations [172]. Perpendicular recording can use materials with a higher anisotropy (and therefore a larger coercivity) because the head writing field penetrates the medium more efficiently in this geometry [222]. In addition the magnetization of PMA materials is more uniform and does not suffer from thermal instability due to magnetization curling observed at the edge (in-plane case). In structures magnetized in-plane various edge domain configurations exist at the saturation remanent state. It is found that the switching field of these elements can strongly depend on

these edge domain configurations. If the edge domains are not controlled, switching field can vary significantly during repeated switching processes [241], this effect is strongly reduced in perpendicularly magnetized structures. From the STT-MRAM technological point of view, it is easier to reverse the magnetization of PMA free layer than the in-plane one [114, 179]. Materials with PMA are being used in GMR and TMR devices, their properties can be easily tailored via appropriate techniques [148, 157, 180, 198].

Recently Manchon and coworkers [112] demonstrated that the oxidation has a significant influence on the magnetic properties of a Pt/Co/AlOx trilayer. For the optimal case in which the Co/AlOx interface is fully oxidized a strong perpendicular magnetic anisotropy arises. It is interesting to study the PMA and its origin in such structure because it can give a simple way to control the oxidation process of MTJ without microfabrication [171]. Moreover, the presence of a sizable interface magnetic anisotropy is extremely interesting for designing MTJs with magnetization perpendicular to the interfaces [113]. Finally from a fundamental prospective the interfacial orbital anisotropy creates an interfacial spin-orbit that can strongly influence the density of states and therefore the MTJs tunnel properties [54].

Systems presenting surface-induced perpendicular anisotropy (PMA) were first predicted by Neél [144] and later, thanks to the advancement of deposition systems, experimentally observed by Gradmann in 1968 [64]. Systems exhibiting PMA were rediscovered in the late 80' [13, 32, 40] due to the possibility to use them for HDD recording media technology. Recently they became the key to study domain wall motion [129], spin transfer torque [128] and tunneling magneto resistance [148]. The next generation of Magnetic Random Access Memory (MRAM) and Hard Disk Drive (HDD) technologies could be based on these physics phenomena.

Ultrathin Co (0.4-0.8 nm thick) has more recently become a very important model system to study current-induced magnetization reversal [67, 114] and electric field control of magnetization [17, 181]. In thin Pt/Co/MOx systems, the surface contributions are enhanced. These contributions are necessary to observe Rashba splitting [128, 129], Spin Hall contribution [105, 191, 219] and Dzyaloshinskii-Moriya Interaction (DMI) [14, 44, 136, 212] which are actively discussed nowadays.

This chapter will be dedicated to the study of ultrathin Cobalt layers, we will compare two systems showing perpendicular magnetic anisotropy (PMA). First we will discuss the $Ta/Pt/Co/AlOx$ system, subsequently we will investigate and compare the previous results with the $Ta/Pt/Co/CoO$ system. On both systems the top metal oxide (MOx) layer will be deposited as a metallic wedge. The PMA origin in these systems will be studied by varying different parameters like nature of the interface, annealing temperature, layer thicknesses and oxidation effect. The role of CoO on the PMA and on the magnetic properties of these

system will be discussed. The presence of an antiferromagnet (such as CoO) in the stack can add a further asymmetric contribution. The key measurements will be performed via Anomalous Hall Effect (AHE) in a cryostat and with a Magneto-Optical Kerr Microscope (MOKE) system.

3.2 Experimental determination of the effective anisotropy

The effective anisotropy energy K_{eff} is the energy required to align the magnetization along its hard axis [39, 77]. K_{eff} can be calculated from the difference in the area of hysteresis loop measured along the hard axis and easy axis directions, as shown in figure 3.1 (area between the two curves). The equation in this case will be:

$$K_{eff}(J/m^3) = \int_{hard\ axis} \mu_0 M \cdot dH - \int_{easy\ axis} \mu_0 M \cdot dH = \int_{H=0}^{H=H_S} \mu_0 \Delta M \cdot dH \tag{3.2}$$

with H_S the saturation field. The other possibility and the choice for this thesis is to extract the value from the anisotropy field H_a (see figure 3.1.). Supposing uniaxial anisotropy then $H_S = H_a$. Deriving from 3.4 the following equation associates K_{eff} to H_a:

$$K_{eff} = \frac{1}{2} \cdot \mu_0 \cdot H_a \cdot M_S \tag{3.3}$$

Where M_S is the saturation magnetization determined via VSM-SQUID (or taken from literature, for Co: $M_{S,Co} = 1.4 \cdot 10^6$ A/m, where not measured first hand).

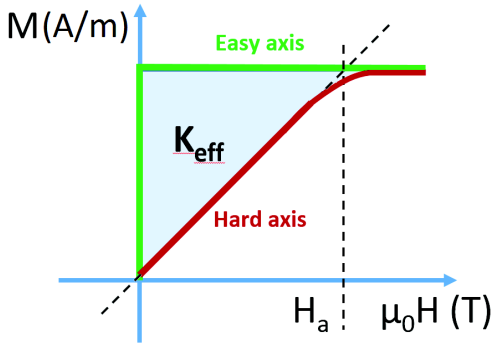

Fig. 3.1 Methods to calculate or extract K_{eff}, by subtracting the areas or using the anisotropy field value.

For our convention, the effective anisotropy is taken <0 if the easy axis lies in plane and >0 if the easy axis lies out of plane [39]. This is illustrated in figure 3.2. On graph 3.2, the product $K_{eff}t_{Co}$ as a function of the Co thickness is shown. The intercept with the vertical axis gives the total interface anisotropy contribution ($K_{S1}+K_{S2}$). The slope gives the volume contribution ($K_V - \frac{1}{2}\mu_0 M_S^2$). K_V can be either positive or negative (depending on the crystal structure). K_V is usually smaller when compared to the demagnetization energy term, this leads to negative slope (figure 3.2).

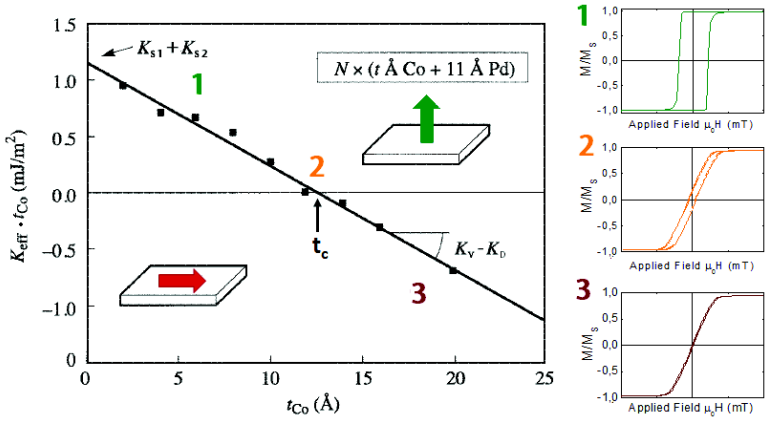

Fig. 3.2 Surface effective anisotropy versus thickness for a Co/Pd multilayers. 1) OOP anisotropy ($K_{eff} > 0$), 2) critical thickness ($K_{eff} \sim 0$) transition between OOP and IP anisotropy and 3) IP anisotropy ($K_{eff} < 0$) and associated relative hysteresis loops (the external field is applied OOP). Figure adapted from [39].

3.3 Origin of the PMA

In magnetic thin films, due to the reduced bulk contribution, the interfaces have a large impact on the magnetic properties. The behavior at the interfaces between a magnetic and the two non magnetic layers is the key ingredient behind the rise of the PMA. Simplifying the problem (see figure 3.3), the effective anisotropy K_{eff} will have two major contributions, the Bulk volume anisotropy K_U and the surface anisotropy K_S. The contribution of K_S became more important as the thickness of the ferromagnetic film t_{FM} decreases.

The bulk contribution in transition metals has two major terms: the magnetocrystalline volume anisotropy (K_V) and the shape anisotropy (K_D). The magnetocrystalline anisotropy in Co originates from its crystallographic structure associated to the spin-orbit coupling (SOC) interaction. This contribution for 3d transition material (such as Co) is smaller than the one for rare-earth atoms, due to the quenching of the orbital moment. Cobalt has a hcp crystallographic structure and in this very anisotropic structure, Co has a mainly uniaxial

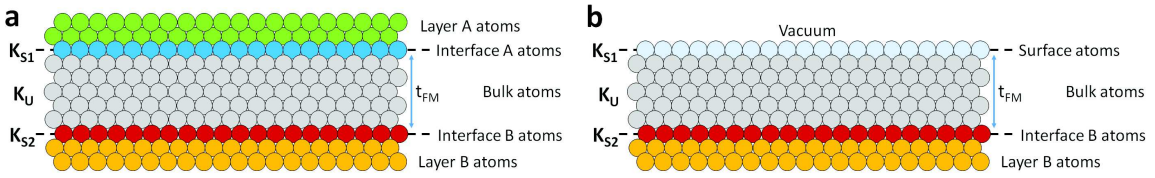

Fig. 3.3 Schematic view of interface and volume anisotropy contribution in thin films. a. The magnetic layer is sandwiched between two interface and b. between an interface and vacuum (adapted from [149]

magnetocrystalline energy of: $K_{V,Co} = 4.1 \cdot 10^5 J/m^3$ (if epitaxially textured) [37]. The shape anisotropy contribution on the other hand originates from the long range dipolar interaction. This is sensitive to the outer boundaries of the sample and produces the demagnetizing field. To minimize the magnetic energy this field favors the magnetization lying parallel to the film plane. The demagnetization energy can be expressed as: $K_D = -1/2\mu_0 M_S^2$ with M_S the saturation magnetization.

These contributions to the effective anisotropy can be summed up as follows :

$$\frac{E}{V} = K_V \sin^2(\theta) - \frac{1}{2}\mu_0 M_S^2 \sin^2(\theta) + \frac{(K_{S1} + K_{S2})}{t_{FM}} \sin^2(\theta) = K_{eff} \sin^2(\theta) \ \ [J/m^3] \tag{3.4}$$

where V is the volume, t_{FM} the thickness of the considered magnetic layer and θ is the angle subtended by the magnetization and the sample normal [77]. Therefore K_{eff} is expressed by:

$$K_{eff} = K_V - \frac{1}{2}\mu_0 M_S^2 + \frac{K_{S1} + K_{S2}}{t_{FM}} \tag{3.5}$$

Usually in multilayers, where the bottom and top interface contribute in the same way, $K_{S1} + K_{S2}$ is noted as $2K_S$. This is not always the case, for example if there is a different contribution from the top Co/MOx and bottom Pt/Co interfaces. In thin films the volume anisotropy $K_{V,Co}$, which is a constant in bulk material, may change. For example strain may induce a magneto-elastic contribution which will vary with thickness (strain relaxation). The crystallographic contribution may also evolve with thickness (in very thin films it is possible to stabilize the fcc phase) and the texture may change during growth.

We can separate $K_{V,Co}$ in two terms. The first term (thickness related) behaves as an interface contribution, that we cannot distinguish from $(K_{S1} + K_{S2})$. The second term (bulk-like) is related to the crystallographic structure of the Co layer that has to be determined using X-Ray Diffraction (XRD) measurements. On the measurement done on the standard

Ta(5nm)/Pt(2.5nm)/Co(1nm)/AlOx(wedge) it was impossible to distinguish the Co peak from the Pt peak (not shown). Therefore, we decided to prepare a test sample with 20 nm of Co deposited on top of a Ta(5nm)/Pt(2.5nm). The obtained spectrum is shown in figure 3.4, the expected lines for the different crystallographic structures are also plotted.

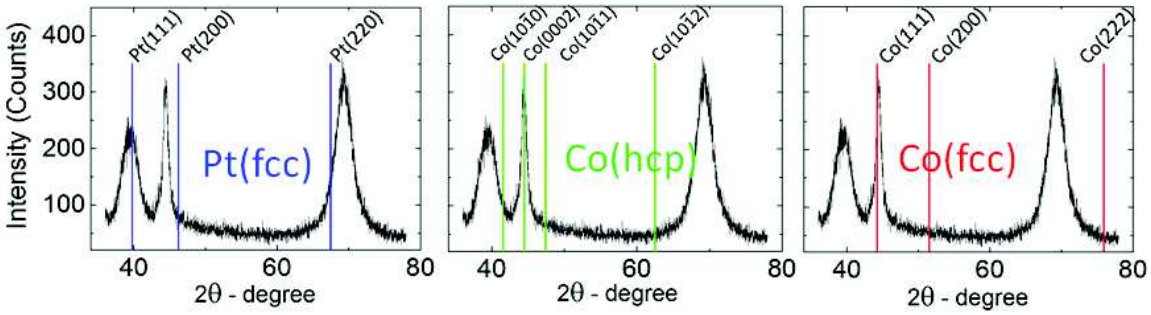

Fig. 3.4 Ta(5nm)/Pt(2.5nm)/Co(20nm) test sample: X-Ray Diffraction spectra and expected lines.

The peaks of the Pt and the Co are clearly distinguishable (see figure 3.4). We can now focus on the Co peak. The distance between the (200)-fcc and the (0002)-hcp Co line is only 2 degrees. The obtained XRD peak is too wide to clearly distinguish between the hcp and fcc cobalt, even when depositing 20nm of Co it was impossible to obtain conclusive information on the Co crystallographic structure. Furthermore we have no information on the structure of 1nm of Co. We will then assume two extreme cases, one where we will consider a perfect hcp structure and the other where we will assume a perfect fcc structure for the Co layer.

Assuming a perfect hcp structure, OOP textured, means that the Co magnetocrystalline energy $K_{V,Co} \sim 4.1 \cdot 10^5 J/m^3$ is comparable to the demagnetization energy $K_{dem} \sim 1.2 \cdot 10^6 J/m^3$. On the other hand if the Co is fcc-structured its magnetocrystalline energy will be largely reduced $K_{V,Co} \sim 2.0 \cdot 10^4 j/m^3$ [224] and its contribution to the anisotropies will be neglected. The two cases will be discussed in section 3.4.1.

In 1954 Néel [144] noticed that the atoms at the interface see a different environment compared to bulk ones due to the breaking of the crystal continuum at the interface leading to different properties when compared to bulk system. His approach, based on the localization of the molecular orbitals, gave a first intuitive picture although is not the most appropriate to describe 3d transition metals. In 1986 Gay and Richer [58] introduced the itinerant electron model (band model) to explain the PMA origins in thin films. The model takes into account the broken crystal symmetry and the Fermi level position at the interface.

The model was later improved by Bruno, that generalized Néel's model to hexagonal close-packed structures in order to determine the magnetic surface anisotropy of cobalt. Bruno estimated that for a surface (see figure 3.3 b), the expected surface anisotropy for 1ML

of Co (or any other transition metal) is in the order of 1 mJ/m^2 [26]. This value strongly depends on the crystal-field parameters and on the 3d band-filling.

The reasons for the reduced symmetry at the surface is the absence of coordination atoms which results in a reduction of the 3d band width. This reduction highly affects the OOP orbitals while only marginally affects the IP ones. As a result a charge transfer occurs in order to reconfigure the population between OOP and IP orbital, this changes the Coulomb energy. Leading to an increase of the shift Δ in the d-orbitals energy of material with low symmetry (to compare to the high symmetry of bulk material). This is represented in figure 3.5.

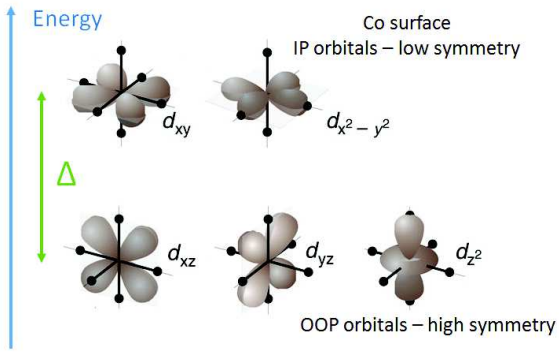

Fig. 3.5 Co d-orbitals and effect of surface broken symmetry. Δ is the difference in energy between OOP and IP orbitals (figure adapted from [182]).

This simplistic picture for the surface case becomes more complicated when we consider interfaces, due to the presence of different surrounding atoms, which leads to include into the picture the nature of coordination between atoms. The two cases for our typical stack will now be briefly discussed. First the interface with Pt (strong spin-orbit coupling and strong crystal field) and then the interface with a metal oxide (MOx) (low spin-orbit coupling).

3.3.1 Pt/Co interface

Pt is an heavy metal and when interfaced with Co causes the hybridization of the 3d Co orbitals with its 5d orbitals. The hybridization combined with the Pt strong spin-orbit coupling will increase the Co orbital momentum, making possible to orient the spin perpendicularly to the interface [142, 230]. One can think of the hybridization as an effective uniaxial crystal field, acting at the interface Pt/Co, which modifies the band structure of the materials. Two different effects play at the interface:

- The crystal field defines the IP orbitals (d_{xy} and $d_{x^2-y^2}$) and OOP orbitals (d_{yz} and d_{xz}) states near the Fermi level.

- The spin-orbit coupling splits even more the IP and OOP states at the interface. The strong SOC will also enhance the Co OOP perpendicular orbital momentum.

This results in an induced Pt spin momentum parallel to the Co one ($M_S(Pt)//M_S(Co)$). The large induced momentum contributes to the interfacial Pt magnetic moment and aligns it parallel to the Co momentum (thanks to the strong spin-orbit coupling).

In conclusion the 3d-5d hybridization (mediated by the d_{xy} and d_{xz} orbitals [224]), combined with the strong SOC is at the PMA origin. The effects on Co is to favor the OOP orbital at the lower energies, while on Pt is to align its magnetic moment with the Co one. This surface induced perpendicular anisotropy is observed when interfacing Co to Pt (or any other heavy metal such as Pd, Au, W, Mo) and is mostly due to the heavy metal layer. The presence of a heavy metal with strong SOC is essential for PMA [142, 148, 237].

3.3.2 Co/MOx interface

More recently a PMA interfacial contribution originating from the magnetic metal/metallic oxide has been observed [132, 170]. This effect is quite general and was observed with almost any metallic oxide [96, 112, 150, 171]. The PMA origins must be independent from the crystalline structure of the oxide layer. A crucial contribution for the PMA arises from the Oxygen, which is responsible for the formation of Co-O bonds[113]. This effect was nicely explained in an ab-initio study on Fe/MgO and Co/MgO interfaces [235] taking into account the weak spin-orbit coupling which characterizes these interfaces. From their calculation the origin of the PMA is due to the interplay of different factors:

- The weak spin orbit coupling allows to remove the degeneracy of the out of plane 3d orbitals.
- Hybridization between d_{xz}, d_{xy} and d_{z^2} favored by the weak Spin-Orbit coupling.
- Hybridization between Co_{3d} and O_{2p} orbitals at the interface between the transition metal and the oxide.

Even a weak Spin-Orbit coupling (SOC) is enough to split the Co band levels around Fermi energy in either the IP and OOP magnetization (figure 3.6a). After the splitting the energy bands hybridize, then the strong overlap between Fe-3d and O-2p orbitals highly modifies the band structure giving rise to a strong crystal field at the interface. From their ab-initio calculation and from experimental results it is clear that this effect is reduced if the interface is under/overoxidized (figure 3.6 b and c). Optimal conditions are therefore necessary to the rise of PMA.

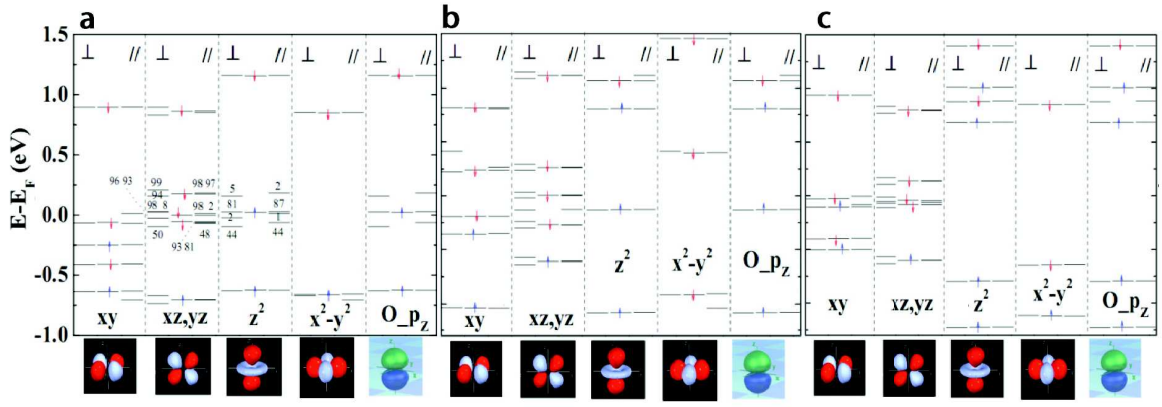

Fig. 3.6 Spin-orbit coupling effect on the orbitals at the Fe/MgO interface for a. perfectly oxidized b. overoxidized c. underoxidized case. Three sub-columns in each column show the band levels for out-of-plane (⊥ on the left) and in-plane (// on the right) orientation of the magnetization as well as for the case with no spin-orbit interaction included (middle). (figure adapted from [235]).

In conclusion PMA at Co/MOx interface comes from the combination of the Co-O bonds with the weak spin-orbit coupling which will split the levels and induces an OOP contribution to the magnetization [235].

3.4 Results and Discussion

3.4.1 Interface anisotropies Co/AlOx

Sample growth and characterisations

The sample for this study was deposited with magnetron sputtering (for details see section 2.1.1). The pressure prior the deposition was $5 \cdot 10^{-7}$ mbar. Our machine allowed the preparation of a: $Ta(5nm)/Pt(2.5nm)/Co(1.2nm)/Al(t_{Al})$ stack deposited on top of a Si(100) substrate with some native silicon oxide (usually 1 to 2nm thick). The top Al layer was deposited with the wedge technique. The Al thickness t_{Al} is varied between 3.5nm and 0.5nm along the wedge axis (for details about the wedge deposition see the beginning of chapter 2). After the metallic Al deposition a plasma oxidation of 90" was performed in situ. The RF power was chosen to be 10W, the Ar and O_2 mixture pressure was $2.5 \cdot 10^{-3}$mbar. Such oxygen plasma allows the formation of a AlOx capping layer and the partly oxidation of the Co layer. To preserve the continuous wedge properties and to avoid intermixing at the interfaces no annealing was performed for this study.

We then proceed to characterize the sample. In order to fit it in the different machines the roughly 8-cm-long wedged sample needed to be cut in eight pieces of roughly 1cm. XRR

analysis was performed on such samples to characterize the wedge structure and obtain the thicknesses value for each layer. The two samples at the edge of the 8cm long wedge (*S8* and *S1*) are not included in this study, because at the very edge of the sample holder, the thickness is not uniform (there is an unwanted thickness gradient when depositing from 100 mm due to non-uniform sputtering rates). The target is 3" = 76.2 mm so the 80 mm sample is longer than the declared uniformity range (which is around 5% when depositing at 100mm over 2"). The XRR results are summarized in table 3.1 from the thinner sample *S2* to the thicker *S7*.

The XRR spectra were recorded with a D8 Discover diffractometer and the fit of table 3.1 were done with the Brucker's LEPTOS software (for details see: 2.3.2). The peculiarity of our deposition methods are confirmed by the XRR picture, we have a common bottom stack $Ta(5nm)/Pt(2.5nm)$ not oxidized. We will assume that the bottom interface Pt/Co is identical for all samples. We have then a continuous evolution of the properties at the top Co interface, from Co/Al to Co/AlOx to Co/CoO/AlOx. The Al layer thickness decrease is roughly 0.5 nm per centimeter along the wedge axis direction. Thanks to the wedge geometry the oxidation could be controlled at the sub-nanometer level. We estimate that the uncertainty on the thicknesses obtained with the XRR technique is around $\sim$0.1nm.

The typical XRR obtained roughness for metallic (non-oxidized) material is in the order of 10% of the thickness. The obtained densities are lower than the nominal bulk one (summarized in table 3.2). For non-oxidized layer such as Pt and Ta they are in the order of 90 ± 5 % of the nominal value. The oxide layer such as AlOx and CoO have their density oscillating around 75 ± 5% of the nominal one. The decrease in density is explained by the existence of a mixture of different amorphous phases, the oxygen plasma also contributes to lower the density because it increases the roughness of the interface. Such lowering of the density is expected in thin sputtered films [49, 56, 88, 169].

Interface anisotropies versus wedge position

We performed Anomalous Hall Effect (AHE) measurements on the pieces cut along the wedge axis (for details about the AHE measurement technique refer to chapter 2.3.1). The temperature for each measurement was 300K and two measurement zones are 1 ± 0.1 cm apart. The external field was applied along the hard magnetization axis in order to extract the anisotropy field for each sample (see figure 3.7).

The anisotropy field follows the wedge evolution. *S7*, *S6* and *S5* have IP easy axis at 300K, *S4* and *S3* show OOP behavior and finally *S2* with a Co thickness inferior to 0.3nm is not ferromagnetic at room temperature. From equation 3.4 and multiplying by t_{FM} we can calculate the surface anisotropy energy for our system E (J/m^2):

Table 3.1 Ta/Pt/Co/CoO/AlOx XRR fit results

	Sample S2			Sample S3		
	Thickness [nm]	Roughness [nm]	Density [g/cm^3]	Thickness [nm]	Roughness [nm]	Density [g/cm^3]
AlOx	0.93	0.57	3.2	1.80	0.60	3.1
CoO	1.00	0.17	4.5	0.65	0.13	3.7
Co	0.28	0.15	7.8	0.67	0.27	7.4
Pt	2.10	0.72	20.9	2.46	0.38	19.1
Ta	4.24	0.60	14.2	4.57	0.61	13.7
SiO_2	1.88	0.29	1.9	1.60	0.25	2.2
$Si_{substrate}$	∞	0.20	2.4	∞	0.26	2.4
	Sample S4			Sample S5		
	Thickness [nm]	Roughness [nm]	Density [g/cm^3]	Thickness [nm]	Roughness [nm]	Density [g/cm^3]
AlOx	2.53	0.57	3.2	2.57	0.52	3.8
CoO	0.10	0.10	4.1	—	—	—
Co	0.95	0.20	7.7	1.13	0.26	8.3
Pt	2.56	0.33	21.0	2.49	0.28	19.0
Ta	4.98	0.56	14.8	5.59	0.54	13.6
SiO_2	1.82	0.23	1.9	1.93	0.25	1.7
$Si_{substrate}$	∞	0.22	2.4	∞	0.24	2.4
	Sample S6			Sample S7		
	Thickness [nm]	Roughness [nm]	Density [g/cm^3]	Thickness [nm]	Roughness [nm]	Density [g/cm^3]
AlOx	3.00	0.68	3.2	3.20	0.59	4.0
Al	1.17	0.43	1.8	1.75	0.39	2.7
Co	1.19	0.26	8.1	1.17	0.17	8.6
Pt	2.48	0.28	20.7	2.63	0.27	21.4
Ta	5.35	0.45	15.5	5.03	0.47	16.6
SiO_2	1.90	0.25	2.1	1.70	0.22	2.2
$Si_{substrate}$	∞	0.18	2.4	∞	0.26	2.4

Table 3.2 Nominal density for the XRR fit.

	AlOx	*Al*	*CoO*	*Co*	*Pt*	*Ta*	*SiO_2*	*Si*
Nominal density [g/cm^3]	3.98	2.7	5.3	8.56	21.44	16.63	2.2	2.39
Fit minimum value [g/cm^3]	3.2	1.8	3.7	7.4	19	13.6	1.8	2.39

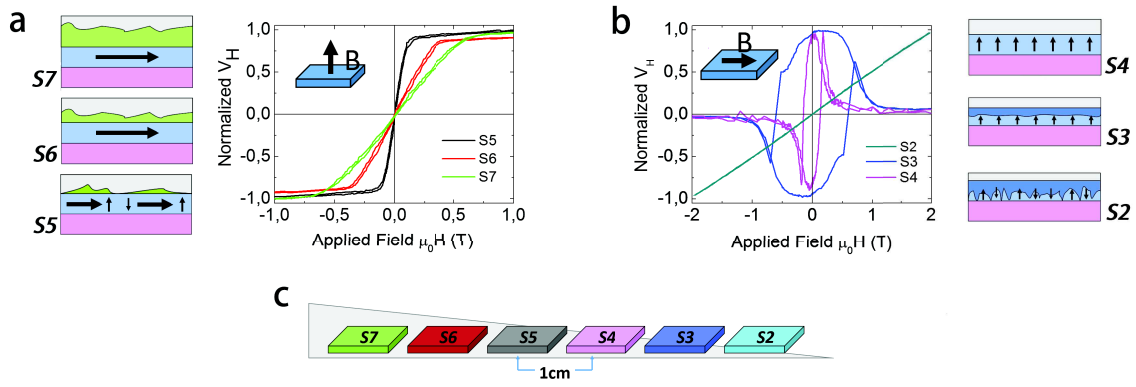

Fig. 3.7 a. and b. show the magnetization behavior along the wedge and the relative IP and OOP measurements at 300K; c. shows the position on the wedge of the various samples.

$$K_{eff} \cdot t_{Co} \ [J/m^2] = -\frac{1}{2}\mu_0 M_S^2 \cdot t_{Co} + K_{S,Pt/Co} + K_{S,Co/MOx} \tag{3.6}$$

From graph 3.7 b. it is possible to notice that, when the magnetization is pointing OOP, the field necessary to rotate it IP is higher in *S3* (900mT) than in *S4* (400mT). On the contrary when the magnetization still lies in-plane (figure 3.7 a.) *S5* is easier to saturate OOP than *S6* and *S7*. A complete list of the measured values is reported in table 3.3. The anisotropies value are expressed in mJ/m^2 while the anisotropy field in mT. Using formula 3.3, we can extract the effective anisotropy field along the wedge (figure 3.8).

Table 3.3 Anisotropies value at 300K

	$\mu_0 H_a$ [mT]	$K_{eff} t_{Co}$ [mJ/m^2]
S7 (IP)	550±2	-0.46±0.02
S6 (IP)	320±2	-0.27±0.01
S5 (IP)	100±2	-0.08±0.01
S4 (OOP)	400±20	+0.27±0.03
S3 (OOP)	900±20	+0.42±0.04

From these values and by using equation 3.6, we can separate the two contributions and isolate the interface $(K_{S1} + K_{S2}) = K_{S1,S2}$ from the demagnetization energy contribution.

This is illustrated in figure 3.9), where we consider the two extreme cases. In figure 3.9a we assume that the Co is fcc structured, while in 3.9 b we assume that is hcp structured. This

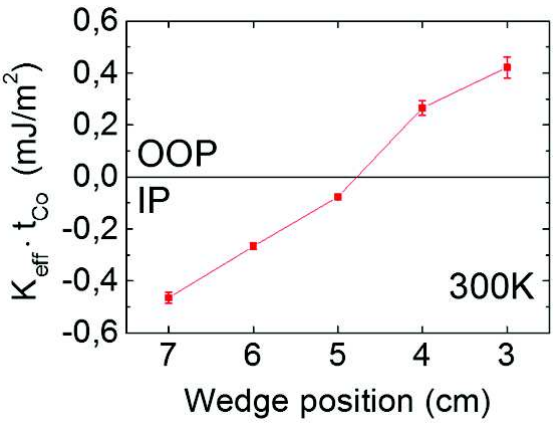

Fig. 3.8 Calculated effective anisotropy values along the AlOx wedge.

distinction does not change the message but is reflected in a vertical shift of the anisotropy values. The calculated values can be found in table 3.4 for the fcc and hcp case respectively.

The error on the thickness will be assumed equal to $\Delta(t_{Co}) = \pm 0.5$Å; a lower value than the expected one for XRR measurements (~ 1). This is due to the wedge technique and to its re-combinatorial aspect which allows a reduced uncertainty for the thicknesses. The error bars on figure 3.9 mostly come from the propagation of the thickness uncertainties on the anisotropies. The uncertainty on the measured saturation field in the OOP case is 10 times larger (20mT compared to 2mT) with respect to the IP case, this is mostly due to the way the value are extracted which is more straightforward and precise for the IP case.

Table 3.4 Effective anisotropy and demagnetization energy at 300K

	fcc-Cobalt		hcp-Cobalt	
	$K_{dem}t_{Co}$ [mJ/m^2]	$K_{(S1,S2)}$ [mJ/m^2]	$K_{dem}t_{Co}$ [mJ/m^2]	$K_{(S1,S2)}$ [mJ/m^2]
S7 (IP)	-1.48±0.06	1.01±0.08	-0.98±0.06	0.52 ±0.08
S6 (IP)	-1.48±0.06	1.21±0.07	-0.98±0.06	0.72 ±0.07
S5 (IP)	-1.42±0.06	1.34±0.07	-0.94±0.06	0.87 ±0.07
S4 (OOP)	-1.17±0.06	1.44±0.09	-0.77±0.06	1.05 ± 0.09
S3 (OOP)	-0.82±0.06	1.25±0.10	-0.54±0.06	0.97 ±0.10

By separating the two contributions it is possible to notice that the total interface anisotropy ($K_{S1,S2}$) is higher in *S4*, which has the best oxidation condition. Therefore, the higher field necessary to rotate the magnetization of *S3* is due the reduced Co layer thickness, which gives a lower demagnetization energy. This is in agreement with the theoretical

explanation by Yang and coworkers [235] who observed a reduction in the Δ shift for the 3d orbitals in overoxidized layer.

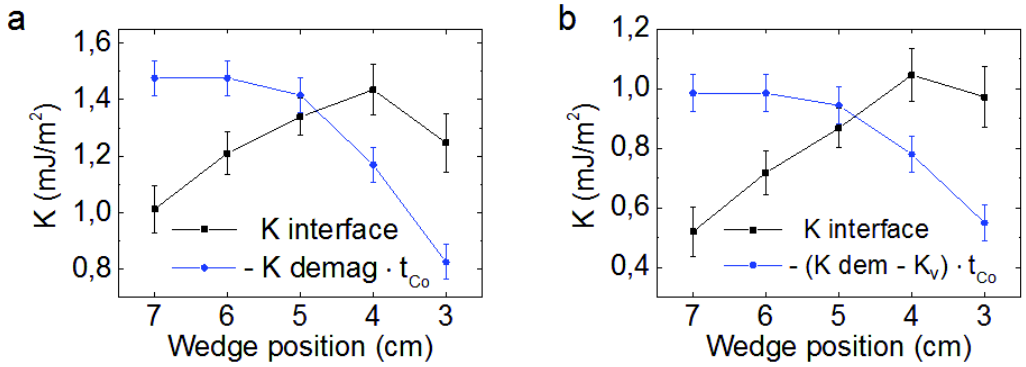

Fig. 3.9 a. Calculated effective anisotropy value and b. Interface anisotropies and demagnetization energy along the AlOx wedge.

Using equation 3.6 and taking a step further we can think that on sample *S7* the contribution to the effective anisotropy arises only from the bottom Pt/Co interface. The top Co/Al does not bring any effective contribution to the PMA (close to zero) [113, 235], because of the presence of 1.75nm of metallic Al, no Co-O bonds should be formed.

For thinner Al thicknesses (sample *S6* and *S5*) some Co-O bonds could be formed, oxygen penetrates easily along grain boundaries and we can not totally exclude Co-O bonds [9, 10, 226], this can explain the increase of the effective anisotropy on those samples. By knowing t_{FM} it is possible to calculate and then subtract the demagnetization energy to the effective anisotropy to obtain the Pt/Co interface contribution which, for the fcc case is: $K_{S,Pt/Co}$ = 1 mJ/m^2. The value will be reduced in the case of hcp cobalt where $K_{S,Pt/Co}$ = 0.5 mJ/m^2. These numbers are comparable to previously reported values obtained in similar systems which roughly vary between 0.5 mJ/m^2 to 1.5 mJ/m^2 depending on the substrate type for Pt/Co interface, oxidation state, possible intermixing at the interface and grain size [31, 32, 77, 112, 171].

Thanks to the wedge geometry, the Pt/Co contribution to the effective anisotropy can be considered constant along the whole sample. The optimal condition for the oxidation are reached in *S4*, which have a strong Co/AlOx contribution to the effective anisotropy. Therefore, on this sample *S4* we can subtract the $K_{S,Pt/Co}$ contribution to the total $K_{(S1,S2)}$ in order to obtain $K_{S,Co/AlOx}$ = (0.45±0.09) mJ/m^2. Following the same strategy we can extract the value for the hcp case, which will be $K_{S,Co/AlOx}$ = (0.52±0.09) mJ/m^2. On *S3* when the oxygen penetrates into the Co layer the contribution of the top interface is reduced to (0.25±0.1) mJ/m^2 due to over oxidation of the interfaces. Indeed the top Co/MOx interface contributes to the OOP anisotropy and its effect is roughly half of the heavy metal Pt magnetic

Co interface contribution. The wedge structure allows a nice and simple way to study the Co/MOx contribution to the PMA.

Interface anisotropies versus temperature

Although much research has been performed so far on systems exhibiting PMA, the temperature dependence of the magnetic anisotropy has been less investigated [77, 188]. A certain number of paper have been published in the 90's [12, 94, 205] although received little attention due the fact that the interests for application are mostly at RT.

Due to the particular geometry of our Pt/Co/AlOx system we have the presence of CoO in the stack. Cobalt oxide (described in section 1.1.1) is a known antiferromagnet, which can have an impact on the magnetic anisotropies when the film is cooled down below CoO Néel temperature T_N. Furthermore, the temperature dependence of the PMA in FM/AFM system is far less studied in the region between the Néel temperature T_N and blocking temperature T_B. In this particular temperature range, due to the lack of technological applications, the anisotropies are far less studied [77]. For these reasons the temperature dependence of the anisotropies along the wedge will now be discussed. Because CoO is not antiferromagnetic at room temperature we performed AHE measurement in a cryostat, where the temperature will be varied between 300K and 5K and the field between +5T and -5T.

First of all we will concentrate on samples which are underoxidized and where no CoO should exist in the stack, therefore we will first observe the temperature behavior of samples *S7*, *S6* and *S5*. Their behaviors is summarized in graph 3.10. *S7* Effective anisotropy changes from -0,39 mJ/m^2 at 5K to -0.42 mJ/m^2 at 275K, on *S6* from -0.18 mJ/m^2 to -0.24 mJ/m^2 and finally on *S5* from -0.048 mJ/m^2 to -0.065 mJ/m^2.

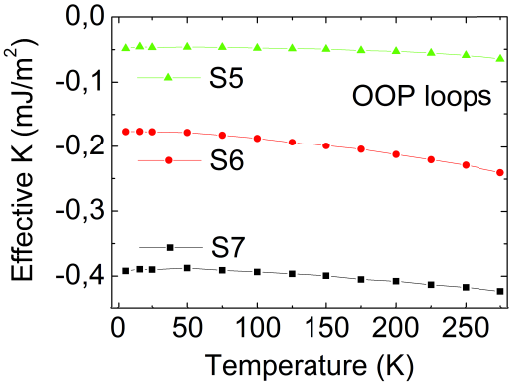

Fig. 3.10 a. Effective anisotropy behavior for underoxidized samples. K_{eff} decreases monotonically with increasing temperature. The easy axis is in-plane.

For these three samples, with no CoO, the perpendicular anisotropy decreases monotonically with increasing temperature (Fig: 3.10). This is in agreement with previous studies on Co/Pt multilayer [205, 207, 239]. The explanation resides in the presence of a positive anisotropy terms which increases with decreasing temperature. One of the possible reasons is the increase of the Pt magnetic moment at low temperature [94, 205]. By remembering formula 3.5 we can note that K_{eff} is mainly composed by $-1/2\mu_0 M_s^2 + K_{(S_1,S_2)}$. The demagnetization term changes like M^2, the surface term changes faster than M^2, the result is a larger OOP contribution at low temperature.

This monotonic behavior changes when we observe samples *S4* and *S3*. These samples show OOP effective anisotropy at room temperature; with decreasing temperature the effect is a strong reduction of the OOP anisotropy. The hysteresis loops measured at different temperatures for sample *S4* are shown in figure 3.12, the behavior for both samples is summarized in figure 3.11 where the effective anisotropy values, taken from IP loops, are plotted. For the IP loops the anisotropy field (H_a) is extracted with a MATLAB fit on the first part of the slope, where the magnetization starts to rotate; when this is not possible (i.e. where the loops are not well defined, for example the 50K and 100K loops in figure 3.12a) the anisotropy field is extracted as the intercept of the slope with $V_H = 0$.

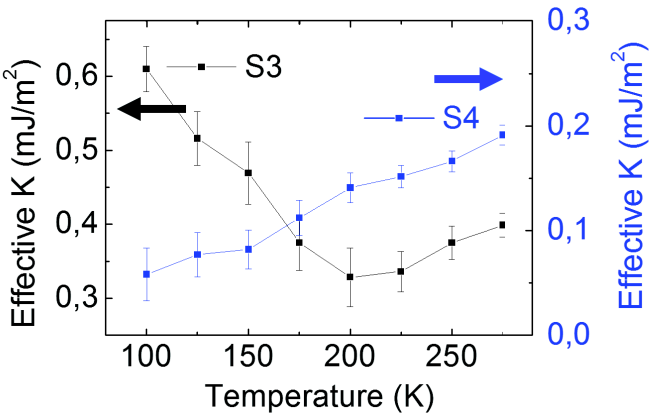

Fig. 3.11 a. Effective anisotropy behavior for *S4* (in blue) and sample *S3* (in black). There is a suppression of K_{eff} with decreasing temperature.

Since the anisotropy of underoxidized Pt/Co layer changes little over these temperature ranges, the strong suppression of the anisotropy must originate from a new effect that comes into play when we decrease the temperature. The XRR evidenced the presence of CoO in *S4* and *S3* we attributed this effect to the CoO which becomes antiferromagnetic at low temperature and could introduce new effect on the magnetic properties when coupled to Co.

We will now focus on *S4*, sample with little CoO in the stack. *S4* shows OOP easy magnetization direction at room temperature. This easy axis is kept until the temperature

drop below 150K; at this temperature a tilt in the OOP loops appears (see figure 3.12 b). The temperature evolution of the hysteresis loops for sample *S4* are shown in figure 3.12. From the IP loops we may notice that there is a monotonous decrease of the effective anisotropy (figure 3.12 a), the magnetization is less and less OOP with decreasing temperature, the anisotropy field is reduced with decreasing temperature. By looking at the OOP loops of figure 3.12b, below 150K this effect is large enough to partially rotate the magnetization easy axis away from the perpendicular direction, producing such tilted loops (see figure 3.12b).

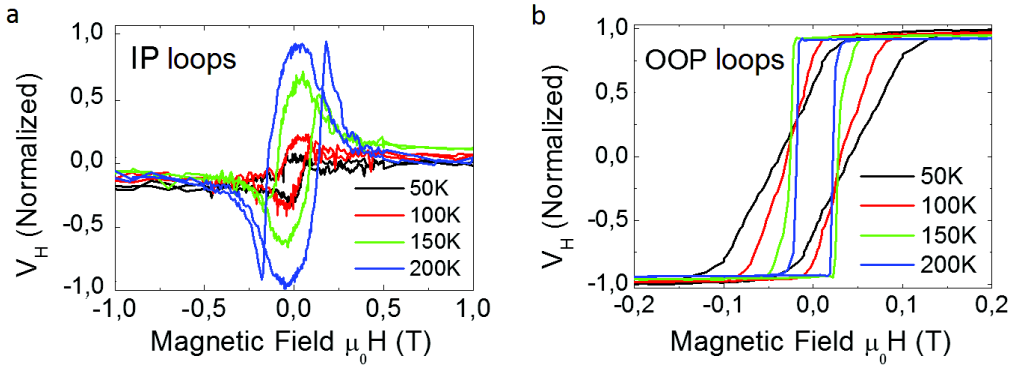

Fig. 3.12 Hysteresis loops of sample *S4* recorded at different temperatures with different external applied field direction a. shows IP loops and b OOP loops.

In figure 3.12 a. we normalized the IP AHE loops with respect to the 200K measurement. In these measurements the Hall voltage is given by $V_H = (R_0 + R_{AHE}M_Z)I$ (refer to section 2.3.1 for details on the Anomalous Hall Effect measurements). Briefly, the first term represent the normal Hall effect whereas the second is the Anomalous Hall Effect (AHE). M_Z is the magnetization component perpendicular to the plane of the sample, therefore, a reduction of V_H mean a loss of OOP magnetization. Below 75K the IP loops completely lose their shape and it was impossible to extract a value for the anisotropy field with this kind of measurement, the magnetization is rotating inside the plane.

A new effect originating from the antiferromagnetic CoO comes into play at low temperature. The effect adds an IP contribution to the anisotropies. This new negative term sums up with the demagnetization energy, together these effects are now overcoming the interface induced anisotropy. The result of the competition between these effects is a tilt of the easy axis from out-of-plane to in-plane direction. A similar reduction takes place on sample *S3* where there is a higher amount of CoO. The reduction of the OOP anisotropy is between 300 and 200K at which temperature a tilt in the loops appears. At 200K there is the appearance of a minimum, below this temperature the effective anisotropy starts to increase again. K_{eff} has a different behavior for the two samples (See figure 3.11). The net

anisotropy for sample *S3* goes from perpendicular to in-plane and then back to perpendicular with decreasing temperature.

On the other hand no minimum appears on *S4* with less CoO in the stack. Is it possible that this minimum appears at lower temperature where the loops loses their shape, and where it is impossible to extract the anisotropy field values with AHE measurements which are only sensitive to the z-component (OOP) of the magnetization. To confirm the temperature behavior VSM-SQUID measurements should be performed along the IP direction of these samples. For sample *S3* the minimum for K_{eff} appears at 200K. This minimum occur at the same temperature at which the loop tilt (similarly to what occur in *S4* at 100K, figure 3.12 b.). 200K and 100K will be the considered CoO ordering temperature for *S3* ad *S4* respectively.

This particular behavior was observed by Shipton and coworkers in a similar system [188]. They studied a CoO/[Co/Pt] magnetic multilayers that exhibit PMA and perpendicular exchange bias. They found that the antiferromagnet CoO layers strongly modify the uniaxial anisotropy of the multilayer structures. The strongest effects due to the CoO layers occur in the vicinity of the Néel temperature T_N, where they observe a suppression of the perpendicular anisotropy. As a result, they observe the net anisotropy of their multilayer system passing from perpendicular to in-plane and then back to perpendicular with increasing temperature. It is possible but unlikely this effect is related to a change in the CoO layer lattice below T_N. A change in the CoO lattice may occur, CoO can transform from cubic to monoclinic and the consequent strain induced changes in the Co/Pt could explain the results [75].

The found temperature dependence is also similar to the results of Leighton et al. [101] and Grimsditch et al. [66] who observed enhanced coercive fields in Fe/FeF_2 samples and induced anisotropy in Ni/FeF_2, respectively. In both cases, the induced contribution is in the direction of the AFM layer anisotropy, the effect reaches a max at T_N (where the loop tilts in our case) and persists even for temperatures superior to T_N. In the proposed models, the effective FM anisotropy includes an AFM layer contribution. This suggests that the net anisotropy of the CoO layers in our samples may be in-plane. This could be (partly) verified with exchange bias measurements, if the exchange bias effect is larger when the cooling field is in-plane compared to out-of-plane. Another and more accurate way to study the CoO would be to utilize synchrotron light like the X-Ray Magnetic Circular Dichroism (XMLD) measurement which can directly probe the AFM layer. The results on field-cooled measurements and preliminary results obtained with XMLD will be presented and discussed in the next chapter on subnanometer exchange bias.

The perpendicular magnetic anisotropy suppression with temperature may be important for magnetic recording applications, in heat assisted magnetic recording system such as STT-MRAM is important to maximize dH_C/dT at the writing temperature. In addition the

switch of the anisotropy from perpendicular to in-plane (or viceversa) with temperature, may enable magnetic devices where anisotropies are tuned with temperature [188]. Sample *S3* loops showed an even more complex behavior: in this sample when cooling down there is an inversion of rotation direction, the physics behind the effect will be fully discussed in the next chapter focused on sample *S3* and field-cooling measurements.

Within the measurement errors, the largest PMA is observed in sample *S4*, where the XRR evidenced only few atomic plane of CoO (CoO is present in the stack and it is enlightened by the temperate measurement and the loss of PMA), the effective perpendicular anisotropy seems to be reduced when a relatively thick CoO layer is formed into the stack (i.e. in sample *S3*).

3.4.2 Interface anisotropies Co/CoO

To better understand the role of the CoO in our multilayer we prepared a wedged sample with the same characteristic as the previous one, although we decided to substitute the top metallic Al with Co. This will give insight on the role of the CoO and its contribution to the effective anisotropy (Co/CoO top interface) and to the changes occurring with decreasing temperature.

Samples growth and characteristic

We prepared via magnetron sputtering a similar sample to compare it to the previous one. We deposited a $Ta(5nm)/Pt(2.5nm)/Co(t_{Co})$ stack on top of a Si(100) substrate with some native silicon oxide. The pressure prior the deposition and plasma parameters are the same as previously described. The top Co layer is once again deposited as a wedge. The Co thickness t_{Co} is varied between 3.5 nm and 0.5 nm along the wedge axis. We performed a reflectivity study and we crosschecked the thicknesses with VSM-SQUID measurements. The values are summarized in table 3.5. The top Co/CoO interface, was done in the following way: first we deposited metallic Cobalt as a wedge and then we proceeded to oxidize it with an oxygen plasma. The interface therefore is not between two different materials (i.e. a Co layer and a CoO layer sputtered from different targets), but is created via with the oxygen plasma, which oxidizes part of the Co.

The thicknesses are similar to those deposited for the AlOx wedge. There is a common bottom part, namely $Ta(5nm)/Pt(2.5nm)$. The top CoO thickness is constant along the wedge and its value is around 2.3nm. The parameter which changes and controls the magnetic properties is the Co layer thickness. The Co thickness for *C7* is 1.5 nm, which is reduced to 0.35 nm in *C2*.

Table 3.5 Ta/Pt/Co/CoO XRR fit results

	Sample C2			Sample C3		
	Thickness [nm]	Roughness [nm]	Density [g/cm^3]	Thickness [nm]	Roughness [nm]	Density [g/cm^3]
CoO	2.39	0.47	4.3	2.38	0.42	4.6
Co	0.35	0.35	7.4	0.60	0.37	7.1
Pt	2.32	0.29	20.2	2.32	0.34	21.0
Ta	4.13	0.34	15.4	4.88	0.52	15.5
SiO_2	1.87	0.26	1.7	1.99	0.25	1.8
$Si_{substrate}$	∞	0.25	2.4	∞	0.19	2.4
	Sample C4			Sample C5		
	Thickness [nm]	Roughness [nm]	Density [g/cm^3]	Thickness [nm]	Roughness [nm]	Density [g/cm^3]
CoO	2.27	0.44	4.8	2.39	0.47	4.8
Co	0.71	0.38	6.7	1.05	0.41	7.35
Pt	2.47	0.37	20.7	2.43	0.35	19.8
Ta	5.10	0.45	15.5	5.31	0.49	14.3
SiO_2	2.00	0.26	1.6	2.24	0.22	1.8
$Si_{substrate}$	∞	0.20	2.4	∞	0.26	2.4
	Sample C6			Sample C7		
	Thickness [nm]	Roughness [nm]	Density [g/cm^3]	Thickness [nm]	Roughness [nm]	Density [g/cm^3]
CoO	2.10	0.47	4.2	2.20	0.54	4.8
Co	1.32	0.30	7.6	1.50	0.29	7.1
Pt	2.35	0.23	19.9	2.43	0.26	19.14
Ta	5.43	0.3	14.5	4.92	0.27	14.1
SiO_2	1.31	0.27	1.8	1.91	0.22	1.9
$Si_{substrate}$	∞	0.20	2.4	∞	0.15	2.4

For this particular sample we wanted a smaller wedge thickness gradient. For this reason we deposited at 100mm (distance between the Co target and the substrate holder) instead of 60mm. The larger distance kept during the deposition of the Co allows to obtain a wedge thickness gradient of roughly 0.25 nm/cm (to compare with the previous 0.5 nm/cm). In this section we will not separate the fcc-Cobalt and the hcp-Cobalt cases; for simplicity we will only consider fcc-Cobalt with ∼0 bulk magnetocrystalline anisotropy.

Interface anisotropies versus wedge position

Following the same procedure adopted for the Aluminum wedge we firstly report a series of measurements done at 300K as a function of the wedge position, the positions along the wedge are sketched in figure 3.13.

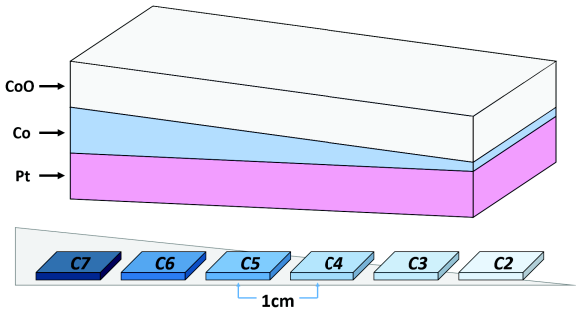

Fig. 3.13 CoO wedge sketch and samples with respect to the wedge axis.

The system characteristics are different compared to the Al wedge. This time there is no evolution of the interfaces. All the samples have the same type of bottom (Pt/Co) and top interfaces (Co/CoO) along the full wedge length. The changing parameter is the demagnetization energy contribution, directly linked to the Co layer thickness. The samples show a strong IP behavior until the critical Co thickness of $\sim$ 0.6 nm is reached. The value for the anisotropy field and the calculated effective anisotropy are summarized in table 3.6 and illustrated in graph 3.14. For the fcc-Co case the demagnetization energy decreases from -1.8 5 mJ/m^2 to -0.74 mJ/m^2 for sample *C7* and *C2* respectively. The interface anisotropy values $K_{(S1,S2)}$ only slightly change along the wedge; the variation between the minimum and the maximum is around 20%, comparable to the thickness uncertainty. We can evidence that the demagnetization energy is the parameter which tailors the magnetic properties behavior. In this case the two interfaces contribution should not change along the wedge axis. Subtracting the demagnetization energy value to the effective anisotropy we found a $K_{(S1,S2)}$ contribution of 0.8-1 mJ/m^2. This value is similar to the one found for the previous set of measurements, for underoxidized sample in which the contribution arises only from the bottom interfaces

($K_{S,Pt/Co} \sim 1$ mJ/m^2). From these measurements it is obvious that the Co/CoO interface is not as efficient as the Co/AlOx interface.

Table 3.6 Anisotropy values

	$\mu_0 H_a$ [mT]	K_{eff} [mJ/m^2]	K_{dem} [mJ/m^2]	$K_{(S1,S2)}$ [mJ/m^2]
C7 (IP)	953±2	-1.00±0.03	-1.85±0.06	0.85±0.1
C6 (IP)	909±2	-0.84±0.03	-1.62±0.06	0.78±0.09
C5 (IP)	665±2	-0.49±0.02	-1.29±0.06	0.80±0.09
C4 (IP)	43±2	-0.02±0.01	-0.87±0.06	0.85±0.07
C3 (OOP)	700±20	0.29±0.03	-0.74±0.06	1.03±0.09

This is somehow comparable to what was previously obtained for sample*S3* (aluminum wedge), where the Al was completely oxidized and the Co layer was half-oxidized. In that case a reduction of the total surface anisotropy was observed, which decreased from 1.5 mJ/m^2 to 1.2 mJ/m^2. We can speculate that the Co/CoO interface is less efficient for the PMA when compared to Co/AlOx interface and that at least for this particular sample its contribution is negligible when compared to the Pt/Co one.

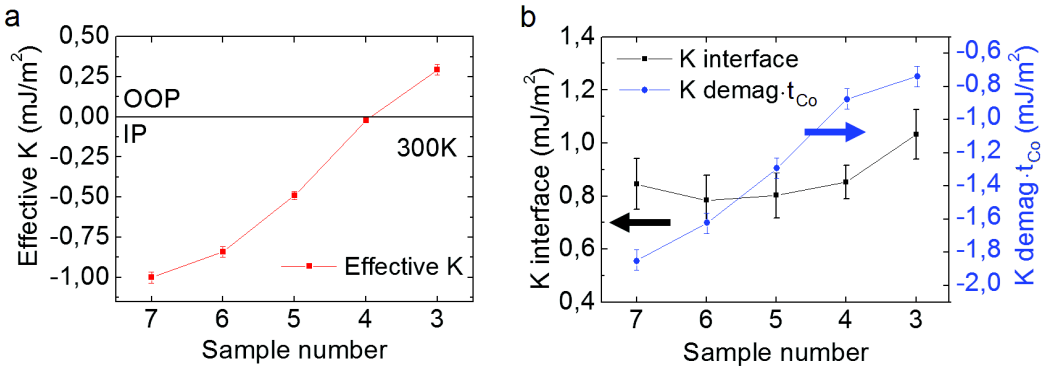

Fig. 3.14 a. Calculated effective anisotropy value and b. Interface anisotropies and demagnetization energy along the CoO wedge for the fcc case

The formation of Co-O bonds is essential for the PMA. This study confirms that to effectively contribute to the perpendicular anisotropy these bonds must be formed at the interface between the Co and another metallic oxide. An over or underoxidation is detrimental for the PMA [235]. In our Pt/Co/CoO wedge sample we could not evidence an anisotropy contribution coming from the top Co/CoO interface. The perpendicular contribution to the effective anisotropy originates solely from the bottom Pt/Co interface. This seems in contrast with what previously found for the Co/AlOx case, where the Co/CoO interface gave a contribution to the PMA.

On the other hand the peculiarity of our Co/CoO sample makes it difficult to compare it to the previous system. This is mainly due to the fact that the quality of the interface is critical for the PMA: it is known that a rough surface would be detrimental for the arise of a perpendicular anisotropy [77, 118, 135]. Moreover the top interface of our sample is not created with different depositions but through an oxygen plasma which may induce large roughness and defects in the oxide layer. In these kind of system a thermal annealing would improve the surface and layer quality, consequently increasing the PMA. This was demonstrated in several other works on Pt/Co/MOx system [32, 49, 96, 112, 150, 171]. For this study we did not perform such an annealing to safeguard the wedge properties and to minimize intermixing.

Interface anisotropies versus oxidation kinetics

For this particular deposition, we also decided not to cap the top CoO layer; we made this choice to investigate the oxidation kinetics of an ultrathin Co layer and its impact on the effective anisotropy. The top 2.3 ± 0.1 nm thick CoO layer was directly into contact with the atmosphere. Due to the slow oxidation kinetics for thin Co thicknesses [195] it was possible to separate the study in two time slots. The first measurements were done soon after the deposition, (within a month period, starting from the *C7* to *C2*), these measurements will be denoted with t=0. The second measurements were performed after one year and denoted with t=365. The measurements were performed in October and November 2013 and 2014 respectively. With increasing time we noticed a change in the anisotropy field of our samples.

All the measured values correspond to a shift towards the OOP zones (the IP samples were easier to magnetize OOP). Sample *C4* showed a change of preferential easy axis, from in-plane to out-of-plane magnetization with an anisotropy field of 700mT. The changes in H_a are resumed in table 3.7. The values of $H_{(a,t=0)}$ were measured soon after the deposition (t=0), the $H_{(a,t=365)}$ values after a period of one year (t=365). All the anisotropy fields are expressed in mT, a representation of the changes can be seen in figure 3.15b.

Table 3.7 Time oxidation kinetics effect on anisotropy values

	$\mu_0 H_{(a,t=0)}$ [mT]		$\mu_0 H_{(a,t=365)}$ [mT]
C7 (IP)	953±2	IP → IP	665±2
C6 (IP)	909±2	IP → IP	550±2
C5 (IP)	665±2	IP → IP	70±2
C4 (IP)	43±2	IP → OOP	600±20
C3 (OOP)	700±20	OOP → OOP	400±20

This effect was partly expected due to the lower t_{Co} and therefore lower demagnetization energy. We also evidence an increase in the interface anisotropy, which seems to become larger with the progression of the oxidation kinetics. For uncapped Co layers, due to exposition with air (and with oxygen, water, CO_2...) in the atmosphere the underneath Co layer kept on oxidizing. A similar study on the oxidation kinetics of Cobalt layer was published by Smardz and coworkers [194, 195]. They observed that Co layer with an initial thickness of $t_{Co} > 5$ nm oxidize practically instantaneously, whereby a constant amount of 2.5 nm of metal is transformed into oxide. On the other hand for 2.5 nm $< t_{Co} < 5$ nm the time constant for oxidation increases considerably and follows linear dependence with decreasing film thickness. Finally for films with $t_{Co} < 2.5$ nm no Co is expected to be left after the complete oxidation. They observed that such state never happens and at low temperature is always possible to measure a magnetic signal. This is probably due to the presence of an intermixing of Pt and Co which creates a magnetic layer which cannot be oxidized.

Globally the effect of the reduced t_{Co} is to push the samples to be more perpendicularly magnetized. Nonetheless sample *C3* shows an inverse behavior. Its anisotropy field passes from 700mT to 400mT after one year time, its Co thickness on the other hand is slightly reduced (see table 3.8). Probably on this sample the Co thickness starts to be critical, with aging it shifted closer to be non magnetic at RT (for thin Co layer the Curie temperature can be inferior to room temperature ($T_C < RT$).

Our deposited CoO wedge samples fell in the <5 nm category. They show changes in magnetic properties and effective anisotropy (table: 3.7). To better understand the change in thickness we perform XRR analysis once again on the wedged samples. An example of spectra is shown in figure 3.15. Apart from the evident change circled on the graph, it is interesting to note the slight shift of the first peaks, which shift towards the left with increasing time. The first peaks of an XRR spectrum are related to the top layer thickness, in this case they indicates a variation in the CoO layer [218]. To verify we repeated the measurement on the Pt/Co/AlOx wedge as well and we could not evidence any change in the magnetic properties. Even 1nm of AlOx was enough to completely stop the oxidation.

To perform the XRR fit, we used the previously determined parameters as a starting point. Therefore we kept fixed the bottom layer parameters and we let the thickness of both the Co and CoO to iterate. The change in thickness is represented in figure 3.16a. The higher the initial amount of Co the higher the amount of Co which oxidizes, the dependence seems to be linear. Sample *C7* had an initial 1.5nm of Co that became 1.03, roughly 0.5nm of extra Co was oxidized after one year. On the same sample the CoO layer changes from 2.39 to 2.78nm.

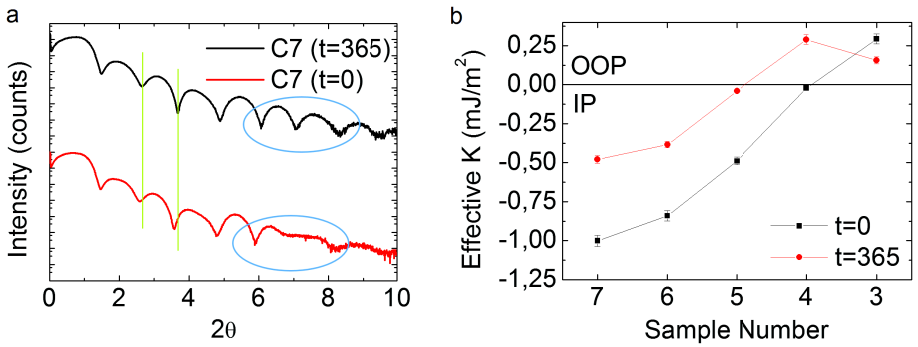

Fig. 3.15 a. XRR spectrum changes after one year for sample *C7*; the circle evidences the most relevant change. b. Extracted effective anisotropy from the H_a values.

There seems to be a mismatch between the transformed Co and the growth of the CoO layer. From the fits it seems that at a certain reduction of Co thickness does not correspond a similar increase of the CoO thickness. For example on sample *C7* the XRR fit evidences that roughly 0.5 nm of Co are oxidized after one year although the corresponding CoO increase is 0.4 nm. Moreover, if we consider that the oxidation process should inflate the thickness, it was calculated that 7Å of Co became roughly 10Å of CoO [109]. This mismatch can be explained with the incertitude on the measured thickness. On the other hand the XRR fit evidences a reduction of the roughness at the Co/CoO interface, this is probably due to the fact the oxidation is becoming more homogeneous. The mismatch disappears on thinner samples.

The results for the Co are summarized in table 3.8. The thickness of the top CoO layer stabilizes around 2.6±0.2 nm for each sample, which is similar (within the error bars) to what was reported by Smardz and coworkers. They reported 2.5 nm as the maximum oxide thickness after which the natural oxidation stops [195]. The non-significative difference could originate from the fact that the two systems are not exactly the same. We initially oxidize the Co layer with an oxygen plasma, therefore the natural oxidation on our sample is through the CoO initially created, while in their case the sample is left to oxidize in air. Normally the process of oxidation vastly depends on the structural properties, in particular the oxygen can be easily transported along grain boundaries by which the oxidation can continue through the material [9, 10, 158, 226]. The oxygen plasma oxidation, which creates a rough surface, may have a role in this and could explain the higher t_{CoO} found for this study. In such a layer it would be easy for the oxygen to penetrate deeper, explaining the slightly higher Co oxide thickness found.

The reported values are those extracted form the XRR fits. From the XRR spectra it is clear that for *C7* and *C6* there is a change in t_{Co}. For thinner samples like *C3* and *C2* the

Table 3.8 Co thickness evolution

	$t_{(Co,t=0)}$ [nm]		$t_{(Co,t=365)}$ [nm]	t_{diff} [nm]
C7	1,50±0.05	→	1.03±0.05	0.47±0.1
C6	1.32±0.05	→	1.00±0.05	0.32±0.1
C5	1.05±0.05	→	0.83±0.05	0.22±0.1
C4	0.75±0.05	→	0.69±0.05	0.06±0.1
C3	0.60±0.05	→	0.56±0.05	0.04±0.1
C2	0.32±0.05	→	0.21±0.05	0.11±0.1

change is reduced and the uncertainty on the XRR does not allow to conclude. The thickness changes are plotted in figure 3.16a versus the initial Co thickness. From the figure we can evidence that it is harder to oxidize thin Co layer compared to thicker ones.

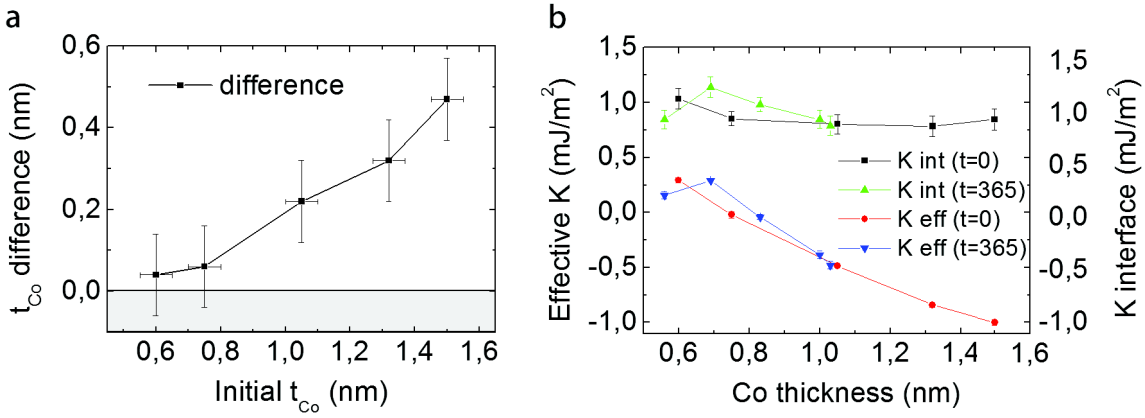

Fig. 3.16 a. Oxidation kinetics versus initial Co thickness. b. interface and effective anisotropy versus the Co thickness.

From figure 3.16b. we can notice that there is an increase of the interface anisotropy with time. Assuming the values extracted from the XRR fit, we can calculate the new effective anisotropy values and compare their time evolution along the wedge axis. In figure 3.16 b, we compared the interface and the effective anisotropy Vs the measured Cobalt thickness. The interface anisotropy $K_{S1,S2}$ increases with time. For same Co thickness $K_{(S1,S2),(t=0)} < K_{(S1,S2),(t=365)}$, see fig: 3.16 b. This might be due to a better interface quality, with a more homogeneous interface between Co and CoO with reduced roughness. The uncertainty on the thicknesses makes it difficult to give a definitive answer and more investigation on such samples should be performed to quantitatively understand the origin of the larger PMA.

Interface anisotropies versus temperature

Similarly to what has been done for the *AlOx* wedge, we will now consider the low temperatures effect on the anisotropies. By doing so we can achieve further insight on the effect of the CoO on the magnetic properties and in particular on the suppression of the OOP anisotropy. It is important to point out that most of the temperature measurements were done at the same time as the first anisotropy field measurements (t=0), and if not specified otherwise that will be the standard. The values for the effective anisotropy for sample with IP magnetization and measured along the hard magnetization axis (OOP) are summarized in table 3.9.

The changes with temperature are plotted in graph 3.17a. From the values it is possible to evidence that the temperature effect is similar to what was previously found. When cooling down, the antiferromagnetic CoO adds an IP component to the anisotropy and modifies the uniaxial behavior. The effect is maximum at 200K for all samples (in figure 3.17 we only show C5-C7 for simplicity), at this temperature all samples showed a minimum for the effective anisotropy.

Table 3.9 Effective anisotropy variation with temperature

Temp K	C7 [mJ/m^2]	C6 [mJ/m^2]	C5 [mJ/m^2]	C4 [mJ/m^2]
275	-1.00	-0.87	-0.61	-0.08
250	-1.10	-0.97	-0.76	-0.23
225	-1.23	-1.11	-0.95	-0.35
200	-1.30	-1.20	-0.98	-0.33
175	-1.27	-1.16	-0.91	-0.26
150	-1.24	-1.08	-0.79	-0.24
125	-1.21	-1.05	-0.75	-0.25
100	-1.19	-1.03	-0.72	-0.25
75	-1.17	-1.01	-0.71	-0.28
50	-1.16	-1.00	-0.72	-0.32
25	-1.16	-1.00	-0.74	-0.39
15	-1.15	-0.98	-0.73	-0.43
5	-1.13	-0.97	-0.74	-0.51

Sample *C3* which has a perpendicular easy axis at room temperature loses its full perpendicular magnetization already at 250K, as shown in figure 3.17b. This further confirms the suppression of the OOP anisotropy due to the presence of AFM CoO. In this latter case the effect arises at higher temperature compared to what was previously found in the Co/CoO/AlOx wedge system. This is probably due to the higher thickness for CoO which leads to a higher ordering temperature T_N [131, 210].

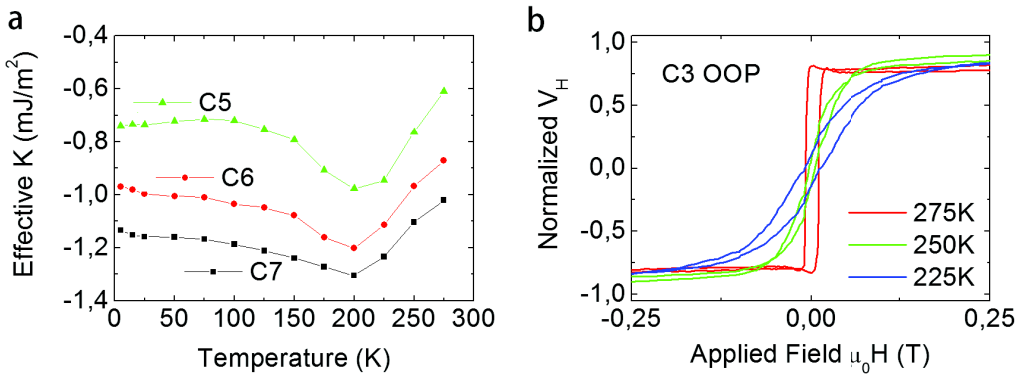

Fig. 3.17 a. Effective anisotropy value for in-plane Co/CoO samples versus decreasing temperature. b. The suppression of the OOP anisotropy on sample *C3* occurs between 275K and 250K.

It was possible to extrapolate a blocking temperature T_B=165±5K for the CoO layer via exchange bias (EB) measurements. This temperature is in good agreement with what was reported for other nm-thick Co/CoO systems [1, 43, 109, 188]. At 165K the AFM CoO layer is completely frozen and its anisotropy is strong enough to pin the FM layer and to induce a EB shift. We can suppose that at slightly higher temperature some CoO grains already start to become AFM. At higher temperature the CoO anisotropy is not high enough to induce a EB shift but is large enough to induced a IP contribution to the magnetization which can be seen by the reduced effective anisotropy. We can explain in the same way what is previously found (section: 3.4.1) for Pt/Co/AlOx samples with a high oxidation in which the XRR picture evidenced the presence of CoO in the stack.

3.4.3 Annealing study

The impact of thermal annealing on such multilayer systems is particularly interesting for industrial applications such as magnetic tunnel junctions (MTJs) [78], magnetic read-head and magnetic random access memories (MRAM) [76]. This is due to the fact that normally industrial processes require some sort of annealing, moreover the anneal stabilizes the layers properties and increases the reproducibility of the characteristics. One of the challenging point is the tunneling transport coming from spin-dependent interfacial density of states and the electronic states within the barrier [214].

MTJ consists of a thin insulating layer, typically AlOx [133] or MgO [162], inserted between two ferromagnetic layers (see section 1.2.4 for details). Shortly after the observation of a large room-temperature tunneling magneto resistance (TMR) by Moodera et al. [133] in AlOx-based magnetic tunnel junction, Sousa et al. [199] demonstrated that a thermal annealing at about 250°C could improve the transport properties of MTJ. The physical

properties of the systems strongly depend on the multilayer characteristic and both the oxidation and the annealing process [55]. The homogeneity of the insulator and the quality of the interfaces deeply influence the transport properties. The optimization of the oxidation process appears to be essential [10].

The impact of a thermal annealing on our Pt/Co/AlOx wedge multilayer sample as investigated through magneto-optical Kerr effect microscope. We recorded the hysteresis loop as a function of annealing temperature along the wedge axis. The x-starting position on the wedge will be the same ($\pm 200 \mu$m) for each analysis. The amplitude of the coercive field, and the mechanism of the magnetization reversal were studied in order to obtain detailed information on the magnetic properties of the stack and their changes with annealing temperature and wedge position.

Usually these studies are performed on few points or on a series of different samples [55, 132, 171]. Our wedge structure and the specific of our MOKE systems (see section 2.3.4) allow us to study in details the properties along the wedge axis and the consequences of the annealing on the PMA and interfaces.To our knowledge such a detailed study was not performed yet.

Homogeneity and optimization of the wedge structure

Prior to this study there were changes in the magnetron sputtering rates, as the DC and RF generator were replaced causing the sputtering rates to change. A second problem which arose after the maintenance was a small leak in the machine, which caused the pressure prior the deposition to pass from $5 \cdot 10^{-7}$mbar to $2 \cdot 10^{-6}$mbar. The type of substrate was also changed, passing from a Si(110) to a Si/SiO_2(250nm) thermally oxidized substrate. This was done in order to eliminate the partial electrical shortcut that was occurring with standard Si(110) at room temperature. This electrical shortcut would have been detrimental for the MTJs study because part of the signal (current) would propagate into the Si and not into the magnetic layer of the device. We also decided to increase the deposited Pt thickness (from 2.5nm to 5nm) in order to obtain a lower resistance for the future bottom electrode of the TAMR devices (see chapter 5).

After the changes, a series of depositions have been carried out to find the suitable parameters to achieve a large PMA in the desired zone. A list of a last series of deposition optimization performed during December 2014 can be found in table 3.10. On the table we emphasize in bold the parameters that were changed in order to find the best PMA zone. x_0 and x_{end} represent the starting and the end of the OOP zone on the wedge axis. The reference zero is taken with respect to the substrate holder of the sputtering machine. A sketch of the system can be found in figure 3.18a. A loop was recorded every millimeter, the value for the

starting and ending of the OOP zone are expressed in centimeter. To clarify the name given to the samples:

- 'Normal' means that the normal procedure for the deposition was followed, in this case the plasma was performed after the top Al metal deposition.
- '60' or '80' after the initial letter are the distances between the substrate and the target for the Al wedge deposition. A higher number means a larger distance which translates into a smaller thickness gradient.
- 'NoPlasma' means that no oxygen plasma was performed on that sample, this was done in order to check if the oxygen plasma is necessary for the PMA.
- 'PostPlasma' indicates that, after a first oxidation in air, a plasma oxidation was performed on the sample.

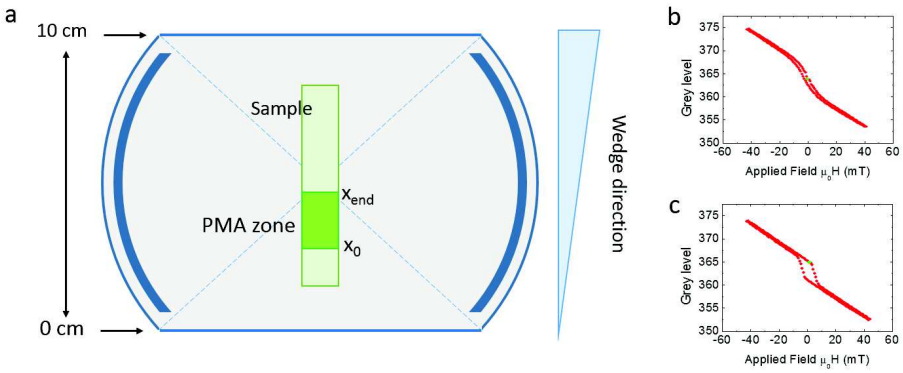

Fig. 3.18 a. Schematic view of the sample holder and sample position, b. beginning of the OOP zone on sample T60mm-Normal, c. Squared loop recorded on sample T60mm-Normal.

We tried to change the Co thickness. For thicker Co layer (dep #8) the PMA shifts towards the zone with thinner Al thicknesses. When decreasing the deposition time (dep #7) we have the opposite effect. This is expected and is related to interplay within optimal oxidation for the Al layer and the Co thickness and the relatives interface anisotropy contribution and demagnetization energy. Increasing the Co deposition time to 14 seconds (dep #9) made us lose the OOP anisotropy. At such thicknesses the demagnetization terms is overwhelming the total interface contribution along the full wedge axis. The total magnetization for such sample lies in-plane. On deposition T60-NoPlasma (#4) we decided to not perform the plasma oxidation. The sample was analyzed and no sign of PMA was found. The oxygen plasma is necessary to reach the good oxidation condition for the top Co/AlOx. In order to

prove that we placed the sample back into the sputtering system to oxidize it in a oxygen plasma with same exact condition. The result (deposition #5) is close to what previously achieved and an OOP anisotropy area is clearly observable. From the series of deposition #1, #2 and #3 performed on a series of different days we can conclude that we obtained a good reproducibility for the area in which the PMA arises.

Table 3.10 Ta/Pt/Co/AlOx deposition optimization

#	Sample name	Deposition details	Magnetic zone (cm)			OOP	
			x_0	x_{end}	tot	Loop	Square
1	T60-Normal	Ta(50s)/Pt(50s)/Co(10s)/Al(7s)	3.5	4.2	0.7	Yes	Yes
2	T60A-Normal	Ta(50s)/Pt(50s)/Co(10s)/Al(7s)	3.4	4.1	0.7	Yes	Yes
3	T60B-Normal	Ta(50s)/Pt(50s)/Co(10s)/Al(7s)	3.5	4.1	0.6	Yes	Yes
4	T60-**NoPlasma**	Ta(50s)/Pt(50s)/Co(10s)/Al(7s)	—	—	—	No	No
5	T60-**PostPlasma**	Ta(50s)/Pt(50s)/Co(10s)/Al(7s)	3.2	3.8	0.4	Yes	Yes
6	T**80**-Normal	Ta(50s)/Pt(50s)/Co(10s)/Al(7s)	4.7	6	1.3	Yes	Yes
7	S60-Normal	Ta(50s)/Pt(50s)/**Co(8s)**/Al(7s)	3.6	4.2	0.6	Yes	Yes
8	U60-Normal	Ta(50s)/Pt(50s)/**Co(12s)**/Al(7s)	3.3	3.8	0.5	Yes	Yes
9	V60-Normal	Ta(50s)/Pt(50s)/**Co(14s)**/Al(7s)	—	—	—	No	No

Coercivity change along the wedge

To perform the annealing study we deposited our multilayer structure on a SiO_2 thermally oxidized substrate, the sputtering sequence was $Ta(50s)/Pt(50s)/Co(10s)/Al(7s)$ (T60-Normal), where the Al is deposited with a wedge geometry. We did not perform an XRR analysis on this sample.

We performed a first accurate KERR scan on the as-deposited sample, we recorded a Kerr loop every 200μm along the wedge axis. The wedged Pt/Co/AlOx sample was then annealed at 250, 300, 350 and 400°C. The anneals were performed in a high vacuum furnace at the Institut Néel, the base pressure was 10^{-8}mbar. The low base pressure theoretically allows to avoid the external absorption of oxygen atoms and the consequential overoxidation of the sample. We annealed for one hour at each temperature and the sample was directly annealed at the desired temperature without performing a temperature ramp. After each annealing we recorded the series of Kerr loops with the same procedure described above. The data were semi-automatically fitted in a MATLAB program.

An example of hysteresis loops is shown in figure 3.20. The scan direction is shown in figure 3.19. The loops were recorded from the thin to the thick part of the wedge. The total length of the sample is $\sim$50 mm, which corresponds to the motor scan length.

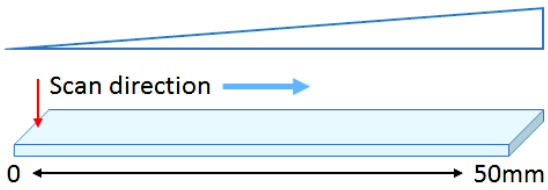

Fig. 3.19 Scan direction in the MOKE microscope.

The data were treated to obtain the most suitable conditions to record the coercive field. When the loops present a well defined saturation we can proceed to subtract the high field slope (calculated in the 40 to 50mT range), in this way we obtain a square loop. The slope at high field should come from the SiO_2 substrate and not from the magnetic layer. The analysis in this case is simple and the coercive field is well defined.

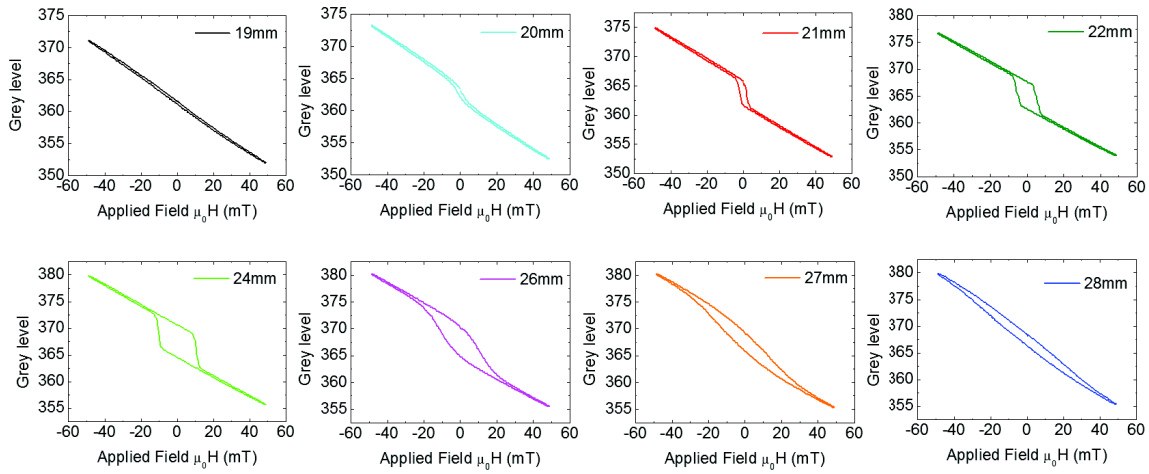

Fig. 3.20 a. Raw Kerr loops along the wedge before the annealing process.

Some problematic arise when the hysteresis loop starts to lose its shape, this is well illustrated by the 28mm loop (see figure 3.20). In this case it is clear that the loop still presents a small coercivity (to compare to the zero coercivity one at 19mm). By adapting the same procedure (subtracting the high field slope) the loop would now look completely open, losing its shape due to the correction and the value for the coercivity would not have any physical meaning. After different tries the choice was to subtract the 80% of the high field slope, this allows us to obtain suitable value for the coercive field. The comparison between the different subtracting methods for the loops measured at 24mm and 28mm are shown in figure 3.21. Subtracting 100% of the high field slope does not give the correct value for the coercivity in the 28mm case, where the loop looks deformed. We needed to be careful, not being well saturated at max field can result in an open loop, from which it would

be impossible to extract a value for H_c. Subtracting only the 80% of it (empirical choice) allows the loops to keep their shape and to extract a correct H_C value in every position along the wedge.

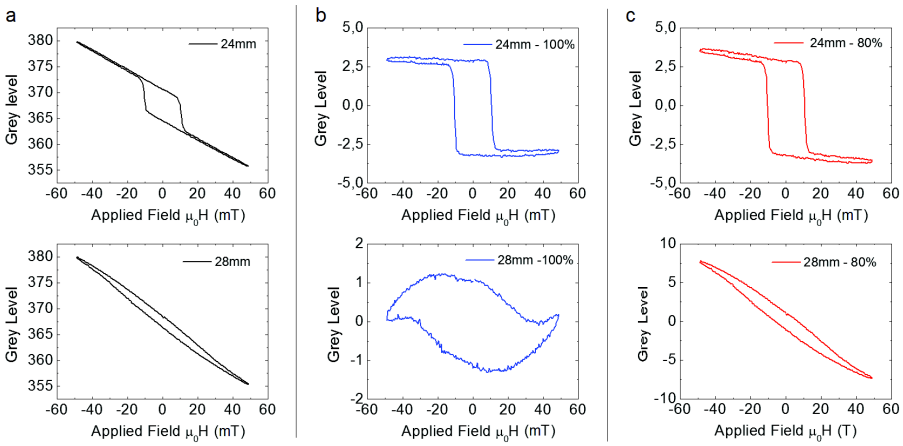

Fig. 3.21 a. original loop, b. subtracting 100% of the high field slope and c. subtracting 80% of the high field slope for the 24mm and 28mm loops measured before the annealing.

In figure 3.22 we show two examples of the extracted coercive field values. The left (H_c Neg) and right (H_c pos) values of the coercivity start to differ when the loops lose their squared shape. This happens for example for the 27 mm and 29 mm loops (shown in figure 3.20). This difference is never larger than 2mT. For the discussion we will use the averaged value between both H_c (H_c Avg) and we will take 1mT as error bar. Previous work on wedge structure as well as anneal and oxidation study on Pt/Co/AlOx trilayers have shown that it is possible to tailor the properties of such systems by playing with oxidation and thermal annealing [49, 112, 113, 132, 170, 171, 199]. In our case it is interesting to study how the wedge geometry, the oxidation and annealing temperature interplay with each other. This can in principle evidence if it exists a zone with nearly perfect conditions or if, due to the redistribution of the oxygen in the oxidized layer there is a plateau of good conditions.

The results after each anneal are summarized in graph 3.23. Each curve represents a different annealing temperature. If the curve is missing it means that we could not evidence an hysteresis loop and therefore we could not extract a value for the coercive field. In the as-deposited sample the maximum coercive field is reached at 24.6 mm with a value of 10 mT. After the 250°C anneal the maximum is moved to 35 mm with a value of 43 mT. For this annealing temperature we obtain the maximum value for the coercive field, indicating good quality for the barrier (which is known to improve upon anneal [132, 170, 199]).

The effect of the first thermal anneal is the shift of the OOP area towards the thicker part of the wedge. The successive anneals confirm this trend. The maximum moves further

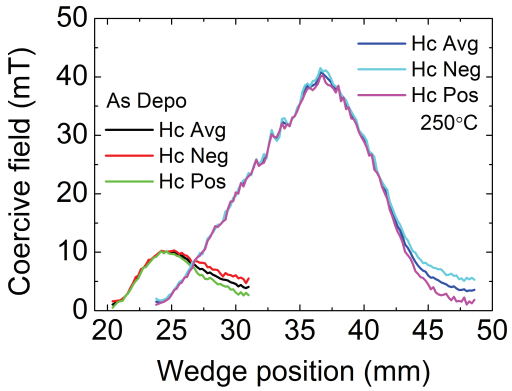

Fig. 3.22 Difference between the positive and negative coercivity for the as deposited sample and after the 250°C anneal.

away from 40.4 mm to 45.4 mm and finally 46.3mm for the 300°C, 350°C and 400°C anneal respectively. Anther noticeable feature regards the maximum value for the coercive field which, after the first increase due the anneal at 250°C, is decreasing with increasing annealing temperature. The field evolves from 24.5mT (at 300°C) to 14 mT (at 350°C) and finally to the value of 4 mT (at 400°C). This low value is probably due to the intermixing at the interfaces: for annealing of ∼400°C Pt and Co start to mix forming a PtCo alloy [55].

On the contrary, at the bottom Pt/Co interfaces for low annealing temperature ($T_{Ann} \leq$ 350°C) there should not occur any intermixing, the thicknesses are preserved and the roughness is reduced upon annealing of 250 to 300°C [55, 118]. The evolution of the magnetic properties in our structure is therefore mainly controlled by the oxidation level of the Co/Al interface. The quality and type of the interfaces also play an important role as well as the Co layer thickness. The top interface is controlled by the Al wedge thickness. Thicker Al means a Co/Al/AlOx system, thinner Al means a Co/AlOx top interface with the possibility to have a CoO layer underneath the AlOx (as evidenced in section 3.4.1).

The role of the Co-O bonds is crucial for the PMA, in particular a good oxidation state should be obtained at the Co/Al interface. The role of the annealing is to thermally induce the diffusion of oxygens atoms from the AlOx layer towards the Co/Al interface. The quality of the interface is known to improve under certain thermal annealing conditions [9, 10, 148, 150].

From this study we wanted to investigate the impact of the thermal annealing on our wedge structure. From literature and similar studies [9, 10, 170] we expected a small plateau for the coercive field which would have originated from the oxygen migration from the Al and Co layer to the Co/Al interface creating a certain area with optimal PMA. Indeed for relatively low annealing temperature of 200-250 °C there is a migration of oxygen from the

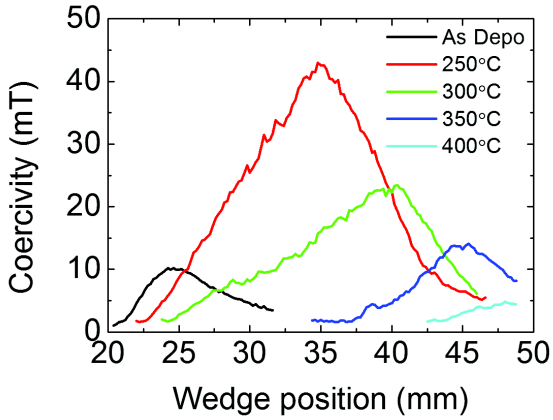

Fig. 3.23 Evolution of the coercive field with respect to the wedge position and annealing temperature.

Co to the Al. Kim et al. studied the particle size distribution of Co/Al upon annealing and observed an improvement already at low annealing temperature [85].

The oxidation kinetics of Co/CoO nano-particles partly embedded in Alumina layer was studied by Chaudhury and coworkers; they showed that the CoO shells disappeared in the Alumina layer at relatively low annealing temperature [35]. Moreover, without oxygen coming from outside the thermal diffusion of oxygen would have favored the formation of Co-O bonds at the interface Co/AlOx as observed in others Pt/Co/AlOx systems [112, 113]; the picture that we predicted was similar to the one shown in figure 3.24b. Therefore we were surprised by the shape of the coercive field after the annealing. The coercivity in the 250°C annealed samples shows a particular triangular shape. It seems that there exists a precise zone on the wedge in which the coercivity shows a maximum. From the literature we would have expected a plateau of maximum conditions for the PMA [112, 170, 171].

Speculating we can imagine the oxidation layout before and after the thermal annealing (see figure 3.24). From the experimental behavior of the coercive field it is possible to imagine a shift of the oxidation towards the thicker part of the wedge sketched in figure 3.24 c. This would imply a non stable content of oxygen, which is absorbed in the multilayer stack during the anneal.

Indeed, it is possible that some oxygen was pumped into the stack. Even with the use of a high vacuum annealing furnace the relatively long anneal (one hour for each temperature) and no capping layer could lead to oxygen absorption. A possible way to directly probe the oxygen concentration would require XRR measurements along the wedge after each annealing. An additional experiment that can be done to further investigate this effect would be to deposit the normal wedge structure, perform the oxygen plasma and then cap the sample with a relatively thick layer. The capping layer would have to be transparent to

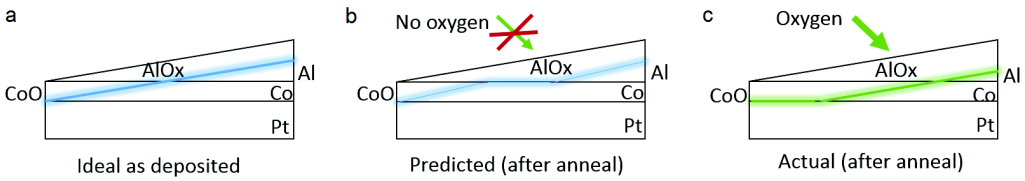

Fig. 3.24 Possible oxidation state along the wedge axis. a. in the as deposited state. b. the predicted picture after thermal annealing and c. the real picture after annealing with the possible inclusion of external oxygen in the stack.

MOKE measurements although thick enough to exclude external oxygen contribution to the evolution of the oxidation profile. More studies should be performed before a definitive answer is proposed.

It can be interesting to try to link the measured OOP coercivity to the anisotropy field. The problem lies in the fact that the magnetization reversal is constituted by a series of local processes, among which the first, named as 'true nucleation', takes place within a defect [62]. According to the Stoner-Wohlfarth model [203], in an ideal high anisotropy system magnetization reversal should occur by coherent rotation, with the coercive field (H_c) being equal to the anisotropy field (H_a). However, in the vast majority of cases the coercive field is much weaker than the anisotropy field. This constitutes the Brown paradox [24] implying that coercivity is not an intrinsic material property but is more due to local defects.

On samples with out-of-plane magnetization, the anisotropy field and the nucleation field are determined by using planar and perpendicular external magnetic field, respectively. On our MOKE systems we are able to apply freely the field on 360 degree but we are not able to apply field higher than 80mT, it is therefore impossible to extract directly the anisotropy field which would give a direct measurement of the PMA strength. However, in experimental analysis, it is common to express the coercive field as a function of the anisotropy field [176]. The relationship can be expressed as follow:

$$\mu_0 H_c = \alpha \cdot \mu_0 H_a \tag{3.7}$$

where α can be taken as a constant in first approximation . To compare we can refer to a previous work carried out by Rodmacq and coworkers at Spintec (CEA - Grenoble) [171] where the influence of oxidation time and thermal annealing on Pt/Co/AlOx trilayers was reported. They were able to measure both the anisotropy field and the nucleation field; the results are summarized in figure 3.25. They defined the nucleation field H_n, which is the field at which the magnetization reversal start. For OOP anisotropy we would have $H_n \approx H_c$

(square loop). H_n is defined as positive for samples with zero remanence (IP easy axis) and negative for squared hysteresis loops (OOP easy axis). We are interested in comparing OOP magnetization area (negative H, represented in yellow on graph 3.25a). The nucleation field does not seem to vary much upon annealing (being in logarithmic scale does not help to see small variations). On the other hand, the variation are visible for the anisotropy field, which reaches its maximum value for an anneal of 300°C.

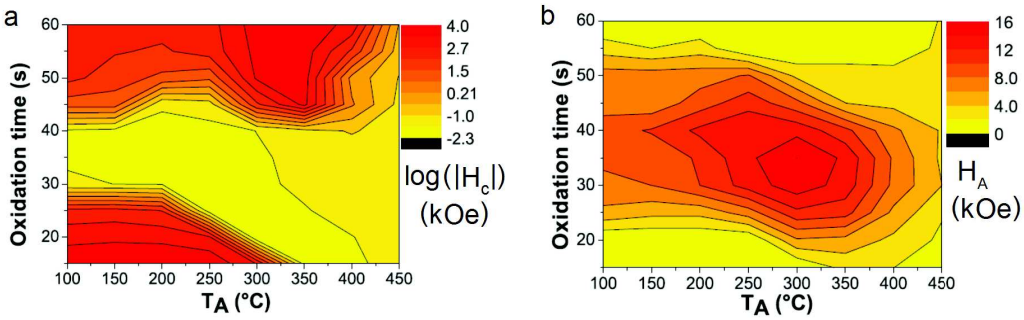

Fig. 3.25 a. Coercive field and b. anisotropy field changes with annealing temperature and oxidation time for Pt/Co/AlOx trilayer. The anneals were performed in a high vacuum furnace for 30 minutes (adapted from [171]).

By using formula 3.7 we can directly link H_c to H_a. In our system the maximum H_a is observed after an annealing of 250°C (see figure 3.23). The lower annealing temperature can be justified by the different annealing time, which is shorter in the reference case (only 30 min, half of the time we used in our study). Indeed, a longer anneal at lower temperature can be compared to a shorter anneal at higher temperature. It is also possible that α is changing upon annealing and that the coercivity decrease (due to fewer pinning defects in the thin film) does not correspond to an anisotropy field decrease. Further investigation should be performed in order to better associate H_c with H_a on our system. The best would be to directly measure the anisotropy field with the MOKE to do so the maximum applied field that can be generated from the Kerr 'KUBE' (see section 2.3.4) must be increased. The field limitation in the 'KUBE' is mostly due the design geometry (and not to the material) a new design for the magnetic poles could solve this problem.

3.5 Conclusions

In this Chapter we studied and discussed the perpendicular anisotropy of ultrathin Co layer in asymmetric Pt/Co/MOx multilayers deposited with a wedge geometry. In these systems the PMA has two contributions, originating from the heavy metal/ferromagnet and the ferromagnet/metal oxide interfaces. The wedge geometry deposition allows to control the

oxidation at the subnanometer scale. Since the bottom Pt/Co interface is in common, it was possible to obtain a gradient of magnetic properties controlled by the Al thickness and the oxidation level, passing from underoxidized Pt/Co/Al/AlOx, to perfectly oxidized Pt/Co/AlOx and finally overoxidized Pt/Co/CoO/AlOx.

The wedge structure allows to conceptually separate the two interfacial contributions. We first performed this analysis at 300K on the Pt/Co/AlOx samples. We calculated the Pt/Co interface contribution in the under-oxidized part. In that configuration only the bottom interface contributes, $K_{S,Pt/Co}$ was found to be $\sim 1mJ/m^2$. This value allows to extract the Co/AlOx contribution to the PMA for perfectly oxidized interfaces ($K_{S,Co/AlOx} \sim 0.45mJ/m^2$). When over-oxidizing the Co layer, this contribution is reduced to$K_{S,Co/CoO} \sim 0.25mJ/m^2$. To understand the role of the over-oxidation, we compared these results with Pt/Co(wedge)/CoO samples. The total effective anisotropy on these sample was found to be $K_{S,tot} \sim 1mJ/m^2$, without consistent variations along the wedge and is mostly due to the bottom Pt/Co interface. This confirms that the overoxidation of the Co layer is detrimental for the PMA.

The evolution of the anisotropies along the wedge as a function of the measurement temperatures revealed the importance of the antiferromagnetic CoO in the stack. It was found that when the CoO became antiferromagnetic it adds a further in-plane contribution to the magnetic anisotropy. This new negative term sums up with the demagnetization energy and the magnetocrystalline energy K_V. The result of the competition between these effects and the interface induced anisotropy is a tilt of the easy axis from the OOP to the IP direction. The Pt/Co/AlOx is one of the model system to study topics such as Rashba splitting, Spin Hall effect and Dzyaloshinskii-Moriya Interaction. The surface asymmetry is crucial for these effects but the presence of a possible CoO layer, which brings a further asymmetric contribution is often overlooked.

The annealing temperature impact on the PMA was studied as a function of the wedge. We performed a series of annealing at different temperatures, after each anneal we recorded the coercive field values along the wedge axis. Our results indicate that annealing at 250 °C for 1h is the best combination which promotes the largest coercivity value. We expected a plateau for the H_c values upon annealing; instead we observed a triangular shape. This indicates that there exists a precise zone where the conditions for the PMA are optimal. On such thin film and due to the rather long annealing we cannot exclude oxygen absorption, which could justify the triangular shape. To eliminate this possibilities a capping layer could be added in order to avoid the oxygen absorption.

The studies presented in this chapter allowed us to obtain a good understanding of the magnetic properties and their evolution along the wedge axis. We intend to capitalize this knowledge to build TAMR devices.

Chapter 4

Exchange Bias in ultrathin Cobalt

4.1 Introduction and Motivation

Exchange Bias (EB) is a physical phenomenon experimentally observed for the first time in 1956 by Meiklejohn and Bean (see figure 4.1a) [125]. The effect was first named "new magnetic anisotropy" and described as an exchange anisotropy. The exchange is the result of the interaction between a ferromagnetic material (FM) and an antiferromagnetic material (AFM). Meiklejohn and Bean observed that the hysteresis loop of Co particles embedded in a CoO shell were shifted along the applied magnetic field axis. The shift occurs when the particles were cooled down under a saturating field from above the Neél temperature (for bulk CoO T_N=293K) down to 77K. The EB loop measured and first published by Meiklejohn and Bean can be seen in figure 4.2 a. This field shift was later named exchange bias field.

The interest in exchange bias systems was renewed by the development of spintronics at first using IP anisotropy but also due to the experimental discovery of the perpendicular surface magnetic anisotropy (PMA) [64]. Due its potential technological application in ultra high density recording system an increasing number of studies have been made on systems with perpendicular exchange bias [164, 229]. Despite the active research, the microscopic origin of EB is still poorly understood [153]. Various models to describe this phenomenon exist (see sections 4.3) nevertheless none is universally accepted and the physics behind EB is still under debate.

In this context, we have investigated the atomic and magnetic structures of ultrathin FM/AFM double-layers which could present exchange coupling, the chosen system is a Co/CoO bilayer. Co/CoO is not only the system in which the EB was firstly discovered [125] but it is considered as an ideal model system due to its combined properties. Indeed, Co/CoO offers a number of advantages over similar systems, which show also the EB effect. First, Co has very good growth properties and presents flat interfaces even for very thin films. Very

good layers can be easily prepared by sputtering and molecular beam epitaxy techniques. Second, the Néel temperature of the bulk oxide is at a convenient temperature of 294K. Third, CoO provides a large EB even for very thin layers, which can easily be prepared by plasma or thermal oxidation [68]. Furthermore, CoO/Co bilayers exhibit straightforward and pronounced EB properties, which qualify them as a model system for detailed investigations of the magnetization reversal process [60, 127].

This is the case although the spin structure of the antiferromagnetic CoO is rather complex. In CoO the spin-orbit interaction and therefore the crystal anisotropy is strong. For bulk CoO the easy axis is reported to be along the (117) directions [173]. The fundamental properties of Co and CoO are described in chapter 1.1.1 and 1.1.1 respectively. However, in very thin layers because of missing neighbors the easy axis has still to be determined. Training effects, which have been observed for CoO/Co, add an additional difficulty. However, training effects can also be useful for the understanding of the metastability of interfaces, as we will describe them further below [20, 43, 60, 65, 167]. The wedge shaped samples were studied with different techniques. The studies were done with temperature variation between 300 and 5K and field up to a maximum of $\pm$7T. The Exchange Bias properties have been mostly investigated via a crosscheck of transport and SQUID-VSM measurements. Synchrotron XMCD, XLD and XRR measurements were performed as well to obtain a deeper understanding of the multilayer properties. The combination of all these experiments allows to obtain a good picture of the structural, electronic and magnetic properties of the analyzed samples.

4.2 Exchange Bias: Qualitative description

As a qualitative description we could think that at room temperature ($RT > T_N$) the CoO AFM layer behaves as a paramagnet and the magnetic properties of the bilayer depend entirely on the Co layer. When the material is cooled down, below its T_N the AFM layer changes from a paramagnetic to an antiferromagnetic state. An interface coupling due to the exchange interaction is observed when cooling the AFM-FM bilayer in the presence of a static magnetic field from a temperature above T_N [153]. The result is a shift of the magnetic loop along the applied magnetic field axis. The schematic of the EB effect can be found in figure 4.1 b. which gives an intuitive description of the exchange bias coupling for a generic FM/AFM bilayer.

If the temperature is not low enough ($T_B < T < T_N$), the AFM will reverse with the FM reversal, resulting in a centered loop with enhanced coercivity. T_B is the blocking temperature of the system. This coercivity enhancement is usually present in every exchange biased

systems (see figure 4.1a). If the anisotropy is high enough and $T < T_B$, the result is a shift of the hysteresis loop H_{EB}. The different phases of the EB process are briefly explained, with reference to figure 4.1b.

1. The temperature T of the system is large enough to unblock the spins in the AFM layer, but lower than the Curie temperature of the ferromagnetic material (T_C), therefore $T_N < T < T_C$.

2. The system is cooled down under a saturating field H to a measuring temperature $T < T_B < T_N$. The AFM orders antiferromagnetically and it couples at the interface with the FM layer along the direction of the applied setting field.

3. The AFM and the FM layers are coupled at the interface. The AFM pins the FM layer along the direction of the cooling field. The field necessary to reverse the FM magnetization becomes larger than for a single FM layer.

4. For large enough applied field, the FM layer reverses and is saturated.

5. When removing the field, the coupling to the AFM spins, which did not rotate during the loop, forces the FM spins to reverse to the initial configuration.

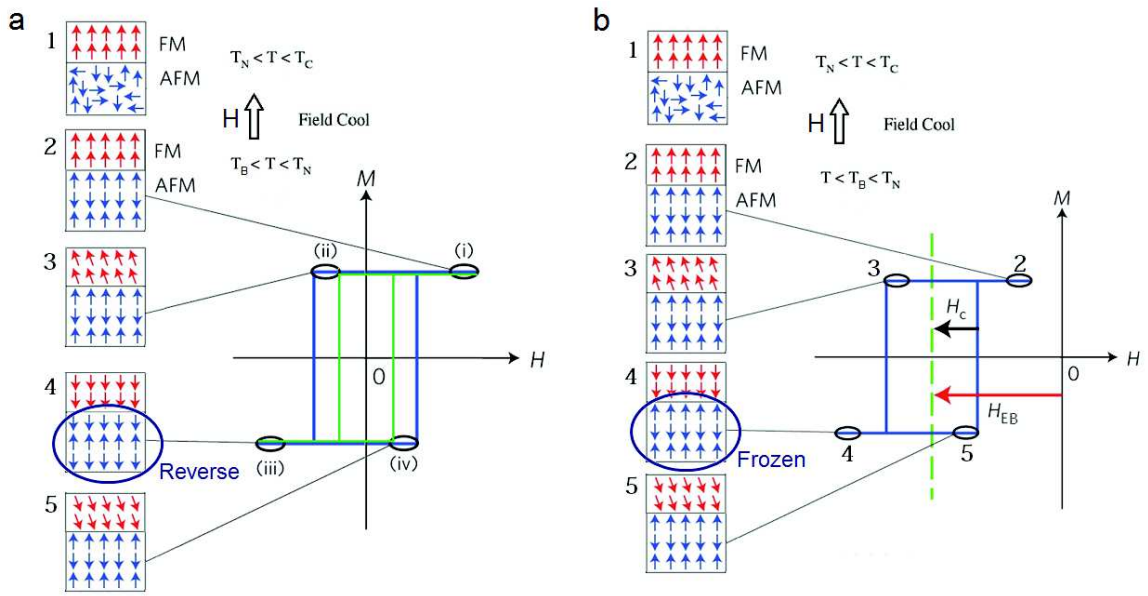

Fig. 4.1 Schematic representation of the possible coupling in a FM/AFM bilayer with OOP spin configurations; a. coercivity enhancement, the AFM anisotropy is not strong enough and the AFM follows the FM layer reversal and b. exchange bias shift, the AFM layer is frozen and does not follow the FM reversal.

Meiklejohn and Bean analyzed this effect by torque measurement. The torque is defined as $T = \partial E/\partial\theta$, and is the derivative of the energy in function of the magnetisation angle θ. A single Co layer, with uniaxial anisotropy, shows a torque proportional to $\sin 2\theta$; while a coupled Co/CoO system shows a $\sin\theta$ dependence along the easy axis, for a schematic view refer to figure 4.2 b. This means that in stable uniaxial conditions two energy minima exists for $\theta = 0\,\text{deg}$ and $\theta = 180\,\text{deg}$. On the other hand, the unidirectional anisotropy of FM/AFM interface leads to a single energy minimum for $\theta = 0\,\text{deg}$. As a consequence a shift in the hysteresis loop appears along the applied H-axis, to compare to the usual symmetrical major loops of single FM layers. A series of microscopic models has been proposed to quantitatively describe the loop shift. They will be grouped by theoretical and chronological approach. Each of them will be briefly discussed in the next paragraph.

4.3 Theory and Models

4.3.1 Meiklejohn and Bean's model

The first model [124, 125] proposed to explain the EB effect assumed a coherent rotation of the FM and the AFM magnetization. This model was proposed by Meiklejohn and Bean and is based on the Stoner-Wohlfarth description of magnetization reversal.

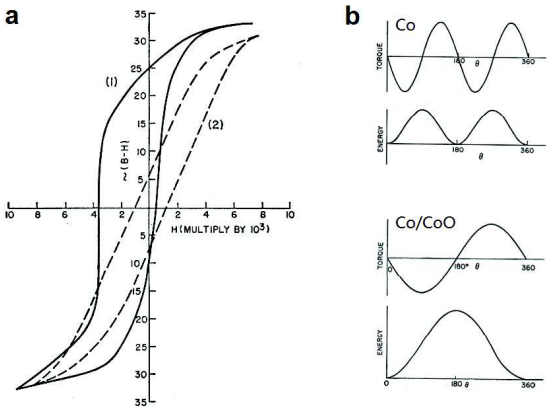

Fig. 4.2 a. Shifted hysteresis loop as reported by Meiklejohn and Bean in 1956 [125]. b. Torque and energy curves for single Co layer and Co/CoO bilayer below T_N [143].

The authors considered a single domain spherical particle at 0K with uniaxial anisotropy. By keeping the same formalism as the original work and by defining the angle θ between the easy axis and magnetization, it is possible to define the free energy per unit volume F as:

$$F = -\mu_0 H M_S \cos\theta + K_{anis} \sin^2\theta \tag{4.1}$$

Taking the derivative $\partial F/\partial\theta$ and searching for maxima and minima, we could define the coercive force of the hysteresis loop as: $H_C = 2K_{anis}/\mu_0 M_S$. Introducing a unidirectional anisotropy term, of the form $-K_U \cos\theta$, the equation 4.1 becomes:

$$F = -\mu_0 H M_S \cos\theta + K_{anis} \sin^2\theta - K_U \cos\theta \tag{4.2}$$

Deriving as before we would find a similar solution with an added effective field term which shift the hysteresis loop. This field can be expressed as:

$$H' = H - \frac{K_U}{\mu_0 M_S} \tag{4.3}$$

This additional term can be rewritten with an explicit definition of the thickness of the FM layer [125], the exchange bias shift can be now be defined as:

$$H_{EB} = \frac{J_{ex}}{\mu_0 M_S \cdot t_{FM}} \tag{4.4}$$

J_{ex} is the interface exchange coupling. Equation 4.4 gives a linear dependence of the H_{EB} shift from the FM layer thickness. This evidences the fact that the EB phenomenon is, in first approximation, an interface effect. The EB is equivalent to an offset field and no effect is expected on H_C. In this model the AFM is rigid and the interface spins are uncompensated. Later Meiklejohn [124] generalized the equation, considering different angles and connecting directly the uniaxial anisotropy to the AFM layer, therefore $K_{anis} \simeq K_{AFM}$. The equation for the energy per unit area becomes:

$$E = -\mu_0 H \cdot M_S \cdot t_{FM} \cos(\theta - \beta) + K_{AFM} \cdot t_{AFM} \sin^2\alpha - J_{ex} \cos(\beta - \alpha) \tag{4.5}$$

α and β are the angles between the magnetization and the easy axes of the AFM and FM respectively. θ is the angle between the field H and the FM anisotropy, for a comprehensive

sketch see figure 4.3a. Minimizing eq 4.5 for α and β, the equilibrium position for the FM and AFM spins are obtained:

$$\begin{cases} \frac{\partial E}{\partial \alpha} = 0 \Rightarrow \sin 2\alpha = \frac{-J_{ex}}{K_{AFM} \cdot t_{AFM}} sin(\beta - \alpha) \\ \frac{\partial E}{\partial \beta} = 0 \Rightarrow \sin(\beta - \alpha) = \frac{H \cdot M_S}{J_{ex}} \sin(\theta - \beta) \end{cases} \tag{4.6}$$

One important consideration derived from the first term of equation 4.6 is that in order to have exchange bias a necessary conditions is: $K_{AFM} \cdot t_{AFM} \gg J_{ex}$, meaning that the antiferromagnet anisotropy energy is much larger than the exchange coupling. In that case the AFM magnetization remains frozen (α constant) and a shift in the hysteresis loop may appear. On the other hand if $K_{AFM} \cdot t_{AFM} \ll J_{ex}$, the AFM moment will rotate with the FM one during the magnetization reversal.

The model gives a first intuitive picture of the EB effects. The EB effect depends on the unknown parameter J_{ex}, assuming $J_{FM} \geq J_{ex} \geq J_{AFM}$, the resulting value for EB is order of magnitude larger than the experimentally observed one. As Kiwi pointed out in a recent topical review on EB system [89], if one adopts these early models as an intuitive guide, one should find the following results:

- Only negative exchange bias should exist (with positive cooling field).
- The uncompensated interfaces should display the largest EB.
- The roughness of the uncompensated interface should increase EB.

Even a fast inspection of experimental results [153] shows that none of these expectations is fulfilled. Positive exchange bias (with positive cooling field) exists and was firstly observed by Nogues and coworkers in 1996 [151]. Large exchange bias were found in system with compensated interface by Kiwi and coworkers in 1999 [91]. The full picture to understand EB is far from being reached and more parameters must be taken into account when modeling the exchange bias.

4.3.2 Domain wall models

Chronologically the second EB model was proposed by Louis Néel in 1967 [145] and later modified by Mauri in 1987 [121]. The idea was to explain the discrepancies that Meiklejohn and Bean's model [124] had with the observed experimental values. Néel proposed that the reduced bias field observed experimentally was due to the formation of a domain wall parallel (DW) to the FM/AFM interface, which drastically reduced the energy required for the magnetization reversal. Néel assumed that when a magnetic field is applied in the opposite

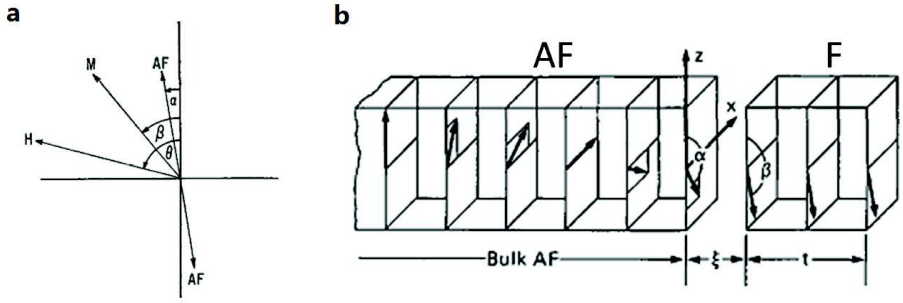

Fig. 4.3 a. Schematic vector diagram for a exchange bias system [124]; b. Magnetic configuration at the FM/AFM interface [121]. The uniaxial anisotropy is along the z-axis and the AFM layer has infinite thickness

direction with respect the cooling field, the spin structure of the AFM is deformed. The AFM domain wall tries to follow FM layer reversal. If the domain wall remains stable a shift appears, otherwise the irreversible change in the AFM reversal contributes to the coercivity of the loop. This model was later re-proposed by Mauri [121]. A sketch for a the spins of a single sublattice is shown in figure 4.3b. In Mauri's paper [121] the FM/AFM system is composed by an infinitely thick AFM layer and a FM layer of thickness t. t is much smaller than the typical FM domain wall size. The domain wall resides solely in the AFM layer. As further approximation, the interface is taken without any roughness effect, therefore the AFM spins are completely uncompensated at the surface. Using the Stoner-Wohlfarth model and the same formalism as in Mauri's paper, the total energy per surface area δ can be written as:

$$\delta = -\mu_0 H M_S t_{FM}(1-\cos\beta) + K_{FM} t_{FM} \cos^2\beta + A_{ex}/\xi[1-\cos(\alpha-\beta)] + \\ +2(1-\cos\alpha)\sqrt{A_{AFM}K_{AFM}} \tag{4.7}$$

Where, ξ is the interface thickness, A_{ex} the exchange energy and A_{AFM} the exchange stiffness. By rewriting equation 4.7 in units of $2\sqrt{A_{AFM}K_{AFM}}$, which is an energy per unit area, we obtain the ratio between the interface coupling and the stiffness of the AFM layer λ, equal to:

$$\lambda = \frac{A_{ex}}{2\sqrt{A_{AFM}K_{AFM}}} \tag{4.8}$$

Two extreme cases can be taken into account: $\lambda \gg 1$ (weak coupling) and $\lambda \ll 1$ (strong coupling). For weak coupling during the FM reversal a domain wall is created in the AFM. The resulting exchange bias is equal to:

$$H_{ex} = \frac{2\sqrt{A_{AFM}K_{AFM}}}{M_S t_{FM}} \tag{4.9}$$

The domain wall term reduces the value of the EB (compared to Meiklejohn and Bean's model). For strong coupling, no domain wall is created. In this case $A_{ex} \propto J_{ex} \cdot a$ with a the AFM lattice parameters. The resulting EB is:

$$H_{ex} = \frac{J_{ex}}{M_S t_{FM}} \tag{4.10}$$

Values similar to Meiklejohn and Bean's model are found in this case and no important differences exist between the two models. Some of the assumptions of this model are debatable, the weak points are the assumption of a FM coupling at the interface and the value for the anisotropy constant. An AFM interface coupling is not only possible, but likely preferable in most cases. Nogues et al. [152] have experimentally confirmed that AFM interface coupling is necessary to observe positive exchange bias. Furthermore, in the magnetic ground state configuration, the FM moments are orthogonal to the bulk AFM easy axis (as pointed out by Koon [92] and confirmed experimentally by Ijiri et al. in 1998 [72]).Finally, for a DW to develop in the AFM, the anisotropy constant K_{AF} has to be quite small; otherwise it is energetically favorable for the DW to form in the FM side as demonstrated by Miller et al. [38, 90, 126].

More recent models based on the formation of domain wall have been developed. The most important is probably the one proposed by Kiwi et al. [89]. Kiwi's model is based on a fully uncompensated AFM structure and it applies to a large variety of systems. The assumed AFM anisotropy is rather large, this high AFM anisotropy leads to considerable energy costs for creating the DW and to a DW width of just a few nm in the AFM. The model by Kiwi also allows for a simple explanation of positive exchange bias. There are still opens question on such model. The existence of domain walls (DW) parallel to the surface is a critical assumption. Under a certain thickness for the AFM layer such domain walls cannot exist.

4.3.3 Random Field model

Twenty years after Néel's publication and contemporaneously to Mauri's model, Malozemoff proposed a model of exchange anisotropy based on the assumption of rough FM/AFM

compensated and uncompensated interfaces [111]. Malozemoff work is based on the random-field Ising model [74]. The considered interface is illustrated in figure 4.4a.

The model is based on the assumption that the random interface roughness gives rise to a random magnetic field that acts on the interface spins. This results in an unidirectional anisotropy which causes the shift of the hysteresis loop. The expression given for the hysteresis loop shift is:

$$H_{EB} = \frac{2}{M_{FM} t_{FM}} \sqrt{\frac{J_{AFM}}{K_{AFM} a}} \tag{4.11}$$

where a is the lattice parameters. Expression 4.11 allowed to reconcile the experimental data with theory, reducing by two orders of magnitude the overestimate derived using the domain wall model [89], which was given by equation 4.10. If we consider that the domain wall length in the AFM is $d_{DW} \propto J_{AFM}/aK_{AFM}$, we have that the exchange bias shift H_{EB} scales as $1/d_{DW}$.

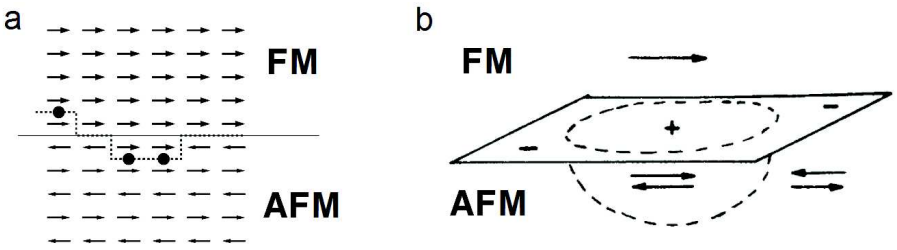

Fig. 4.4 a. AFM rough interface with frustrated interactions marked by full dots.The dashed line marks the boundary between the FM and the AFM b. Examples of spin configuration for an AFM atomic step (adapted from [111]).

Despite the reasonable estimate for H_{EB} this model has a severe drawback: it crucially depends on a defect concentration at the interface which is not consistent with experimental results [89]. This random model approaches have been implemented in other works carried out by Zang et al. [240] and Schulthess and Butler which showed that Malozemoff's random interface field and Koon's orthogonal magnetic arrangement, rather than being in conflict, could be combined to provide an explanation of EB and the coercive field value [29, 89].

4.3.4 Polycrystalline model for exchange bias

All the previous models have the limitation of considering a single crystal structure for the EB system. For technological applications, most of the exchange bias systems are deposited with magnetron sputtering (see section 2.1.1) which gives polycrystalline structures. Therefore,

it is important to include into the discussions the polycrystalline structure and in particular for the AFM layer. The first theoretical approach of this type was proposed by Takano et al. [208]. In their model they considered a compensated AFM structure in which the orientation of the grain is randomly distributed, see picture 4.5 for a sketch. They consider a size distribution of the grains and a single contribution of each grain to the exchange bias through a non-zero moment. Through a series of Monte Carlo simulations for different parameters (i.e grains contribution, size, roughness, ...) and by superposing the results they reach the conclusion that roughly only 1% of the total inter-facial spins contributes to the EB (i.e. the uncompensated ones). That would justify the low experimentally observed exchange bias values compared to theoretical ones. The simulations also proved a correlation between the grain size L and the EB value expressed by: $H_{EB} \propto L^{-1}$.

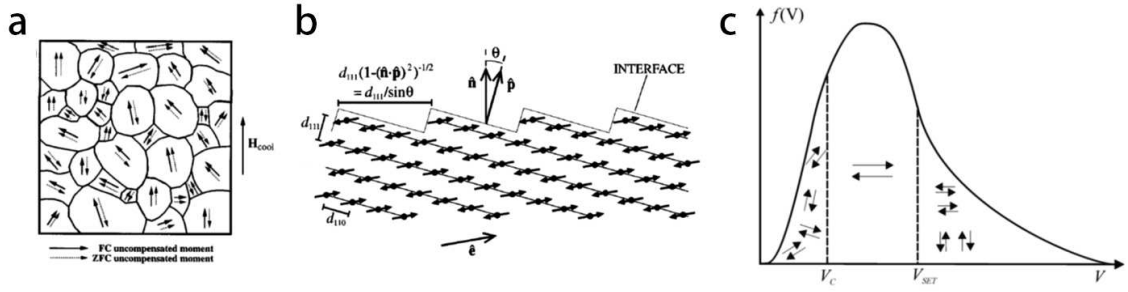

Fig. 4.5 a. Polycrystalline structure orientations of AFM grains: after the field cooling the AFM align along their uniaxial direction following the cooling field direction [208]. b. AFM compensated spins configuration in a rough interface [208]. c. Schematic representation of AFM grain size distribution after field cooling [220].

Temperature behavior

The temperature has a major impact on the stability of the AFM grain. The evolution of EB system with temperature was first described by Meiklejohn and Bean [125], who observed a quasi-linear decrease of H_{EB} with temperature. When the blocking temperature is reached (H_{EB} goes to zero) a peak in the coercivity is generally observed [69]. Fulcomer and Charap later proposed the first temperature model for polycrystalline structure [52]. They considered a distribution of non-interacting AFM grains with different sizes and volumes coupled with the FM layer. The model takes into account thermal fluctuation effect on the grains, with an energy barrier $\delta E = K_{AFM} \cdot V$ to reverse the grain spin. V is the volume of the considered AFM grain. According to its volume, each grain contributes differently to the hysteresis loop. In the model they consider a wide distribution of grain sizes (figure 4.5c), at a fixed temperature three contributions for the AFM grains exist:

- Small grains, where $KV \ll K_BT$, which are superparamagnetic (they suffer from thermal fluctuation) and reverse continuously, partially contributing to the coercivity.
- Grains with weak anisotropy and strong coupling, they are trained during the hysteresis loop and contribute to the coercivity enhancement.
- Frozen grains, which maintain their coupling with the FM layer during the loop and contribute to the exchange bias.

Increasing the temperature, the thermal fluctuations increase and the fraction of frozen grains is reduced. At the blocking temperature T_B all grains contribute to coercivity. For $T > T_N$ the AFM totally uncouples from the FM, the resulting loop theoretically depends solely on the FM layer. This is a first modelization, it describes with a good accuracy the behavior in temperature of exchange bias and is generally considered as correct. The only big inconsistency appears when approaching 0K, at this temperature according to Fulcomer and Charap's model, all grains are blocked and frozen, and no contribution to the coercivity exists anymore.

Recently O'Grady proposed a polycrystalline model based on the grain size distribution which was experimentally observed [154, 220]. The model considers a lognormal distribution of AF grain volumes (see figure 4.5 c. for an idea of the distribution after field cooling). The stability of the grains and their contribution to the hysteresis loop is defined by their volume at the considered temperature. The ratio of grains that take part into the EB shift is defined by the integral between two critical volumes V_C and V_{SET} over a given volume distribution $f(V)$, expressed by equation 4.12:

$$H_E \propto \int_{V_C}^{V_{SET}} f(V)dV \tag{4.12}$$

where V_C is the critical volume under which the grains are thermally unstable at the chosen temperature. V_{SET} is the setting volume over which the grains are not coupled. A series of measurements for different grain volume distributions and for different setting temperatures validated this model for polycrystalline sputtered exchange bias system.

4.4 Sub Nanometer Exchange Bias

Now we will apply our wedged multilayer to study exchange bias in the sub nanometer limit, where both the FM and the AFM are just a few monolayers (ML) thick. The exchange bias effect is intensively used in GMR sensors, where coupling the ferromagnetic (F) layer to an

AF layer is a common trick to improve the stability of the pinned layer. Indeed, very soft layers are required for high sensitivity sensing but reference layers must keep their magnetic moment stable under applied field. Exchange bias between the reference layer and an AF pinning layer induces an unidirectional anisotropy which stabilizes the chosen magnetic moment direction. EB is still subject of research in particular at the nanoscale which will be the limit for planar devices; the existence of EB below a certain AFM thickness is still an issue. Our Co/CoO model system allows to get further insight on the physics governing the EB effect.

From a fundamental prospective, to study EB down to the atomic layer regime and to quantitatively describe the magnetic properties of the active ferromagnetic layers provides a perfect model system to compare to existing EB models and also to study surface magnetic anisotropies. Compared to the periodic multilayer which have being used previously as model systems, we do not need to assume the identity of layers and interfaces. This gives us a simpler physical picture, although the low amount of active magnetic volume could provide a challenge when measuring.

To study exchange bias in such nanometer regime is also a challenge for different reasons. First of all, controlling sub-nm deposition or oxidation is difficult and requires ultra-high vacuum environment followed by appropriate capping. With the current technology it is still challenging to prepare and control such structures. Non-capped Co samples oxidize in air and form nm-thick CoO layer (e.g. for thick Co layer 2.5nm of CoO are almost instantly formed when in contact with air), furthermore non-capped Co keep oxidizing and its magnetic properties evolve in time [195]. The best capping layer to protect Co from oxidation has been discussed [53], metallic Al seems a common and good choice. When Aluminum oxide (Al_2O_3) enters in contact with Co it enhances the OOP anisotropy [96, 132]. A detailed analysis of this effect was previously discussed in chapter **??**.

Monso et al. [132] showed that controling the oxidation of a $Si/Pt/Co/Al_2O_3$ structure was possible and leads to a large surface induced perpendicular anisotropy. For this work we decided to over-oxidize such a multilayer to prepare a Co/CoO bilayer. In order to precisely study the impact of the CoO layer, the sample was prepared with an Al wedge. In this way it was possible to obtain, on the same substrate, under-oxidized and over-oxidized regions. The transition is smooth, the oxidation change is in the order of 5Å/cm as can be extracted from table 4.1. The advantage of such method is having identical Pt/Co bottom interface and a uniform Co contents (in a metallic or oxidized state) along the whole sample. For details about the sample deposition please refer to chapter 2. On such samples we combine XRR, VSM-SQUID and AHE transport measurements. The results were crosschecked to

have access to the magnetic properties of such samples. The study of Co/CoO bilayer in the subnanometer regime could answer and open different questions:

- What is the thickness limit for exchange bias?
- Does CoO keep a strong magnetocrystalline anisotropy even in the subnanometer regime?
- What will be the blocking temperature for the ultrathin Co/CoO system?
- What models can explain these effects?
- Is it possible to quantitatively justify the EB existences in such ultrathin CoO layer

4.4.1 Samples details

The general idea behind the sample deposition is described in chapter 2. The sputtering sequence allows to prepare a $Ta(5nm)/Pt(2.5nm)/Co(1.2nm)/Al(t_{Al})$ stack deposited on top of Si(110) substrate. The top Al layer is deposited with a wedge and the Al thickness. t_{Al} is varied between 3.5nm and 0.5nm along the wedge axis. The preparation procedure is fully described in chapter 3.4.1. The salient points are:

1. The oxidation through the Al allowed us to control the oxidation of the Co layer at the sub-nanometer scale.
2. The system is stable in time, the Al capping stopped the oxygen to further penetrate and fully oxidize the Co.
3. No annealing was performed in order to preserve the wedge properties and to avoid intermixing at the interfaces.
4. The sample was then cut into equal pieces to fit it into the measurement systems.

The schematic of the wedge and sample is shown in figure 4.6 and the XRR results are resumed in table 4.1. The results for this particular wedge deposition and its sketch has already been shown in chapter 2.3.2 and fully discussed in chapter 3.1. For simplicity we choose to show the main results again here to ease the reading (see table 4.1.

The XRR thicknesses were crosschecked with VSM-SQUID magnetometer measurements, in order to validate the thickness values. To calculate those values we assumed that the Cobalt layer's magnetization is the one of bulk Cobalt $\mu_0 \cdot M_{Co} = 1.71$ T at 300K. From the magnetic moment values and utilizing the formula $m_S = M_{Co} \cdot t_{Co} \cdot Area$ it was possible

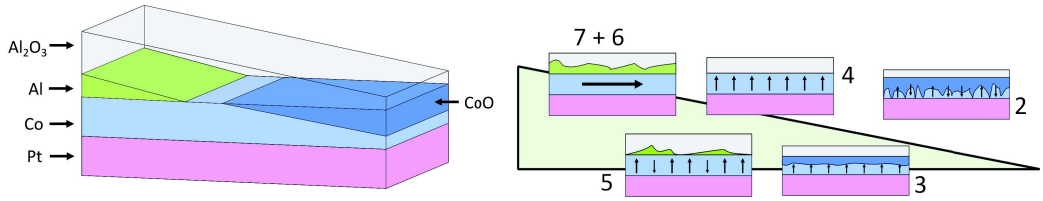

Fig. 4.6 Schematic view of the wedge structure. The samples are referenced along the wedge and an intuitive oxidation state for each sample is shown

to extract t_{Co} Co thicknesses value of the different samples; the values are summarized in table 4.2.

The *Area* of the different samples was calculated with micrometer error $\sim 0.01 \cdot 10^{-5} m^2$. We utilize the KERR microscope motors and camera to pinpoint and to model the surface as a polygon to calculate the surface area of each sample. In hexagonal cobalt, the magnetic moment of a Cobalt (0001) atomic layer (ML) is $2.79 \cdot 10^{-4} [A \cdot m^2/m^2]$ at 300 K and the ML are at a distance of 0.204 nm from each other. Since we cannot separate the Pt and the Co contributions, ferromagnetic Pt will be modeled as being Co in these VSM data.

The measured values of *S3* and *S6* agree with the XRR ones. In particular, for *S3* the measured m_S at 300K is $2.14 \cdot 10^{-8} A \cdot m^2$, which divided by the surface area of $3.02 \cdot 10^{-5} m^2$ gives $9.5 \cdot 10^{-4} A \cdot m^2/m^2$. The experimental magnetic moment corresponds to 3.3 ML and agrees with the XRR thickness (0.67 nm) (1ML of Co is 0.204nm thick [109]). For *S6* the obtained value is 1.1 nm in good agreement with the 1.2 nm obtained via XRR measurements. The 1Å discrepancy corresponds to a 10% relative error. However, considering the roughness, which gives an idea on the incertitude on the XRR thicknesses and the VSM-SQUID limitation (reproducibility) this value fits well into the error bars. In the next section the temperature and exchange bias measurements conducted on the Al wedge system will be shown in details and thoroughly discussed.

4.4.2 Results and Discussions

To magnetically characterize our samples Anomalous Hall Effect (AHE) measurements were performed in a liquid He cooled cryostat. The temperature was varied between 300K and 5K and the applied field between -5T and +5T. More information on the cryostat system can be found in chapter 2.3.1 on Materials and Methods. First no field cooled procedure was applied. All the measurements reported in the next two paragraphs are done in zero field cool (ZFC) condition. The magnetic field applied to the sample during the cooling was solely the

Table 4.1 Ta/Pt/Co/CoO/Al_2O_3 XRR fit results

	Sample S2		Sample S3		Sample S4	
	Thickness [nm]	Roughness [nm]	Thickness [nm]	Roughness [nm]	Thickness [nm]	Roughness [nm]
Al_2O_3	0.93	0.57	1.80	0.60	2.53	0.57
CoO	1.00	0.17	0.65	0.13	0.10	0.10
Co	0.28	0.15	0.67	0.27	0.95	0.20
Pt	2.10	0.72	2.46	0.38	2.56	0.33
Ta	4.24	0.60	4.57	0.61	4.98	0.56
SiO_2	1.88	0.29	1.60	0.25	1.82	0.23
$Si_{substrate}$	∞	0.20	∞	0.26	∞	0.22
	Sample S5		Sample S6		Sample S7	
	Thickness [nm]	Roughness [nm]	Thickness [nm]	Roughness [nm]	Thickness [nm]	Roughness [nm]
Al_2O_3	2.57	0.52	3.50	0.68	3.20	0.59
Al	—	—	1.17	0.43	1.75	0.39
Co	1.13	0.26	1.19	0.26	1.17	0.17
Pt	2.49	0.28	2.48	0.28	2.63	0.27
Ta	5.59	0.54	5.35	0.45	5.03	0.47
SiO_2	1.93	0.25	1.90	0.25	1.70	0.22
$Si_{substrate}$	∞	0.24	∞	0.18	∞	0.26

remanence of the coil, estimated to be a few mT. When a field cooling procedure was used it will be explicitly specified in the text.

Coercivity enhancement

We will now focus our attention on the magnetic properties at low temperature, focusing on the effect of the CoO on the coercivity. First of all we can notice how the two under-oxidized samples (*S7* and *S6*) show a clear In-Plane (IP) behavior for the magnetization. *S5* is closer to have Out-Of-Plane easy-axis although, due to the lacking of Co-O bonds, there is a low contribution from the top surface, therefore even at low temperature its magnetization is intermediate between OOP and IP configuration. Finally *S4* and *S3* show Out-Of-Plane (OOP) behavior (the top Co/Al_2O_3 interface anisotropy contributes to the perpendicular easy-axis). Finally, *S2* is over-oxidized and shows no-ferromagnetic behavior at RT, at low temperature it was impossible to fully saturate the sample. The different OOP loops recorded at 5K can be seen in figure 4.7.

Table 4.2 VSM-SQUID: magnetization measurement and thickness values

Sample	m_S $[A \cdot m^2]$	Area $[m^2]$	t_{VSM} [nm]	t_{XRR} [nm]
S6	$4.53 \cdot 10^{-8}$	$2.93 \cdot 10^{-5}$	1.10	1.19
S3	$2.14 \cdot 10^{-8}$	$3.02 \cdot 10^{-5}$	0.69	0.67

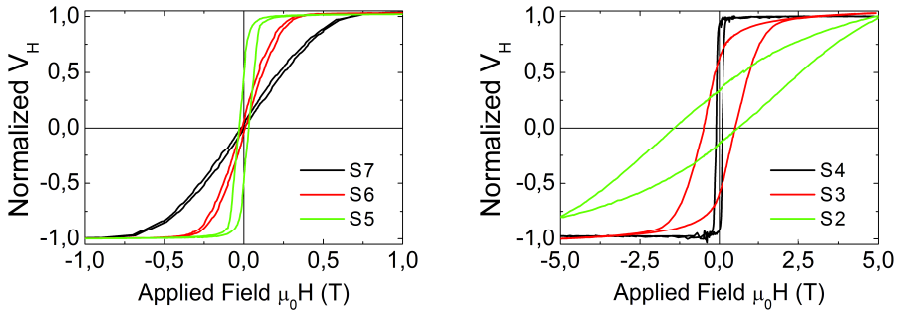

Fig. 4.7 ZFC out-of-plane loops recorded at 5K for sample $Ta/Pt/Co/CoO/Al_2O_3$.

The values of the coercive field with decreasing temperature extracted from OOP AHE measurements are shown in figure 4.8. For under-oxidized samples such as *S6* and *S7* (the values super-impose with each other): H_C increases of a factor three with temperature, passing from the value of 3mT at 300K to 10mT at 5K. On *S5* the coercivity increases by a factor ten, passing from 3mT at 300K to 30mT at 5K. These relatively low coercivity enhancement indicates a close-to-zero CoO contribution. The behavior is different when we consider samples with CoO in the stack (as evidenced by the XRR fit). In *S4*, for a temperature below 75K, there is a clear change in slope for H_C, which reaches the final value of 100mT at 5K. For *S3*, which has a higher amount of CoO, the H_C enhancement starts early, around 200K and reaches the final value of $\mu_0 H_C$=500mT. The enhancement in the last case is above a factor one hundred. This increase is much stronger than the expected one for uncoupled FM layers (which typically behave similarly to *S6*). This enhancement is commonly observed in EB systems [6, 65, 100, 153, 208] and is mainly due to the distribution of the AFM grain sizes, which translates into a blocking temperature distribution. Therefore there is a progressive increase in the grain interfacial stiffness as they approach T_B, a higher field must be provided in order to complete the magnetization reversal.

We believe that this coercivity enhancement is due to the antiferromagnetic ordering of the CoO present in the overoxidized samples. The enhancement happens when the AFM CoO comes into play, the reduced thickness of the FM layer can not explain such an enhancement, moreover it can not justify a change of behavior (change of slope) when decreasing the

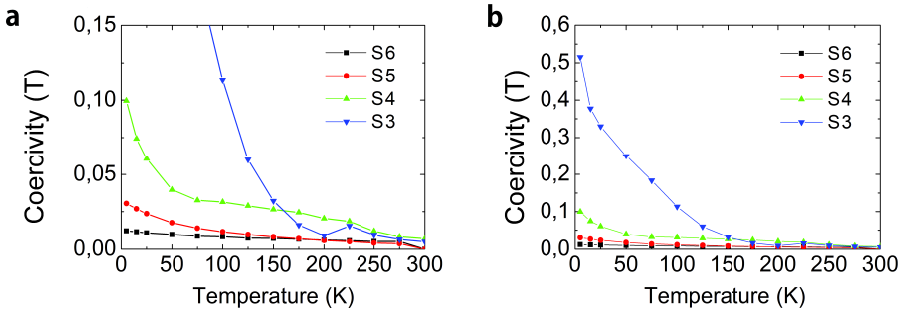

Fig. 4.8 a. Coercive field values as a function of temperature on sample with no CoO contribution. b. Zoom on the coercivity enhancement value for *S3*. The values are taken from OOP measurements

temperature below a certain critical ones (75K for sample *S4* and 200K for sample *S3*).

To define the real T_N of an AFM when coupled with a FM is not a trivial matter; many effects come into play, like the magnetic proximity effect, which causes the ferromagnetic layer to substantially influence the ordering temperature of the antiferromagnetic layer [102]. To determine such a value is not the objective of this work. For simplicity we will defineT_N the Néel temperature of the Co/CoO bilayer. A reduced Néel temperature (compared to the bulk one $T_N = 293K$) is expected in ultrathin CoO layers [6, 109]. A comprehensive study of the decrease of T_N, with respects to the AFM thicknesses, was performed by Tang and coworkers [210] who reported a sudden decrease of T_N for film thicknesses below 20Å (see fig 4.9).

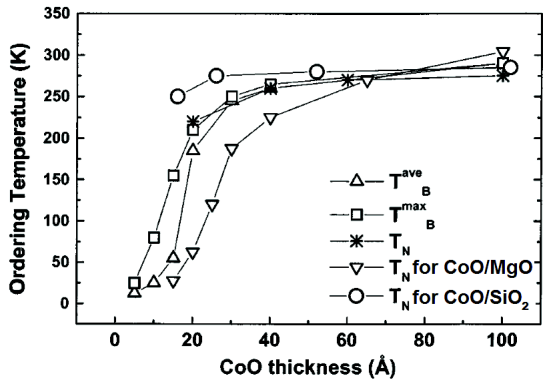

Fig. 4.9 Ordering temperatures: T_B^{ave} from peak in ZFC/FC magnetization, T_B^{max} from ZFC/FC bifurcation, T_N from specific heat peak vs CoO layer thickness in $(CoO(t_{CoO})/SiO_2(50\text{Å})_{25}$ MLs. Also shown are T_N for CoO/MgO and T_N for CoO/SiO_2 ML taken from DC magnetic susceptibility peak (adapted from [210]).

Looking at figure 4.9, it is clear that the expected T_N for CoO alone is lower than for a Co/CoO bilayer. The effect of the metallic Co when placed in contact with the CoO

is to increase its Néel temperature. Looking at figure 4.8a, one may notice a peak in the coercivity for *S3* (in blue in the graph) when its Néel temperature is reached around 225K. The observation of a coercivity peak is coherent with the models for EB and it was observed as well in other works [65, 69, 89] (see section 4.3). The peak is mainly due to the distribution of the AFM grains blocking temperatures; at T_N all grains contribute to the coercivity.

Loss of remanence

The coercivity enhancement is not the only temperature effect on our system. Together with the coercive field enhancement we studied the remanence of the hysteresis loops when cooled down in ZFC. Figure 4.10 summarizes the remanence behavior with temperature for the different samples.

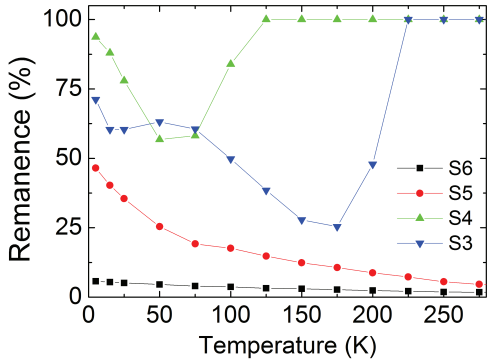

Fig. 4.10 Remanence behavior in ZFC conditions. An hysteresis loop was recorded at each temperature and the remanence value was extracted from each loop.

We attribute 100% remanence value to fully OOP hysteresis loop; an example is the 225K loop in figure 4.12 a. Sample *S3* and *S4* show an abrupt drop of remanence at 200K and 100K respectively. The remanence loss originates from a tilt in the hysteresis loop, an example for sample *S3* is shown in figure 4.12. The tilt corresponds to the paramagnetic/antiferromagnetic phase transition of the CoO layer. Lowering the temperature below T_N the effect is the antiferromagnetic ordering of the CoO, which below that temperature starts to play a role on the magnetic properties of the multilayer. Below this temperature spins are ordered inside the AFM CoO grains and the observed drop in remanence is a consequence of exchange coupling between the AFM and the FM spin.

The loss occurs at different temperatures (figure 4.10), and is related to the CoO amount. The higher the amount of CoO, the sooner the remanence will drop. A higher CoO volumes means a higher ordering temperature for the AFM [210]. For *S3* the remanence goes from 100% at 225K to 24% at 175K and indicates that the Co/CoO exchange coupling is strong

enough to overcome the net OOP anisotropy of the FM layer. For *S4* (less CoO) the drop in remanence goes from 100% at 125K to 55% at 75K. In *S4* the remanence loss, induced by the exchange coupling is reduced due to the low amount of CoO, which is not able to tilt the Co magnetization as much as in the previous case.

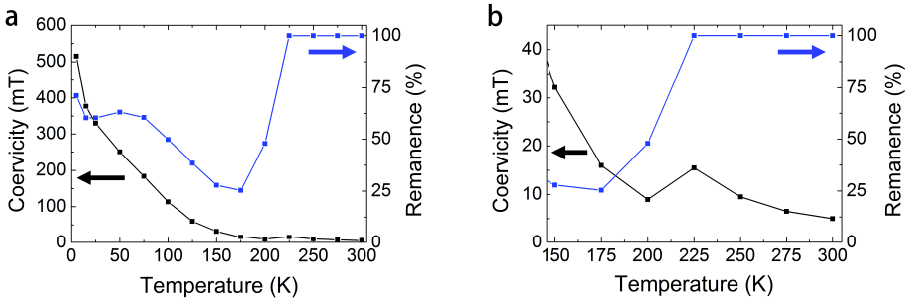

Fig. 4.11 a. Temperature dependence for the OOP coercivity and remanence for sample *S3*; b. zoom on the temperature at which the remanence drops.

Due to the polycrystalline nature of our samples, the IP component of the magnetic easy axis is likely to be randomly distributed. Consequently the drop in remanence at zero applied field is most probably the consequence of an inhomogeneous reversal in the FM layer [202]. Examining figure 4.12 a. one may notice that the inhomogeneous magnetization loss, appearing at 175K, can be easily saturated OOP with a relatively low applied field (150mT to return to a value close to $\sim 85\%$). At 175K most of the AFM grains still follows the FM magnetization and can be reversed. This is not anymore the case at lower temperature, for example at 5K more than 3T are necessary to saturate the magnetization. From these remanence drop we deduced the Néel temperature for *S3* of $\sim$225K which is in good agreement with the coercivity peak appearing at the same temperature. The curves for the loss of remanence and the coercivity enhancement behavior for sample *S3* are superimposed in figure 4.11 a. and by looking at the zoomed figure 4.11 b. it is clear that the coercivity peak coincides with the loss of remanence.

By looking at the hysteresis loop for *S3* and *S4*, is clear that the antiferromagnet CoO layers strongly modify the uniaxial anisotropy of the underneath Co layer. The strongest effects due to the CoO layers occurs in the vicinity of the Néel temperature. At lower temperature the remanence starts to increase again. This happens at 150K for*S3* and at 50K for *S4*. This increase is not due to the arising a new OOP anisotropy contribution but is linked to the increasing of the coercive field. A further decrease in temperature from 175 K to 5 K leads to a strong coercivity enhancement. For *S3* the coercive field goes from 16 mT (175K) to 515 mT (5K). Figure 4.11 a. shows the higher remanence registered at zero bias. From this figure it is clear that the increase of the remanence at zero field bias corresponds to the

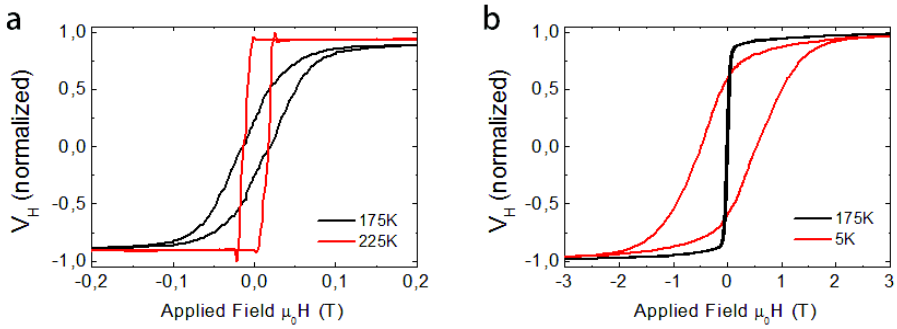

Fig. 4.12 Anomalous Hall effect data for sample *S3* measured at different temperatures, the loops are measured with OOP magnetic field (normalized with respect to the spontaneous magnetization of the sample). All data correspond to ZFC.

coercivity enhancement which starts to arise at the same temperature. Similar results on the suppression of the perpendicular anisotropy at the CoO Néel temperature were previously observed and published by Shipton et al. [188]. We describe this suppression (loss of remanence and tilt in the hysteresis loop) as the arise of a new contribution which originates from the coupling of CoO layer with the Co layer. This is discussed, with respect to the PMA of the Co/AlOx wedge, in chapter 3.4.1.

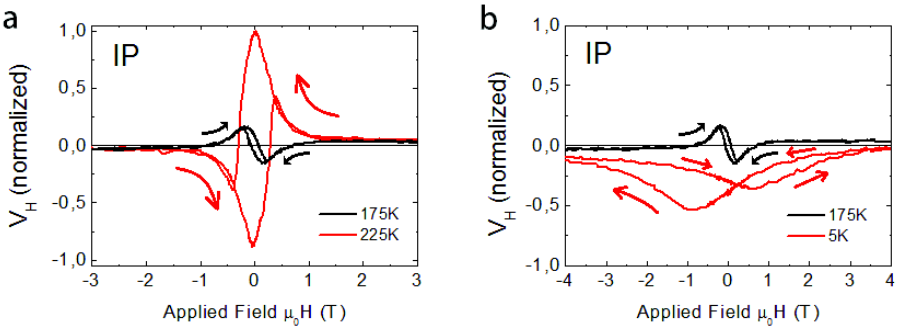

Fig. 4.13 Anomalous Hall effect data for sample *S3* measured at different temperature with IP magnetic field (with respect to the spontaneous magnetization of the sample). All data correspond to ZFC.

Another manifestation of the exchange between Co and CoO is the inversion of the magnetization rotation which appears in IP Hall loops between 200K and 175K. The rotation sense changes from counterclockwise (at 225K) to clockwise (at 175K) as can be seen in figure 4.13a. At 225 K we observe a classical IP Hall loop for perpendicular magnetized sample: after IP saturation the magnetization rotates back in the direction (+M) corresponding to the small (+H) out of plane component of the positive in plane field due to misalignment. At 175 K however, the magnetization changes sign and rotates in the opposite direction with respect to the applied field. To understand the inversion of the Hall loop rotation we have

carried out simulations based on the Stoner-Wohlfarth model. We assume that our model system possesses a single easy axis and that the anisotropy energy per unit volume can be defined as:

$$E = K_u \sin^2(\alpha - \theta) - \mu_0 H_{applied} M \cos(\theta - \phi) \tag{4.13}$$

where K_u is the uniaxial anisotropy, ϕ is the misalignment between the film plane and the direction of the applied field, α is the angle between the film plane and the easy axis and finally θ is the angle between the film plane and the magnetization (the angles are defined as in figure 4.14).

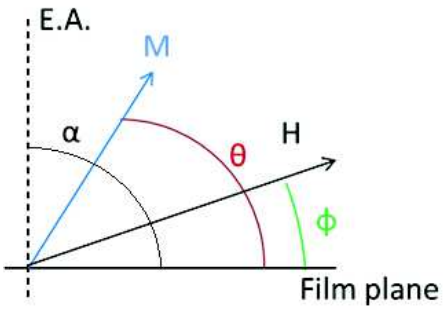

Fig. 4.14 Definition of the axis for the Stoner-Wohlfarth model.

The Stoner-Wohlfarth simulation can be seen in figure 4.15. To reproduce the experimental situation, the applied magnetic field is slightly misaligned with the film plane (in both case: θ=5°). For the first simulation (classical case) the easy axis angle is α=85°and after positive field in plane saturation the magnetization is rotating in the direction of the applied magnetic field (counterclockwise) and reaching the +M value. For the second simulation (clockwise rotation), the easy axis angle is modified to α=100°. In this configuration, the magnetization after positive in plane saturation is now rotating against the applied magnetic field (clockwise) and reaching the –M value. Therefore, the Stoner-Wohlfarth simulations suggest that the rotation direction inversion is due to a partial reorientation of the magnetization easy axis direction, which is induced by the exchange coupling with the AFM spins.

Despite this rotation direction inversion, at 175K the IP Hall loop is still keeping its odd symmetry which indicates that the AFM spins are reversed during the switching of the Co layer. This is not anymore the case at 5K (figure 4.13b) where the odd symmetry is broken. In that case the FM layer is in the –H direction during the cooling to 5 K and the AFM spins become partially frozen in that direction, inducing an unidirectional anisotropy in the magnetization rotation which rotates clockwise for decreasing field and counterclockwise

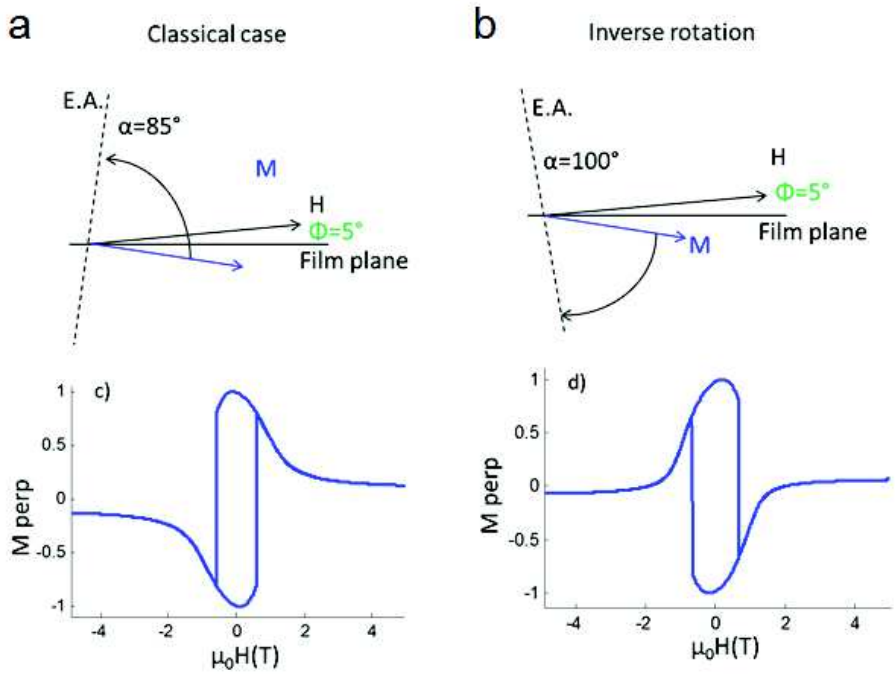

Fig. 4.15 Simulation parameters for the two cases, a. the classical case and b. the inverse rotation. The change in the easy axis direction, due to the CoO effect, explains the rotation inversion.

for increasing field. When the FM layer is prepared in the + H direction before cooling the unidirectional anisotropy is in the +H direction, see figure 4.16. Such unidirectional anisotropy can be easily induced by a frozen OOP component of the CoO spins as in a uniaxial anisotropy system, the two directions of rotation are almost energetically equivalent for a magnetic field applied close to the hard axis direction.

From this rotation direction inversion of the Hall loop we can deduce that the effective field of the CoO spins is stronger than the misalignment field for $\mu_0 H_{mis} = 0.7 \cdot T \cdot \sin(3°) = 35mT$. We can notice that while an OOP unidirectional anisotropy is present for the IP reversal, the OOP loops present a negligible OOP exchange bias (figure 4.12b). Indeed, without OOP field cooling the magnetization is rotating partially IP when the Néel temperature is reached (drop in remanence at 200K) and this prevents the magnetization to be 100% OOP when the blocking temperature is reached and thus reduces the OOP CoO spin component.

Subnanometer exchange bias: Field cooled measurement

In this chapter, the magnetic properties of sample*S3* are carefully investigated. In particular we will concentrate on the analysis of field cooled (FC) measurements of the hysteresis loop

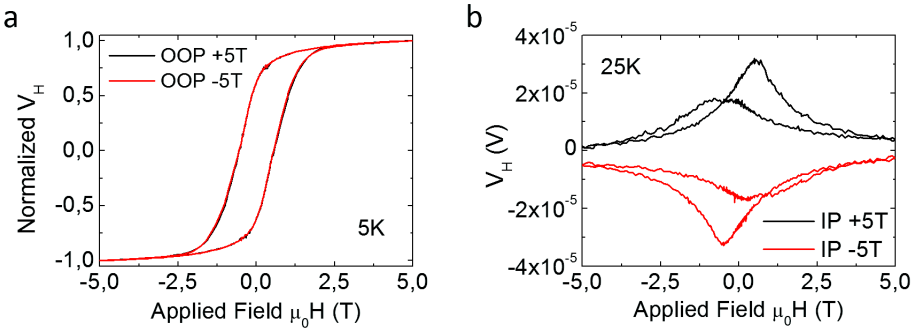

Fig. 4.16 Anomalous Hall effect data for sample *S3*, the Cobalt was prepared at 300K with a +5T or a -5T field. The field was then removed and a ZFC cooling procedure was applied. a. OOP loops recorded at 5K and b. IP loops recorded at 25K. There is a clear effect on IP loops that is not present in the OOP ones.

at different temperatures. The EB measurements were performed in the cryostat system (ref: 2.3.1) with the following measurement protocol:

1. The sample and the sample holder are placed into the cryostat. The superconducting coil is set to zero field.

2. The cryostat is heated up to T=300K, a temperature above the Néel temperature T_N of bulk CoO although inferior to the Curie temperature T_C of our system. The Curie temperature of bulk Co is 1392 K, even in the subnanometer regime for the Co layer (t_{Co}=0.67nm) we observed a magnetic response at 300K. Therefore $T_N < T < T_C$.

3. After a certain time ($\sim$ 30min, to let the temperature and the system stabilize), a saturation field of +5T is set in the cryostat.

4. The heating system is then switched off and the temperature of the cryostat is brought to the desired measuring temperature T_{meas}.

5. Once T_{meas} is reached (and has stabilized) the field is removed. An hysteresis loop is then recorded. The sequence is 0T $\rightarrow$ +5T, +5T $\rightarrow$ -5T, -5T $\rightarrow$ +5T and +5T $\rightarrow$ 0T.

6. After the first loop is recorded a second, third and fourth loop are performed as well in order to study the training effect at that specific temperature.

Any protocol deviation will be specified in the text (i.e. if different values of saturation field were used while performing the field cooling). Between two different temperature measurements the system is always heated up back to 300K and the above procedure is applied again. During the measurement of the hysteresis loop, the steps between each

measuring field were varied: the choice was made in order to obtain a loop in a reasonable amount of time while maintaining a good field step resolution. A single 0T $\rightarrow$ +5T increment includes 260 measurement points. A total hysteresis loop will have more than 1000 points. This will assure a good resolution on the hysteresis loop features. The usual choice for the transport measurements is illustrated in table 4.3.

Table 4.3 Field steps

Interval	Field step	Number of steps
0 T $\rightarrow$ 100 mT	2mT	50/260
100 mT $\rightarrow$ 500 mT	5mT	80/260
500 mT $\rightarrow$ +1 T	10mT	50/260
+1 T $\rightarrow$ +3 T	50mT	60/260
+3 T $\rightarrow$ +5 T	100mT	20/260

By adopting this procedure we try to evidence the sub-nanometer exchange bias effect in the two promising sample *S4* and *S3*. On *S4* the field cooled loops and the zero field cool loops look exactly the same, the amount of CoO in this sample is not large enough to create an exchange bias even at 5K. The ZFC and +5T FC loops are shown in figure 4.17 a: no difference exists between the two and no shift is observed, the coercive field difference is $\sim$ 10mT, which will be the uncertainty for the measurement and is probably due to the remanence of the coil at zero field. On the other hand, when applying the same procedure to *S3* we observe a clear exchange bias effect. The loops recorded at different temperatures are shown in 4.17 b. and the EB values before and after the training effect are summarized in table 4.4 and plotted in figure 4.18 a.

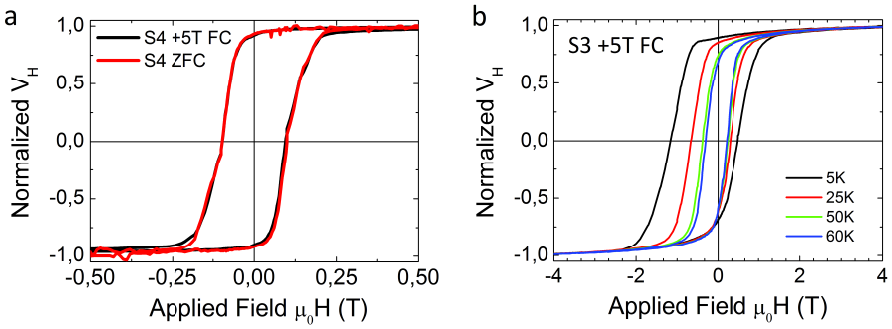

Fig. 4.17 a. ZFC and +5T FC hysteresis loops for S4 measured at 5K. b. +5T FC hysteresis loops for S3 recorded at different temperatures.

The EB shift was found to be equal to 0.66T at 5K (+5T FC). To compare this value to other similar works in literature we can use the EB surface energy, which is defined as:

$E_{EB} = \mu_0 \cdot M_{Co} \cdot t_{Co} \cdot H_{EB}$. With $\mu_0 H_{EB} = 660$mT, $t_{Co} = 0.67$nm and $M_{Co} = 1.4 \cdot 10^6 A/m$, the magnetization value for bulk Co, the resulting EB surface energy is E_{EB}=0.62 mJ/m^2 at 5K. For the trained loop, this value is reduced to E_{EB}=0.40 mJ/m^2 at 5K. Despite the strong EB shift due to the thin FM layer, when normalized in terms of energy, the resulting value for E_{EB} is comparable with literature values which (for CoO systems) are of the order of 0.4mJ/m^2 to 3.5mJ/m^2 when calculated at 10K [16, 109, 153, 195].

Table 4.4 Exchange bias values for *S3*:

Temperature	$\mu_0 H_{EB}$ first loop	$\mu_0 H_{EB}$ trained loop
5K	-0.66 T	-0.43 T
25K	-0.35 T	-0.24 T
50K	-0.14 T	-0.10 T
60K	-0.09 T	-0.07 T

The blocking temperature (T_B) was extracted from the intersection with $E_{EB} = 0$ axis of the linear fit of the EB(T) values and is equal to: $T_B = 67 \pm 5K$. T_B is only marginally reduced compared to nanometer thick layers. For relatively thicker CoO layers (2.5nm) T_B is around 180K [16, 93, 109, 188]. This is also close the blocking temperature of 165K $\pm$ 5K that we found in our Pt/Co(t_{Co})/CoO(2.5nm) wedge sample study (see section 3.4.2).

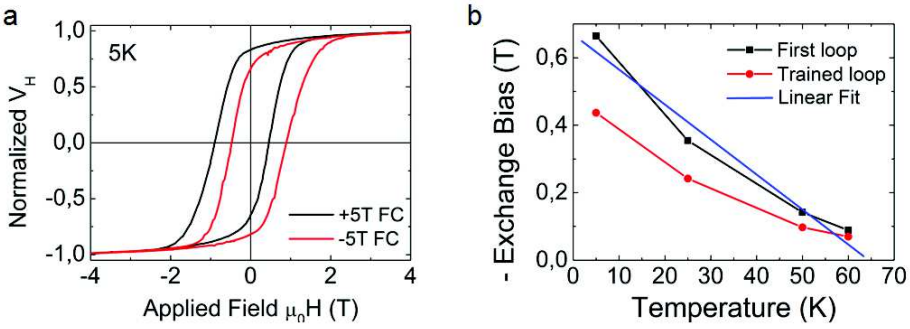

Fig. 4.18 a. Symmetrical behavior for positive and negative field cool b. Exchange Bias values for first loops and trained ones.

The existence of an exchange bias with ultrathin CoO layer can be quantitatively justified with a model which takes into account the thermal activation energy and the size of the CoO grains. Indeed, the reduced T_B value compared to T_N is presumably related to the small size of the AFM grains in our layer. By comparing the thermal activation energy and the energy to reverse the CoO in our system it is possible to obtain the minimum size of the AFM CoO grains to originate the EB effect. At 70 K the thermal activation energy would be:

$$E_{70K} = \ln \frac{\tau}{\tau_0} k_B T_B \simeq 30 \cdot k_B T_B = 3 \cdot 10^{-20} \ [J] \tag{4.14}$$

Where the measuring time τ equal to 1 hour. The attempt frequency τ_0 is classically taken as 1ns and T_B is the blocking temperature for our system. Equation 4.14 must be compared to the energy necessary to reverse a CoO grain, therefore we have the following equivalence:

$$E_{70K} \sim E_{CoO} = K_{S,CoO} \cdot S_{CoO} \tag{4.15}$$

where S_{CoO} is the grain surface and $K_{S,CoO}$ the CoO anisotropy per surface unit area in our system. $K_{S,CoO}$ may be calculated from the CoO bulk anisotropy. In 1957 Kanamori [79], ab-initio calculated the CoO anisotropy and found it to be: $K_{V,CoO} = 28 MJ/m^3$. It is unlikely that a sub-nanometer thick layer keeps the same anisotropy as bulk material, although knowing that we are overestimating $K_{S,CoO}$ and in order to compare the two energies, we can transform the volume anisotropy in surface anisotropy. Considering that 1.2nm of Co became Co=0.67nm and CoO=0.65nm; that means that we have roughly 6 monolayers (ML) of Co (we have to divide 1.2nm by 0.204nm which the typical plane thickness for 1ML of hexagonal Co). Therefore we obtain 3.4ML of Co which gives 2.6ML of transformed CoO. From literature [109] 7Å of Co becomes 10Å of CoO, therefore one CoO plane would be 0.29nm thick. Multiplying this value by 2.6ML we would obtain 0.75nm of CoO which is close to the XRR value of 0.67. Therefore, we have roughly 2.6ML of CoO and neglecting the interface exchange (J_{ex}), the anisotropy energy of the CoO layer becomes:

$$K_{S,CoO,1ML} = K_{V,CoO} \cdot t_{1ML} = 7.53 mJ/m^2 \times 2.5 ML \rightarrow K_{S,CoO} = 18,8 \ mJ/m^2 \tag{4.16}$$

where $K_{S,CoO,1ML}$ and t_{1ML} are the magnetocrystalline anisotropic energy and the thickness of one atomic plane (one monolayer = 1ML) of CoO. Finally by comparing equation 4.16 with equation 4.15, and by substituting we deduce $S_{CoO} \sim 1.2 nm^2$. We deduced that the CoO layer keep a strong anisotropy despite its sub-nanometer thickness. Even assuming a reduced CoO anisotropy, the results still held, if $K_{V,CoO}$ is one order of magnitude lower (as calculated by Smardz et al. $K_{AF} > 4.5 MJ/m^3$ [195]) the minimum average size for the CoO AFM grains, to guarantee a blocking temperature of 70K, would be $\sim 4nm$.

O'Grady and coworkers demonstrated that the individual grains in the antiferromagnetic layer of exchange bias systems possess a single AFM domain and reverse over an energy

barrier which is grain volume dependent. They showed that the AF grains are not coupled to each other and behave independently. They also calculated that the average diameter of AFM grains in polycrystalline thin films (sputtered system) is in the range 5-15 nm for nanometer thick CoO layers [154, 220]. Therefore the size of the grains in our sputtered systems is likely to be at least of that order of magnitude, which justified the existence of an EB even in the subnanometer regime.

This high pinning efficiency (of the AFM CoO grains) and the existence of an exchange bias even in such sub-nanometer regime may depend on the number of uncompensated AFM interfacial spins which increased with the reduction of CoO grain size [208, 220]. This behavior is particularly favorable in CoO system due to the nature of the exchange between Co and oxygen atoms at the grain boundaries. To prove the field symmetry of the EB effect we performed negative field cooling. We measured the loops recorded after +5T and -5T field cooling at 5K (figure 4.18 a). The symmetric behavior is respected and the absolute values for the positive and negative EB are experimentally identical, the difference of the two EB absolute value shift is less than 15mT.

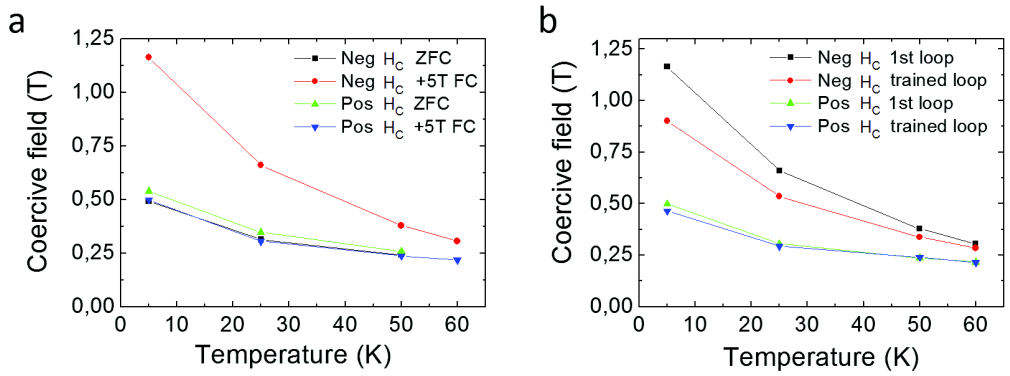

Fig. 4.19 Absolute value for a. the coercive field behavior with and without field cooling. b. the coercive field behavior of trained loops.

The coercive behavior with field in different condition such as ZFC, +5T FC, 1st loop and further trained loops are illustrated in figure 4.19 a. and b. respectively. Four consecutive loops measured on the same sample are shown in figure 4.20 a. to study the training effect. From the graphs it is clear that the exchange bias induced a unidirectional anisotropy which mostly modifies the negative field coercivity. Those values are resumed in table 4.5.

Such unidirectional coercivity enhancement has been observed in perpendicular exchange bias systems and explained by a distribution of blocking temperatures in the AFM grains [65]. The explanation is based on the idea that the smallest AFM grains are not frozen at 5K and still follow the ferromagnet during its reversal. We can consider a model system with two types of grains the smallest grains are rotating with the ferromagnet while the biggest

Table 4.5 $\mu_0 H_C$ behavior at the negative magnetization reversal for *S3*:

Temperature	$\mu_0 H_C$ ZFC	$\mu_0 H_C$ +5T FC 1st loop	$\mu_0 H_C$ FC 2nd loop
5K	-0.49 T	-1,16 T	-0,90 T
25K	-0.31 T	-0,66 T	-0,54 T
50K	-0.24 T	-0,38 T	-0,34 T
60K	—	-0,31 T	-0.28 T

grains are frozen (see figure 4.20 b.). After saturation in the positive cooling field direction all the uncompensated spins are tilted in the positive direction creating an OOP effective field which increases the coercive field in the negative direction. On the contrary after saturation in the negative direction the smallest grains have rotated in the negative direction while the biggest grains are still in the positive direction and the OOP effective field is reduced. The reversibility/irreversibility of such system were studied; an example of measurement can be seen in figure 4.20 c. The loops were recorded in ZFC conditions. After a first complete loop (0T to +5T to -5T and back to 0T) we start to perform another one, after reaching +5T we went back to -1.5T, at that field we stopped and we start increase the field again, till the saturation field of +5T was reached. The same procedure was then followed and the field was stopped at -1T, then -0.5T and finally at 0T to go back one last time to +5T. The sign of the field variation is shown with arrows on the loops in figure 4.20 c.

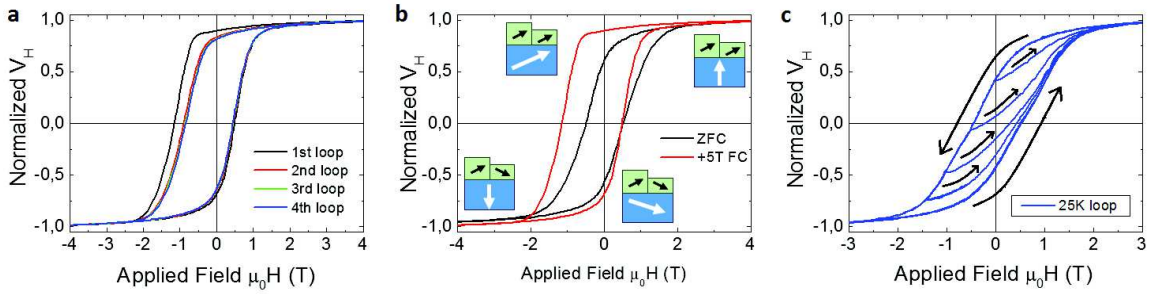

Fig. 4.20 a. Training effect on four consecutive loops measured on the same sample at 5K with a +5T FC and no heating in between two loops. b. ZFC and +5T FC loops differences and two grain's model for magnetization reversal. c. Irreversible/reversible loops recorded at 25K.

From the loop it is possible to evidence a half and half ratio between reversible and irreversible processes,. This picture agrees with the two grain's model utilized to describe the coercive field behavior. If the system were completely irreversible, the reversal process (when removing the applied field to go back to zero) would have been a flat line. On the contrary if the system was completely reversible, the reversal process would have perfectly

followed the precedent hysteresis line, making impossible to distinguish between the two and the loop would be a single curve. Our case falls in the middle between these two extremes.

Subnanometer exchange bias: IP and OOP measurements

The exchange bias has also been measured via VSM-SQUID magnetometer, the sample had to be cut as shown in figure 4.21 a. in this way also the IP EB could been measured. The two half cut samples $S3_{thick}$ and $S3_{thin}$ were both characterized.

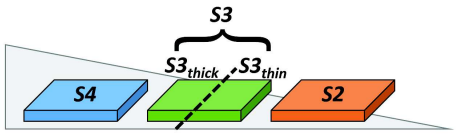

Fig. 4.21 Schematic view of the wedge samples for the VSM-SQUID measurements.

Sample $S3_{thin}$ is less interesting from the subnanometer EB point of view. First of all because the amount of CoO is close to 1nm, secondly due to the low volume of magnetic Co, it was difficult to obtain a clear signal with magnetometer measurements. To remain in the sub-nanometer range for both the AFM and FM layer, we will therefore focus on sample $S3_{thick}$: $Ta(5nm)/Pt(2.5nm)/Co(0.8nm)/CoO(0.5)/Al_2O_3(2.1nm)$. This cut sample has been remeasured OOP in the transport system for comparison. The VSM-SQUID and the cryostat AHE hysteresis loops are identical from an experimental point of view and can be seen in figure 4.22 for 5K and 25K. The small differences may be due to the fact that the two systems were not measured in the same way. The VSM measures the response of the magnetic active volume, while in the cryostat the measurement is based on the Anomalous Hall Effect. The difference in coercive field is less than 50mT.

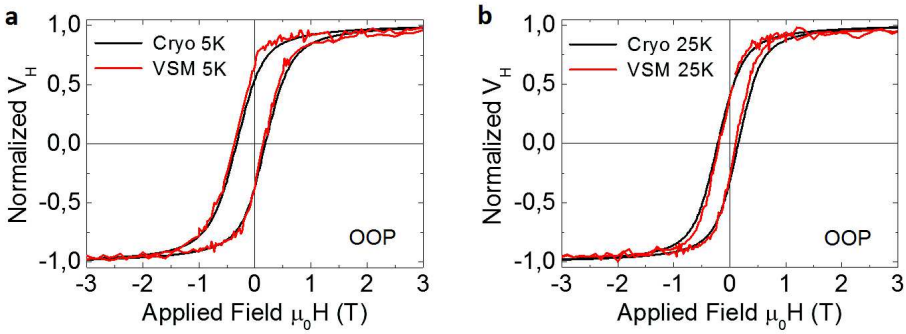

Fig. 4.22 Comparison between VSM-SQUID and cryostat AHE measurements.

When field cooling down below T_N the coercive field and remanence are stronger for the IP loops compared to OOP loops, a comparison of the IP and OOP field cooled loops

measured at 5K, 25K and 50K can be seen in figure 4.23. Both directions show hysteresis indicating that the FM easy axis is at an intermediate position between IP and OOP. On the other hand the exchange bias shift is larger in the OOP direction. A comparison between ZFC and +5T FC for OOP and IP direction can be seen in figure 4.24. The IP and OOP exchange bias fields are respectively $\mu_0 H_{EB//} = 90$ mT and $mu_0 H_{EB\perp} = 180$ mT at 5K. The full list of H_{EB} and H_C values for sample $S3_{thick}$ is summarized in table 4.6. The lower values compared to the cryostat one are expected due to the reduced t_{Co} thickness.

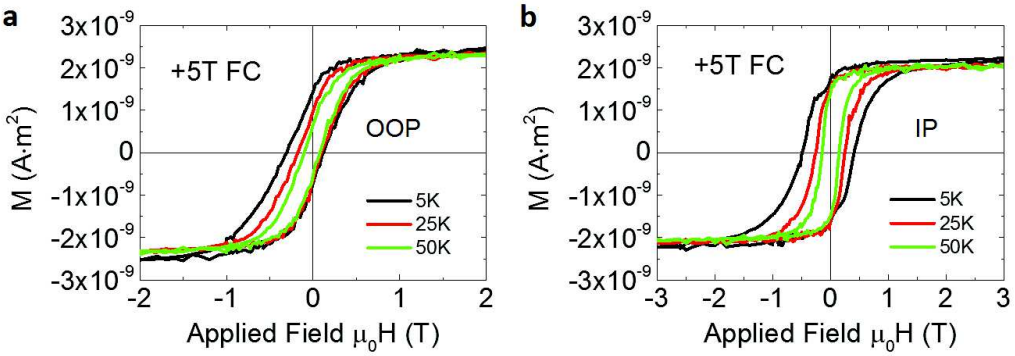

Fig. 4.23 a. OOP and b. IP hysteresis loops recorded at different temperatures for $S3_{thick}$.

By transforming $\mu_0 H_{EB\perp} = 180mT$ in exchange bias energy we obtain $E_{EB} = 0.21 mJ/m^2$ comparable with the previous values of 0.63 mJ/m^2 and 0.40 mJ/m^2 and consistent with literature [109]. The linearly extracted blocking temperature is only slightly inferior ($60 \pm 7K$ to compare to $67 \pm 5K$) respect to the one previously found. The presence of both IP and OOP exchange bias reveals also the presence of both IP and OOP CoO magnetic moments at the interface. The Out-Of-Plane EB seems to be more efficient with respect to the in plane direction $H_{EB\perp} \approx 2 \cdot H_{EB//}$ while the coercivity is higher in the IP direction $H_{C//} \approx 2 \cdot H_{c\perp}$.

In previous works, in a similar system but with textured structure and larger thicknesses, the opposite has been found [109]. However comparison of such complex systems is delicate when you consider that the texture of the FM/AFM layers are very dependent on the growth conditions and that even for same growth conditions the exchange field can show oscillations as a function of the AF thickness due to finite size effects [6]. For the IP loops we tried different field coolings. There is no difference in cooling down with +5T, +2T or +1T, with this applied field we surpass the saturation field to completely magnetize the Co at RT (the saturation anisotropy field is slightly inferior to 1T (see picture 4.25).

For this field there is no difference in the loops at low temperature and a EB shift with respect to ZFC measurement is present (see picture 4.25 a. and b). On the other hand when cooling fields of 0.5T and 0.2T are used, the shift disappears and the loops are symmetric with respect to zero (see picture 4.25 c. and d.). This happens when the field applied during

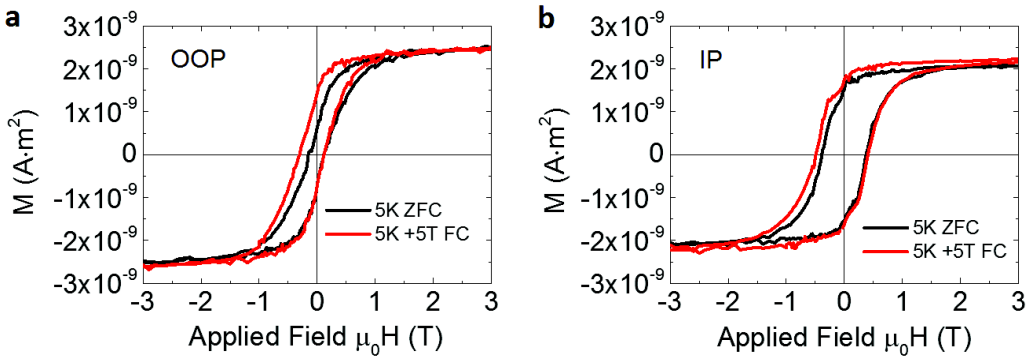

Fig. 4.24 a. OOP and b. IP hysteresis loops comparison between ZFC and +5T FC for sample$S3_{thick}$ recorded at 5K.

Table 4.6 List of values for the perpendicular and parallel EB (H_{EB}) and coercivity (H_C) for sample $S3_{thick}$ at 5K:

Temperature	$\mu_0 H_{EB\perp}$	$\mu_0 H_{C\perp}$	$\mu_0 H_{EB//}$	$\mu_0 H_{C//}$
5K	-188 mT	245 mT	-90 mT	460 mT
25K	-90 mT	140 mT	-0,30 mT	260 mT
50K	-13 mT	90 mT	-0,05 mT	150 mT

the field cooled procedure is not strong enough to completely saturate the FM Co. This is expected and confirms that the EB shift is not an artifact of the system (like a shift of the field scale). Another proof, that the EB can exist even in a subnanometer thickness regime, relies on the fact that the effect scales linearly with the temperature (which is typical of every EB system [16, 89, 153]). The shift observed in figure 4.25 d. is equal to 70mT and is comparable with the EB value (90mT) found for IP loops at 5K. The remanence at zero field is also $\sim$ 10% higher for the high FC loops.

To conclude we demonstrate that it is possible to control the oxidation of a Co/CoO bilayer. We fabricated ultrathin F/AF structures in which we can control the partial oxidation of the magnetic layer at the atomic scale (1.2 nm of Co becomes 0.65nm of Co + 0.67nm of CoO). Even in the subnanometer regime we could evidence the existence of a strong exchange bias which was observed both IP and OOP up to a blocking temperature of 67±5K, which is only marginally reduced when compared to nm-thick CoO system ($\sim$180K). We demonstrate that the CoO keeps a large magnetocrystalline anisotropy even in the ML regime. A domain size S_{CoO} of at least 1.2nm^2 (or $\sim$4nm^2 for reduced magnetocrystalline anisotropy) justifies the only marginally reduced T_B. The AFM domain size is likely to be at least that size in sputtered system. The exchange bias has real features, it decreases linearly with temperature, it is symmetric with respect to field cooling procedure (+5T and -5T field cooled)

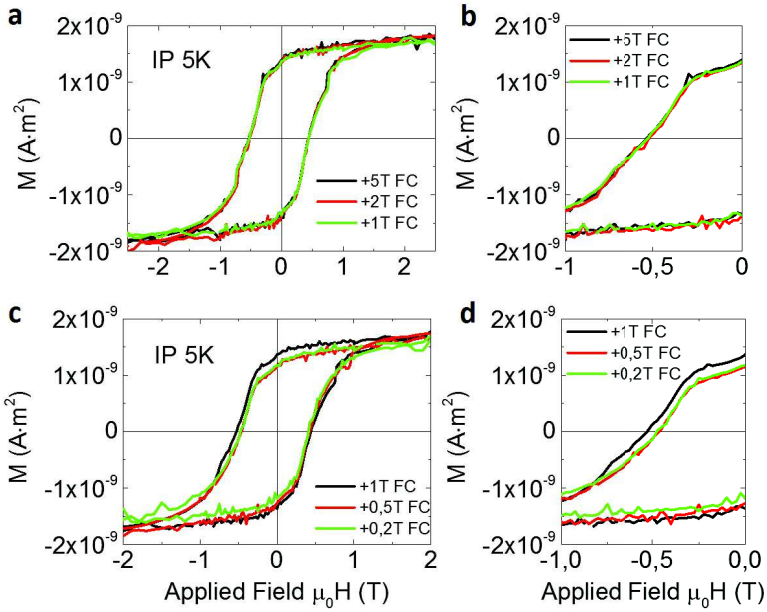

Fig. 4.25 $S3_{thick}$ IP hysteresis loops cooled down with different field. a. and b. With a field higher than the saturation field. c. and d. With a field lower than the saturation field

and disappears if the field cooling is performed below the FM anisotropy field saturation point.

Synchrotron experiment

This study was done in a collaboration with Helio Tolentino and Aline Ramos (Institut Néel). In order to investigate the Co and CoO atomic magnetic structure we used synchrotron light at the PGM line of the National Synchrotron Light Laboratory in Brazil. The study was done on a similarly grown sample. We performed X-ray magnetic circular dichroism (XMCD) measurement, which is the difference between two X-ray absorption spectra (XAS) taken in a magnetic field, with the two opposite circular polarization and X-Ray Magnetic Linear Dichroism (XMLD) measurements which are sensitive to differences in orbital occupation.

These techniques are nicely explained in the Ph.D Thesis of Anne Lamirand [97], a colleague who worked at the Institut Néel. We can briefly resume them here: XMCD probes uncompensated order (ferro/ferri) because it is proportional to the magnetization (M). XMCD is based upon absorption of X-rays at the well defined absorption edges of core electronic levels. Consequently, the magnetic properties of different elements present in the investigated sample can be separated (i.e Co and Co^{2+}), which is a big advantage compared to techniques that provide information about the average magnetic properties of a sample (like VSM-SQUID). Another advantage is that by measuring the difference in X-ray

absorption between left and right polarized light and using the so-called sum-rules, it is possible to get separate quantitative information about the spin magnetic moment and the orbital magnetic moment [236]. Due to the mean free path of the electrons, XMCD is a surface sensitive technique.

Ferromagnetic metals are usually best studied with X-Ray Magnetic Circular Dichroism (XMCD) spectroscopy. On the other hand, oxides are usually antiferromagnetic and are studied with X-Ray Magnetic Linear Dichroism (XMLD) spectroscopy. Indeed XMLD can probe compensated order (ferri/antiferro) because it is proportional to the square of the magnetization (M^2). Hence XMLD is a high-quality tool to investigate magnetic properties of antiferromagnets (difficult to measure by other methods, because insensitive to external applied field). XMLD can probe most of the AFM and in particular CoO which is of interest for this thesis. Therefore, the objective of this study was to get information on the spin configuration of the AFM and FM layers.

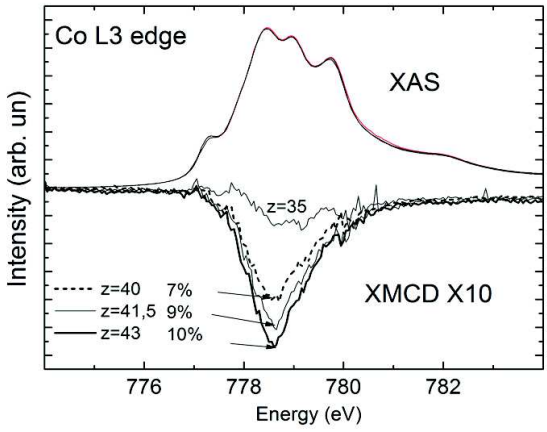

Fig. 4.26 XMCD and XAS spectra for the synchrotron analyzed sample. The different z's indicate different positions along the wedge axis.

To begin we measured the X-ray magnetic circular dichroism (XMCD) spectra. We measured the Co L3 edge signal of the XMCD at the saturation. For hexagonal close-packed (hcp) Co the signal should be around 50%. The absorption peak was taken in different positions along the wedge axis of the sample. The measurement will be named PGM_z with z the position along the wedge. The most promising is at z=43mm (0 mm is at the beginning of the wedge). PGM_{43} shows the highest Co signal. The Co L3 edge signal is roughly 10% of the maximum L3 (see picture 4.26). From the signal we deduced that at z=43mm only 1/4 of the Co is metallic. This number is compared with XRR measurement, made at the same z-position, the results are shown in table 4.7.

The XRR results show that 0.60nm of Co are metallic and that there is 0.75nm of oxide. The XRR gives a almost half and half ratio. To understand the discrepancies with the synchrotron XAS spectrum further studies are necessary. We can speculate that the two techniques do not measure in the same way. XRR is based on monitoring the reflected intensity of a X-Ray beam at grazing incident angle, XAS and more particularly the X-ray absorption near edge technique (XANES) is much more elemental specific, for example it can distinguish the oxidation states Co and Co^{2+}. This distinction is impossible in XRR measurements, which detect the total electron density.

Table 4.7 XRR fit results for PGM_{43}

	Thickness [nm]	Roughness [nm]	Density [g/cm^3]
Al_2O_3	1.65	0.44	3.4
CoO	0.75	0.43	5.3
Co	0.6	0.30	7.2
Pt	2.56	0.18	19.4
Ta	5.25	0.35	14.3
SiO_2	0.96	0.13	2.2
$Si_{substrate}$	∞	0.18	2.4

First we measured one hysteresis loop for the sample PGM_{43} at room temperature. We choose to utilize E=778.8eV (maximum of the XMCD signal) and we performed a loop between 2T and -2T with 0.1T step. The first hysteresis loop was done with circular positive polarization, the second one with negative polarization. The final cycle is the difference between those two and is shown in figure 4.27 a. and b. The compensation between the two polarizations was not good during all the beam time, it was specially difficult to stabilize for low applied field $H \sim 0T$. The coercive field is rather small: its value is below the measurement precision limit of 100mT. The system was then cooled down to 10K and the hysteresis loops were measured again with the same parameter used for 300K. The maximum field of 2T was not large enough to saturate the magnetization. Therefore we probably performed a minor loop (see picture 4.27 a. and b.). Under this measurement condition the coercive field was in the order of 1.3T and there is no sign of EB.

Finally we measured for the X-ray linear dichroism signal at the L3 peak of Co. The signals with IP or OOP applied fields look the same (see figure 4.28 a.); this could indicate an isotropic spin orientation for the Co due the polycrystalline structure of our film, and we can not say anything about the CoO spin's orientation. Figure 4.28 b. shows the two spectra at 300K and 10K, the difference between the two spectra may be due to the CoO entering

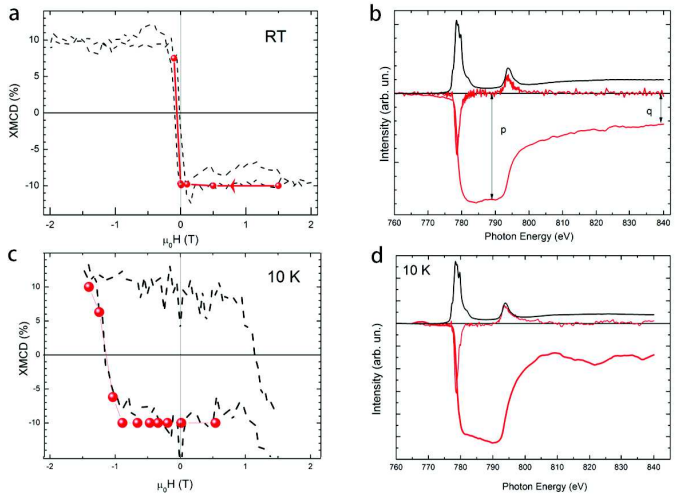

Fig. 4.27 XMCD spectra and hysteresis loops measured at 300K (a and b) and at 10K (c and d).

its AFM state, but to be more precise further investigation needs to be performed. We were also looking for information on the coupling between the Co and the CoO. On a similar work on a crystalline CoO/FePt double layer [98] it was found that the coupling is perpendicular. Other works performed on thicker Co/CoO bilayer found the opposite [167]. We do not have any conclusive results on such matter and further study should be performed to enlighten the physics and the spin magnetic properties.

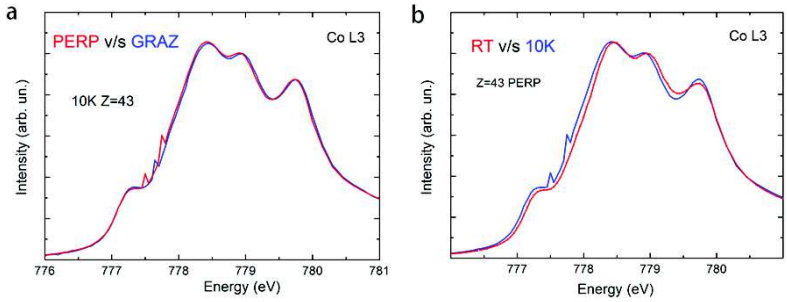

Fig. 4.28 XLD spectra recorded with a. polarization IP and OOP and b. at different temperatures.

4.5 Conclusions

We have investigated exchange-bias in Pt/Co/AlOx ultrathin films. We demonstrated that we can control the oxidation of Co through an Al wedge at the atomic layer scale and obtain a Pt/Co/CoO/Al_2O_3 system, with sub-nanometer Co and CoO layer thicknesses showing OOP anisotropy at room temperature. The characterization of the magnetic properties of the Co

layer at various temperatures allowed to further evidence the presence of CoO via coercivity enhancement, loss of remanence, unidirectional anisotropy and exchange bias.

The observed coercivity enhancement which is typical of any exchange bias system and is due to the antiferromagnetic ordering of the CoO. A peak in the coercive field is observed when the Néel temperature of the Co/CoO bilayer is reached around 225K.

The loss of perpendicular remanence is a direct consequence of exchange coupling between the AFM and the FM spin. We attributed this loss to the presence of an IP component in the CoO anisotropy which appears shortly after the paramagnetic/antiferromagnetic transition of the CoO layer (the tilt in the hysteresis loop first emerges around 200K). Another effect is the inversion of IP Hall loop magnetization rotation direction, which appears around 175K. This inversion was understood with simulations based on the Stoner-Wohlfarth model and is caused by a partial reorientation of the magnetization easy axis due to the exchange coupling between the Co and CoO. The Hall loops odd symmetry is definitely broken at 5K where the AFM spins become frozen in one direction. The preferential orientation can be chosen by preparing the Co layer at RT.

We observed an exchange-bias effect up to a blocking temperature of 70K. This effect is present despite the sub-nanometer thicknesses of both the ferromagnetic Co and antiferromagnetic CoO layers. A model based on the thermal activation energy and the size of the CoO grains justify the existence of the EB and the only marginally reduced T_B (when compared to nanometer thick layers). These results rule out some of the exchange bias models based on the formation of domain walls inside the AFM layer and parallel to the AFM/FM interface based on Mauri's model [4, 166]. Such domain wall cannot exist in our ultrathin bilayer. We also deduced that even if reduced to a few monolayers the CoO keeps a strong magnetocrystalline anisotropy.

The evidence of both IP and OOP exchange bias means that both IP and OOP frozen spins can be induced in the CoO upon field cooling. The out of plane EB is more efficient with respect to the In-Plane direction $H_{EB\perp} \approx 2 \cdot H_{EB//}$, while the coercivity is higher in the IP direction $H_{C//} \approx 2 \cdot H_{c\perp}$. To understand the spin configuration we performed X-Ray Magnetic Linear Dichroism (XMLD) and X-Ray Magnetic Circular Dichroism (XMCD) measurements in the PGM line of the National Synchrotron Light Laboratory in Brazil. The results seem to point in the direction of an isotropic CoO spin distribution, this explains the existence of both IP and OOP exchange bias. Due to the uncertainty on the synchrotron measurement results, to obtain conclusive answers on the AFM/FM coupling and on the spin configuration in the Co and CoO layer, further studies should be performed.

Chapter 5

Tunnel Anisotropic Magneto Resistance

5.1 Introduction and Motivation

Nowadays devices are based on Giant Magnetoresistance (GMR) and Tunnel Magnetoresistance (TMR), which are the two most important phenomena exploited in spintronics (see chapter 1.2). Magnetic tunnel junctions (MTJs) can exhibit very large changes in resistance when the relative alignment of the electrode magnetic moments is switched [161]. Indeed, TMR and GMR provide a way of relating the magneto-resistance response directly to the ferromagnetic exchange splitting of the carrier bands without involving the Spin-Orbit Coupling (SOC). Large magnetoresistances in these devices are, nevertheless, obtained at the expense of an increased structure complexity (i.e. the spin valve structure, see chapter 1.2.3). This complexity is necessary to guarantee independent and different magnetization switching characteristics and spin transport coherence between the ferromagnetic layers [160].

The larger magnetoresistance generally found in TMR devices compared to GMR ones is due to the fact that tunneling depends critically on hybridization between states in the metal on one side and in the barrier on the other. A specific constraint common to GMR and TMR devices is the need of (at least) two magnetically decoupled ferromagnetic layers, of which magnetic moments can be made parallel or antiparallel in some controlled manner [106]. The history of spintronics (and physics in general) has plenty of cases of effects that were neglected at first and were later rediscovered. For spintronics the best example would be the TMR effect, first observed in 1975 by Jullière [78], rediscovered in 1995 thanks to Moodera and Miyazaki [130, 133] and then exploited only five years later in magnetic field sensors, and in 2005 in Hard Disk Drives technology.

By following the same logic and taking a step back, before GMR and TMR a simpler effect was used in reading heads of hard disk drives (HDD), which exploited the anisotropic magnetoresistance (AMR) of Fe-Ni alloys. There, the resistance variation is a manifestation

of the Spin-Orbit Coupling (SOC) and it appears under a simple rotation of the magnetization with respect to the electrical current flowing into the device. The resistivity is not isotropic because the magnetization direction provides a privileged axis for the spin-orbit perturbation. The effect measured is of the order of a few percent at RT. Thus one can think of a new device in which the resistance variation would result from the change in the tunnel probability across a barrier, resulting from the rotation of the moment in a magnetic element which affects the Spin-Orbit Coupling (SOC). This is Tunnel Anisotropic Magnetoresistance (TAMR).

Compared to AMR, the advantage of TAMR is the fact that the tunneling process filters out a fraction of the electronic phase space and that the SOC is usually stronger at interfaces [33]. SOC was first incorporated in the calculations of a tunnel junction made of GaMnAs / GaAlAs / GaMnAs, where GaMnAa is a diluted ferromagnetic semiconductor (DMS), by Brey et al. in 2004 [22] (see figure 5.1 a). They studied the relation between tunnel magnetoresistance (TMR) and spin polarization in such structure with strong spin-orbit interactions. They discover that the presence of strong spin-orbit interaction modifies the conventional relation between TMR and spin polarization of the electrodes. Moreover, as a result of the strong spin-orbit interactions, TMR also depends on the angle between current flow direction and the electrode magnetization. The TAMR was identified for the first time and the idea to build original spin valves with new functionalities was proposed [22].

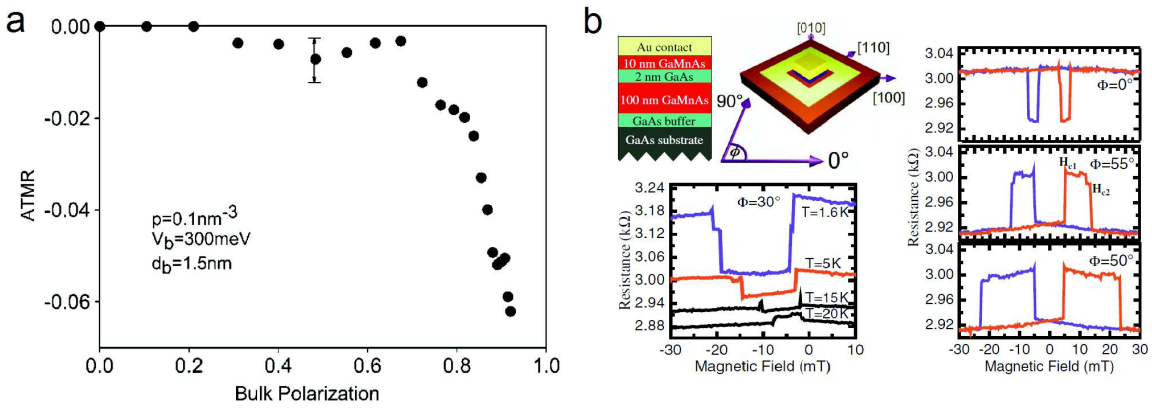

Fig. 5.1 a. Anisotropic TMR (TAMR) in GaMnAs/GaAlAs/GaMnAs as a function of the bulk polarization as first reported by Brey et. al [22]. b. Spin-valve-like effect results from strong spin-orbit coupling in a normal-metal/insulator/DMS tunneling device based on (Ga,Mn)As [63].

Large TAMR effects were recently observed in distinctly different MTJs constituted by a semiconductor heterostructures in which the ferromagnetic electrodes are made of GaAs doped with Mn [63, 175]. An example of measurement on a diluted ferromagnetic semiconductor can be seen in figure 5.1 b. This behavior is caused by the interplay of the anisotropic density of states in (Ga,Mn)As with respect to the particular magnetization

reversal process in this material [63]. Furthermore, studies of TAMR effects in ferromagnetic semiconductor tunneling devices showed that TAMR response can in principle be stronger and richer than TMR [22, 63, 233], reaching MR signal larger than 400% at low temperature [175]. It is believed that SOC plays an important role in the Ga(Mn,As), the TAMR effect could be attributed to a significant anisotropy in the DOS associated to the magnetization direction along different crystal axes [177]. New spintronics features were discovered in DMS due to TAMR and were reported by Ruster et al. [175] as follows:

- Both normal and inverted spin-valve-like signals, depending on the angle of the applied field with respect to the (100) crystallographic direction.

- A large non hysteretic magnetoresistance for magnetic fields perpendicular to the interfaces. A TAMR occurs when rotating the angle of the magnetization even in zero applied field, indicating that it must be related to the absolute rather than the relative orientations of the ferromagnetic layers.

- Enormous amplification of the effect at low bias and temperatures (TAMR of a $\sim$400% at 4K).

Compared to TMR, the TAMR was found to decrease much faster with temperature, which indicates that the tunneling DOS anisotropy deteriorates faster than the tunneling electron spin polarization. Indeed, the TMR signal scales with the magnetization of the ferromagnetic electrodes whereas the TAMR signal depends on the magnetic anisotropy, which decreases with increasing temperature as a power law of the magnetization. The first TAMR work was done on DMS. These materials have the advantage of a better compatibility with usual semiconductor materials used in micro and nanoelectronics. Among the DMS the most carefully studied is (Ga,Mn)As, in which meticulous optimization of growth techniques has led to reproducible materials properties and ferromagnetic transition temperatures above 150 K, although still far below room temperature [2]. To successfully incorporate spins into existing semiconductor technology, one has to resolve technical issues such as efficient injection, transport, control and manipulation, and detection of spin polarization as well as spin-polarized currents. Recent advances in materials engineering hold the promises of realizing spintronics devices in the near future [110, 232]. In general the low transition temperature makes DMS materials not suitable for real applications. There is need to utilize generic ferromagnets with strong SO coupling and high Curie temperature. Therefore, parallel to the studies on DMS the scientific community turned its attention towards metallic ferromagnetic materials as a possible alternative route.

5.1.1 Tunnel Anisotropic Magneto Resistance in Metal

The theoretical works on TAMR in metallic ferromagnets shortly followed after the DMS works. In 2006 Shick et al. [187] predicted the TAMR effect in ferromagnets, including high Curie temperature transition metal systems. A detailed investigation of the TAMR is motivated both by its intricate relativistic quantum transport nature and by its potential in more versatile alternatives to TMR devices. TAMR devices on the other hand will not require two independently controlled ferromagnetic electrodes or spin-coherent tunneling to generate an appreciable signal [82, 120, 186].

A first observation of spin-valve-like effects in thermally evaporated Co/AlOx/Au tunnel junctions (see inset of figure 5.2a) was reported by Liu and coworkers in 2008 [106]. They measured a tunneling anisotropic magnetoresistance which depends on the relative orientation of the magnetization direction of the Co electrode with respect to the current direction (see figure 5.2 a). They attributed this effect to a two-step magnetization reversal and to an anisotropic density of states resulting from spin-orbit interaction [106]. In that case the current was passing through a small Au island and the transport was in the Coulomb blockade regime which enhances the TAMR effect [18]. This paper was shortly followed by a publication from Uemura et al. in 2009 [216], where they investigated the magnetic and transport properties of fully epitaxial CoFe/n-GaAs junctions [216].

In the same year, another measure of TAMR in transition metal structures was reported by Park and coworkers [160] (shown in figure 5.2 b). The TAMR signal has uniaxial symmetry. The transport characteristics of TAMR tunneling devices are expected to be strongly influenced by the nature of the surface layers of the ferromagnetic electrode. The much larger TAMR signal fund in *sample A* compared to *sample B* (represented on the left and right side of figure 5.2b respectively) is due to the presence of a Pt layer. The Pt layer induces an additional moment and a strong SO-coupling in the two adjacent Co layers. The choice for the transition metals, the thickness and the composition of the films to optimize the SO-coupling and exchange splitting of layers adjacent to the tunnel barrier are crucial for the TAMR [160]. Compared to GMR and TMR, TAMR has the advantage that it requires only one magnetic electrode. This opens the way to exploring a number of new materials for spintronics devices, since the growth of the desired magnetic materials can be realized above an underlayer which can be almost freely selected [159].

Another potential advantage of TAMR is the fact that the magnetic element is not necessarily ferromagnetic since AMR exists as well in antiferromagnets (AFM). This in itself opens largely the possible search for suitable magnetic materials [116, 192]. The simpler stack and the large variety of AFM materials could allow much easier integration of TAMR-based spintronics devices and a viable route towards antiferromagnetic spintronics.

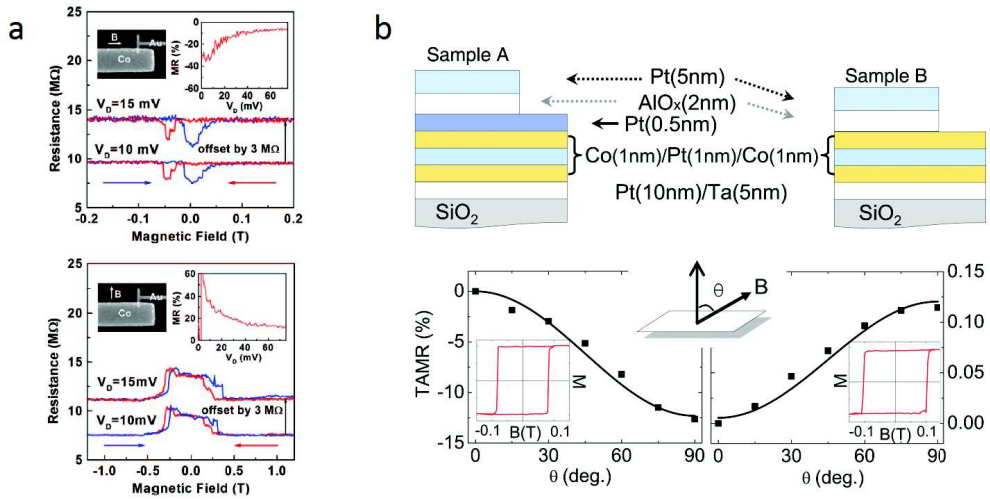

Fig. 5.2 a. Tunneling magnetoresistance vs magnetic field measured on a Co/AlOx/Au junction at 4.2 K with the field direction applied parallel and perpendicular to the long (easy) axis of the Co electrode (see inset) [106]. b. TAMR in vertical tunnel devices with a ferromagnetic $(Co/Pt)_N$ multilayer electrode and a nonmagnetic Pt counter-electrode separated by an AlOx amorphous barrier [160].

Indeed, one of the scenarii that may lead to next breakthroughs in the field of spintronics foresees a replacement of ferromagnetic electrodes by antiferromagnets (AFMs). The rigidity to external magnetic fields and the absence of stray fields make AFMs particularly favorable materials for ultrafast and ultrahigh-density spintronics [191]. The possibility of AFM dynamics with a time constant of a few femtoseconds has been predicted theoretically [147]. Experimentally, the ultrafast dynamics of an antiferromagnet is still an intriguing question, although an ultrafast spin reorientation is possible in AFM and can be induced by an ultrashort laser pulse or a photomagnetic pulse [86, 87]; real devices are far from being realized. AFM spintronics is intriguing, one of the major challenges is related to the higher requirements on the structural quality and transport coherence through interfaces which are significantly more stringent in the case of AFMs [186]; the simplest stack of a TAMR devices could allow to overcome this bottleneck.

An example of spin-valve like tunnel device based on antiferromagnet is shown in figure 5.3a. The external magnetic field is sensed by the NiFe ferromagnet, which via exchange spring, rotates the AFM IrMn. The tunneling transport is governed by the rotation of the antiferromagnet IrMn. The NiFe magnetization change is along the easy axis and therefore does not alter the DOS nor the magnetoresistance (0°and 180°NiFe magnetization directions are equivalent). 130% effect was measured at 4K; on the other hand the signal was very low at room temperature [159].

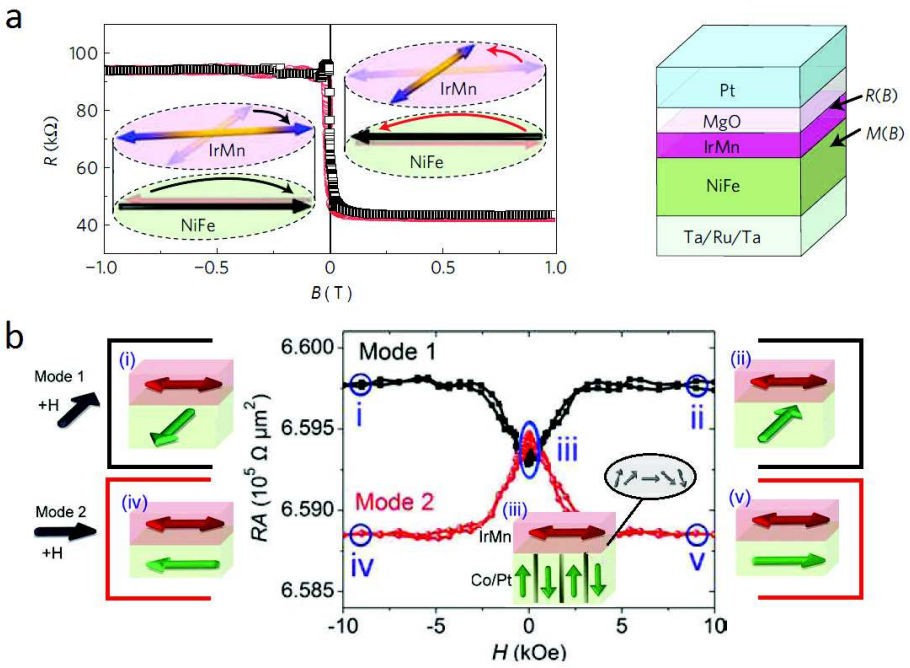

Fig. 5.3 a. A spin-valve-like AFM-tunnel device, a 130% MR signal was recorded at low temperature. The insets illustrate the rotation of AFM moments in IrMn through the exchange-spring effect of the NiFe measured [159]. b. Room temperature TAMR. The field is applied in-plane orthogonal to the easy-direction (mode 1) and along the easy-direction (mode 2). The schematic of the spins for the five states between Co/Pt and IrMn are sketched [228].

In figure 5.3b. the use of a thicker layer of IrMn (from 4 to 20nm) allowed the measurement of TAMR effect at room temperature [228]. The effect is maximized for IrMn thicknesses between 4 and 6 nanometers, for these thicknesses the totality of the IrMn is in exchange-spring with the Co/Pt (the calculated domain wall width is $\sim$7.8nm). The TAMR effect is strongly reduced when the IrMn layer thickness is increased above 6nm, supporting the idea that the TAMR is controlled by the exchange-spring twisting of the IrMn. Furthermore, Wang and coworkers verified that the room-temperature OOP-TAMR behavior in antiferromagnet-based [Pt/Co]/IrMn/AlOx/metal (metal = Pt, Au, Cu, Al) junctions is insensitive to the top non-magnetic metal electrodes. Similar out-of-plane signals are detected for different electrodes, in contrast to the varied shapes of in-plane TAMR curves which are most likely attributed to the differences in the multidomain structure of the magnetic electrode [225].

To summarize, the TAMR effect allows an attempt to develop metal spin valve-like devices based on a single ferromagnetic (or antiferromagnetic) electrode, where the MR response can be achieved without the independent switching between parallel and antiparallel magnetizations of two ferromagnetic layers [103, 216].

In addition, the simple TAMR structure may be a viable solution to incorporate antiferromagnet in a spintronic structure which might offer an advantage in terms of stability since the magnetic moments in the structure are immune to stray field (AFM do not couple to the magnetic field) which may be present in the environment [115, 116]. Therefore TAMR can be considered as a new possible effect which could be exploited in AFM based spintronics devices. An issue would be to control the magnetization of the AFM with common means, because the AFM does not couple with external magnetic field, therefore some other means must be found to orient the magnetization. One of the pioneer material that is being tested is Fe-Rh system. Fe-Rh alloys go through a phase transition with temperature passing from being antiferromagnetic at low temperature to ferromagnetic at high temperature; the temperature of the transition can be tuned by playing on the composition. Therefore one can imagine to heat the Fe-Rh, orient its magnetization with an external field and cool it down below its transition temperature [7, 189]. In this sense, work have been performed by Marti and coworkers in a recent publication, where they implemented a room temperature antiferromagnetic memory transistor [115].

TAMR has been successfully measured in ferromagnets in 2008 [54, 106, 160, 216] and examples of incorporation of an AFM in the TAMR stack have been successfully performed in 2011 [116, 159] at the beginning of this thesis work. Moreover the effect still exists at room temperature, which was effectively proven in 2012 [228]. The feasibility of devices based on AFM material have been demonstrated by Marti et al in 2014 [115].

From a more fundamental (and current technology related) point of view, TAMR can be used to better understand the physics of TMR devices. Many aspects of TMR remain poorly understood despite extensive experimental and theoretical efforts. Of particular interest is the influence of the detailed electronic structure of the MTJ on the bias voltage dependence of the spin-polarized tunneling [95]. One way to probe such an effect is to consider the angular dependence of the tunneling resistance, or the tunneling anisotropic magnetoresistance (TAMR) when the electrode's moments are rotated in large magnetic fields [54].

There is a need to further study this effect to reveal its full potentiality and many questions regarding the TAMR still need a definitive answer. The TAMR origin is still unclear; there is an interplay between the crystalline structure and the interface asymmetry. The TAMR dominant effect is still yet to be understood and seems to be system related [21, 33]. The role of the interfaces, insulating barrier and temperature on the TAMR effect still need further investigation. The TMR properties critically depend on the barrier nature; the role of the barrier still need to be clarified.

5.1.2 Ideas for this study

The idea of this study was to systematically measure the TAMR on our Pt/Co/AlOx model system along the wedge axis. Indeed our Pt/Co/AlOx wedged structure is an ideal model system to further investigate the TAMR effect and the laws governing its physic because we are interested in the interfaces contribution to the TAMR. We demonstrated that we have a good control on the oxidation and on the interface evolution in the sub-nanometer scale.

We have a Pt/Co interface, which originates both a large asymmetric behavior and a large SOC which seems to be necessary to obtain a large signal [160]. The Pt/Co is the common bottom electrode of our system and does not change along the full wedge length. On the other hand the particular geometry allows us to study the TAMR as a function of the oxidation. We will be able to study the TAMR signal as a function of the Co thickness and furthermore to possibly include the subnanometer antiferromagnetic CoO layer into the discussion. As we have demonstrated in chapter 3 and chapter 4, the CoO is capable of tilting the magnetization and to create an exchange bias field. Potentially the AFM CoO will play an important role in the designed TAMR signal. It would be really interesting to combine electric field and TAMR measurement on such thin Co/CoO bilayer system in order to play with the anisotropies of our system.

The nature of the insulating layer and the interfaces strongly affect the TAMR, similarly to MTJs which properties depend critically on the tunnel barrier. The role of the barrier for the TAMR effect still needs to be clarified. The top interfaces of our wedged system (and therefore the insulating barrier) changes along the wedge: the multilayer stack passes from being Pt/Co/Al/AlOx to Pt/Co/AlOx and to Pt/Co/CoO/AlOx. The thickness of the barrier also evolves as a function of the wedge. The thickness of the barrier and the nature of the anisotropies at interfaces will be taken into account when discussing TAMR.

Finally, it is important to emphasize that when designing the TAMR devices, all the parts of the samples will experience the same processes, making the systematic study even more compelling. To study TAMR on such original system could bring additional information on the physics governing this effect.

5.2 Results and Discussion

5.2.1 Implementing a device

To fully characterize the devices along the wedge a series of depositions, lithography and etching processes have been performed in order to define the device geometry and the TAMR electrodes. A description of the photolithography steps can be found in section 2.2; while

the deposition methods are described in section 2.1 of this thesis. After a first trial period in which a simple geometry have been utilized to measure I-V curves at 300K we decided to complicate the device geometry. We added a Hall bar under each magnetic tunnel junction in order to be able to characterize both the magnetic and the electrical properties at the same time.

Design of Experiment

To safeguard the wedge properties and systematically investigate the TAMR without cutting the samples into smaller pieces we design a mask able to cover the 2-inch long typical substrate used for this study. We will now describe the procedure to design the geometry of the devices. In order to do so a sequence of depositions, lift off and etching have been performed. The substrates chosen for this study are two inch Si/SiO_2(250 nm) thermally oxidized. The 250 nm of SiO_2 eliminates the possibility of electrical short circuit through the substrate, which we first encountered with Si(100) substrate, where at 300K part of the current was flowing through the Si and not in the active part of the device.

On top of the SiO_2 substrate we first spincoat the photoresist and then we open the bottom electrode and Hall bars geometry (shown in figure 5.4). In each geometry figure we will show the top view for the mask design (in purple on the left), the 3D device stack (in the center) and the side view of the devices geometry (on the right). Two masks were usually designed, one for lift-off and one for etching, basically one is the negative of the other. Because it is easier to see the geometry, in figure 5.4 (purple) we have shown the etching mask.

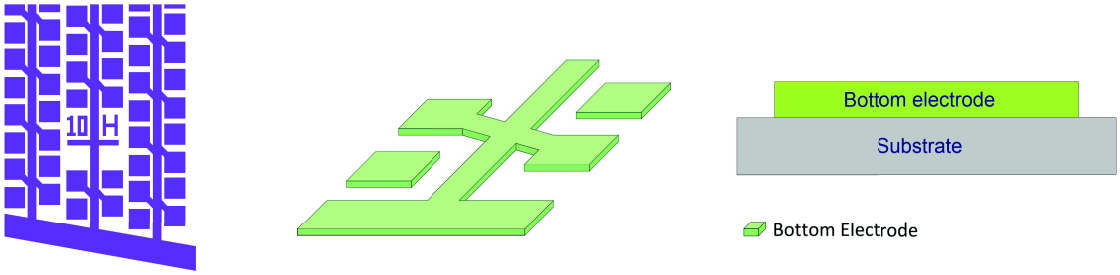

Fig. 5.4 Bottom electrode and Hall bar geometry.

After the geometry is designed, a Ta(5nm)/Pt(5nm) bilayer is deposited with magnetron sputtering to create the Hall bars. The chosen thicknesses assure a low resistance of the bottom electrode. If we consider the Pt bulk resistivity $\rho_{Pt} \sim 10^{-6}\Omega$cm, using $R = \rho_{Pt}\frac{l_{pads}}{A}$, where the Pt thickness is $t_{Pt} = 5nm$, the lateral size of the Hall bar is $s_{Hall} = 100\mu m$ and the distance between two pads $l_{pads} = 500\mu$m we would obtain a resistance $R_{pads} \sim 100\Omega$. The

measured resistance between two adjacent pads was slightly larger R_{meas} ∼250Ω although in the same order of magnitude. If we consider that the Pt resistivity in thin layer is increased (compared to bulk) we are close to what is expected.

The resistance of the whole pads' line is then around ∼2500Ω, 10 x 10 junctions can simultaneously fit into the sample holder (the total lateral size of the sample is around 5mm). This resistance will be negligible when compared to the resistance of tunnel junction (∼ MΩ-GΩ). The pads are 250μm wide, their size allows to easily perform the microbonding to electrically connect them to the substrate holder. Moreover the design of the mask allows to minimize the number of contacts for the current line (only two contacts are necessary for each line). In this way more junctions can be connected and measured without removing the sample from the cryostat (there are a total of 16 available connections on the sample holder).

After the bottom electrode is defined, we proceed to open the micro-pillar geometry with lift-off technique, see figure 5.5. The pillars have a lateral size of 80 μm, and their composition is Co(1.2nm)/Al(t_{wedge}). The wedge structure allows to have an area with in-plane and out-of-plane magnetization along the wedge axis, controlled by thickness of the top Al barrier and finally to have a zone with an antiferromagnetic CoO layer incorporated into the stack.

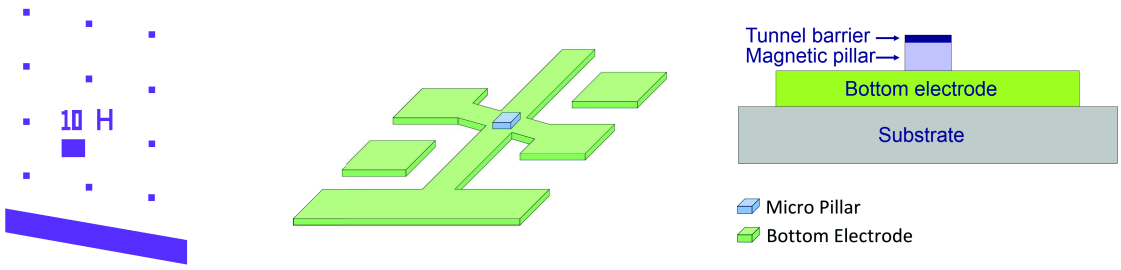

Fig. 5.5 Magnetic pillar and tunnel junction geometry.

To electrically insulate the bottom electrode and to define the electrical current path (which must flow through the tunnel junction), we need to deposit an insulating layer. Therefore, a mask was designed to have openings on the pads (in order to later perform the microbonding connections) and on top of the magnetic pillar (see figure 5.6).

The designed mask allowed to achieve both the electrical insulation of the pads and the definition of the current path. On the inset of figure 5.6 the opening created on top of the magnetic pillar is shown. The openings on the insulating mask were made size chose-able, three masks were designed with different lateral size of 20, 30 and 50 μm, the idea was to tune the resistance area of the tunnel junction. The insulation is performed with a 30nm thick Alumina layer deposited with atomic layer deposition technique (see section 2.1.2). This

thick layer guarantees a very good electrical insulation. We performed some test without opening the insulating layer geometry, the measured breakdown voltage tension between two pads was above 25V. The designed tunnel junctions operates at a bias voltage between 100mV and 1V. This allows a large region to operate the tunnel junction without worrying of possible electrical short circuit between pads.

These tests (without designing the insulating layer geometry) had a double objective, the first was to check the electrical insulation. The second was to check the possible formation of ears (see section 2.2) during the lift off of the magnetic pillar. This could have compromised the electrical design of the junctions, because an electrical current could have been flown through the ears short circuiting the tunnel barrier. The tests allow to rule out this possibility.

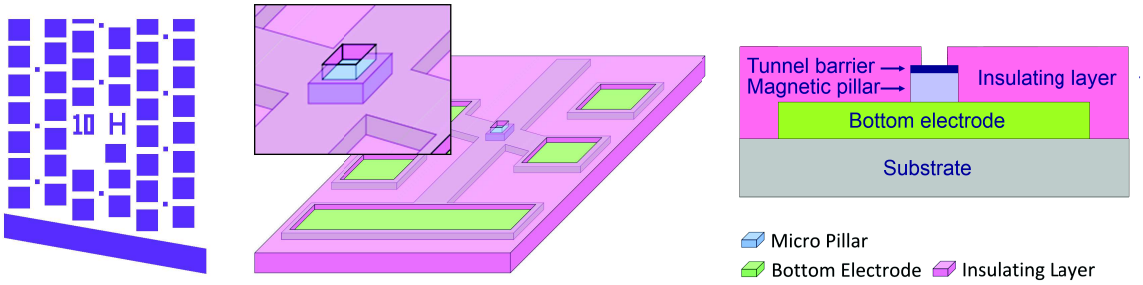

Fig. 5.6 Insulating layer geometry.

The last step is the deposition of the top electrode, which was performed with an electron beam evaporator gun (technique described in section 2.1.3). We deposited 15nm of Ti followed by 100nm of Au. The Titanium is used as a wetting layer; its role is to partly oxidized when placed into contact with the Alumina guaranteeing a good adhesion with the underneath layer. After depositing some nanometer, the Ti recovers its metallic state bonding with the top Au layer. Different tests delineate 15nm as the minimum amount of Ti that guarantees good adhesion. The top electrodes are 250μm wide; a sketch of the complete geometry is shown in figure 5.7.

As can be seen in figure 5.7, where the final geometry is sketched, it is possible to microbond the electrical wires directly on the desired electrodes without damaging the tunnel junction. The electron current path is defined by the device geometry.

Final device geometry

Despite all the efforts put into the optimization of the lithography process (in order to characterized the TAMR device from both the magnetic and electric points of view), we were unable to measure a suitable TAMR signal on such a complicated structure. Various tests

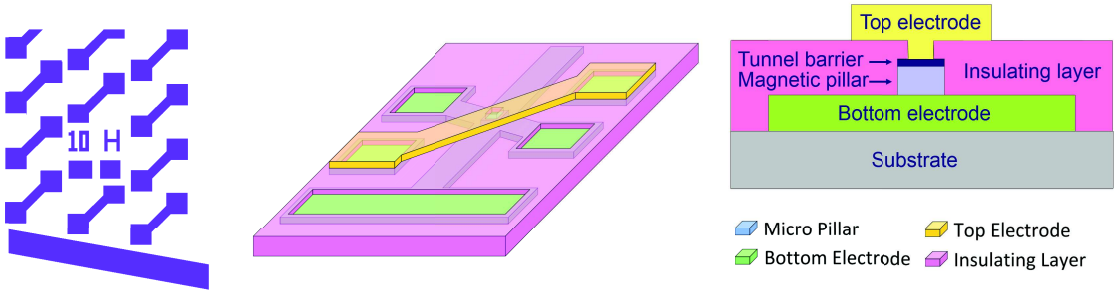

Fig. 5.7 Top electrode geometry.

have been performed to find out the possible problems, like the insulating barrier ones which were previously described. The numbers of the necessary process steps complicated this task. We solved the majority of the problems due to microfabrications, and we arrived to enlighten the following two main challenges:

- The electric properties of the AlOx barrier deposited at the Institut Néel (CNRS-Grenoble) are not sufficiently good to obtain a working MTJ. Tests on unprocessed samples resulted in a 90% ratio of short circuited junctions. The tests were performed by taking the top electrode directly on top of the Alumina layer (without performing any lithography). The defects in the tunnel barrier that cause the electric short circuit are probably due to the plasma oxidation which not only oxidizes but partly damages the deposited Al layer. Indeed, this was confirmed by tests done on tunnel barrier oxidized in atmosphere, where the Al layer was left in air to oxidize. In this case we managed to obtain working MTJs although without the oxygen plasma oxidation it was impossible to obtain the desired magnetic properties and to control the wedge geometry.

- The MICROPOSIT developer used to develop the S1818 photoresist partly etches the AlOx layer, reducing its quality and causing a shift of the magnetic properties. On samples measured before and after being in contact with the developer we see a shift of the OOP zone toward the thicker part of the wedge.

The first issue was overcome by using samples deposited at SPINTEC (CEA-Grenoble). These samples have the same Pt/Co/AlOx multilayer structure as those deposited at the CNRS but demonstrated to have a higher quality AlOx barrier. We performed the same test on unprocessed sample, which results in 90% of working tunnel junctions.

Actually at the beginning of this thesis and before deciding to complicate the devices' geometry we used a simpler geometry, which allowed us to measure working tunnel junctions

at room temperature. Therefore, to minimize the impact of the etching performed by the MICROPOSIT developers, we updated that geometry and we designed a simpler device (see figure 5.8a), in which two lithography steps were sufficient to open the tunnel barrier. The process is the following: we deposited the whole Ta/Pt/Co/AlOx wedge structure on top of the SiO_2 substrate. After the deposition of the multilayer structure a series of tunnel junctions (20, 30 or 50μm wide) are created directly on top of the multilayer. As before, to create the insulating layer a 30nm thick Al_2O_3 layer was deposited with Atomic Layer Deposition.

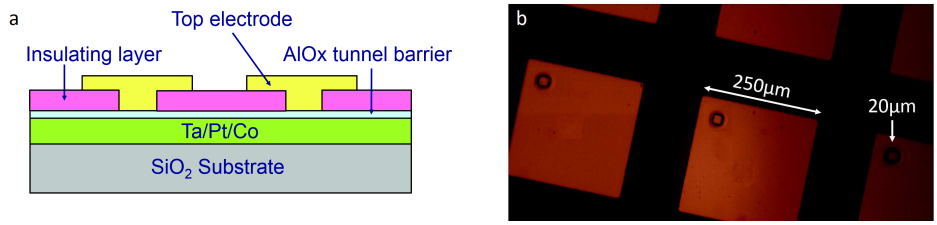

Fig. 5.8 a. Sketch of the simpler two-step geometry and b. tunnel junctions position with respect to the gold pads

On top of it we opened gold top electrode contacts (250μm wide) on which the microbonding is performed. As can be seen in figure 5.8b, the tunnel junctions are not placed in the center of the gold pads; this allows to perform the microbond on a safe area, without the risk of damaging the tunnel openings.

The bottom electrode is taken directly on the Ta/Pt/Co: to do that we removed a part of the thick insulating alumina layer and then we contact directly to the underneath layer. To check the quality and the resistance of the wire-bond on the bottom electrode, two different contacts (at opposite sides of the sample) were taken and the electrical resistance between them was measured each time.

The electrical resistance between the two bottom electrode contacts (taken at the opposite side of the sample) is usually in the order of the $\sim 100\Omega$ (the resistance is lower with respect to the Hall bar geometry because the current is not confined in a small area). The double bottom electrode contacts are also useful for the measurement point of view. Indeed, it is possible to lose electric contacts during the cooling-down procedure (the bonding wire detaches from the sample or from the sample holder). To have two working bottom electrode contacts minimizes the risk of losing one electrode.

Even with this simple configuration we were limited to study only the thick Alumina barrier region, because thinner regions resulted in short circuited electrodes. This is probably due to the MICROPOSIT developers. We were aware of the etching problem, although we greatly underestimated its importance which was understood only at the end of this thesis. For these reasons it was hard to obtain a suitable working magnetic tunnel junction with good

magnetic and good electrical properties. One of the possible way to overcome it would be to deposit a metallic layer on top of the Al_2O_3 barrier (after the plasma oxidation) in order to protect it from the developer (i.e. a capping layer of some nm of Pt); this procedure remains to be tested and can be simply implemented in future devices.

In the beginning we were interested in perpendicularly magnetized samples, the idea was to first characterize the simpler Pt/Co/Al_2O_3 samples and then to try to incorporate the antiferromagnetic CoO in the stack, changing the structure to Pt/Co/CoO/Al_2O_3. To obtain OOP anisotropy in the thicker regions a 250°C anneal was performed, the perpendicular anisotropy on such area was confirmed with KERR measurement at room temperature.

Concerning the electrical measurement point of view, optimal working conditions would have been to have tunnel resistance high enough, to be able to state that the resistance changes are due to Tunnel Anisotropic MagnetoResistance (TAMR), and not due, for example to the AMR of the underneath layer, but low enough to be easily measured with our electronic equipments. This is summarized in figure 5.9, where the good working window is shown (assuming 20x20μm^2 junction).

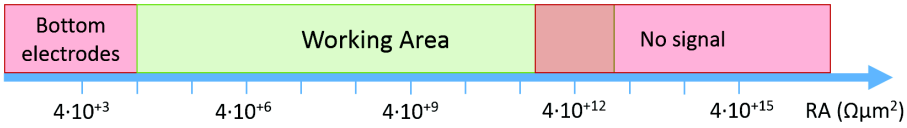

Fig. 5.9 Working window for the magnetic tunnel TAMR devices, represented on a logarithmic scale of the resistance area of the MTJ (assuming a 20x20μm^2).

The ideal resistance area (RA) ranges from 10M $\Omega\mu m^2$ to $10G\Omega\mu m^2$. It is important to measure the MTJ in the linear part of the I-V curves, because when exiting from the linearity other effects (independents from the SOC) come into play and the TAMR magnitude is reduced; we took care of choosing our bias voltage set point into the linear part of the MTJ.

5.2.2 Characterizations of the Tunnel Barrier

Brinkman's and Simmons' models

We start by electrically characterizing the properties of the magnetic tunnel junction. To observe a tunnel current a voltage difference has to be applied across the barrier. In this subsection the current as a function of the voltage and the current variation with the barrier height and thickness are discussed. Brinkman [23] and Simmons [190] have used a simplified free electron model to fit the experimental current-voltage characteristics. These models are often used to obtain the barrier height and thickness with a good approximation to the real

values [197]. The influence of a voltage over the barrier is to change the potential energy of the barrier, see figure 5.10.

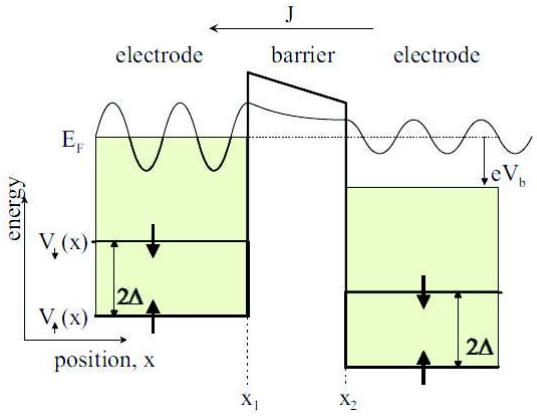

Fig. 5.10 The potential of a magnetic tunnel junction for a spin-up and spin-down electron.

In the low voltage limit, where the tunnel probability does not change, the tunnel current is proportional to the applied voltage. Above a certain voltage value, the change in the tunnel probability becomes important (it is like if the electrons see a reduced barrier height and width), this leads to an exponential increase of the tunnel current, which exits from the linearity [78]. Simmons found a simplified equation to describe the current density behavior in a tunnel junction [190]:

$$\begin{aligned} J(V_b) = &\frac{e}{(2\pi)^2\hbar d^2}\left\{\left(\phi - \frac{eV_b}{2}\right) exp\left[-2d\sqrt{\frac{2m}{\hbar}\left(\phi - \frac{eV_b}{2}\right)}\right]\right\} + \\ &-\frac{e}{(2\pi)^2\hbar d^2}\left\{\left(\phi + \frac{eV_b}{2}\right) exp\left[-2d\sqrt{\frac{2m}{\hbar}\left(\phi + \frac{eV_b}{2}\right)}\right]\right\} \end{aligned} \tag{5.1}$$

where V_b is the bias voltage, ϕ is the average barrier height above the Fermi level expressed in eV and d is the barrier thickness. If as in our case, the two electrodes are made of different materials we can introduce an asymmetry parameter $\Delta\phi = \phi_{right} - \phi_{left}$ to take into account for the tilted barrier. We can then approximate the current density by a Taylor expansion to the third power. The analytical expression for the current density will now be:

$$J(V_b) = G_0\left[V_b - \left(\frac{\sqrt{2me}}{24\hbar}\frac{d\Delta\phi}{\phi^{3/2}}\right)V_b^2 + \left(\frac{2me^2}{24\hbar^2}\frac{d^2}{\phi}\right)V_b^3\right][A/m] \tag{5.2}$$

where G_0 is the conductance at zero bias voltage and is equal to:

$$G_0 = 7.9 \cdot 10^9 \frac{\phi^{1/2}}{d} exp\left(-2d\sqrt{\frac{2m\phi}{\hbar^2}}\right)[\Omega^{-1}m^{-1}] \tag{5.3}$$

The standard S.I. units for the parameters are used. The model assumes thick (>nm) and high barrier (>1eV). The temperature and thermal fluctuations are not included in the model (T=0K). Equation 5.2 was used to fit the measured I-V curves. An example of fit is shown in figure 5.11a, in which a MTJ is fitted.

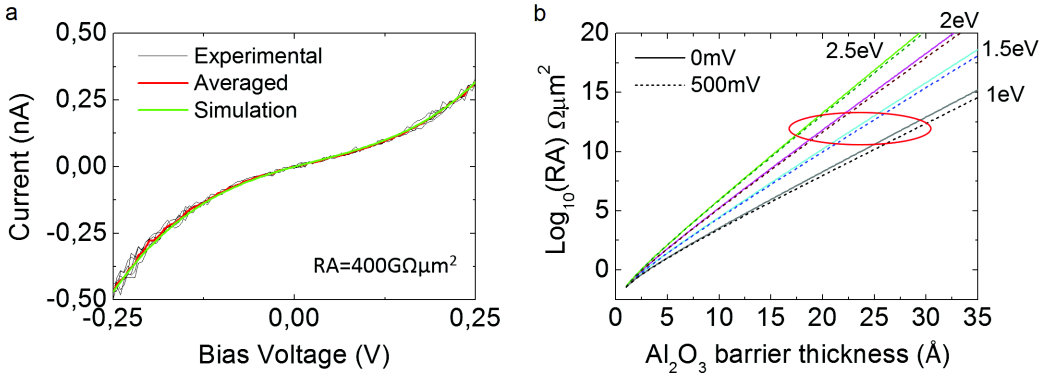

Fig. 5.11 a. Example of I-V curves recorded at 300K. A total of six I-V were recorded on the same junction. The average and the fit curve form the model are also shown. b. Simulation of the Resistance Area value as a function of the Al_2O_3 barrier thickness for 0 and 500mV bias and barrier height from 1eV to 2.5eV, the RA is plotted in logarithmic scale.

The idea for this model is to obtain a first and fast understanding of the electrical and barrier properties of the MTJs. The thickness (d), height (ϕ) and asymmetry ($\Delta\phi$) of the tunnel barrier were obtained with the fit. d is usually 2 to 3.5nm wide, in accord with the expected deposited thickness and XRR measurements. The barrier height ϕ is usually between 1.2eV to 2.5eV and the asymmetric parameter $\Delta\phi$ below $\pm$1eV. These values are realistic when comparing with literature regarding experimental Alumina barriers [197].

To further investigate the RA dependence from the physical characteristic of the tunnel barrier we performed various simulations, the results are summarized in figure 5.11b. In particular we used equation 5.2 to simulate the RA behavior for barrier height from 1eV to 2.5eV (with 0.5eV steps) at bias voltages of 0 and 500mV as a function of the barrier thickness (from 0 to 3.5nm). In this particular simulation (figure 5.11b) we decided not to include the asymmetric term, which is fixed and equal to zero. The red circles in figure 5.11b, indicates the zone corresponding to RA in the range of $10^{+12}\Omega\mu m^2$, values close to what

was obtained in the experimental measurements, corresponding to Al_2O_3 thicknesses varying from 1.5nm to 3nm depending on the barrier height.

The tests on the MTJs were done in order to understand the limits for the applied voltage (i.e the breakdown voltage) and the reproducibility of I-V curves made on the same junction. The break-down tension was found to be of a few volts (1V to 2V), depending on the junction characteristic. An example of reproducibility is given in figure 5.11a (plotted in black) where six I-V curves recorded on the same MTJ are shown. There are a small variations between each measurement in the order of 5% of the measured signal.

Temperature behavior

We then proceed to cool down the system, the TAMR effect on Pt/Co/Al_2O_3 structure is more likely to be observed at low temperature [106, 160, 227]. We did not extend the I-V model further (i.e. by adding the temperature dependence of the MTJs); nevertheless we observed the MTJs behavior in temperature. We measured the current as a function of the temperature between 300K and 10K. The tests were done on test junctions, without the desired magnetic and electrical properties. We chose a highly resistive MTJ, where it would have been unlikely to measure a suitable TAMR signal. The measured temperature behavior cannot be very different from relatively less resistive junctions, this allowed us to obtain a good understanding of the temperature effect on the tunnel probability in our MTJs. The measured current as a function of temperature is plotted in figure 5.12.

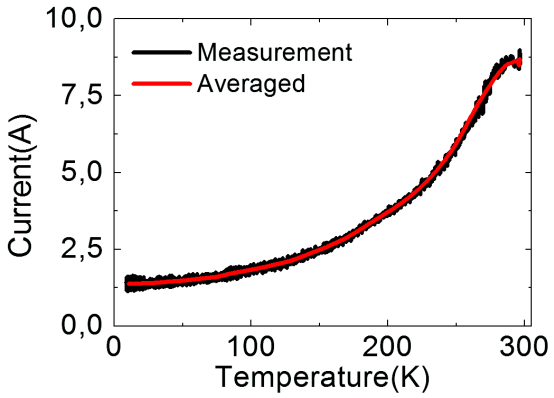

Fig. 5.12 Tunneling current variation with temperature. The applied bias voltage is 2V.

In the Brinkman and Simmons free-electron model, the tunnel elastic probability does not depend on the temperature. In reality, the temperature contribution causes the electron to be excited above the Fermi level, leaving more holes below the Fermi level. The tunnel probability increases with the energy of the electron (hot electrons have a higher probability

of passing through the barrier junction). Decreasing the temperature causes a reduction of the current because electrons are less excited.

The current of ferromagnetic tunnel junctions was found to decrease with decreasing T, see figure 5.12. A spin-independent conductance was invoked to explain the variation of the junction resistance with T, which is in principle small for a defect-free tunnel barrier [108, 197]. On the other hand, in experimental devices there is a contribution of spin independent current, described by hopping of electrons through localized states in the barrier.

There are two main models to describe the temperature dependence. A first model considers that the directed inelastic hopping of electrons through metal-insulator-metal tunnel junctions strongly depends on the temperature and increases like a power law $G(T) \propto T^{4/3}$ [234]. The second model considers the possibility that the charge is transported via phonon-induced tunneling of electrons between localized states which are randomly distributed in energy and position. The obtained electrical conductivity has the form: $G(T) \propto exp\left[-(\alpha/k_BT)^{\frac{1}{4}}\right]$, where α depends on the density of states at the Fermi level and from material parameters [5].The main message, without entering in the mechanism of each model, is that the hopping through the localized states becomes less and less dominant with decreasing temperature. In our case, shown in figure 5.12, this happens around 100K, below this temperature the change in current is roughly 0.1 nA every 30K. Temperature-dependent measurements in ferromagnetic tunnel junctions can be used to study the surface properties of ferromagnetic materials [185].

5.2.3 TAMR measurements

In this section we will present the measurements performed on a TAMR device. Due to the high resistive behavior of our tunnel junction, the bias voltage necessary to obtain a measurable signal was rather high. With a bias voltage of 500mV we were barely above the linear response of the MTJ, see figure 5.13a. Therefore, a bias voltage value of 500mV was chosen for the following measurements. The spontaneous magnetization of the sample lies OOP; the perpendicular anisotropy was obtained after a 250°C thermal anneal and confirmed by MOKE measurement at RT.

The experimental geometry is shown in figure 5.13 b, while the multilayer structure is shown in figure 5.13 c. At zero applied field, the magnetization of the sample lies along its easy axis and points OOP. As shown in figure 5.13b, the external field is applied along the sample plane. If the external applied field is strong enough the magnetization will align itself with the field, rotating from OOP to the IP position. A first measurement on such system was performed at 5K and is shown in figure 5.14. The voltage bias was kept fixed at 500mV and the applied field was looped between $\pm$5T with field steps of 25mT.

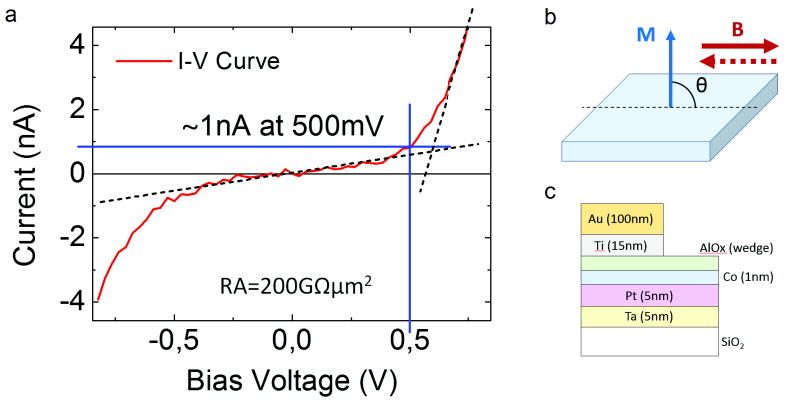

Fig. 5.13 a. I-V curve measured at 5K with resistance area $RA = 200G\Omega\mu m^2$. b. The experimental setup geometry with in-plane field and c. the multilayer structure are sketched.

At zero applied field the measured current is ∼1nA, this value is reduced to 0.92 nA when an external field of ±5T is applied, the effect (larger than the noise) depends on the applied field, which rotates the magnetization from its out-of-plane easy axis to in-plane. There is a non negligible noise component, roughly equal to 25pA (2.5% of the total signal). The same measurement was then performed at 10K and 25K, the results are shown in figure 5.15 a. and b. respectively.

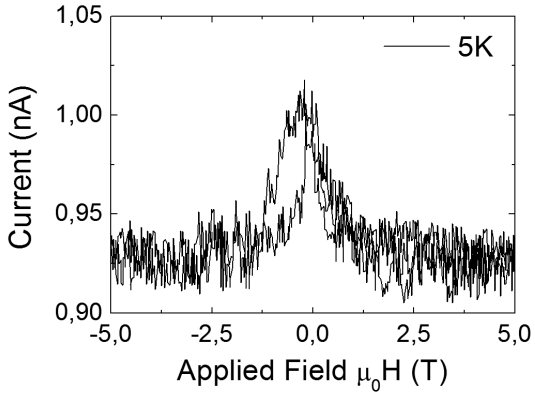

Fig. 5.14 Measured current in function of the in-plane applied field at 5K. In zero applied field the magnetization is pointing out of plane (easy direction).

The measured current at zero bias field is around 1nA for the 10K measurement, which is similar to what obtained with the 5K one. The current is slightly higher for the 25K measurement. This higher value is probably due to the higher temperature at which the measurement was done, which corresponds to a higher conductance for the tunnel junction [185]. In both cases the measured current is reduced when an external field is applied. The current value changes from ∼ 1nA to 0.925nA and 0.975nA for the 10K and 25K

measurements respectively. The noise level is stable (around 25pA) and does not vary with the temperature.

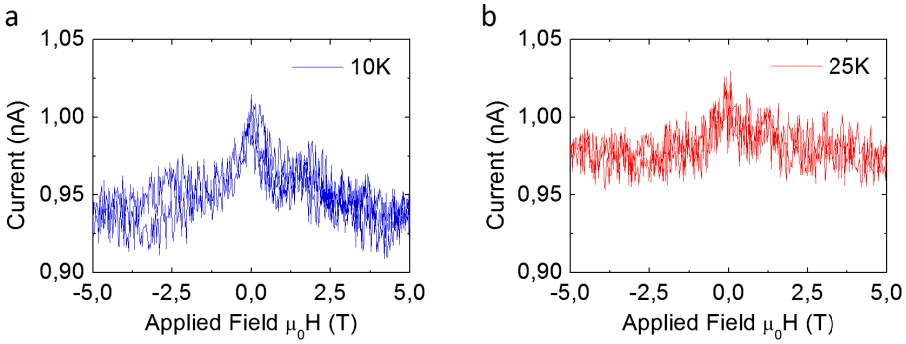

Fig. 5.15 Measured current in function of the in-plane applied field at a. 10K and b. 25K. In zero applied field the magnetization is pointing out of plane (easy direction).

The effect on the 5K measurement (see figure 5.14) seems not field symmetric. This can be due to the antiferromagnetic CoO which, even in ZFC condition, can slightly shift the hysteresis loop and therefore the TAMR. The asymmetry seems to be reduced in the 10K and 25K measurements (see figure 5.15 a and b respectively), indicating that the shift appears only at very low temperature. Unfortunately, the junction died when we heated-up the system back to 300K, to perform a proper field cooled measurement.

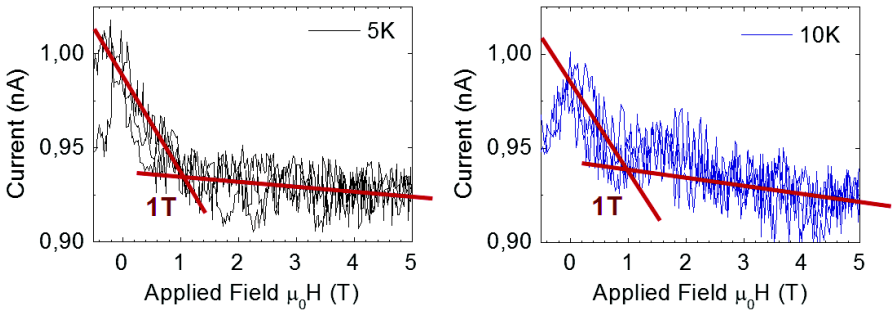

Fig. 5.16 Intersection of the high filed slope and the decreasing current due to the rotation of the magnetization. The extrapolated value indicates the field at which the magnetization rotates in-plane (calculated on the positive field).

We can extrapolate the field at which the magnetization seems to completely rotate in-plane. In order to do so, we extrapolate the intersection of the high positive field slope (where no shift is present), with the decreasing of the electrical current due to the rotation of the magnetization, this is illustrated in figure 5.16. The extrapolated switching field is (1 ± 0.2)T and does not vary between 5K and 10K, the high uncertainty is due to the low signal to noise ratio.

From the current values and remembering that the applied voltage is 500mV, we can obtain the resistance change with applied field, which is in the order of (50±5)MΩ for the 5K measurement. The change is reduced as the temperature increases. At 10K the change is ∼(37.5±5)MΩ, at 25K it is only around (25±5)MΩ, we could not evidence any effect at 50K. The electrical resistance drop is shown in figure 5.17, where the 5K, 10K and 25K electrical resistance and field values are plotted versus the measurement time. This temperature dependence is typical of some TAMR system [106, 160].

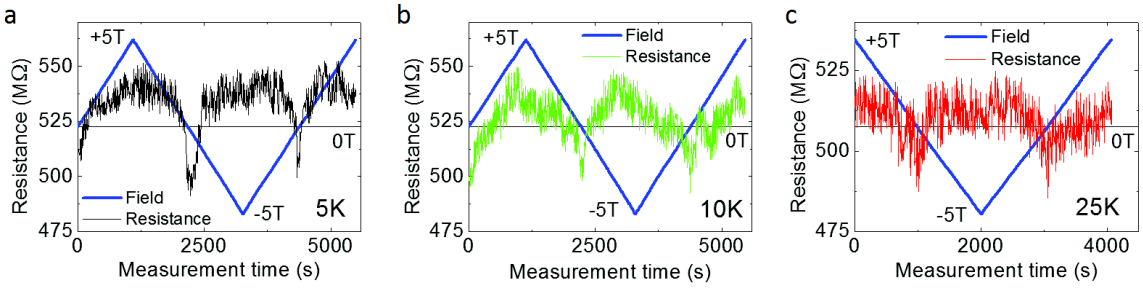

Fig. 5.17 Resistance and field plotted versus the measurement time for a. 5K, b. 10K and c. 25K measured on the same MTJ.

Analysis of the TAMR

Is it possible that the measured resistance change is related to the AMR of the underneath layer in which the current is flowing? This is unlikely to be true. First of all the measured resistance for the underneath layer is around 100Ω, five orders of magnitude smaller than the measured change which is in the order of 10MΩ, this alone can already exclude that the measured signal is due to the AMR of the Pt/Co layer. Moreover there is no reason for the AMR to change that much in a small temperature interval [61, 123].

We can also compare the AMR value measured on similar Pt/Co/AlOx multilayer. The measurement was done in parallel to anomalous Hall effect measurements on unpatterned sample. The measured AMR change is lower than 1% at 5K. It is worth to note that we did not measure it with the optimal contact geometry (the four contacts were in a square geometry and not in line, see section 2.3.1), but the real AMR value cannot differ much from the observed one. This confirms that the measured resistance change can not be due to the AMR of the Pt/Co underlayer. We can now reasonably exclude that the measured signal change is due to the AMR of the system.

There is another effect that might come into play and that must be considered, observing the temperature behavior of a MTJ we have seen that the current value depends on the temperature, see figure 5.18. Therefore, the current change can still be due to a temperature

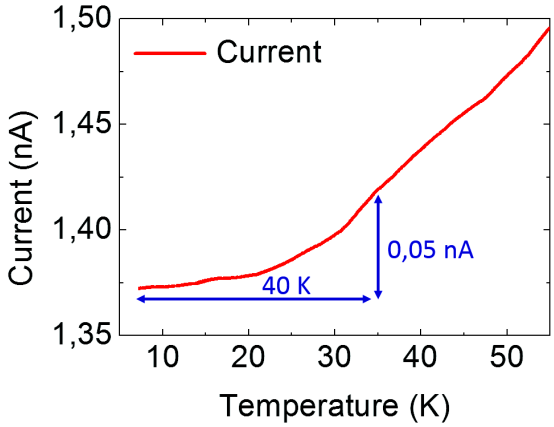

Fig. 5.18 a. Typical tunnel current characteristic as a function of the temperature. At low temperature a 0.05nA increase occurs over a 40K temperature change.

change in the cryostat system. To discuss the possible temperature effect on TAMR the 5K current signal and applied field versus measurement time are plotted in figure 5.19a.

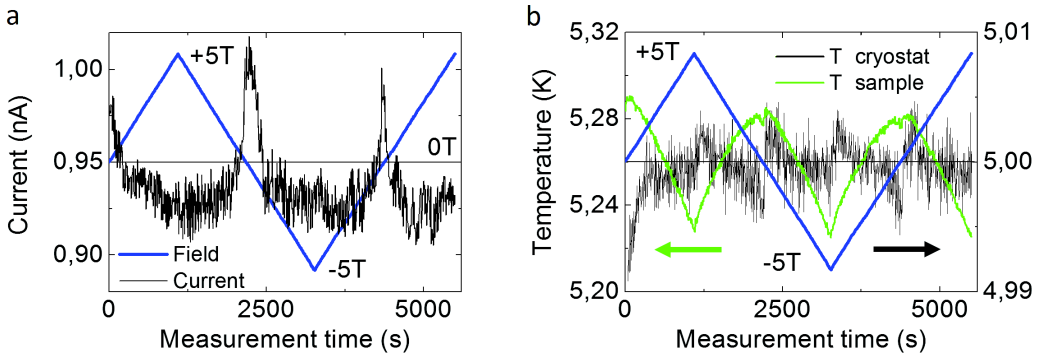

Fig. 5.19 a. Measured current and applied field plotted as a function of the measurement time. Magnetoresistive effect on the two temperature sensors, the data refers to the 5K measurement.

As evidenced from the graph 5.19 a, the measurement time is quite long; the time necessary to perform a full loops (0→+5T→-5T→+5T→0T) with 0.25mT step is around one and half hour. The temperature of the system must be stable, within a certain margin, for the whole measurement period. The cryostat system has two main temperature sensors dedicated to the temperature measurement, one which measures the cryostat temperature and one which measures the temperature of the sample holder. We can observe their behavior to understand the system temperature stability.

As can be seen on figure 5.19b, the sample temperature (in green) follows the field evolution, at zero applied field it measures a larger temperature than at high field. At zero field the resistance value is 5.29K which changes to 5.23K at $\pm 5T$, the difference

between the two temperature is ∼60mK. From figure 5.19b (in black) we can see the cryostat temperature behavior which, after a first transient part, is less sensitive to the applied field and its total variation is less than 10mK over $\pm 5T$. This variation is due to the fact that the temperature sensors are slightly magnetoresistive, which means that their resistance will change accordingly to the applied field. This is reflected in a change of temperature because the sensors associate the measured resistance to the temperature, through a calibration curve. Even if this temperature change is not real, the cryostat temperature regulation system will try to compensate this variation.

A good way to understand the magnetoresistive effect is to observe the behavior of the heating system. The heating system is the one responsible for the temperature regulation inside the cryostat and is influenced by the temperature variation recorded by the sensors. In figure 5.20 the measured current and the voltage command heating are plotted.

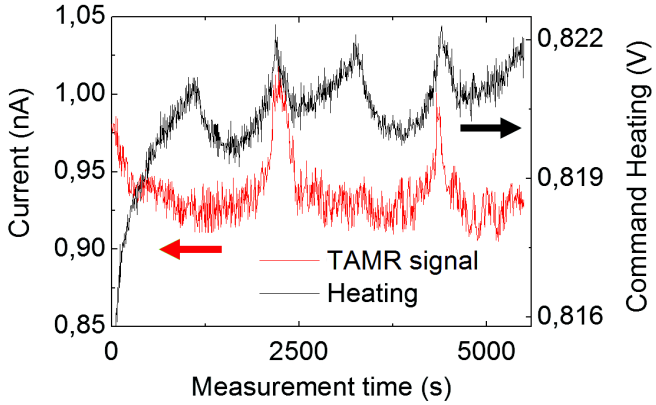

Fig. 5.20 Measured current and command heating as a function of the measurement time. The data refers to the 5K measurement.

From figure 5.20 is clear that the nanocurrent (in red) and the command heating (in black) do not have the same correlation. Moreover as can be seen in figure 5.18a, the current change with temperature is very small, a temperature difference of 40K is necessary to have a 0.05nA current change. The TAMR effect is larger at 5K with respect to 10K and 25K, on the other hand the sensors magnetoresistive effect is not very T-dependent between 5K 10K and 25K, confirming that the current variation is not due to a temperature effect.

To summarize:

- The current change is symmetric with field, when the magnetization is pointing OOP a higher current value is measured (corresponding to a lower resistance) this value is reduced when a strong IP field is applied. Moreover, the current change with field is reduced with increasing temperature, these are typical of TAMR in Pt/Co/AlOx system.

- The high MTJ resistance value combined with a low resistance of the Pt/Co underneath layer (and the relative low AMR signal measured in similar structures) rules out the possibility of measuring a simple AMR signal.
- The low MTJ current dependence with temperature (0.05nA for 40K at low temperature), the missing symmetry between the heating command and the measured TAMR and the good thermal stability of our system rule out the possibility to be measuring a simple temperature effect.

We are confident that the measured current and resistance changes with applied field is indeed a TAMR signal. We can now try to compare our system to similar ones in which ferromagnetic TAMR was measured. To do that and similarly to what has been done by Park [160] (T. Jumgwirth's group), we can define the TAMR signal as:

$$TAMR = \frac{R(\mu_0 H) - R(0)}{R(0)} \tag{5.4}$$

where $R(\mu_0 H)$ is the resistance as a function of the applied in plane field and $R(0)$ the minimum of the resistance, found for zero applied field when M is pointing OOP. We can then proceed to plot the TAMR signal as percentage for the three temperature measurements, see figure 5.21. From the graphs in figure 5.21 it is clear that the TAMR depends on temperature. The effect is around 10±2.5% at 5K to decrease at 7.5±2.5% at 10K and finally around 5±2.5% at 25K. This is visually shown in figure 5.22a, b and c respectively.

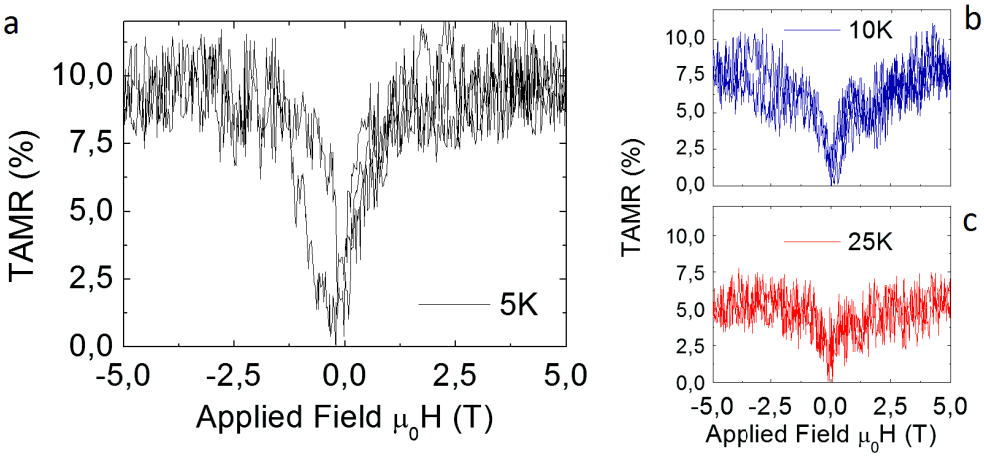

Fig. 5.21 TAMR signal calculated as $(R(\mu_0 H) - R(0))/R(0)$ measured at a. 5K, b. 10K and c. 25K

We can compare our results to what obtained by Park and coworkers, on a similar structure (see figure 5.22c) in which the magnetic layer is placed directly into contact with

an AlOx tunnel barrier. They have a [Co(1nm)/Pt(1nm)/Co(1nm)] trilayer while in our case we have a simple Co(1nm) layer. We obtained the same TAMR behavior, a lower resistance is measured when the magnetization is pointing along its easy direction (OOP in both cases), the resistance is higher when the magnetization is rotated by the external applied field.

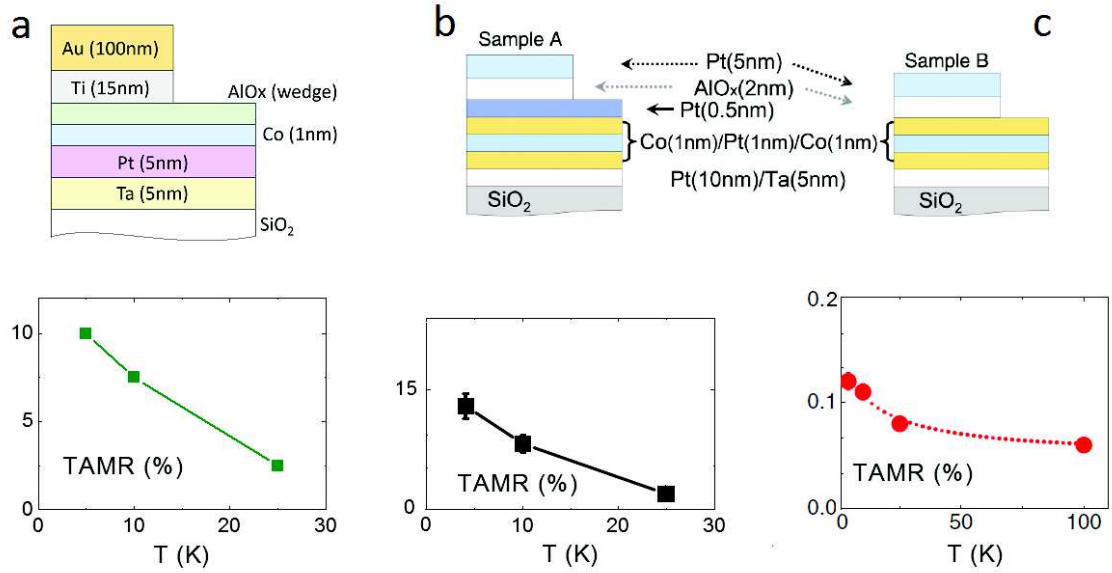

Fig. 5.22 In the upper panel the schematic layer structures is represented. On the lower panel the TAMR signal dependence with temperature is shown for a. our TAMR device, b. and c. similar systems studied by the group of Jungwirth [160].

When comparing the magnitude of both TAMR signals, we obtained an effect enhanced by two order of magnitude, we measured 10% TAMR change at 5K to compare to only 0.1% obtained in their case (figure 5.22c). This is similar to what was obtained by Park in a similar structure, where a Pt(0.5nm) layer was added between the AlOx tunnel barrier and the underneath [Co/Pt/Co] trilayer (figure 5.22b) [160].

The fast decrease of the TAMR effect with temperature (see figure 5.22a) is also similar to what was observed by Park in their sample with the Pt(0.5nm) insertion (figure 5.22b). A possible explanation for the higher TAMR effect observed in our system (compared to the similar structure, see figure 5.22c) is probably linked to the fact that in our sample most of the anisotropies contribution came from the interface Co/AlOx. The optimum Al oxidation creates an additional anisotropy effect at the interface with the tunnel barrier which is controlling the TAMR effect. On Park's sample B the tunnel barrier is placed into contact with a multilayer structure with relatively thick layers. In that configuration the anisotropies should mainly arise from the Co/Pt interfaces which are not placed directly into contact with the AlOx barrier globally reducing the TAMR effect. Indeed when a thin Pt(0.5nm) layer

was inserted between the tunnel barrier and the underneath multilayer the TAMR effect rose up to 15% (see figure 5.22b). The larger effect was attributed to the strong SO-coupling in the thin Pt layer.

5.3 Conclusions

We have investigated the TAMR effect in perpendicularly magnetized Pt/Co/AlOx tunnel devices with just one magnetic electrode. We applied a fixed bias voltage of 500mV and we measured the current response as a function of the applied field. The voltage was chosen to maximize the output current without exiting the linear response of the MTJs (as shown in figure 5.13a). The field was applied in the sample plane, its effect is to rotate the magnetization from the OOP easy axis to the IP position. The external magnetic field affects the MTJ resistance, which shows a minimum at 0T and increases for both positive and negative applied fields. We identify the switching fields where the magnetization definitely resides in plane as $\sim \pm 1$T. The TAMR signal decreases with increasing temperature, passing from 10% at 5K, to 7.5% at 10K and 5% at 25K, finally in the measurement at 50K we did not evidence any effect.

We have analyzed the possible artifacts of our system and we arrived at the conclusion that what we measured is indeed TAMR. This is supported by the large resistance change across the tunnel barrier with applied field ($\sim 50M\Omega$ at 5K) and by the absence of correlation between the measured signal and the possible temperature variations in our system (due to magnetoresistive effect on the temperature sensors).

During the work on MTJ devices we identified and solved various challenges. The bottleneck was the fabrication of tunnel junctions with good electrical and magnetic properties safeguarding the wedge geometry. The resistances of the working MTJs were, in general, very large and close to the limit of our working area. As a consequence the noise level ($\sim$25pA) was 2.5% of the total signal ($\sim$1nA), whereas the TAMR effect was 10% in our best sample. The large RA limited and prevented the systematic investigation of the TAMR effect in the wedge geometry.

With the cumulated experience we can provide some feedbacks for the nanofabrication of future devices. The main challenge is to lower the RA of the MTJs. We were limited to analyze rather thick Al_2O_3 barriers, which were necessary to avoid the electrical short circuit of the MTJs. One of the major issues was caused by the lithography developing chemistry, which was found to partly etch the Al_2O_3 layer damaging the tunnel barrier. One solution to overcome this problem could be to add a protective metallic layer on top of the tunnel barrier. This layer will prevent the contact of the underneath Al_2O_3 with the lithography

developer during the microfabrication steps. One further simple improvement to increase the measurement window for the MTJ could be to deposit a thicker bottom electrode, in order to lower the resistance of the contact pads' line.

A complete understanding of the TAMR is far from being achieved and further studies should be performed to fully grasp the mechanism governing this effect. Nevertheless, we measured an effect two order of magnitude larger than what was previously reported in similar systems. This could be achieved by a careful control of the oxidation at the interfaces. Indeed, the enhanced TAMR effect in our system is probably due to the large anisotropy contribution which comes directly from the Co/Al_2O_3 interface. We have developed a method where we can carefully control both the thicknesses and the oxidation level of FM/AFM/MOx layer, this system look very promising for future investigation of the TAMR effect.

General Conclusions

The initial objective of this thesis was the fabrication of Magnetic Tunnel Junctions with a single magnetic electrode, to systematically investigate the Tunneling Anisotropic Magneto Resistance effect in Pt/Co/AlOx wedged system. However, engineering these structures proved to be a real challenge. To obtain simultaneously good electrical and magnetic properties safeguarding the wedge structure and the integrity of the tunnel barrier revealed to be a no trivial matter. To achieve our goal there was a need to carefully investigate the Pt/Co/AlOx properties and to understand their interplay.

At the time of this project proposition, few works on TAMR in transition metal structures had been reported [159, 160], mostly from the group led by Tomáš Jungwirth. We decided to choose these reference works as starting point to further investigate the effect in a more systematical way. The idea was to apply at the TAMR devices the wedge structure, which was first developed at Spintec - CEA by Monso and coworkers [132].

The Pt/Co/AlOx trilayer was chosen to be the main structure of our study for its excellent magnetic properties. In particular, Co has good growth properties and very flat interfaces even for ultrathin films and as a matter of facts high quality interfaces are critical for the TAMR. The oxygen plasma, combined with the wedged deposition, allowed us to achieve a very good control on the oxidation level in our stack. The possibility to create an ultrathin Co layer placed directly in contact with a optimally oxidized Al_2O_3 tunnel barrier could be used to study the TAMR in structures with large surface anisotropy contribution. Furthermore, the strong anisotropy contribution originates directly at the (magnetic metal)/(tunnel barrier) interface, possibly enhancing the TAMR effect.

To accomplish our objectives we first studied and characterized the different properties of the Pt/Co/AlOx multilayer structures and their evolution as a function of the wedge. We could control and tune the magnetic properties in a continuous way by controlling the oxidation level of the top interface as a function of the deposited Al thickness. We realized the potentiality of this technique and we decided to partly overoxidized our multilayer to obtain Pt/Co/CoO/AlOx structures, where both thicknesses for the Co and CoO are in the subnanometer regime. Bulk CoO is a known antiferromagnet and has a relatively low

Néel temperature of 294K, which is very convenient for low temperature studies. On the other hand, we did not know if only a few monolayers of CoO could possibly impact the magnetic properties of our system. Several questions arose: are a few monolayers of CoO antiferromagnetic? Can they be exchange-coupled to the Co layer? What is the potential effect on the TAMR? And on the magnetic properties? The literature could not help us, because in reported works the oxide thickness are usually well above the nanometer. Thanks to the fundamental nature of this thesis we could address several of these questions and we could investigate how the ultrathin CoO affected our system. The results of this systematical study along the full wedge length, from underoxidized Pt/Co/Al/AlOx, to perfectly oxidized Pt/Co/AlOx and finally overoxidized Pt/Co/CoO/AlOx are summarized in the conclusion of Chapter 3, where we investigated the origin of the PMA in (heavy metal)/(magnetic metal)/(metal oxide) trilayer. The evolution of the anisotropies along the wedge as a function of the measurement temperatures revealed the importance of the antiferromagnetic CoO in the stack. It was found that not only few monolayer of CoO can be antiferromagnetic, but that the CoO adds a further in-plane contribution to the magnetic anisotropy. This new negative term sums up with the demagnetization energy, the results of the competition between these effects and the interface induced anisotropy is a tilt of the easy axis from the OOP to the IP direction. These results allowed us to obtain a good understanding of the magnetic properties of our stack and to address several effects of CoO on the system anisotropy. The idea was both to deepen the understanding on the PMA and to integrate this knowledge in the building of TAMR devices.

We decided to study and characterize the Co/CoO bilayer. By controlling the Co oxidation we created a Co(0.6nm)/CoO(0.6nm) bilayer in which both thicknesses, for the ferromagnetic and antiferromagnetic layers, are in the subnanometer regime. We performed field cooled measurements on such system, with both in-plane and out-of-plane applied external field, and we carefully analyzed the results. We found that few atomic planes of CoO were sufficient not only to strongly affect the magnetic properties of our stack at low temperature, but even to create an exchange bias anisotropy. The results on the exchange bias are summarized in the conclusions of Chapter 4. To our knowledge this is the first time that the exchange bias effect is reported in the sub-nanometer regime, which would be the ultimate limit for planar devices. These results help to rule out some of the exchange bias models based on the formation of domain walls inside the AFM layer and parallel to the AFM/FM interface, as such domain wall cannot exist in our ultrathin bilayer. The results also support the idea that CoO keeps a large anisotropy even in the ultrathin subnanometer regime. It is interesting to point out that the TAMR properties critically depend on the interface between the magnetic layer and the tunnel barrier. In our Co/CoO configuration, they would be governed by the

AFM layer, placed directly into contact with the Al_2O_3 barrier. The possibility to control the TAMR with the AFM CoO layer in exchange coupling with the underneath Co was one of the potentials of our system. To study the exchange bias with the TAMR effect could provide a new understanding of such controversial topic. Indeed, despite the active research, the microscopic origin of the exchange bias is still poorly understood. Various models to describe this phenomenon exist, nevertheless none is universally accepted. In our system, the TAMR response would be directly associated to the AFM magnetic moments possibly granting new insight on the AFM spins distribution and on the nature of the exchange coupling.

In parallel to these studies we proceed in the design of TAMR devices. At first we planned to engineer MTJs in which the electrical and magnetic properties could be measured at the same time. To achieve our goal we worked on the design of the device and on the micro and nanofabrication. We solved a series of challenges, testing every fabrication step, improving and implementing solutions to the various issues that we encountered. A major issue resided in the initial quality of the tunnel barrier. The Al_2O_3 barrier realized through the oxygen plasma oxidation had poor electrical properties. The number of microfabrication steps complicated the identification of this problem, which resulted critically important in building working TAMR devices. The barrier is the core of the devices because the tunnel probability governs the TAMR. The problem was identified by performing various tests on unpatterned (as-deposited) samples, where the electrical contacts were taken with a simple drop of epoxy glue placed directly on top of the Al_2O_3 layer. The obtained results indicated a large number of electrical short circuited electrodes (90%). Due to the barrier fragility, the number of working devices was reduced to zero after the full lithography process.

Another issue comes from the developer (used in the microfabrication as developing chemical agent for the photoresist), which was found to slightly etch the Al_2O_3 layer, greatly compromising the integrity of the barrier. These challenges were only partly solved by switching to samples fabricated at Spintec - CEA and by simplifying the device geometry, reducing the number of lithography steps. The reduction of the structure complexity comes at the expenses of the possibility to simultaneously measure both electrical and magnetic properties. Even with this simpler configuration we were limited to study regions with a relatively thick Alumina barrier. Thinner regions all resulted in short circuited electrodes, where we could not evidence any tunneling behavior and the resistances were indistinguishable from the bottom electrode ones ($< 500\Omega$). As a consequence the resistance areas of the working MTJs were particularly large, closer to the limit of our working windows. Due to these problems not only we could not perform the systematic study that was initially planned, but we had to strive to measure a suitable TAMR signal. The large RA had an impact on the noise level, which represented roughly 2.5% of the total signal, whereas the TAMR effect

in our best sample was ∼10% at 5K, rapidly decreasing with increasing temperature. The 10% effect is the best value ever observed in such systems, two orders of magnitude larger than what was previously reported. The large effect could be achieved by a careful control of the oxidation level at the interfaces. Indeed, the enhanced TAMR in our system is probably due to the large anisotropy contribution which comes directly from the perfectly oxidized Co/Al_2O_3 interface, which governs the effect. The results on the TAMR are summarized in the conclusions of Chapter 5. In the same section, thanks to the cumulated experience, we also provided some solutions for the micro and nanofabrication of future devices. One of the proposed improvement is to protect the Al_2O_3 tunnel barrier from the developer by adding a thin metallic capping layer.

This manuscript shed new light on the role of ultrathin CoO layer in asymmetric structures and on the interplay of magnetism and interface's anisotropies. In order to obtain new insight we utilized a method to tune the properties in a continuous and controlled way while pushing one dimension to the lowest limit. More specifically, we carefully explored the magnetic properties of the Pt/Co/AlOx system. The Pt/Co/AlOx is one of the model systems to study topics such as Rashba splitting, spin Hall effect, spin transfer torque and Dzyaloshinskii-Moriya interaction. The surface asymmetry is crucial for these effects. The possible presence of a CoO layer, which brings a further asymmetric contribution, was overlook in previous studies. With this thesis work we proved that few monolayers of CoO greatly modify the energy balance of the system and that can partially reorient the magnetization easy axis and even induce an exchange bias anisotropy at low temperature. These energies have the same order of magnitude as the interfaces anisotropies and the Dzyaloshinskii-Moriya interaction, all of them are in the mJ/m^2 range. Therefore, the CoO presence must be considered in the energy balance of the system. Even if CoO loses its magnetic property at 300K, it is still in its Co^{2+} hybridized form, which has a large spin-orbit coupling. The large SOC can play an important role on the magnetic configuration of the stack.

On the other hand, the work on the TAMR is far from being finished. The physics governing this effect is rather complex and similar systems can show very diverse TAMR responses depending on their structure, applied magnetic field, bias voltage and measuring temperature. With the experience gathered in the past three years, we proposed simple improvements to avoid some of major issues encountered during this thesis work (i.e. adding a protective capping layer). The effort on understanding the TAMR actively continues. The incorporation of antiferromagnetic material as active part to control the device response was achieved during the past years by Park and coworkers [159] at low temperature and measured for the first time at room temperature by Wang et al. [228]. The interest on the TAMR then moved towards pure antiferromagnetic spintronics devices. One very interesting material

is FeRh, which goes through a FM to AFM transition as a function of the temperature. A room temperature antiferromagnetic memory transistor, based on this material, was realized by Marti and coworkers in 2014 [115]. The road towards antiferromagnetic spintronics was opened by the TAMR and hold the promises to be a very interesting playground for spintronics research in the future. To conclude, the method developed in this thesis allowed to precisely control both the thicknesses and the oxidation level of FM/AFM/MOx ultrathin layers and the fine tuning of the magnetic interfaces. This method offers an elegant way of studying the properties of multilayer and can be adopted to design many different and relevant systems in the future.

References

[1] Akdogan, N., Yagmur, A., Ozturk, M., Demirci, E., Ozturk, O., and Erkovan, M. (2015). Interface induced manipulation of perpendicular exchange bias in Pt/Co/(Pt,Cr)/CoO thin films. *Journal of Magnetism and Magnetic Materials*, 373:120 – 123.

[2] Akiho, T., Uemura, T., Harada, M., Matsuda, K.-i., and Yamamoto, M. (2011). Suppression of in-plane tunneling anisotropic magnetoresistance effect in Co2MnSi/MgO/n-GaAs and CoFe/MgO/n-GaAs junctions by inserting a MgO barrier. *Applied Physics Letters*, 98(23).

[3] Aleskovskii, V. B. and Koltsov, S. I. (1974). Molecular Layering (ML). *J. Appl. Chem. USSR.*, 47:2207.

[4] Ali, M., Marrows, C. H., and Hickey, B. J. (2003). Onset of exchange bias in ultrathin antiferromagnetic layers. *Phys. Rev. B*, 67:172405.

[5] Ambegaokar, V., Halperin, B. I., and Langer, J. S. (1971). Hopping Conductivity in Disordered Systems. *Phys. Rev. B*, 4:2612–2620.

[6] Ambrose, T. and Chien, C. L. (1996). Finite-Size Effects and Uncompensated Magnetization in Thin Antiferromagnetic CoO Layers. *Phys. Rev. Lett.*, 76:1743–1746.

[7] Annaorazov, M., Asatryan, K., Myalikgulyev, G., Nikitin, S., Tishin, A., and Tyurin, A. (1992). Alloys of the Fe-Rh system as a new class of working material for magnetic refrigerators. *Cryogenics*, 32(10):867–872.

[8] Arden, W., Brillouët, M., Cogez, P., Graef, M., Huizing, B., and Mahnkopf, R. (2010). Morethan-Moore white paper. *Version*, 2:14.

[9] Bae, J. S., Shin, K. H., and Lee, H. M. (2002a). Microstructural observation on effect of oxidation method of AlOx in magnetic tunnel junction by high resolution transmission electron microscopy. *Journal of Applied Physics*, 91(10):7947–7949.

[10] Bae, J. S., Shin, K. H., Lee, T. D., and Lee, H. M. (2002b). Study of the effect of natural oxidation and thermal annealing on microstructures of AlOx in the magnetic tunnel junction by high-resolution transmission electron microscopy. *Applied Physics Letters*, 80(7):1168–1170.

[11] Baibich, M. N., Broto, J. M., Fert, A., Van Dau, F. N., Petroff, F., Etienne, P., Creuzet, G., Friederich, A., and Chazelas, J. (1988). Giant Magnetoresistance of (001)Fe/(001)Cr Magnetic Superlattices. *Phys. Rev. Lett.*, 61:2472–2475.

[12] Barthelemy, A., Fert, A., Etienne, P., Cabanel, R., and Lequien, S. (1992). Temperature dependence of the interface anisotropy in Fe(001)/Ag(001) superlattices. *Journal of Magnetism and Magnetic Materials*, 104:1816 – 1818.

[13] Bayreuther, G., den Broeder, F., Carcia, P., Li, Z., and Zeper, W. (1993). Proceedings of the International Symposium on Magnetic Ultrathin Films, Multilayers and Surfaces Effect of sputter-deposition processes on the microstructure and magnetic properties of Pt/Co multilayers. *Journal of Magnetism and Magnetic Materials*, 121(1):452 – 460.

[14] Belmeguenai, M., Adam, J.-P., Roussigne, Y., Eimer, S., Devolder, T., Kim, J.-V., Cherif, S. M., Stashkevich, A., and Thiaville, A. (2015). Interfacial Dzyaloshinskii-Moriya interaction in perpendicularly magnetized Pt/Co/AlO ultrathin films measured by Brillouin light spectroscopy. *Phys. Rev. B*, 91:180405.

[15] Berger, L. (1970). Side-Jump Mechanism for the Hall Effect of Ferromagnets. *Phys. Rev. B*, 2:4559–4566.

[16] Berkowitz, A. and Takano, K. (1999). Exchange anisotropy - a review. *Journal of Magnetism and Magnetic Materials*, 200(1-3):552–570.

[17] Bernand-Mantel, A., Herrera-Diez, L., Ranno, L., Pizzini, S., Vogel, J., Givord, D., Auffret, S., Boulle, O., Miron, I. M., and Gaudin, G. (2013). Electric-field control of domain wall nucleation and pinning in a metallic ferromagnet. *Applied Physics Letters*, 102(12).

[18] Bernand-Mantel, A., Seneor, P., Bouzehouane, K., Fusil, S., Deranlot, C., Petroff, F., and Fert, A. (2009). Anisotropic magneto-Coulomb effects and magnetic single-electron-transistor action in a single nanoparticle. *Nature Physics*, 5(12):920–924.

[19] Binasch, G., Grünberg, P., Saurenbach, F., and Zinn, W. (1989). Enhanced magnetoresistance in layered magnetic structures with antiferromagnetic interlayer exchange. *Phys. Rev. B*, 39:4828–4830.

[20] Binek, C., He, X., and Polisetty, S. (2005). Temperature dependence of the training effect in a Co/CoO exchange-bias layer. *Phys. Rev. B*, 72:054408.

[21] Bode, M., Pascal, R., Dreyer, M., and Wiesendanger, R. (1996). Nanostructural and local electronic properties of Fe/W (110) correlated by scanning tunneling spectroscopy. *Physical Review B*, 54(12):R8385.

[22] Brey, L., Tejedor, C., and Fernandez-Outon, L Endez-Rossier, J. (2004). Tunnel magnetoresistance in GaMnAs: Going beyond Julliere formula. *Applied Physics Letters*, 85(11):1996–1998.

[23] Brinkman, W. F., Dynes, R. C., and Rowell, J. M. (1970). Tunneling Conductance of Asymmetrical Barriers. *Journal of Applied Physics*, 41(5):1915–1921.

[24] Brown, W. F. (1963). *Micromagnetics*. Number 18. Interscience Publishers.

[25] BRUKER (2015). DIFFRAC plus LEPTOS - The Comprehensive Nanometer X-ray Analysis Tool. *BRUKER*.

[26] Bruno, P. (1989). Tight-binding approach to the orbital magnetic moment and magnetocrystalline anisotropy of transition-metal monolayers. *Phys. Rev. B*, 39:865–868.

[27] Bruno, P. and Chappert, C. (1991). Oscillatory coupling between ferromagnetic layers separated by a nonmagnetic metal spacer. *Physical Review Letters*, 67(12):1602.

[28] Buschow, K. H. J. (2003). *Handbook of magnetic materials*, volume 15. Elsevier.

[29] Butler, W., Zhang, X.-G., Schulthess, T., Nicholson, D., Oparin, A., and MacLaren, J. (1999). First principles modeling of magnetic random access memory devices. *Journal of applied physics*, 85(8):5834–5839.

[30] Butler, W. H., Zhang, X.-G., Schulthess, T. C., and MacLaren, J. M. (2001). Spin-dependent tunneling conductance of Fe/MgO/Fe sandwiches. *Phys. Rev. B*, 63:054416.

[31] Carcia, P. F. (1988). Perpendicular magnetic anisotropy in Pd/Co and Pt/Co thin film layered structures. *Journal of Applied Physics*, 63(10):5066–5073.

[32] Carcia, P. F., Meinhaldt, A. D., and Suna, A. (1985). Perpendicular magnetic anisotropy in Pd/Co thin film layered structures. *Applied Physics Letters*, 47(2):178–180.

[33] Chantis, A. N., Belashchenko, K. D., Tsymbal, E. Y., and van Schilfgaarde, M. (2007). Tunneling Anisotropic Magnetoresistance Driven by Resonant Surface States: First-Principles Calculations on an Fe(001) Surface. *Phys. Rev. Lett.*, 98:046601.

[34] Chappert, C., Fert, A., and Van Dau, F. N. (2007). The emergence of spin electronics in data storage. *Nature materials*, 6(11):813–823.

[35] Chaudhury, A., Gragnaniello, L., Ma, T., Surnev, S., and Netzer, F. (2013). Alumina-Supported Array of Co Nanoparticles: Size-Dependent Oxidation Kinetics. *The Journal of Physical Chemistry C*, 117(35):18112–18119.

[36] Chiba, D., Kawaguchi, M., Fukami, S., Ishiwata, N., Shimamura, K., Kobayashi, K., and Ono, T. (2012). Electric-field control of magnetic domain-wall velocity in ultrathin cobalt with perpendicular magnetization. *Nature Communications*, 3:888.

[37] Daalderop, G. H. O., Kelly, P. J., and Schuurmans, M. F. H. (1990). First-principles calculation of the magnetocrystalline anisotropy energy of iron, cobalt, and nickel. *Phys. Rev. B*, 41:11919–11937.

[38] Dahlberg, E. D., Riggs, K., and Prinz, G. A. (1988). Magnetotransport: An ideal probe of anisotropy energies in epitaxial films (invited). *Journal of Applied Physics*, 63(8):4270–4275.

[39] den Broeder, F., Hoving, W., and Bloemen, P. (1991). Magnetic anisotropy of multilayers. *Journal of Magnetism and Magnetic Materials*, 93:562 – 570.

[40] den Broeder, F. J. A., Kuiper, D., van de Mosselaer, A. P., and Hoving, W. (1988). Perpendicular Magnetic Anisotropy of Co-Au Multilayers Induced by Interface Sharpening. *Phys. Rev. Lett.*, 60:2769–2772.

[41] Dieny, B., Speriosu, V. S., Metin, S., Parkin, S. S., Gurney, B. A., Baumgart, P., and Wilhoit, D. R. (1991a). Magnetotransport properties of magnetically soft spin-valve structures. *Journal of Applied Physics*, 69(8):4774–4779.

[42] Dieny, B., Speriosu, V. S., Parkin, S. S. P., Gurney, B. A., Wilhoit, D. R., and Mauri, D. (1991b). Giant magnetoresistive in soft ferromagnetic multilayers. *Phys. Rev. B*, 43:1297–1300.

[43] Dobrynin, A. N. and Givord, D. (2012). Exchange bias in a Co/CoO/Co trilayer with two different ferromagnetic-antiferromagnetic interfaces. *Phys. Rev. B*, 85:014413.

[44] Dzyaloshinsky, I. (1958). A thermodynamic theory of weak ferromagnetism of antiferromagnetics. *Journal of Physics and Chemistry of Solids*, 4(4):241–255.

[45] Egelhoff, W. F., Chen, P. J., Powell, C. J., Stiles, M. D., McMichael, R. D., Lin, C., Sivertsen, J. M., Judy, J. H., Takano, K., Berkowitz, A. E., Anthony, T. C., and Brug, J. A. (1996). Optimizing the giant magnetoresistance of symmetric and bottom spin valves (invited). *Journal of Applied Physics*, 79(8):5277–5281.

[46] Fert, A. (2008a). Nobel Lecture: Origin, development, and future of spintronics. *Rev. Mod. Phys.*, 80:1517–1530.

[47] Fert, A. (2008b). The present and the future of spintronics. *Thin Solid Films*, 517(1):2–5.

[48] Fert, A. and Campbell, I. A. (1968). Two-Current Conduction in Nickel. *Phys. Rev. Lett.*, 21:1190–1192.

[49] Fettar, F., Garad, H., Ortega, L., Ramos, A., Zawilski, B., Plaindoux, P., Auffret, S., Rodmacq, B., and Dieny, B. (2009). Investigation of Metallic/Oxide Interfaces in Pt/Co/AlOx Trilayers by Hard X-Ray Reflectivity. *Magnetics, IEEE Transactions on*, 45(10):3905–3908.

[50] Feynman, R. P. (1967). *The character of physical law*, volume 66. MIT press.

[51] Friedrich, B. and Herschbach, D. (2003). Stern and Gerlach: How a bad cigar helped reorient atomic physics. *Physics Today*, 56(12):53–59.

[52] Fulcomer, E. and Charap, S. H. (1972). Thermal fluctuation aftereffect model for some systems with ferromagnetic/antiferromagnetic coupling. *Journal of Applied Physics*, 43(10):4190–4199.

[53] Gan, L., Gomez, R. D., Powell, C. J., McMichael, R. D., Chen, P. J., and Egelhoff, W. F. (2003). Thin Al, Au, Cu, Ni, Fe, and Ta films as oxidation barriers for Co in air. *Journal of Applied Physics*, 93(10):8731–8733.

[54] Gao, L., Jiang, X., Yang, S.-H., Burton, J. D., Tsymbal, E. Y., and Parkin, S. S. P. (2007). Bias Voltage Dependence of Tunneling Anisotropic Magnetoresistance in Magnetic Tunnel Junctions with MgO and Al_2O_3 Tunnel Barriers. *Phys. Rev. Lett.*, 99:226602.

[55] Garad, H., Ortega, L., Ramos, A. Y., Joly, Y., Fettar, F., Auffret, S., Rodmacq, B., Dieny, B., Proux, O., and Erko, A. I. (2013). Competition between CoOx and CoPt phases in Pt/Co/AlOx semi tunnel junctions. *Journal of Applied Physics*, 114(5).

[56] Garad, H., Ortega, L., Ramos, A. Y., Marcus, J., Gay, F., Fettar, F., Auffret, S., Rodmacq, B., and Dieny, B. (2011). The contribution of X-ray specular reflectometry to the oxygen-induced magnetic properties in Pt/Co/AlOx. *Journal of Applied Physics*, 109(7).

[57] Garcia, F., Moritz, J., Ernult, F., Auffret, S., Rodmacq, B., Dieny, B., Carnarero, J., Pennec, Y., Pizzini, S., and Vogel, J. (2002). Exchange bias with perpendicular anisotropy in $(Pt\text{-}Co)_n$-FeMn multilayers. *Magnetics, IEEE Transactions on*, 38(5):2730–2735.

[58] Gay, J. G. and Richter, R. (1986). Spin Anisotropy of Ferromagnetic Films. *Phys. Rev. Lett.*, 56:2728–2731.

[59] Gerlach, W. and Stern, O. (1922). Das magnetische moment des silberatoms. *Zeitschrift für Physik A Hadrons and Nuclei*, 9(1):353–355.

[60] Gierlings, M., Prandolini, M. J., Fritzsche, H., Gruyters, M., and Riegel, D. (2002). Change and asymmetry of magnetization reversal for a Co/CoO exchange-bias system. *Phys. Rev. B*, 65:092407.

[61] Gil, W., Görlitz, D., Horisberger, M., and Kötzler, J. (2005). Magnetoresistance anisotropy of polycrystalline cobalt films: Geometrical-size and domain effects. *Phys. Rev. B*, 72:134401.

[62] Givord, D., Rossignol, M., and Barthem, V. M. (2003). The physics of coercivity. *Journal of magnetism and magnetic materials*, 258:1–5.

[63] Gould, C., Rüster, C., Jungwirth, T., Girgis, E., Schott, G. M., Giraud, R., Brunner, K., Schmidt, G., and Molenkamp, L. W. (2004). Tunneling Anisotropic Magnetoresistance: A Spin-Valve-Like Tunnel Magnetoresistance Using a Single Magnetic Layer. *Phys. Rev. Lett.*, 93:117203.

[64] Gradmann, U. and Muller, J. (1968). Flat Ferromagnetic, Epitaxial 48Ni/52Fe(111) Films of few Atomic Layers. *physica status solidi (b)*, 27(1):313–324.

[65] Gredig, T., Krivorotov, I. N., Eames, P., and Dahlberg, E. D. (2002). Unidirectional coercivity enhancement in exchange-biased Co/CoO. *Applied Physics Letters*, 81(7):1270–1272.

[66] Grimsditch, M., Hoffmann, A., Vavassori, P., Shi, H., and Lederman, D. (2003). Exchange-Induced Anisotropies at Ferromagnetic-Antiferromagnetic Interfaces above and below the Néel Temperature. *Phys. Rev. Lett.*, 90:257201.

[67] Grollier, J., Cros, V., Hamzic, A., George, J. M., Jaffres, H., Fert, A., Faini, G., Ben Youssef, J., and Legall, H. (2001). Spin-polarized current induced switching in Co/Cu/Co pillars. *Applied Physics Letters*, 78(23):3663–3665.

[68] Gruyters, M. and Riegel, D. (2000). Optimized exchange biasing by controlled in situ oxidation. *Journal of Applied Physics*, 88(11):6610–6613.

[69] Hagedorn, F. B. (1967). Exchange Anisotropy in Oxidized Permalloy Thin Films at Low Temperatures. *Journal of Applied Physics*, 38(9):3641–3645.

[70] http://www.itrs.net/ (2015). The International Technology Roadmap for Semiconductors. *ITRS*.

[71] http://www.webelements.com/ (2015).

[72] Ijiri, Y., Borchers, J. A., Erwin, R. W., Lee, S.-H., van der Zaag, P. J., and Wolf, R. M. (1998). Perpendicular Coupling in Exchange-Biased F_3O_4/CoO Superlattices. *Phys. Rev. Lett.*, 80:608–611.

[73] Ikeda, S., Hayakawa, J., Ashizawa, Y., Lee, Y. M., Miura, K., Hasegawa, H., Tsunoda, M., Matsukura, F., and Ohno, H. (2008). Tunnel magnetoresistance of 604% at 300K by suppression of Ta diffusion in CoFeB/MgO/CoFeB pseudo-spin-valves annealed at high temperature. *Applied Physics Letters*, 93(8).

[74] Imbrie, J. Z. (1984). Lower critical dimension of the random-field Ising model. *Physical review letters*, 53(18):1747.

[75] Jauch, W., Reehuis, M., Bleif, H. J., Kubanek, F., and Pattison, P. (2001). Crystallographic symmetry and magnetic structure of CoO. *Phys. Rev. B*, 64:052102.

[76] Jin, J. S. and Lee, J. S. (2007). Electron-Phonon Interaction Model and Prediction of Thermal Energy Transport in SOI Transistor. *Journal of Nanoscience and Nanotechnology*, 7(11):4094–4100.

[77] Johnson, M. T., Bloemen, P. J. H., den Broeder, F. J. A., and de Vries, J. J. (1996). Magnetic anisotropy in metallic multilayers. *Reports on Progress in Physics*, 59(11):1409.

[78] Julliere, M. (1975). Tunneling between ferromagnetic films. *Physics Letters A*, 54(3):225 – 226.

[79] Kanamori, J. (1957). Theory of the Magnetic Properties of Ferrous and Cobaltous Oxides, II. *Progress of Theoretical Physics*, 17(2):197–222.

[80] Kang, H. and Beauchamp, J. L. (1985). Pulsed laser evaporation and ionization of solid metal targets. Implications for studying the gas-phase reactions of laser-generated atoms and ions. *The Journal of Physical Chemistry*, 89(15):3364–3367.

[81] Katine, J. A., Albert, F. J., Buhrman, R. A., Myers, E. B., and Ralph, D. C. (2000). Current-Driven Magnetization Reversal and Spin-Wave Excitations in Co/Cu/Co Pillars. *Phys. Rev. Lett.*, 84:3149–3152.

[82] Khan, M. N., Henk, J., and Bruno, P. (2008). Anisotropic magnetoresistance in Fe/MgO/Fe tunnel junctions. *Journal of Physics: Condensed Matter*, 20(15):155208.

[83] Kiessig, H. (1931a). Interference of X-rays in thick layers. *Annalen der Physik*, 10:769 788.

[84] Kiessig, H. (1931b). Investigations into the total reflexion of Roetgen rays. *Annalen der Physik*, 10:715 768.

[85] Kim, J.-G. and Ha, J.-G. (2006). Particle size distribution and GMR in Co/AlO granular thin films by annealing. *Materials Chemistry and Physics*, 96(2-3):307 – 310.

[86] Kimel, A., Kirilyuk, A., Tsvetkov, A., Pisarev, R., and Rasing, T. (2004). Laser-induced ultrafast spin reorientation in the antiferromagnet $TmFeO_3$. *Nature*, 429(6994):850–853.

[87] Kimel, A., Kirilyuk, A., Usachev, P., Pisarev, R., Balbashov, A., and Rasing, T. (2005). Ultrafast non-thermal control of magnetization by instantaneous photomagnetic pulses. *Nature*, 435(7042):655–657.

[88] Kishimoto, S., Hashiguchi, T., Ohshio, S., and Saitoh, H. (2008). Density Investigation by X-ray Reflectivity for Thin Films Synthesized Using Atmospheric CVD. *Chemical Vapor Deposition*, 14(9-10):303–308.

[89] Kiwi, M. (2001). Topical review: Exchange bias theory. *Journal of Magnetism and Magnetic Materials*, 234:584 – 595.

[90] Kiwi, M., Mejía-López, J., Portugal, R., and Ramirez, R. (1999a). Exchange bias model for Fe/FeF2: Role of domains in the ferromagnet. *EPL (Europhysics Letters)*, 48(5):573.

[91] Kiwi, M., Mejia-Lopez, J., Portugal, R. D., and Ramirez, R. (1999b). Exchange-bias systems with compensated interfaces. *Applied Physics Letters*, 75(25):3995–3997.

[92] Koon, N. C. (1997). Calculations of Exchange Bias in Thin Films with Ferromagnetic/Antiferromagnetic Interfaces. *Phys. Rev. Lett.*, 78:4865–4868.

[93] Kosub, T., Makarov, D., Schletter, H., Hietschold, M., and Albrecht, M. (2011). Interplay between the antiferromagnetic spin configuration and the exchange bias effect in $[Pt/Co]_8/CoO/Co_3Pt$ trilayers. *Phys. Rev. B*, 84:214440.

[94] Kowalewski, M., Schneider, C. M., and Heinrich, B. (1993). Thickness and temperature dependence of magnetic anisotropies in ultrathin fcc Co(001) structures. *Phys. Rev. B*, 47:8748–8753.

[95] Kubota, H., Fukushima, A., Yakushiji, K., Nagahama, T., Yuasa, S., Ando, K., Maehara, H., Nagamine, Y., Tsunekawa, K., Djayaprawira, D. D., et al. (2008). Quantitative measurement of voltage dependence of spin-transfer torque in MgO-based magnetic tunnel junctions. *Nature Physics*, 4(1):37–41.

[96] Lacour, D., Hehn, M., Alnot, M., Montaigne, F., Greullet, F., Lengaigne, G., Lenoble, O., Robert, S., and Schuhl, A. (2007). Magnetic properties of postoxidized Pt/Co/Al layers with perpendicular anisotropy. *Applied Physics Letters*, 90(19):192506.

[97] Lamirand, A. D. (2014). *Epitaxial growth, atomic structure and exchange coupling of ultrathin bilayers of oxides on metals*. PhD thesis, Grenoble University - Physique de la matière condensée et du rayonnement.

[98] Lamirand, A. D., Soares, M. M., Ramos, A. Y., Tolentino, H. C. N., De Santis, M., Cezar, J. C., de Siervo, A., and Jamet, M. (2013). Robust perpendicular exchange coupling in an ultrathin CoO/PtFe double layer: Strain and spin orientation. *Phys. Rev. B*, 88:140401.

[99] Lee, B. W., Alsenz, R., Ignatiev, A., and Van Hove, M. A. (1978). Surface structures of the two allotropic phases of cobalt. *Phys. Rev. B*, 17:1510–1520.

[100] Leighton, C., Nogués, J., Jönsson-Åkerman, B. J., and Schuller, I. K. (2000). Coercivity Enhancement in Exchange Biased Systems Driven by Interfacial Magnetic Frustration. *Phys. Rev. Lett.*, 84:3466–3469.

[101] Leighton, C., Suhl, H., Pechan, M. J., Compton, R., Nogués, J., and Schuller, I. K. (2002). Coercivity enhancement above the Néel temperature of an antiferromagnet/ferromagnet bilayer. *Journal of Applied Physics*, 92(3):1483–1488.

[102] Lenz, K., Zander, S., and Kuch, W. (2007). Magnetic Proximity Effects in Antiferromagnet/Ferromagnet Bilayers: The Impact on the Néel Temperature. *Phys. Rev. Lett.*, 98:237201.

[103] Li, P., Guo, B., and Bai, H. (2011). Large anisotropic magnetoresistance across the Schottky interface in all oxide ferromagnet/semiconductor heterostructures. *EPL (Europhysics Letters)*, 94(5):57007.

[104] Lide, D. R. (2004). *CRC handbook of chemistry and physics*. CRC press.

[105] Liu, L., Lee, O. J., Gudmundsen, T. J., Ralph, D. C., and Buhrman, R. A. (2012). Current-Induced Switching of Perpendicularly Magnetized Magnetic Layers Using Spin Torque from the Spin Hall Effect. *Phys. Rev. Lett.*, 109:096602.

[106] Liu, R. S., Michalak, L., Canali, C. M., Samuelson, L., and Pettersson, H. (2008). Tunneling Anisotropic Magnetoresistance in Co/AlOx/Au Tunnel Junctions. *Nano Letters*, 8(3):848–852. PMID: 18254603.

[107] Lu, J. and Lee, C. G. (2012). Numerical estimates for energy of sputtered target atoms and reflected Ar neutrals in sputter processes. *Vacuum*, 86(8):1134 – 1140.

[108] Lu, Y., Li, X., Xiao, G., Altman, R., Gallagher, W., Marley, A., Roche, K., and Parkin, S. (1998). Bias voltage and temperature dependence of magnetotunneling effect. *Journal of applied physics*, 83(11):6515–6517.

[109] Maat, S., Takano, K., Parkin, S. S. P., and Fullerton, E. E. (2001). Perpendicular Exchange Bias of Co/Pt Multilayers. *Phys. Rev. Lett.*, 87:087202.

[110] MacDonald, A., Schiffer, P., and Samarth, N. (2005). Ferromagnetic semiconductors: moving beyond (Ga, Mn) As. *Nature Materials*, 4(3):195–202.

[111] Malozemoff, A. (1987). Random-field model of exchange anisotropy at rough ferromagnetic-antiferromagnetic interfaces. *Physical review B*, 35(7):3679.

[112] Manchon, A., Ducruet, C., Lombard, L., Auffret, S., Rodmacq, B., Dieny, B., Pizzini, S., Vogel, J., Uhlivr, V., Hochstrasser, M., and Panaccione, G. (2008a). Analysis of oxygen induced anisotropy crossover in Pt/Co/MOx trilayers. *Journal of Applied Physics*, 104(4):043914.

[113] Manchon, A., Pizzini, S., Vogel, J., Uhli, V., Lombard, L., Ducruet, C., Auffret, S., Rodmacq, B., Dieny, B., Hochstrasser, M., and Panaccione, G. (2008b). X-ray analysis of oxygen-induced perpendicular magnetic anisotropy in trilayers. *Journal of Magnetism and Magnetic Materials*, 320(13):1889 – 1892.

[114] Mangin, S., Ravelosona, D., Katine, J. A., Carey, M. J., Terris, B. D., and Fullerton, E. E. (2006). Current-induced magnetization reversal in nanopillars with perpendicular anisotropy. *Nat Mater*, 5(3):210–215.

[115] Marti, X., Fina, I., Frontera, C., Liu, J., Wadley, P., He, Q., Paull, R., Clarkson, J., Kudrnovskỳ, J., Turek, I., et al. (2014). Room-temperature antiferromagnetic memory resistor. *Nature materials*, 13(4):367–374.

[116] Marti, X., Park, B. G., Wunderlich, J., Reichlova, H., Kurosaki, Y., Yamada, M., Yamamoto, H., Nishide, A., Hayakawa, J., Takahashi, H., and Jungwirth, T. (2012). Electrical Measurement of Antiferromagnetic Moments in Exchange-Coupled IrMn/NiFe Stacks. *Phys. Rev. Lett.*, 108:017201.

[117] Martinez Boubeta, C., Clavero, C., Garcia-Martin, J. M., Armelles, G., Cebollada, A., Balcells, L., Menendez, J. L., Peiro, F., Cornet, A., and Toney, M. F. (2005). Coverage effects on the magnetism of Fe/MgO(001) ultrathin films. *Phys. Rev. B*, 71:014407.

[118] Mathet, V., Devolder, T., Chappert, C., Ferre, J., Lemerle, S., Belliard, L., and Guentherodt, G. (2003). Morphology and magnetic properties of Pt/Co/Pt sandwiches grown by argon sputter deposition. *Journal of Magnetism and Magnetic Materials*, 260(1-2):295 – 304.

[119] Mathon, J. and Umerski, A. (2001). Theory of tunneling magnetoresistance of an epitaxial Fe/MgO/Fe(001) junction. *Phys. Rev. B*, 63:220403.

[120] Matos-Abiague, A. and Fabian, J. (2009). Anisotropic tunneling magnetoresistance and tunneling anisotropic magnetoresistance: Spin-orbit coupling in magnetic tunnel junctions. *Phys. Rev. B*, 79:155303.

[121] Mauri, D., Siegmann, H. C., Bagus, P. S., and Kay, E. (1987). Simple model for thin ferromagnetic films exchange coupled to an antiferromagnetic substrate. *Journal of Applied Physics*, 62(7):3047–3049.

[122] McElfresh, M. (1994). *Foundamentals of magnetism and magnetic measurement*. Purdue University.

[123] McGuire, T. and Potter, R. (1975). Anisotropic magnetoresistance in ferromagnetic 3d alloys. *Magnetics, IEEE Transactions on*, 11(4):1018–1038.

[124] Meiklejohn, W. H. (1962). Exchange Anisotropy-A Review. *Journal of Applied Physics*, 33(3):1328–1335.

[125] Meiklejohn, W. H. and Bean, C. P. (1957). New Magnetic Anisotropy. *Phys. Rev.*, 105:904–913.

[126] Miller, B. H. and Dahlberg, E. D. (1996). Use of the anisotropic magnetoresistance to measure exchange anisotropy in Co/CoO bilayers. *Applied Physics Letters*, 69(25):3932–3934.

[127] Miltenyi, P., Gierlings, M., Keller, J., Beschoten, B., Guntherodt, G., Nowak, U., and Usadel, K. D. (2000). Diluted Antiferromagnets in Exchange Bias: Proof of the Domain State Model. *Phys. Rev. Lett.*, 84:4224–4227.

[128] Miron, I., Gaudin, G., Auffret, S., Rodmacq, B., Schuhl, A., Pizzini, S., Vogel, J., and Gambardella, P. (2010). Current-driven spin torque induced by the Rashba effect in a ferromagnetic metal layer. *Nature Materials*, 9:230–234.

[129] Miron, I., Moore, T., Szambolics, H., Buda-Prejbeanu, L., Auffret, S., Rodmacq, B., Pizzini, S., Vogel, J., Bonfim, M., Schuhl, A., and Gaudin, G. (2011). Fast current-induced domain-wall motion controlled by the Rashba effect. *Nature Materials*, 10:419–423.

[130] Miyazaki, T. and Tezuka, N. (1995). Giant magnetic tunneling effect in Fe/Al_2O_3/Fe junction. *Journal of Magnetism and Magnetic Materials*, 139(3):L231–L234.

[131] Molina-Ruiz, M., Lopeandía, A. F., Pi, F., Givord, D., Bourgeois, O., and Rodríguez-Viejo, J. (2011). Evidence of finite-size effect on the Néel temperature in ultrathin layers of CoO nanograins. *Phys. Rev. B*, 83:140407.

[132] Monso, S., Rodmacq, B., Auffret, S., Casali, G., Fettar, F., Gilles, B., Dieny, B., and Boyer, P. (2002). Crossover from in-plane to perpendicular anisotropy in Pt/CoFe/AlOx sandwiches as a function of Al oxidation: A very accurate control of the oxidation of tunnel barriers. *Applied Physics Letters*, 80(22):4157–4159.

[133] Moodera, J. S., Kinder, L. R., Wong, T. M., and Meservey, R. (1995). Large Magnetoresistance at Room Temperature in Ferromagnetic Thin Film Tunnel Junctions. *Phys. Rev. Lett.*, 74:3273–3276.

[134] Moore, G. E. (1965). Cramming more components onto integrated circuits. *Electronics*, 38(8).

[135] Morawe, C. and Zabel, H. (1995). Structure and thermal stability of sputtered metal/oxide multilayers: The case of Co/Al_2O_3. *Journal of Applied Physics*, 77(5):1969–1976.

[136] Moriya, T. (1960). Anisotropic superexchange interaction and weak ferromagnetism. *Physical Review*, 120(1):91.

[137] Mott, N. (1936). The electrical conductivity of transition metals. 153(880):699–717.

[138] Mott, N. F. (1949). The basis of the electron theory of metals, with special reference to the transition metals. *Proceedings of the Physical Society. Section A*, 62(7):416.

[139] Murthy, V. (2003). *Structure and properties of engineering materials.* Tata McGraw-Hill Education.

[140] Myers, H. P. and Sucksmith, W. (1951). The Spontaneous Magnetization of Cobalt. *Proceedings of the Royal Society of London A: Mathematical, Physical and Engineering Sciences*, 207(1091):427–446.

[141] Nagaosa, N., Sinova, J., Onoda, S., MacDonald, A. H., and Ong, N. P. (2010). Anomalous Hall effect. *Rev. Mod. Phys.*, 82:1539–1592.

[142] Nakajima, N., Koide, T., Shidara, T., Miyauchi, H., Fukutani, H., Fujimori, A., Iio, K., Katayama, T., Nývlt, M., and Suzuki, Y. (1998). Perpendicular Magnetic Anisotropy Caused by Interfacial Hybridization via Enhanced Orbital Moment inCo/Pt Multilayers: Magnetic Circular X-Ray Dichroism Study. *Phys. Rev. Lett.*, 81:5229–5232.

[143] Néel, L. (1949). Théorie du trainage magnétique des ferromagnétiques en grains fins avec application aux terres cuites. *Ann. Geophys.*, 5(99):99–136.

[144] Néel, L. (1954). Anisotropie magnétique superficielle et surstructures d'orientation. *J. Phys. Radium*, 15(4):225–239.

[145] Néel, L. (1967). Etude théorique du couplage ferro-antiferromagnétique dans les couches minces. *Ann. Phys. (Paris)*, 2:61–80.

[146] Nevot, L. and Croce, P. (1980). Caracterisation des surfaces par reflexion rasante de rayons X. Application a l'etude du polissage de quelques verres silicates. *Rev Phys Appl*, 15 (3):761 779.

[147] Ney, O., Trzeciecki, M., and Hubner, W. (2002). Femtosecond dynamics of spin-dependent SHG response from NiO(001). *Applied Physics B*, 74(7-8):741–744.

[148] Nistor, L., Rodmacq, B., Ducruet, C., Portemont, C., Prejbeanu, I., and Dieny, B. (2010). Correlation Between Perpendicular Anisotropy and Magnetoresistance in Magnetic Tunnel Junctions. *Magnetics, IEEE Transactions on*, 46(6):1412 –1415.

[149] Nistor, L. E. (2011). *Magnetic tunnel junctions with perpendicular magnetization: anisotropy, magnetoresistance, magnetic coupling and spin transfer torque switching*. PhD thesis, Grenoble University.

[150] Nistor, L. E., Rodmacq, B., Auffret, S., and Dieny, B. (2009). Pt/Co/oxide and oxide/Co/Pt electrodes for perpendicular magnetic tunnel junctions. *Applied Physics Letters*, 94(1).

[151] Nogués, J., Lederman, D., Moran, T., and Schuller, I. K. (1996). Positive Exchange Bias in Fe F 2-Fe Bilayers. *Physical review letters*, 76(24):4624.

[152] Nogués, J., Leighton, C., and Schuller, I. K. (2000). Correlation between antiferromagnetic interface coupling and positive exchange bias. *Physical Review B*, 61(2):1315.

[153] Nogues, J. and Schuller, I. K. (1999). Exchange bias. *Journal of Magnetism and Magnetic Materials*, 192(2):203 – 232.

[154] O'Grady, K., Fernandez-Outon, L. E., and Vallejo Fernandez, G. (2010). A new paradigm for exchange bias in polycrystalline thin films. *Journal of Magnetism and Magnetic Materials*, 322(8):883–899.

[155] O'Handley, R. C. (2000). *Modern magnetic materials: principles and applications*, volume 830622677. Wiley New York.

[156] Ohmori, H., Hatori, T., and Nakagawa, S. (2008). Perpendicular magnetic tunnel junction with tunneling magnetoresistance ratio of 64% using MgO (100) barrier layer prepared at room temperature. *Journal of Applied Physics*, 103(7):07A911.

[157] Ouyang, H., Han, Y.-H., Lo, S.-C., Su, C.-H., Shiu, Y.-R., Lin, K.-W., Desautels, R. D., and van Lierop, J. (2010). Tailoring perpendicular magnetic anisotropy in ultrathin Co/Pt multilayers coupled to NiO. *Phys. Rev. B*, 81:224412.

[158] Paladino, A. E. and Coble, R. L. (1963). Effect Of Grain Boundaries on Diffusion-Controlled Processes in Aluminum Oxide. *Journal of the American Ceramic Society*, 46(3):133–136.

[159] Park, B. G., Wunderlich, J., Martí, X., Holý, V., Kurosaki, Y., Yamada, M., Yamamoto, H., Nishide, A., Hayakawa, J., Takahashi, H., Shick, A. B., and Jungwirth, T. (2011). A spin-valve-like magnetoresistance of an antiferromagnet-based tunnel junction. *Nat Mater*, 10(5):347–351.

[160] Park, B. G., Wunderlich, J., Williams, D. A., Joo, S. J., Jung, K. Y., Shin, K. H., Olejnik, K., Shick, A. B., and Jungwirth, T. (2008). Tunneling Anisotropic Magnetoresistance in Multilayer-(Co/Pt)/AlOx/Pt Structures. *Phys. Rev. Lett.*, 100:087204.

[161] Parkin, S., Jiang, X., Kaiser, C., Panchula, A., Roche, K., and Samant, M. (2003). Magnetically engineered spintronic sensors and memory. *Proceedings of the IEEE*, 91(5):661–680.

[162] Parkin, S. S., Kaiser, C., Panchula, A., Rice, P. M., Hughes, B., Samant, M., and Yang, S.-H. (2004). Giant tunnelling magnetoresistance at room temperature with MgO (100) tunnel barriers. *Nature materials*, 3(12):862–867.

[163] Parrat, L. G. (1954). Surface studies of solids by total reflexion of x-rays. *Physical Review*, 95:359 369.

[164] Plumer, M. L., Van Ek, J., and Weller, D. (2012). *The physics of ultra-high-density magnetic recording*, volume 41. Springer Science & Business Media.

[165] QuantumDesign (2015). Magnetic Property Measurement System - SQUID VSM User's Manual. *Quantum Design*.

[166] Queste, S., Dubourg, S., Acher, O., Soret, J.-C., Barholz, K.-U., and Mattheis, R. (2005). Microwave permeability study for antiferromagnet thickness dependence on exchange bias field in nife/lrmn layers. *Journal of Magnetism and Magnetic Materials*, 288:60 – 65.

[167] Radu, F., Etzkorn, M., Siebrecht, R., Schmitte, T., Westerholt, K., and Zabel, H. (2003). Interfacial domain formation during magnetization reversal in exchange-biased CoO/Co bilayers. *Phys. Rev. B*, 67:134409.

[168] Ranno, L. (2014). Introduction to magnetism. *JDN 20 - Neutrons et Magnetisme*, 13.

[169] Ringpfeil, C., Lutzenkirchen-Hecht, D., and Frahm, R. (2007). In-situ investigations of magnetron sputtering processes with laboratory X-ray equipment. *Thin Solid Films*, 515(14):5597–5600.

[170] Rodmacq, B., Auffret, S., Dieny, B., Monso, S., and Boyer, P. (2003). Crossovers from in-plane to perpendicular anisotropy in magnetic tunnel junctions as a function of the barrier degree of oxidation. *Journal of Applied Physics*, 93(10):7513–7515.

[171] Rodmacq, B., Manchon, A., Ducruet, C., Auffret, S., and Dieny, B. (2009). Influence of thermal annealing on the perpendicular magnetic anisotropy of Pt/Co/AlOx trilayers. *Phys. Rev. B*, 79:024423.

[172] Ross, C. A. (2001). Patterned magnetic recording media. *Annual Review of Materials Research*, 31(1):203–235.

[173] Roth, W. L. (1958). Magnetic Structures of MnO, FeO, CoO, and NiO. *Phys. Rev.*, 110:1333–1341.

[174] Ruderman, M. A. and Kittel, C. (1954). Indirect exchange coupling of nuclear magnetic moments by conduction electrons. *Physical Review*, 96(1):99.

[175] Ruster, C., Gould, C., Jungwirth, T., Sinova, J., Schott, G. M., Giraud, R., Brunner, K., Schmidt, G., and Molenkamp, L. W. (2005). Very Large Tunneling Anisotropic Magnetoresistance of a (Ga,Mn)As/GaAs/(Ga,Mn)As Stack. *Phys. Rev. Lett.*, 94:027203.

[176] Sagawa, M. and Hirosawa, S. (1988). Coercivity and microstructure of R-Fe-B sintered permanent magnets. *Le Journal de Physique Colloques*, 49(C8):C8–617.

[177] Saito, H., Yuasa, S., and Ando, K. (2005). Origin of the Tunnel Anisotropic Magnetoresistance in $Ga_{1-x}Mn_xAs/ZnSe/Ga_{1-x}Mn_xAs$ Magnetic Tunnel Junctions of II-VI/III-V Heterostructures. *Phys. Rev. Lett.*, 95:086604.

[178] Sarma, S. D. (2001). A new class of device based on electron spin, rather than on charge, may yield the next generation of microelectronics. *American Scientist*, 89(6):516.

[179] Sbiaa, R., Lua, S. Y. H., Law, R., Meng, H., Lye, R., and Tan, H. K. (2011a). Reduction of switching current by spin transfer torque effect in perpendicular anisotropy magnetoresistive devices. *Journal of Applied Physics*, 109(7).

[180] Sbiaa, R., Meng, H., and Piramanayagam, S. N. (2011b). Materials with perpendicular magnetic anisotropy for magnetic random access memory. *physica status solidi - Rapid Research Letters*, 5(12):413–419.

[181] Schellekens, A., Van den Brink, A., Franken, J., Swagten, H., and Koopmans, B. (2012). Electric-field control of domain wall motion in perpendicularly magnetized materials. *Nature Communications*, 3:847.

[182] Schmitz-Antoniak, C., Schmitz, D., Borisov, P., de Groot, F. M., Stienen, S., Warland, A., Krumme, B., Feyerherm, R., Dudzik, E., Kleemann, W., et al. (2013). Electric in-plane polarization in multiferroic $CoFe_2O_4/BaTiO_3$ nanocomposite tuned by magnetic fields. *Nature communications*, 4.

[183] Schneider, C. M., Bressler, P., Schuster, P., Kirschner, J., de Miguel, J. J., and Miranda, R. (1990). Curie temperature of ultrathin films of fcc-cobalt epitaxially grown on atomically flat Cu(100) surfaces. *Phys. Rev. Lett.*, 64:1059–1062.

[184] Schrön, A., Rödl, C., and Bechstedt, F. (2012). Crystalline and magnetic anisotropy of the 3 d-transition metal monoxides MnO, FeO, CoO, and NiO. *Physical Review B*, 86(11):115134.

[185] Shang, C. H., Nowak, J., Jansen, R., and Moodera, J. S. (1998). Temperature dependence of magnetoresistance and surface magnetization in ferromagnetic tunnel junctions. *Phys. Rev. B*, 58:R2917–R2920.

[186] Shick, A. B., Khmelevskyi, S., Mryasov, O. N., Wunderlich, J., and Jungwirth, T. (2010). Spin-orbit coupling induced anisotropy effects in bimetallic antiferromagnets: A route towards antiferromagnetic spintronics. *Phys. Rev. B*, 81:212409.

[187] Shick, A. B., Máca, F., Mašek, J., and Jungwirth, T. (2006). Prospect for room temperature tunneling anisotropic magnetoresistance effect: Density of states anisotropies in CoPt systems. *Phys. Rev. B*, 73:024418.

[188] Shipton, E., Chan, K., Hauet, T., Hellwig, O., and Fullerton, E. E. (2009). Suppression of the perpendicular anisotropy at the CoO Neel temperature in exchange-biased CoO/[Co/Pt] multilayers. *Applied Physics Letters*, 95(13).

[189] Shirane, G., Nathans, R., and Chen, C. (1964). Magnetic moments and unpaired spin densities in the Fe-Rh alloys. *Physical Review*, 134(6A):A1547.

[190] Simmons, J. G. (1963). Generalized Formula for the Electric Tunnel Effect between Similar Electrodes Separated by a Thin Insulating Film. *Journal of Applied Physics*, 34(6):1793–1803.

[191] Sinova, J., Culcer, D., Niu, Q., Sinitsyn, N., Jungwirth, T., and MacDonald, A. (2004). Universal intrinsic spin Hall effect. *Physical review letters*, 92(12):126603.

[192] Sinova, J. and Zutic, I. (2012). New moves in the spintronics tango. *Nature materials*, 11(5):368–371.

[193] Slonczewski, J. (1996). Current-driven excitation of magnetic multilayers. *Journal of Magnetism and Magnetic Materials*, 159(1-2):L1–L7.

[194] Smardz, L., Kobler, U., and Zinn, W. (1991). Temperature and thickness dependence of unidirectional magnetic anisotropy effects in Co/CoO thin films. *Vacuum*, 42(4):283–285.

[195] Smardz, L., Kobler, U., and Zinn, W. (1992). Oxidation kinetics of thin and ultrathin cobalt films. *Journal of Applied Physics*, 71(10):5199–5204.

[196] Smit, J. (1955). The spontaneous hall effect in ferromagnetics I. *Physica*, 21(6-10):877 – 887.

[197] Smits, A. A. (2001). *Tunnel Junction: noise and barrier characterization*. PhD thesis, Eindhoven University of Technology. ISBN 90-386-1809-3.

[198] Sort, J., Baltz, V., Garcia, F., Rodmacq, B., and Dieny, B. (2005). Tailoring perpendicular exchange bias in [Pt/Co]-IrMn multilayers. *Phys. Rev. B*, 71:054411.

[199] Sousa, R. C., Sun, J. J., Soares, V., Freitas, P. P., Kling, A., da Silva, M. F., and Soares, J. C. (1998). Large tunneling magnetoresistance enhancement by thermal anneal. *Applied Physics Letters*, 73(22):3288–3290.

[200] Sproul, W., Christie, D., and Carter, D. (2005). Control of reactive sputtering processes. *Thin Solid Films*, 491(1-2):1–17.

[201] Stiles, M. and Zangwill, A. (2002). Anatomy of spin-transfer torque. *Physical Review B*, 66(1):014407.

[202] Stiles, M. D. and McMichael, R. D. (2001). Coercivity in exchange-bias bilayers. *Phys. Rev. B*, 63:064405.

[203] Stoner, E. C. and Wohlfarth, E. P. (1948). A Mechanism of Magnetic Hysteresis in Heterogeneous Alloys. *Philosophical Transactions of the Royal Society of London. Series A, Mathematical and Physical Sciences*, 240(826):599–642.

[204] Stuart, R. V. and Wehner, G. K. (1964). Energy Distribution of Sputtered Cu Atoms. *Journal of Applied Physics*, 35(6):1819–1824.

[205] Sugimoto, T., Katayama, T., Suzuki, Y., Hashimoto, M., Nishihara, Y., Itoh, A., and Kawanishi, K. (1992). Temperature dependence of perpendicular magnetic anisotropy in Co/Au and Co/Pt multilayers. *Journal of Magnetism and Magnetic Materials*, 104:1845 – 1846.

[206] Suntola, T. and Antson, J. (1977). U.s. patent.

[207] Suzuki, T. (1995). Coercivity mechanism in (CoPt) and (CoPd) multilayers . *Scripta Metallurgica et Materialia*, 33(10-11):1609 – 1623. Proceedings of an Acta Metallurgica Meeting on Novel Magnetic Structures and Properties.

[208] Takano, K., Kodama, R. H., Berkowitz, A. E., Cao, W., and Thomas, G. (1997). Interfacial Uncompensated Antiferromagnetic Spins: Role in Unidirectional Anisotropy in Polycrystalline $Ni_{81}Fe_{19}$/CoO Bilayers. *Phys. Rev. Lett.*, 79:1130–1133.

[209] Tang, D. D. and Lee, Y.-J. (2010). *Magnetic memory: fundamentals and technology*. Cambridge University Press.

[210] Tang, Y. J., Smith, D. J., Zink, B. L., Hellman, F., and Berkowitz, A. E. (2003). Finite size effects on the moment and ordering temperature in antiferromagnetic CoO layers. *Phys. Rev. B*, 67:054408.

[211] Tannous, C. and Gieraltowski, J. (2008). The Stoner-Wohlfarth model of ferromagnetism. *European Journal of Physics*, 29(3):475.

[212] Thiaville, A., Rohart, S., Jué, É., Cros, V., and Fert, A. (2012). Dynamics of Dzyaloshinskii domain walls in ultrathin magnetic films. *EPL (Europhysics Letters)*, 100(5):57002.

[213] Thomson, W. (1856). On the Electro-Dynamic Qualities of Metals: Effects of Magnetization on the Electric Conductivity of Nickel and of Iron. *Proceedings of the Royal Society of London*, 8:546–550.

[214] Tsymbal, E. Y., Mryasov, O. N., and LeClair, P. R. (2003). Spin-dependent tunnelling in magnetic tunnel junctions. *Journal of Physics: Condensed Matter*, 15(4):R109.

[215] Uchida, E., Fukuoka, N., Kondoh, H., Takeda, T., Nakazumi, Y., and Nagamiya, T. (1964). Magnetic Anisotropy Measurements of CoO Single Crystal. *Journal of the Physical Society of Japan*, 19:2088.

[216] Uemura, T., Imai, Y., Harada, M., Matsuda, K.-i., and Yamamoto, M. (2009). Tunneling anisotropic magnetoresistance in epitaxial CoFe/n-GaAs junctions. *Applied Physics Letters*, 94(18).

[217] Uhlenbeck, G. E. and Goudsmit, S. (1925). Ersetzung der Hypothese vom unmechanischen Zwang durch eine Forderung bezüglich des inneren Verhaltens jedes einzelnen Elektrons. *Naturwissenschaften*, 13(47):953–954.

[218] Ulyanenkov, A. (2006). Novel methods and universal software for HRXRD, XRR and GISAXS data interpretation. *Applied Surface Science*, 253(1):106 – 111. Proceedings of the E-MRS 2005 Spring Meeting Symposium P: Current trends in optical and X-ray metrology of advanced materials for nanoscale devicesEMRS 2005 - P.

[219] Valenzuela, S. O. and Tinkham, M. (2006). Direct electronic measurement of the spin Hall effect. *Nature*, 442(7099):176–179.

[220] Vallejo-Fernandez, G., Fernandez-Outon, L. E., and O'Grady, K. (2008). Antiferromagnetic grain volume effects in metallic polycrystalline exchange bias systems. *Journal of Physics D: Applied Physics*, 41(11):112001.

[221] Van der Pauw, L. (1958). A Method of Measuring Specific Resistivity and Hall Effect of Discs of Arbitrary Shapes. *Philips Research Reports*, 13:1 9.

[222] Victora, R. and Shen, X. (2005). Composite media for perpendicular magnetic recording. *Magnetics, IEEE Transactions on*, 41(2):537–542.

[223] Walter, C. (2005). Kryder's law. *Scientific American*, 293(2):32–33.

[224] Wang, D.-s., Wu, R., and Freeman, A. J. (1993). Magnetocrystalline anisotropy of Co-Pd interfaces. *Phys. Rev. B*, 48:15886–15892.

[225] Wang, J., Sannomiya, T., Shi, J., and Nakamura, Y. (2013a). Perpendicular magnetic anisotropy and perpendicular exchange bias in sputter-deposited CoO/CoPt multilayer. *Journal of Applied Physics*, 113(17):170 714.

[226] Wang, J.-S. and Evans, A. (1998). Measurement and analysis of buckling and buckle propagation in compressed oxide layers on superalloy substrates. *Acta Materialia*, 46(14):4993 – 5005.

[227] Wang, K., Tran, T. L. A., Brinks, P., Sanderink, J. G. M., Bolhuis, T., van der Wiel, W. G., and de Jong, M. P. (2013b). Tunneling anisotropic magnetoresistance in Co/AlO_x/Al tunnel junctions with fcc Co (111) electrodes. *Phys. Rev. B*, 88:054407.

[228] Wang, Y. Y., Song, C., Cui, B., Wang, G. Y., Zeng, F., and Pan, F. (2012). Room-Temperature Perpendicular Exchange Coupling and Tunneling Anisotropic Magnetoresistance in an Antiferromagnet-Based Tunnel Junction. *Phys. Rev. Lett.*, 109:137201.

[229] Weller, D. and Moser, A. (1999). Thermal effect limits in ultrahigh-density magnetic recording. *Magnetics, IEEE Transactions on*, 35(6):4423–4439.

[230] Weller, D., Wu, Y., Stöhr, J., Samant, M. G., Hermsmeier, B. D., and Chappert, C. (1994). Orbital magnetic moments of Co in multilayers with perpendicular magnetic anisotropy. *Phys. Rev. B*, 49:12888–12896.

[231] Wolf, S., Treger, D., and Chtchelkanova, A. (2006). Spintronics: The Future of Data Storage? *MRS Bulletin*, 31:400–403.

[232] Wolf, S. A., Awschalom, D. D., Buhrman, R. A., Daughton, J. M., von Molnar, S., Roukes, M. L., Chtchelkanova, A. Y., and Treger, D. M. (2001). Spintronics: A Spin-Based Electronics Vision for the Future. *Science*, 294(5546):1488–1495.

[233] Wunderlich, J., Jungwirth, T., Kaestner, B., Irvine, A. C., Shick, A. B., Stone, N., Wang, K.-Y., Rana, U., Giddings, A. D., Foxon, C. T., Campion, R. P., Williams, D. A., and Gallagher, B. L. (2006). Coulomb Blockade Anisotropic Magnetoresistance Effect in a Ga/Mn/As Single-Electron Transistor. *Phys. Rev. Lett.*, 97:077201.

[234] Xu, Y., Ephron, D., and Beasley, M. R. (1995). Directed inelastic hopping of electrons through metal-insulator-metal tunnel junctions. *Phys. Rev. B*, 52:2843–2859.

[235] Yang, H. X., Chshiev, M., Dieny, B., Lee, J. H., Manchon, A., and Shin, K. H. (2011). First-principles investigation of the very large perpendicular magnetic anisotropy at Fe/MgO and Co/MgO interfaces. *Phys. Rev. B*, 84:054401.

[236] Yokoyama, T., Nakagawa, T., and Takagi, Y. (2008). Magnetic circular dichroism for surface and thin film magnetism: Measurement techniques and surface chemical applications. *International Reviews in Physical Chemistry*, 27(3):449–505.

[237] Yoo, I., Kim, D.-K., and Kim, Y. K. (2005). Switching characteristics of submicrometer magnetic tunnel junction devices with perpendicular anisotropy. *Journal of Applied Physics*, 97(10).

[238] Yuasa, S., Nagahama, T., Fukushima, A., Suzuki, Y., and Ando, K. (2004). Giant room-temperature magnetoresistance in single-crystal Fe/MgO/Fe magnetic tunnel junctions. *Nature materials*, 3(12):868–871.

[239] Zhang, H., Wang, Y., Zheng, G., Shen, J., Shan, Z., and Sellmyer, D. (1993). The temperature dependence of perpendicular anisotropy in Co/Pt and Co/Au multilayer films. *Magnetics, IEEE Transactions on*, 29(6):3376–3378.

[240] Zhang, S., Dimitrov, D., Hadjipanayis, G., Cai, J., and Chien, C. (1999). Coercivity induced by random field at ferromagnetic and antiferromagnetic interfaces. *Journal of magnetism and magnetic materials*, 198:468–470.

[241] Zheng, Y. and Zhu, J.-G. (1997). Switching field variation in patterned submicron magnetic film elements. *Journal of Applied Physics*, 81(8):5471–5473.

Abstract:

In the context of studying magnetic and spintronics phenomena occurring at the nanoscale, we investigated several aspects of Pt/Co/AlOx asymmetric structures. One of the objectives of this thesis was the control of the oxidation and the tailoring of the magnetic properties of these multilayers. We combined structural (X-Ray Reflectivity), transport (Anomalous Hall Effect) and magnetic measurements (VSM-SQUID), to study the interplay of magnetic and interfacial effects. One objective was to analyze the role that few monolayers (MLs) of CoO (which can form when overoxidizing the Al layer), could have on the properties of the stack. We used a wedge deposition techniques to control the oxidation on a subnanometer scale. We established that few MLs of CoO largely affect the total anisotropy of the stack. To further investigate the impact of the CoO, we engineered ultrathin Co(0.6nm)/CoO(0.6nm) bilayers. We performed field cooled measurements on this system and we found a large exchange bias anisotropy. These results indicate that the CoO keeps a large anisotropy even in the ML regime, help to rule out some of the models proposed to explain the exchange bias effect and imply that the usually neglected CoO presence must be considered in the energy balance of the system. We build perpendicular Tunneling Anisotropic MagnetoResistance (TAMR) devices based on the Pt/Co/AlOx structure. The TAMR is a relatively new spintronics effect in which the rotation of the magnetization in a single magnetic electrode (combined with the Spin-Orbit Coupling) can cause a change of the tunnel probability, which manifests as a magnetoresistance effect. We demonstrated that a careful control of the interface oxidation is crucial for the TAMR effect. The large induced magnetic anisotropy allowed us to achieve enhanced TAMR values compared to similar Pt/Co/AlOx structures.

Keywords: Spintronics, Nanomagnetism, Perpendicular Magnetic Anisotropy (PMA), Exchange Bias, Tunnel Anisotropic MagnetoResistance (TAMR), Asymmetric Systems, Pt/Co/AlOx, Co/CoO

Résume:

Dans le cadre de l'étude des phénomènes magnétiques et de la spintronique qui sont présents aux échelles nanométriques nous avons étudié différents aspects de structures asymétriques de Pt/Co/AlOx. L'un des objectifs de cette thèse est le contrôle de l'oxydation et des propriétés magnétiques de ces multicouches. Nous avons combiné les mesures structurales (réflectivité de rayons X), transports (Effet Hall anormal), et magnétiques (VSM-SQUID) afin de déterminer les rôles des effets d'interface sur le magnétisme. Un objectif était d'analyser le rôle de quelques monocouches (MCs) de CoO (qui peuvent se former lors de suroxydation) sur les propriétés de la multicouche. Nous avons utilisé une technique de dépôt avec gradient d'épaisseur d'Al pour contrôler l'oxydation à l'échelle nanométrique. Nous avons établi que quelques monocouches (MCs) de CoO ont un impact sur l'anisotropie de la multicouche. Pour approfondir l'effet de la couche de CoO, nous avons construit des bicouches ultrafines de Co(0.6nm)/CoO(0.6nm). Nous avons effectué une mesure de refroidissement sous champ sur ce système et trouvé un fort effet de champ d'échange. Ces résultats indiquent que la couche CoO garde une forte anisotropie même pour la limite des monocouches et permet de réfuter certains modèles sur l'effet de champ d'échange et indique que les couches de CoO, généralement négligées, doivent être prises en considération dans le bilan énergétique du système. Nous avons construit un dispositif de mesure perpendiculaire de la MagnétoRésistance Tunnel Anisotrope (TAMR) à partir de la structure Pt/Co/AlOx. La TAMR est un effet de spintronique relativement récent dans lequel la rotation d'aimantation dans une électrode magnétique (combiné avec un couplage spin-orbite) peut entrainer un changement de la probabilité de l'effet tunnel, ce qui se manifeste comme un effet de magnétorésistance. Nous avons démontré qu'un contrôle précis de l'état d'oxydation est essentiel pour l'effet de TAMR. La forte anisotropie magnétique induite nous permet d'atteindre des valeurs de TAMR plus forte, comparée à celles de structures similaires de Pt/Co/AlOx.

Mots clés: Spintronique, Nanomagnétisme, Anisotropie Magnétique Perpendiculaire (PMA), Champ d'échange, MagnétoRésistance Tunnel Anisotrope (TAMR), Système asymétriques, Pt/Co/AlOx, Co/CoO